

---

Doctoral Dissertations

Student Theses and Dissertations

---

2013

## Synthetic aperture radar-based techniques and reconfigurable antenna design for microwave imaging of layered structures

Mojtaba Fallahpour

Follow this and additional works at: [https://scholarsmine.mst.edu/doctoral\\_dissertations](https://scholarsmine.mst.edu/doctoral_dissertations)



Part of the [Electrical and Computer Engineering Commons](#)

Department: **Electrical and Computer Engineering**

---

### Recommended Citation

Fallahpour, Mojtaba, "Synthetic aperture radar-based techniques and reconfigurable antenna design for microwave imaging of layered structures" (2013). *Doctoral Dissertations*. 1847.

[https://scholarsmine.mst.edu/doctoral\\_dissertations/1847](https://scholarsmine.mst.edu/doctoral_dissertations/1847)

This thesis is brought to you by Scholars' Mine, a service of the Missouri S&T Library and Learning Resources. This work is protected by U. S. Copyright Law. Unauthorized use including reproduction for redistribution requires the permission of the copyright holder. For more information, please contact [scholarsmine@mst.edu](mailto:scholarsmine@mst.edu).



SYNTHETIC APERTURE RADAR-BASED TECHNIQUES AND  
RECONFIGURABLE ANTENNA DESIGN FOR MICROWAVE IMAGING OF  
LAYERED STRUCTURES

by

MOJTABA FALLAHPUR

A DISSERTATION

Presented to the Faculty of the Graduate School of the  
MISSOURI UNIVERSITY OF SCIENCE AND TECHNOLOGY

In Partial Fulfillment of the Requirements for the Degree

DOCTOR OF PHILOSOPHY

in

ELECTRICAL ENGINEERING

2013

Approved by

Dr. Reza Zoughi, Advisor  
Dr. Richard E. DuBroff  
Dr. David J. Pommerenke  
Dr. Kristen M. Donnell  
Dr. Von L. Richards

© 2013

Mojtaba Fallahpour

All Rights Reserved

## ABSTRACT

In the past several decades, a number of microwave imaging techniques have been developed for detecting embedded objects (targets) in a homogeneous media. New applications such as nondestructive testing of layered composite structures, through-wall and medical imaging require more advanced imaging systems and image reconstruction algorithms (post-processing) suitable for imaging inhomogeneous (i.e., layered) media.

Currently-available imaging algorithms are not always robust, easy to implement, and fast. Synthetic aperture radar (SAR) techniques are some of the more prominent approaches for image reconstruction when considering low loss and homogeneous media. To address limitations of SAR imaging, when interested in imaging an embedded object in an inhomogeneous media with loss, two different methods are introduced, namely; modified piecewise SAR (MPW-SAR) and Wiener filter-based layered SAR (WL-SAR).

From imaging system hardware point-of-view, microwave imaging systems require suitable antennas for signal transmission and data collection. A reconfigurable antenna which its characteristics can be dynamically changed provide significant flexibility in terms of beam-forming, reduction in unwanted noise and multiplicity of use including for imaging applications. However, despite these potentially advantageous characteristics, the field of reconfigurable antenna design is fairly new and there is not a methodical design procedure. This issue is addressed by introducing an organized design method for a reconfigurable antenna capable of operating in several distinct frequency bands. The design constraints (e.g., size and gain) can also be included. Based on this method, a novel reconfigurable coplanar waveguide-fed slot antenna is designed to cover several different frequency bands while keeping the antenna size as small as possible.

## ACKNOWLEDGMENTS

I am grateful with all of my being to my family. I believe I never could have embarked on my Ph.D. journey and finished it without an overwhelming support from my lovely mother and father. I am thankful to my sister for her help and especially for tutoring me in the past when I was trying to self-study over the summer to go directly from the third grade to the fifth grade in elementary school. I owe my older brothers for helping me be prepared for every new high school year over the summer.

I cordially would like to thank my advisor, Dr. Reza Zoughi, for providing me with this opportunity to come here and do my Ph.D. I am thankful for the kind support, encouragement, and the many hours he has devoted to me. I not only learned many technical things from him but also how to look at the world from a different perspective. His statement, “you create your own world”, helped me to find my path in early days in here when I was trying to adapt to the place.

I would like to thank Dr. Richard E. DuBroff, Dr. David J. Pommerenke, Dr. Von L. Richards, and Dr. Kristen M. Donnell for serving on my committee and for their valuable effort and the time they spent on my dissertation.

I would also like to thank all my dear teachers, colleagues, and friends, at Applied Microwave Nondestructive Testing Lab (amntl) and Electromagnetic Compatibility (EMC) lab, in particular Dr. Jun Fan, Dr. Sergiy Kharkovsky, Dr. Mohammad Tayeb Ghasr, Dr. Joseph T. Case, Dr. Hamed Kajbaf, Mr. Ashkan Hashemi, Mr. Ali Foudazi, Mr. Arpit Kothari, Mr. Matthew Kempin, and Mr. Sanjay Tadepally.

I would like to acknowledge the American Society for Nondestructive Testing (ASNT) for supporting this work partially by granting me a Graduate Fellowship Award (2009). Also, this research was in part sponsored by the Army Research Laboratory and was accomplished under Cooperative Agreement Number W911NF-10-2-0077. The views and conclusions contained in this document are those of the authors and should not be interpreted as representing the official policies, either expressed or implied, of the Army Research Laboratory or the U.S. Government. The U.S. Government is authorized to reproduce and distribute reprints for Government purposes not withstanding any copyright notation herein.

## TABLE OF CONTENTS

	Page
ABSTRACT .....	iii
ACKNOWLEDGMENTS .....	iv
LIST OF ILLUSTRATIONS .....	viii
LIST OF TABLES .....	xiv
NOMENCLATURE .....	xv
SECTION	
1. INTRODUCTION .....	1
1.1. BACKGROUND AND MOTIVATIONS .....	1
1.2. OBJECTIVES AND OVERVIEW OF DISSERTATION .....	7
2. FIELD CALCULATION IN A LAYERED STRUCTURE USING GREEN'S FUNCTION .....	9
2.1. INTRODUCTION .....	9
2.2. WAVE PROPAGATION INSIDE A PLANAR LAYERED STRUCTURE ..	12
2.3. A POINT SOURCE EMBEDDED IN A LAYERED STRUCTURE.....	13
2.3.1. Propagation Factor in Region 1 ( $z \in \text{layer } n, z' \in \text{layer } m, n < m$ ) .....	15
2.3.2. Propagation Factor in Region 2 ( $z \in \text{layer } n, z' \in \text{layer } m, n = m$ ) .....	15
2.3.3. Propagation Factor in Region 3 ( $z \in \text{layer } n, z' \in \text{layer } m, n > m$ ) .....	16
2.3.4. Scalar Green's Function Calculation for Layered Structure .....	16
2.3.5. Examples .....	16
2.4. A VECTOR DISTRIBUTED SOURCE IN A LAYERED STRUCTURE .....	20
2.4.1. Calculation of $\bar{\bar{G}}_e(\vec{r}, \vec{r}')$ .....	22
2.4.2. Calculation of $\bar{\nabla} \times \bar{\bar{G}}_e(\vec{r}, \vec{r}')$ .....	25
2.4.3. Embedded Electric Dipole Antenna in a Layered Structure. ....	28
2.5. CONCLUSION .....	29
3. SAR-BASED MICROWAVE IMAGING OF EMBEDDED ACIVE TARGETS .	31
3.1. INTRODUCTION .....	31
3.2. RELATIONSHIP BETWEEN QUALITATIVE IMAGE AND COLLECTED DATA.....	34

3.3. SAR ALGORITHM.....	37
3.4. MODIFIED PIECEWISE SAR ALGORITHM .....	38
3.5. WIENER FILTER-BASED SAR .....	40
3.6. SIMULATIONS .....	43
3.6.1. Finding a Radiating Trace in a Single Layer PCB .....	45
3.6.2. Locating Radiating Traces in Multilayered PCB. ....	51
3.6.3. Experimental Result .....	55
3.7. CONCLUSION.....	58
4. MONOSTATIC SAR-BASED MICROWAVE IMAGING OF EMBEDDED PASSIVE OBJECTS.....	59
4.1. INTRODUCTION .....	59
4.2. MONOSTATIC SAR AND MPW-SAR .....	60
4.3. MONOSTATIC WL-SAR .....	60
4.4. SIMULATION AND MEASUREMENT SETUP .....	61
4.5. SIMULATION RESULTS .....	63
4.5.1. Detecting Corrosion in Reinforcing Steel Bars in Concrete Structures .	63
4.5.2. Intra-Wall Imaging .....	69
4.5.3. Through-Wall Imaging.....	73
4.6. EXPERIMENTAL RESULTS .....	75
4.7. 3D IMAGE RECONSTRUCTION.....	81
4.8. CONCLUSION: COMPARING PERFORMANCE OF DIFFERENT IMAGING METHODS .....	86
5. ANTENNA DESIGN FOR HARDWARE PART OF MICROWAVE IMAGING SYSTEM .....	88
5.1. INTRODUCTION.....	88
5.2. SUMMARY OF ANTENNA MINIATURIZATION TECHNIQUES .....	89
5.2.1. Topology-Based Miniaturization Techniques .....	90
5.2.1.1 Fractal antennas. ....	90
5.2.1.2 Reactively loaded antennas.....	93
5.2.1.3 Antenna with engineered ground plane. ....	99
5.2.1.4 Meander antennas.. ....	101
5.2.2. Material-Based Miniaturization Techniques .....	102



5.2.2.1 Application of high dielectric constant substrate.....	102
5.2.2.2 Metamaterial - based miniaturization techniques. ....	104
5.3. SUMMARY ON MINIATURIZED WIDEBAND ANTENNAS.....	105
5.3.1. Miniaturization of LPDA Antenna Using Fractal Tree.....	108
5.3.2. Meander Wide Band Antennas.....	110
5.3.3. Corrugation.....	112
5.4. RECONFIGURABLE ANTENNAS .....	114
5.4.1. Reconfigurable Antenna Based on Different Switch Technologies.....	115
5.4.2. Reconfigurable Antenna Design Using Varactor Diode .....	120
5.4.3. Reconfigurable Antenna Using Tunable Materials .....	122
5.5. CONCLUSION.....	123
6. DESIGN AND IMPLEMENTATION OF RECONFIGURABLE ANTENNAS .	125
6.1. INTRODUCTION .....	125
6.2. APPROACH AND METHODOLOGY FOR DESIGNING RECONFIGURABLE ANTENNAS .....	125
6.3. DESIGN AND IMPLEMENTATION OF A PROTOTYPE RECONFIGURABLE ANTENNA.....	131
6.3.1. Design 1: Reconfigurable Antenna Covering Three Bands at UHF / L . ....	131
6.3.1.1 Adding reconfigurability to the antenna.....	136
6.3.1.2 Fabrication, test, and measurement.....	145
6.3.2. Design 2: Reconfigurable Antenna Covering Four Different Bands at VHF/UHF/L.....	149
6.3.3. Design3: Reconfigurable Antenna Covering Four Different Bands at VHF/UHF/L.....	159
6.3.4. Gain Pattern Measurement .....	169
6.4. CONCLUSION.....	181
7. SUMMARY AND FUTURE WORK.....	183
BIBLIOGRAPHY.....	187
VITA.....	200

## LIST OF ILLUSTRATIONS

	Page
Figure 1.1. A general view of a microwave imaging system.....	2
Figure 1.2. An embedded object in a planar layered structure. ....	5
Figure 2.1. Planar wave reflection and transmission at boundaries of a planar layered structure ( $\rho = \text{TEM, TE, TM}$ ). ....	9
Figure 2.2. An embedded distributed source in a planar layered structure.....	12
Figure 2.3. Calculated real part of $E_z$ . ....	18
Figure 2.4. Calculated real part of $E_z$ . ....	18
Figure 2.5. Calculated scalar Green's function for Example 2.....	19
Figure 2.6. Calculated scalar Green's function for Example 3.....	21
Figure 3.1. Using a collection of distributed probes to measure field distribution for an embedded active target inside of a planar layered structure.....	32
Figure 3.2. Flow-chart of MPW-SAR.....	40
Figure 3.3. Flowchart of the WL-SAR algorithm.....	44
Figure 3.4. Configuration of Simulation 1.....	46
Figure 3.5. Calculated electric field distribution. ....	46
Figure 3.6. Collected data at 10 GHz.....	47
Figure 3.7. Image for Simulation 1.....	49
Figure 3.8. Calculated $ \bar{G}^{RT} _{\text{Region}}^2 /  \bar{G}^{RT} _{\text{max}}^2$ for two different values of $z' = -0.6\text{ cm}$ and $z' = -3\text{ cm}$ at 10 GHz. ....	50
Figure 3.9. Images for Simulation 1 using WL-SAR. ....	51
Figure 3.10. Simulation 2.....	53
Figure 3.11. Calculated $ \bar{G}^{RT} _{\text{Region}}^2 /  \bar{G}^{RT} _{\text{max}}^2$ for three different values: $z' = -1\text{ cm}$ , $z' = -14\text{ cm}$ , and $z' = -38\text{ cm}$ .....	53
Figure 3.12. Reconstructed images for Simulation 2 using WL-SAR.....	54
Figure 3.13. Reconstructed images for Simulation 2 after introducing extra loss.....	55
Figure 3.14. Measurement setup for Experiment 1.....	56
Figure 3.15. Image for Experiment 1.....	57
Figure 3.16. Reconstructed image for Experiment1 using WL-SAR( $\alpha = -35\text{ dB}$ ). ....	57

Figure 4.1. Simulation 1.....	64
Figure 4.2. Image for Simulation 1.....	66
Figure 4.3. Calculated $ \bar{G}^{RT} _{Region}^2 /  \bar{G}^{RT} _{max}^2$ for two different values $z' = -2.5\text{ cm}$ , and $z' = -8.5\text{ cm}$ at 10 GHz. ....	66
Figure 4.4. Images for Simulation 1 using WL-SAR.....	67
Figure 4.5. Image for Simulation 1 using modified WL-SAR with $\alpha = -50\text{ dB}$ .....	68
Figure 4.6. Simulation 2.....	69
Figure 4.7. Produced images for Simulation 2.....	70
Figure 4.8. Calculated $ \bar{G}^{RT} _{Region}^2 /  \bar{G}^{RT} _{max}^2$ for two different values $z' = -2\text{ cm}$ , and $z' = -12\text{ cm}$ at 10 GHz.....	72
Figure 4.9. Produced image for Simulation 2 using WL-SAR with $\alpha = -30\text{ dB}$ .....	72
Figure 4.10. Simulation 3.....	73
Figure 4.11. Produced images for Simulation 3.....	75
Figure 4.12. Produced image for Simulation 3 using WL-SAR with $\alpha = -35\text{ dB}$ .....	76
Figure 4.13. Sample R4.....	76
Figure 4.14. Image for Experiment 1.....	77
Figure 4.15. Produced image for Experiment 1 using WL-SAR with $\alpha = -40\text{ dB}$ .....	78
Figure 4.16. Sample R2.....	79
Figure 4.17. Reconstructed images for R2 for different scans.....	80
Figure 4.18. Reconstructed images for R2 using WL-SAR ( $\Gamma_{x'}$ ) ( $\alpha = -50\text{ dB}$ ).....	81
Figure 4.19. Measurement setup for flipped R4 sample to be used for 3D image reconstruction (Experiment 3).....	82
Figure 4.20. Reconstructed 3D images for R4 flipped at X-band.....	83
Figure 4.21. One slice at $z = -9.5\text{ cm}$ of the produced volumetric image for flipped R4 sample.....	84
Figure 4.22. Reconstructed 3D images for R4 at K-band.....	85
Figure 4.23. One slice at $z = -1.8\text{ cm}$ of the produced volumetric image for R2 sample.....	86
Figure 5.1. Koch curve generations [29]. ....	91
Figure 5.2. Koch snowflake geometry in different iterations. ....	91
Figure 5.3. Sierpinski gasket geometry over different iterations.....	92
Figure 5.4. Minkowski island fractal geometry over different iterations. ....	92
Figure 5.5. CPW-fed modified Koch fractal slot antenna. ....	93

Figure 5.6. Capacitor-loaded PIFA.....	94
Figure 5.7. Measurement and simulation results for loaded and unloaded PIFA [90]. ....	94
Figure 5.8. Capacitive loaded HF slot loop antenna.....	95
Figure 5.9. Measurement and simulation results for HF slot loop antenna with/without L-section matching circuit [90]. .....	95
Figure 5.10. Miniaturized resonant slot antenna [92]. .....	96
Figure 5.11. $S_{11}$ for miniaturized resonant slot antenna [92]. .....	97
Figure 5.12. Symmetrically loaded slot antenna and its feed designed to operate at 300 MHz [93]. .....	97
Figure 5.13. Simulated and measured $S_{11}$ for symmetrically loaded slot antenna [93]. ....	98
Figure 5.14. Miniaturized folded-slot antenna fed by capacitively coupled CPW line [94]. .....	98
Figure 5.15. Antenna with DGS. ....	99
Figure 5.16. Miniaturized microstrip antenna with dumbbell shaped DGS [98]. ....	100
Figure 5.17. A comparison between return loss of the antenna with DGS and conventional antenna without DGS [98]. .....	100
Figure 5.18. Evolution of a circularly polarized compact meandered-grid microstrip antenna from a solid microstrip antenna.....	101
Figure 5.19. ALEN ALN-9540 squiggle RFID tag [104]. .....	101
Figure 5.20. Optimized miniaturized spiral meander line antenna (unit: mm) [105]. ....	102
Figure 5.21. Two different slot spiral antennas (twin and double twin slots) etched on high permittivity dielectric material [107]. .....	103
Figure 5.22. Measured return loss.....	104
Figure 5.23. Rectangular patch antenna.....	105
Figure 5.24. Fractal tree log-periodic dipole antenna [112]. .....	108
Figure 5.25. $VSWR$ of the fractal tree log periodic dipole antenna [112]. .....	108
Figure 5.26. Configuration of improved fractal tree LPDA [113]. .....	109
Figure 5.27. The gain of improved fractal tree LPDA [113]. .....	109
Figure 5.28. Optimized meander Archimedean spiral antenna [114]. .....	110
Figure 5.29. $VSWR$ of meander Archimedean spiral antenna and classic one [114]. ....	110
Figure 5.30. UWB tapered horn antenna with zigzag arms to improve performance at low frequencies [115]. .....	111
Figure 5.31. Measured $S_{11}$ of the fabricated horn antenna with zigzag arms [115]. ....	111
Figure 5.32. The introduced UWB antenna in [118]. .....	112
Figure 5.33. Return loss for different configurations shown in Fig. 5.30 [118]. .....	113

Figure 5.34. Carrier-to-noise ratios for a GPS module connected to multiband and reconfigurable antennas with a 2.4 GHz jamming signal injected for a limited time [25].	114
Figure 5.35. Reconfigurable ground-slotted patch antenna loaded with PIN diode switches [122].	117
Figure 5.36. Polarization reconfigurable PIN diode-loaded slotted-patch antenna [119],[123].	118
Figure 5.37. Reconfigurable UWB antenna using MEMS [119],[125].	119
Figure 5.38. Open/closure domains for Reed switch in the switch plane [126].	120
Figure 5.39. Prototype reconfigurable hexagonal patch antenna with reed switch.	120
Figure 5.40. Reconfigurable dual-band slot antenna using varactor loading [27].	121
Figure 5.41. The varactor diode-loaded resonant elliptical slot antenna	122
Figure 5.42. Reconfigurable patch antenna using tunable conductivity silicon [128]-[129].	123
Figure 6.1. Flow-chart for designing a regular antenna.	127
Figure 6.2. Flow-chart for optimization procedure which may be used in antenna design.	128
Figure 6.3. Flow-chart for designing a reconfigurable antenna using switching methodology.	130
Figure 6.4. Investigated bow-tie antenna and several of its investigated modified versions (red arrow shows excitation source and blue arrow shows PIN diode).	132
Figure 6.5. Different versions of nonuniform bow-tie antenna (red arrow shows excitation source).	133
Figure 6.6. Some of the modified versions of ring slot antenna with slot line loading.	134
Figure 6.7. Investigated CPW-fed square slot antenna with different tuning stubs.	135
Figure 6.8. Optimally designed Antenna 3	137
Figure 6.9. Simulated $S_{11}$ for Antenna 3 using CST Microwave Studio.	137
Figure 6.10. Some of the investigated ideas on Antenna 3 to reduce its resonant frequency.	139
Figure 6.11. Optimally-designed Antenna 2	139
Figure 6.12. Simulated $S_{11}$ of Antenna 2 using CST Microwave Studio.	140
Figure 6.13. Optimally designed Antenna 1	140
Figure 6.14. Simulated $S_{11}$ of Antenna 1 using CST Microwave Studio.	141
Figure 6.15. The final antenna design with PIN diode-loaded slots.	142

Figure 6.16. PIN diode with its forwarded-biased and reversed-biased equivalent circuit models. ....	142
Figure 6.17. Simulated $S_{11}$ of the proposed frequency reconfigurable antenna (with PIN diodes incorporated into the design) operating at three bands (Design 1). ....	144
Figure 6.18. Gain pattern of the proposed reconfigurable antenna.....	144
Figure 6.19. The built designed antenna (Design 1) on 62 mil FR4 substrate (bare board). ....	145
Figure 6.20. DC biasing network for the PIN diode installation over a slot trace.....	146
Figure 6.21. Built designed antenna (Design 1) on 62 mil FR4 substrate with the PIN diodes and DC biasing lines. ....	146
Figure 6.22. Implemented antenna (Design 1) installed on the measurement setup. ....	147
Figure 6.23. Measurement results for all three configurations (Design 1). ....	148
Figure 6.24. Two investigated ideas to reduce the lowest operating frequency of the proposed reconfigurable antenna in the first design. ....	150
Figure 6.25. Some of the considered configurations with Design 1 to achieve the lowest possible operating frequency.....	151
Figure 6.26. Different ways of incorporating capacitively-loaded slot loop to the modified proposed antenna.....	152
Figure 6.27. Schematic view of the proposed reconfigurable antenna to cover four bands at VHF/UHF/L (Design 2). ....	153
Figure 6.28. Reflection coefficient for antenna Design 2. ....	155
Figure 6.29. Reflection coefficient for antenna Design 2. ....	155
Figure 6.30. Reflection coefficient for antenna Design 2. ....	156
Figure 6.31. Reflection coefficient for antenna Design 2. ....	156
Figure 6.32. Built antenna Design 2.. ....	157
Figure 6.33. Modified antenna (Design 2) simulated in CST Microwave Studio with the symmetric plane ( $H_t = 0$ ) assumption. ....	158
Figure 6.34. Schematic view of the proposed reconfigurable antenna to cover four bands at VHF/UHF/L (Design 3). ....	160
Figure 6.35. Simulation results for all the four different configurations of Design 3. ...	162
Figure 6.36. Input impedance of antenna (Design 3) with and without matching network presence. ....	163
Figure 6.37. Implemented designed antenna (Design 3) on 62 mil FR4 substrate.....	164
Figure 6.38. Antenna Design 3 with all the PIN diodes and DC bias lines installed ....	165
Figure 6.39. Reflection coefficient for antenna Design 3. ....	165

Figure 6.40. Reflection coefficient for antenna Design 3 .....	166
Figure 6.41. Reflection coefficient for antenna Design 3 .....	167
Figure 6.42. Reflection coefficient for antenna Design 3 .....	168
Figure 6.43. Feeding line for the antenna Design 3 .....	169
Figure 6.44. Measurement setup to measure pattern of commercially available BicoLOG20300 antenna. ....	170
Figure 6.45. BicoLOG20300 antenna's gain versus frequency [142]. ....	170
Figure 6.46. BicoLOG pattern measurement setup. ....	171
Figure 6.47. BicoLOG's measured normalized horizontal pattern at 60, 350, 460, and 860 MHz. ....	172
Figure 6.48. BicoLOG's measured normalized vertical pattern at 60, 350, 460, and 860 MHz. ....	172
Figure 6.49. Gain pattern measurement setup for antenna Design 3 at four different cases. ....	173
Figure 6.50. Two measurement setups to measure designed antenna (Design 3) pattern. ....	174
Figure 6.51. Measured and simulated co-polarized XY-plane gain of antenna Design 3 .....	177
Figure 6.52. Measured and simulated cross-polarized XY-plane gain of antenna Design 3 .....	178
Figure 6.53. Measured and simulated co-polarized XZ-plane gain of antenna Design 3 .....	180
Figure 6.54. Measured and simulated cross-polarized XZ-plane gain of antenna Design 3 .....	181

## LIST OF TABLES

	Page
Table 4.1. Comparing Performance of SAR, PW-SAR, MPW-SAR, and WL-SAR.....	87
Table 5.1. Comparing sizes of three different classical broadband antennas to cover a bandwidth from $\lambda_U$ to $\lambda_L$ (moreover, size for $f_L=50$ MHz is listed in fourth row).....	107
Table 5.2. A comparison of PIN diode, FET, and MEMS switches [119]-[121] .....	117
Table 5.3. Comparison of miniaturized antenna design techniques .....	124
Table 6.1. Optimally-calculated dimensions of Antenna 3.....	136
Table 6.2. Generating three different configurations by turning PIN diodes ON and OFF.....	143
Table 6.3. Optimally calculated dimensions of reconfigurable antenna (Design 1).....	143
Table 6.4. Comparing simulation and measurement results for Design 1 (criteria: $S_{11} \leq -10$ dB) .....	149
Table 6.5. Generating four different configurations by turning PIN diodes ON and OFF.....	154
Table 6.6. Optimally calculated dimensions of reconfigurable antenna ( Design 3 )....	161
Table 6.7. Generating four different configurations by turning PIN diodes and SW0 ON and OFF ( Design 3 ) .....	162



## NOMENCLATURE

Symbol	Description
CPW	Coplanar Waveguide
EMC	Electromagnetic Compatibility
EMI	Electromagnetic Interference
FFT	Fast Fourier Transform
MPW-SAR	Modified Piecewise Synthetic Aperture Radar
OEW	Open-Ended Waveguide
$G^P$	Path Green's Function
PW-SAR	Piecewise Synthetic Aperture Radar
RFID	Radio Frequency Identification
$\Gamma$	Reflectivity Function or Qualitative Image
$G^{RT}$	Round-Trip Green's Function
SAR	Synthetic Aperture Radar
TEFMPW-SAR	TE Mode W/ Fresnel Transmission Coefficients SAR
TEGMPW-SAR	TE Mode W/ Generalized Transmission Coefficients SAR
TMFMPW-SAR	TM Mode W/ Fresnel Transmission Coefficients SAR
TMGMPW-SAR	TM Mode W/ Generalized Transmission Coefficients SAR
VNA	Vector Network Analyzer
WL-SAR	Wiener Filter-Based Layered Synthetic Aperture Radar

# 1. INTRODUCTION

## 1.1. BACKGROUND AND MOTIVATIONS

In the past two decades, composite structures, made of electrically insulating materials (i.e., dielectric materials), have found their utility in a wide variety of applications including those in surface transportation, aerospace, construction, power generation, utilities, maritime, and many more. Many of these structures are composed of several layers of different dielectric materials such as glass-fiber reinforced polymer (GFRP) skins, foam, balsa wood and ceramics. These layers are then bonded together using very thin layers of adhesive resulting in thick sandwich composites (i.e., inhomogeneous or layered structure). Inspection of these composite structures, for detecting undesired flaws or indications, may present serious challenges to standard nondestructive testing and evaluation (NDT&E) techniques such as ultrasonic, X-ray and eddy current testing [1]-[2]. This is partially due to the relatively thick nature of some of these composites; attenuation and scattering caused by the various layers; low electrical conductivity associated with the layers; difficulty in detecting thin planar defects that commonly appear in these structures; and non-contact and one-sided requirements of some inspections. On the contrary, it is shown that electromagnetic (EM) imaging techniques have great potential for inspecting these structures [2].

Development of electromagnetic imaging techniques, for the purpose of detecting and evaluating hidden or embedded objects in a structure, has been the focus of investigation by those involved in the fields of nondestructive testing and evaluation, applied geophysics, biomedical, and radar and remote sensing [3]-[7]. EM imaging techniques may be called based on imaging frequency band (e.g., microwave (covering the frequency range of ~300 MHz – 30 GHz), millimeter wave (covering the frequency range of 30 GHz – 300 GHz), or terahertz (covering the frequency range of ~300 GHz – 3 THz)) [4],[8]. In here, the focus is on microwave and millimeter wave bands and hereon EM imaging is referred to as microwave imaging.

A general view of a microwave imaging system is shown in Fig. 1.1. The imaging system is composed of two general parts, namely: the hardware and post-processing (imaging algorithm).

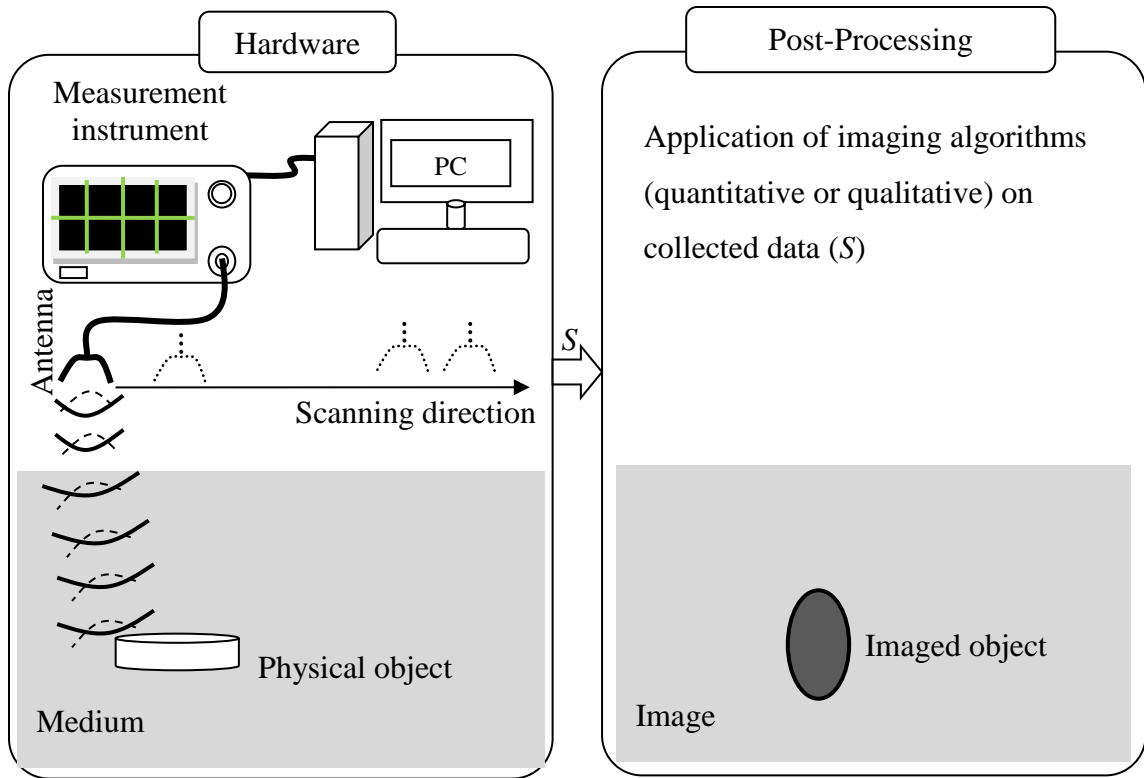


Figure 1.1. A general view of a microwave imaging system.

The hardware portion is composed of the measurement setup (i.e., sample and scanning table), antenna, measurement instrument, and recording tools. When imaging a passive object, the antenna which is connected to a measurement instrument (i.e., a vector network analyzer (VNA)) transmits an EM wave (at a certain frequency or frequency bands) toward the sample under test (SUT). The contrast among the electrical properties of the object (i.e., permittivity, permeability, and conductivity) and the surrounding material causes a scattered/reflected signal to be radiated in all directions. A portion of the scattered wave is then collected by the receiving system (or transceiver). In practice, this data is often measured as reflection coefficient or  $S_{11}$  (when using a calibrated VNA). The antenna subsequently moves to all selected positions within a preset scanning area and data from all these locations are collected. This type of data collection is known as the “*monostatic*” case. If the transmitter and the receiver are at different locations it will be a “*bistatic*” case. On the other hand and for active targets, there is no need to have

transmitter antenna since the target itself radiates EM signal which can be collected by the receiving antenna.

The primary function of the post-processing portion is then to process the “*collected data*” and determine the electrical (i.e., electrical and magnetic property distribution) and geometrical parameters (i.e., shape, size and location) of an imaged object or estimate a reflectivity function (i.e., qualitative image) from the collected data [3],[5]-[7],[9]-[16]. During past several decades, many different techniques (algorithms) have been developed for these purposes. In general, these techniques can be classified as either quantitative imaging techniques or qualitative imaging techniques [9]. Quantitative imaging techniques or inverse scattering methods give the electrical and geometrical properties (distributions) of an imaged object by solving a nonlinear inverse problem. The nonlinear inverse problem is commonly solved iteratively while within each iteration, the problem is linearized using Born or distorted Born approximations. This procedure is known as forward iterative solution [9]-[16]. Required computational resources (i.e., time and computer memory) and calculation complexity are the major disadvantages associated with these techniques [9]. On the other hand, qualitative imaging techniques calculate a reflectivity function or qualitative image to represent the object/target profile. Most of the techniques that belong to this category use migration-based algorithms to reconstruct the unknown image profile. Migration-based techniques include a wide variety of approaches and methods [5]-[7],[9]. The collected data, consisting of reflected or scattered field data from an object or source, can be migrated or back-propagated to the object/target location by adding appropriate time shift (in time domain) or phase shift (in frequency domain), respectively. Therefore, a successful range migration can result in a focused image of the object/target. Synthetic aperture radar (SAR), ground penetrating radar (GPR), range-Doppler algorithm, frequency-wave number migration algorithm ( $\omega$ -k or F-K), matched-filter migration, and chirp-scaling migration all belong to the qualitative imaging class [9]. Qualitative imaging methods usually invoke simplifying assumptions which may reduce the accuracy of the technique in comparison with quantitative imaging. However, qualitative imaging techniques are usually robust and relatively fast (non-iterative).

Despite extensive efforts to develop microwave imaging techniques for free-space and homogeneous media, there are few reported works that consider embedded objects inside layered composite structures or in general an inhomogeneous media (e.g., concrete structures, human body, etc.). Moreover, new applications such as smart environment with embedded wireless sensor networks, navigation and wireless communication systems, through-wall imaging, and medical imaging have spurred additional interest and accelerated the demands for robust imaging techniques applicable to inhomogeneous media [17]-[22]. Imaging of planar layered structures, as a special and most applicable case of inhomogeneous media, has attracted significant attention in the past two decades. However, only a few imaging algorithms applicable to these structures are introduced that belong to the quantitative imaging class [10]-[16]. In [9], a qualitative imaging technique is proposed that uses a SAR migration algorithm to image embedded objects in a planar layered structure. The efficacy of the algorithm is proved and demonstrated only for a two-dimensional (2D) two-layer medium consisting of air and ground. Moreover, for applications such as through-wall imaging, a few modified versions of SAR algorithm are introduced and used. These techniques, as an improvement over SAR, incorporate transmission coefficients for the air-to-wall discontinuity in the SAR image formation in spatial domain [17], [20], [22]. The produced image is consequently improved. However, the algorithms in [17], [20], and [22] are developed in spatial domain which makes the implementation of them difficult and increases the processing time.

Lack of robust and fast qualitative imaging techniques for layered structures and the high demand for these techniques has been the motivation to conduct the research presented herein. In this work, an embedded passive object or active target in a general planar layered dielectric structure is considered (Fig. 1.2).

As an antenna located at the top layer (usually contained in air) scans, transmits an electromagnetic signal, and collects a portion of scattered/reflected signal from the layered structure and embedded object. The collected signal by the measurement instrument is then fed into currently-available imaging algorithms to produce an image. One of these techniques is the classical or conventional SAR [20]. This technique is one of the most well-known imaging techniques, which was initially developed for free-space

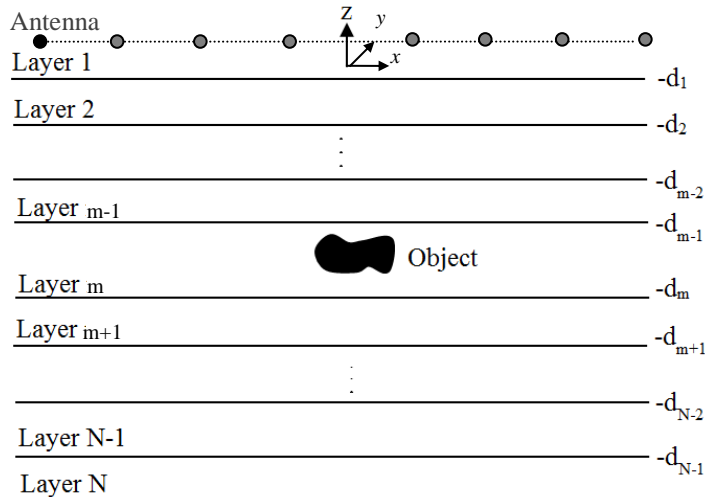


Figure 1.2. An embedded object in a planar layered structure.

or homogenous media [3]-[5]. The basic idea is to compensate for the traveling phase delay by adding appropriate phases to the collected data followed by a coherent summation in order to provide a synthetically-focused image. This type of conventional SAR algorithm is slow but may be accelerated by using the well-known  $(\omega-k)$  or  $(F-K)$  algorithm that first transforms the collected data into its spatial spectrum, and then processes the data in spectral domain to form the image [21]. This algorithm has the distinct advantage of using fast Fourier transform (FFT) algorithms possessing significantly low computational complexity. This is hereafter referred to as the “SAR” algorithm in this work. Unfortunately, for most layered structures the resulting image using SAR becomes unfocused and object locations are incorrectly positioned (i.e., shifted from where they should actually be). Moreover, when considering a lossy layer in the path between the scanning antenna and the object, SAR algorithm is unable to properly determine the location of an embedded object. These limitations stem from the following underlying assumptions in the SAR algorithm. First, SAR assumes that the background medium is homogenous and as such it does not consider the electrical or physical properties of different layers when compensating for phase delay. Second, it does not account for multiple reflections at the discontinuities between different layers. Third, it only compensates for traveling phase delay and does not compensate for the signal attenuation.

To address the first limitation of the SAR algorithm, a method, referred to as modified piecewise SAR (MPW-SAR) is developed in here, which takes into account the electrical and physical properties of each layer at a time (hence, piecewise). As a modification over piece-wise SAR (PW-SAR) [23], the modeling and inclusion of discontinuity between layers using transmission coefficients is studied. The results show that this technique is suitable for objects with high dielectric contrast compared with their surrounding material (i.e., strong scatterers). However, this technique does not account for multiple reflections within any given layer in the structure. Moreover, MPW-SAR is not suitable for imaging embedded objects/targets inside lossy materials since it does not consider EM signal attenuation.

Consequently, to address all of the three limitations of SAR, another method was developed, which is referred to as Wiener filter-based layered SAR (WL-SAR). After mathematical manipulations a closed-form expression is derived for imaging embedded objects/targets in a layered structure. This mathematical expression indicated that the procedure to obtain an image from collected data can be cast into a deconvolution procedure. Since the Wiener filter-based deconvolution method is an efficient deconvolution technique, it was selected for solving the deconvolution problem and finding the desired reflectivity function (i.e., qualitative image).

On the other hand, from hardware point of view, microwave imaging systems require an antenna to collect electromagnetic reflections from sample under test. From imaging point of view, the selection of scanning antenna is also important. Finer cross-range resolution is achieved through wider beamwidth and scanning area, and finer range resolution is achieved through wider bandwidth (BW) [24]. Moreover, if the object is embedded in an unknown media, having an antenna which its characteristics (i.e., operating frequency band, polarization, and pattern) can be dynamically changed is required for locating/imaging purposes. This requires that antennas cover a wide range of characteristics, or antennas whose various important characteristics can be tuned. To address bandwidth problem, wideband or multiband antennas may be employed. However, interference issues along with relative bulkiness (i.e., overall dimensions), limit the utility of wideband antennas for this purpose [25]-[28]. Alternatively, multiband antennas, which address more than one band at a time [29]-[30], still require receivers

with effective out-of-band noise rejection filters in their front-end circuitry [25]. Moreover, covering a wide range of distinct frequency bands using multiband antennas is quite a challenge. On the contrary, a frequency reconfigurable antenna only covers one frequency band at time but it can quickly switch to another configuration and cover a different desired band. Therefore, the noise (or any unwanted interference) is less than interference/noise in multiband or wideband antennas. Moreover, having an antenna with polarization and/or pattern reconfigurability is very useful for imaging applications. Despite many advantages offered by reconfigurable antennas, the topic is fairly recent, and there is not a robust and methodical design procedure for reconfigurable antennas.

The significant potential for using reconfigurable antennas for microwave imaging systems and currently growing multiradio communication devices was the motivation to devote part of the research to compact reconfigurable antenna design, simulation and implementation. A methodical reconfigurable antenna design procedure is introduced and explained. Moreover, three different versions of a novel reconfigurable coplanar waveguide (CPW)-fed slot antenna are designed that cover three/four distinct bands with reasonable gain. The designed antennas can be used for wireless multiradio communication applications (e.g., wireless sensor networking).

## **1.2. OBJECTIVES AND OVERVIEW OF DISSERTATION**

In summary, goals and objectives of this endeavor can be outlined as:

1. Address issues of SAR for imaging of planar layered structures by introducing modified piecewise SAR and Wiener filter-based layered SAR methods.
2. Verification of efficacy of the introduced imaging methods through simulations and measurements.
3. Introduction of a method to design compact reconfigurable antennas.
4. Simulation, test, and measurement of prototype compact reconfigurable antennas which are designed using the proposed method.

To address the objectives and goals, thesis is organized as follow. In Section 2, calculation of electric (E) and magnetic (H) field distribution inside of a layered structure which is excited with an embedded vector distributed source will be discussed. The



obtained equations will be used in Section 3 to define qualitative image concept and its relationship with the sampled field at the scanning area (i.e., collected data). To image an embedded source in a layered structure, initially SAR algorithm will be used and its limitations will be explained. Then, modified piecewise SAR method will be introduced to address the issues, partly. Later, a comprehensive method (i.e., WL-SAR) will be introduced which can address all the SAR limitations. In Section 4, developed MPW-SAR and WL-SAR methods will be modified in an appropriate way to be used for imaging embedded passive objects in a layered structure. In Section 5, a brief review of currently-available antenna miniaturization techniques and reconfigurable antenna design methods will be given. In Section 6, a procedure for reconfigurable antenna design will be introduced and then, the proposed method is used to design a prototype antenna with certain characteristics. The outcome by itself is a novel class of compact reconfigurable antennas. Three different versions of this novel antenna which can cover three or four distinct frequency bands at VHF/UHF/L bands will be designed, simulated, and tested.

## 2. FIELD CALCULATION IN A LAYERED STRUCTURE USING GREEN'S FUNCTION

### 2.1. INTRODUCTION

In the past decades, there have been extensive efforts to analyze electromagnetic wave propagation inside of a layered structure [31]-[32]. The source of incident wave is commonly assumed to be far enough away from the layered structure so that far-field assumptions can be invoked and the incident wave can be considered as a uniform plane transverse electromagnetic (TEM) wave in spatial domain. Given the planar boundaries and the incident wave front, then the behavior of the incident wave could be easily studied. Similar to transmission lines, it is then assumed that at the boundary, the incident planar wave decomposes into two planar waves, namely; reflected and transmitted waves, as shown in Fig. 2.1. Subsequently, at each interface between layers  $i$  and  $j$  reflection coefficient ( $R_{ij}$ ) and transmission coefficient ( $T_{ij}$ ) are defined to express the complex weight for the transmitted and reflected waves, respectively. Later, by applying boundary conditions (i.e., continuity of tangential components of electric E-field and magnetic H-fields), these coefficients are calculated [31]-[32].

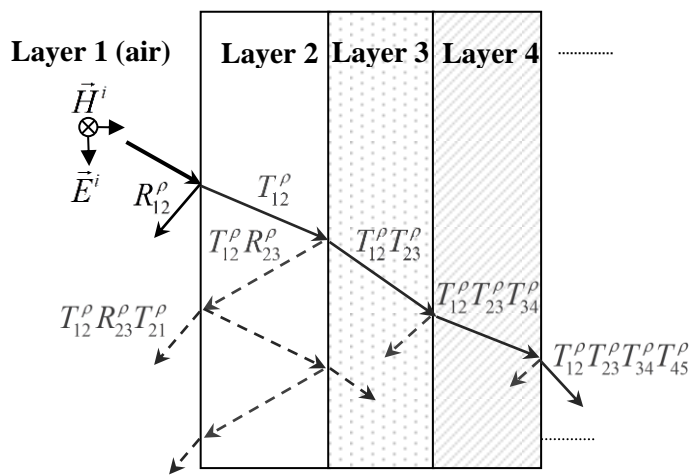


Figure 2.1. Planar wave reflection and transmission at boundaries of a planar layered structure ( $\rho = \text{TEM, TE, TM}$ ).

Although, incident TEM wave assumption may be valid for many practical applications (i.e., transmitting source located relatively far from the layered structure), it does not satisfy the requirements of cases in which the two are relatively close and plane wave assumption no longer holds. In general, from microwave imaging point of view and for many practical applications involving NDT&E, breast tumor detection, through-wall imaging, etc. for an “*active target*” which is defined as an embedded EM source or for an embedded passive (non-self-radiating) object inside of a layered structure illuminated by a secondary EM source, the assumption of TEM planar wave radiation is no longer valid. Therefore, for the ability to properly image an object/target (e.g., for determining its shape, electrical properties, depth within the structure, etc.), a less approximated and more complete EM formulation of the fields within the layered structure is required. This has been the subject of investigations in the past [33]-[38]. Based on the proposed ideas in these works, the incident wave is no longer planar and is more appropriately described as being spherical and is decomposed into two components, namely; transverse electric (TE) and transverse magnetic (TM) waves or modes. Subsequently, Weyl or Sommerfeld identities are used to transform these modes separately into spectral domain (similar to Fourier transform) [33]-[38]. In this way, Weyl or Sommerfeld identities decompose a spherical wave (in spatial domain) into planar or cylindrical waves (in spectral domain), respectively [36]-[37]. Since the boundaries are planar, Weyl identity is preferred over Sommerfeld identity. Then, similar to TEM planar wave case in spatial domain, the reflected and transmitted waves at each boundary interface in the layered structure and for each mode can be calculated [36]. Later, by coherent summation of all reflected and transmitted waves inside each layer, the total field distribution is calculated anywhere inside of the layered structure in spectral domain. An inverse transform can transform back the spectral domain field into spatial domain. When the source is assumed to be a point source, the whole procedure results in what is referred to in the literature as the “*Green’s function of a layered structure*” [33]-[38]. This terminology and its concept are very similar to *impulse response function* which has been widely used in circuit theory [39]. In fact, Green’s function can be seen as the spatial domain analog of impulse response function in time domain. The Green’s function provides a spatial distribution of fields anywhere inside of a layered structure

when the source of excitation is confined to a point (i.e., “point source”). Then, assuming the layers are homogeneous, linear, isotropic time-invariant medium (i.e., simple time invariant medium) and so, superposition rule can be used to calculate the field distribution for a distributed source from the Green’s function by performing a simple integration.

From microwave imaging point of view, the Green’s function of a layered structure is used for two distinct reasons. First, it is used to analyze a known layered structure with embedded source(s) or object(s) to calculate field distribution anywhere inside the structure. Then, the calculated field is sampled over a known (usually) two-dimensional spatial region, commonly referred to as the collected imaging data (or simply collected data). The collected data may then be incorporated into any number of imaging algorithms (techniques) to produce an image of the layered structure and any embedded object or source. Second, imaging methods, especially quantitative imaging methods, use the Green’s function of the layered structure in image reconstruction procedure. An approximate model of the layered structure is constructed which is known as “*forward model*”. Having the forward model, the field distribution can be calculated over a desired sampling region and subsequently compared with experimentally-collected data by defining an appropriate error function. If the error is bigger than a preset threshold, then the quantitative methods invoke an iterative procedure to update different parameters of the forward model in order to minimize the error (i.e., a forward-iterative approach [9]-[16]).

Hence, Green’s function calculation and its implementation are very required for microwave imaging of layered structures. Therefore, in this section, a brief discussion of Green’s function and field calculation inside planar layered structures will be provided. Given that the development of Green’s function for layered structures has been studied in the literatures [33]-[38], only the necessary equations are shown along with any pertinent modifications.

## 2.2. WAVE PROPAGATION INSIDE A PLANAR LAYERED STRUCTURE

Consider an embedded passive object or active source in a layered planar structure, as shown in Fig. 2.2. The layered structure is assumed to be inhomogeneous only in the  $z$ -direction, but it is assumed to be homogeneous and infinite in extent in the  $x$ - and  $y$ -directions. Moreover, each layer is assumed to be simple time-invariant medium. Then, a general situation can be assumed where an electric current density ( $\vec{J}$ ) and magnetic current density ( $\vec{M}$ ) exist simultaneously on the surface of the object (Fig. 2.2). These currents could have been induced by an external source on the passive object [31].

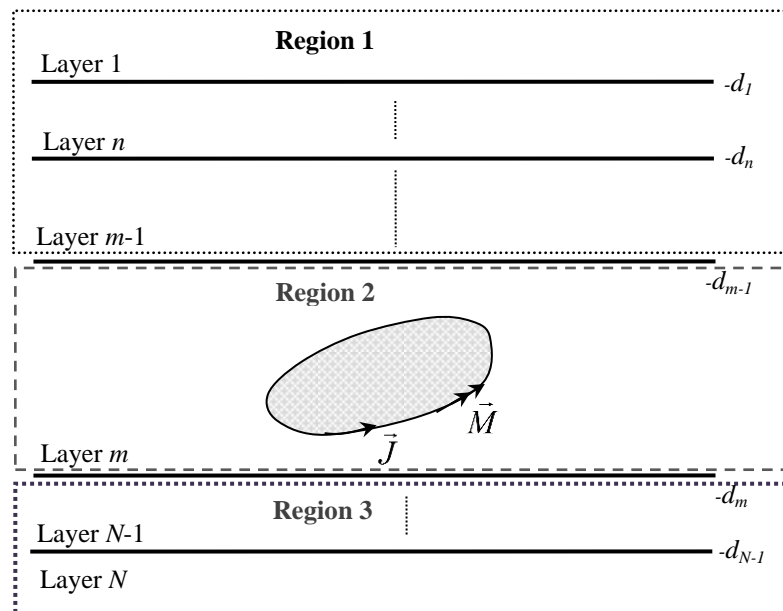


Figure 2.2. An embedded distributed source in a planar layered structure.

These two types of currents generally can excite TE waves and/or TM waves. For TE wave, electric field is transverse to the  $z$ -direction and does not have any component in the  $z$ -direction, while for the TM wave, the magnetic field is transverse to the  $z$ -direction and does not have any component in the  $z$ -direction [36].

To calculate the electric and magnetic fields inside the layered structure for each mode (TE or TM), different techniques have been proposed in the literatures [33]-[38].

However, these techniques are not outlined in an organized manner. Consequently, here an organized and step-by-step discussion on calculating electric and magnetic fields inside a layered structure will be presented. First, the simplest case is considered by replacing a vector distributed source with a scalar point source. In accordance to the available literatures [36]-[38], the scalar field is calculated everywhere inside the layered structure for a point source. This scalar field is referred as *scalar Green's function*. The scalar Green's function transforms a scalar source into a scalar field distribution. Then, a general case will be considered where the source is composed of distributed vector electric and magnetic current (density) sources (as in Fig. 2.2). In accordance with [36]-[38], the required expressions for calculating the vector E- and H-fields inside the layered structure will be provided by defining a dyadic Green's function. In contrast with scalar Green's function, a dyadic Green's function can be used to transform a vector source into a vector field.

### 2.3. A POINT SOURCE EMBEDDED IN A LAYERED STRUCTURE

Consider a point source located at  $\vec{r}' = (x', y', z')$  inside of a homogenous background material with a relative permittivity and permeability of  $\epsilon_b$  and  $\mu_b$ , respectively. Then, the scalar field distribution or propagation factor [38] of the point source ( $F_{point}$ ) in spatial domain at an observation point of  $\vec{r} = (x, y, z)$  can be calculated as [31]:

$$F_{point}(R) = \frac{e^{-jK_b R}}{4\pi R}, \quad (1)$$

where,  $R$  is the distance between the source and the observation point given by:

$$R = |\vec{r} - \vec{r}'| = \sqrt{(x - x')^2 + (y - y')^2 + (z - z')^2}. \quad (2)$$

Also,  $K_b$  is wavenumber and is given by:

$$K_b = 2\pi f \sqrt{\mu_b \varepsilon_b \mu_0 \varepsilon_0}, \quad (3)$$

where,  $\varepsilon_0$  and  $\mu_0$  are permittivity and permeability of free-space, respectively, and  $f$  is the operating frequency. As indicated by (1), the field distribution wave front is spherical (i.e., a spherical wave). By applying the well-known transformation, Weyl identity, the spherical wave fronts can be transformed into planar wave fronts in the spectral domain as [36]-[38]:

$$\frac{e^{-jk_b R}}{4\pi R} = \frac{-j}{8\pi^2} \int_{-\infty}^{+\infty} \int_{-\infty}^{+\infty} \frac{e^{-jK_x(x-x')} e^{-jK_y(y-y')} e^{-jK_z|z-z'|}}{K_z} dK_y dK_x, \quad (4)$$

where  $K_x$ ,  $K_y$ , and  $K_z$  are wavenumbers in  $x$ -,  $y$ -, and  $z$ -directions, respectively. Also,  $K_z$  relates to  $K_x$  and  $K_y$  by the following dispersion relation:

$$K_b^2 = K_z^2 + K_x^2 + K_y^2. \quad (5)$$

Equation (4) can be alternatively written as:

$$\frac{e^{-jk_b R}}{4\pi R} \underset{F_{xy}^{-1}}{\overset{F_{xy}}{\rightleftharpoons}} \frac{-j}{2} \frac{e^{-jK_z|z-z'|}}{K_z}, \quad (6)$$

where  $F_{xy}$  and  $F_{xy}^{-1}$  are the 2D Fourier transform and inverse 2D Fourier transform in  $K_x$  and  $K_y$ , respectively. In fact, (4) shows that any spherical wave in spatial domain, can be represented as planar waves, propagating in the  $z$ -direction, in  $K_z$  domain. Thus, now the reflection and transmission coefficients of the planar waves at layer interfaces can be readily obtained [31], [32], [36].

Now, assume that the point source located at  $\vec{r}' = (x', y', z')$  is embedded in layer  $m$  of the layered structure shown in Fig. 2.2. The observation point is assumed to be at  $\vec{r} = (x, y, z)$  in layer  $n$ . The propagation factor may now be calculated for three different regions of interest (Fig. 2.2), namely: a) Region 1, for layers with index  $n < m$ , b) Region 2, for layers with index  $n = m$ , and c) Region 3, for layers where their index  $n > m$ . For

each region, a separate propagation factor or ( $F$ ) can be calculated and then from  $F$ , scalar Green's function or  $g(\vec{r}, \vec{r}')$  can be constructed, as outlined below.

**2.3.1. Propagation Factor in Region 1** ( $z \in \text{layer } n, z' \in \text{layer } m, n < m$ ). For this region, the total field in spectral domain is the superposition of upward and downward traveling waves, which can be shown as [36]-[38]:

$$F^\rho(\vec{K}_s, z, z') = A_n^{+, \rho} \left[ e^{-jK_{nz}z} + e^{jK_{nz}(z+2d_{n-1})} \tilde{R}_{n,n-1}^\rho \right], \quad (7)$$

where,  $\rho$  represents TE or TM modes, and  $d_i$  is the boundary between layer  $i$  and layer  $i+1$ . Also,  $\vec{K}_s = K_x \hat{x} + K_y \hat{y}$ ,  $K_{iz}$  is  $K_z$  in layer  $i$  and  $\tilde{R}_{i,i-1}^\rho$  is generalized reflection coefficient between layer  $i$  and layer  $i-1$  for a wave traveling from layer  $i$  toward layer  $i-1$  with mode of propagation corresponding to  $\rho$ . Moreover,  $A_n^{+, \rho}$  is a coefficient which was calculated through a recursive procedure in [36] as:

$$A_n^{+, \rho} = e^{-jK_{nz}d_n} \tilde{T}_{nn}^\rho e^{jK_{nz}d_{m-1}} \left[ e^{jK_{mz}z'} + e^{-jK_{mz}(z'+2d_m)} \tilde{R}_{m,m+1}^\rho \right] \tilde{M}_m^\rho \tilde{M}_n^\rho, \quad (8)$$

where  $\tilde{M}_i^\rho$  is defined as,

$$\tilde{M}_i^\rho = [1 - \tilde{R}_{i,i+1}^\rho \tilde{R}_{i,i-1}^\rho e^{-j2K_{iz}(d_i - d_{i-1})}]^{-1}. \quad (9)$$

Moreover,  $\tilde{T}_{i,q}^\rho$  is generalized transmission coefficient between layer  $i$  and layer  $q$  for mode of propagation of  $\rho$  [36].

**2.3.2. Propagation Factor in Region 2** ( $z \in \text{layer } n, z' \in \text{layer } m, n = m$ ). For this region, the total field in spectral domain is the superposition of upward and downward traveling waves and the source (equation (6)) which can be shown as [36]-[38]:

$$F^\rho(\vec{K}_s, z, z') = e^{-jK_{mz}|z-z'|} + B_m^\rho e^{jK_{mz}z} + D_m^\rho e^{-jK_{mz}z} \quad (10)$$

where,  $B_m^\rho$  and  $D_m^\rho$  are calculated in [36] as:



$$B_m^\rho = e^{jK_{mz}d_{m-1}} \tilde{R}_{m,m-1}^\rho \left[ e^{-jK_{mz}|d_{m-1}+z'|} + e^{-jK_{mz}(d_m-d_{m-1})} \tilde{R}_{m,m+1}^\rho e^{-jK_{mz}|d_m+z'|} \right] \tilde{M}_m^\rho, \quad (11)$$

$$D_m^\rho = e^{-jK_{mz}d_m} \tilde{R}_{m,m+1}^\rho \left[ e^{-jK_{mz}|d_m+z'|} + e^{-jK_{mz}(d_m-d_{m-1})} \tilde{R}_{m,m-1}^\rho e^{-jK_{mz}|d_{m-1}+z'|} \right] \tilde{M}_m^\rho. \quad (12)$$

**2.3.3. Propagation Factor in Region 3** ( $z \in \text{layer } n, z' \in \text{layer } m, n > m$ ). For this region, field in spectral domain is the superposition of upward and downward traveling waves which can be shown as [36]-[38]:

$$F^\rho(K_s, z, z') = A_n^{-,\rho} \left[ e^{jK_{mz}z} + e^{-jK_{mz}(z+2d_n)} \tilde{R}_{n,n+1}^\rho \right], \quad (13)$$

where  $A_n^-$  is a coefficient which was calculated through a recursive procedure in [36] as:

$$A_n^{-,\rho} = e^{jK_{mz}d_{n-1}} \tilde{T}_{nm}^\rho e^{-jK_{mz}d_m} \left[ e^{-jK_{mz}z'} + e^{jK_{mz}(z'+2d_{m-1})} \tilde{R}_{m,m-1}^\rho \right] \tilde{M}_m^\rho \tilde{M}_n^\rho. \quad (14)$$

**2.3.4. Scalar Green's Function Calculation for Layered Structure.** The scalar Green's function of a planar layered structure for mode of propagation of  $\rho$  is related to  $F^\rho(z, z')$  by [38]:

$$\begin{aligned} g^\rho(\vec{r}, \vec{r}') &= \frac{-j}{8\pi^2} \int_{-\infty}^{+\infty} \int_{-\infty}^{+\infty} \frac{e^{-jK_x(x-x')} e^{-jK_y(y-y')}}{K_{mz} |\vec{K}_s|^2} F^\rho(\vec{K}_s, z, z') dK_y dK_x \\ &= \frac{-j}{2} F_{xy}^{-1} \left( \frac{F^\rho(\vec{K}_s, z, z')}{K_{mz} |\vec{K}_s|^2} \right), \end{aligned} \quad (15)$$

Invoking the Fourier transform definition and then using fast Fourier transform (FFT), (15) can be easily implemented using a computer program (e.g., MATLAB [40]).

**2.3.5. Examples.** In here, in order to provide some physical insight about the wave propagation inside of a layered structure, scalar Green's function distribution for there different configurations are calculated and presented by implementing (15).

The first example, Example 1, is similar to the problem which was posed and solved in [41]. A two-layer structure with an embedded electric line-source was

considered. As an approximation, here the line source is replaced with a point source to be able to use currently developed scalar Green's function. In a cross section, a line source can be well-approximated by a point source. The two layers are consist of air and a lossless dielectric with  $\epsilon_r = 3$ . The boundary between air and the dielectric was set at  $z = 0$  and the layers were assumed to be infinitely-extended in the  $z$ -direction (i.e., layers are infinite half-space). The point source which radiates at 6 GHz was positioned at  $(0, 0, -5)$  cm and then two cases were considered. In the first case, the source was assumed to be in air. Then, [41] used its proposed method to calculate real part of the  $z$  component of the electric field (i.e.,  $E_z$ ). The available online code in [42] was used to reproduce the reported result in [41] and the reproduced field distribution is shown in Fig. 2.3. On the other hand, later, in this section, it will be shown that  $E_z$  is proportional to the scalar Green's function, and so, (15) can be used to calculate a field distribution proportional to  $E_z$ . Since  $E_z$  is not zero, the mode of propagation for the waves inside of the layered structure is not TE. Then, for the field calculations, TM mode scalar Green's function was used (i.e.,  $\rho = \text{TM}$ ). In Fig. 2.3, the calculated scalar Green's function distribution using (15) is compared with the reported  $E_z$  in [41]. As the figure shows, the calculated field by implementing (15) is in a very good agreement with the outcome of [41]. Moreover, it is instructive to see how the wave fronts bend when the EM wave propagates across the boundary. The wave fronts are spaced closer in the dielectric layer than in air, as expected.

In the second case, the air and dielectric layers are swapped and the source is assumed to be embedded inside the dielectric medium. In Fig. 2.4, the calculated scalar Green's function using (15) is compared with the distribution of the  $E_z$  which was reported in [41]. As the figure shows, the calculated field by implementing (15) is in a very good agreement with the outcome of [41]. Similar other observations, to that in Case 1, can also be made in this case.

In the second example, Example 2, a point source is assumed to be embedded in a five-layer structure. The location of the source which operates at 6 GHz is assumed to be  $(0, 0, -17.5)$  cm and the mode is assumed to be TE. The dielectric constant of each layer is selected in a way to create a good contrast between layers. First layer extends from  $z = 0$  to positive infinity in the  $z$ -direction with a dielectric constant of  $\epsilon_r = 2$ . Second

layer is 10 cm thick with dielectric constant is  $\epsilon_r = 4 - 0.02j$ . The third layer is 15 cm thick and its dielectric constant is  $\epsilon_r = 9 - 0.03j$ . The fourth layer is 16 cm thick and its dielectric constant is  $\epsilon_r = 2.5$ . The bottom layer extends to negative infinity in the  $z$ -direction and its dielectric constant is  $\epsilon_r = 5$ .

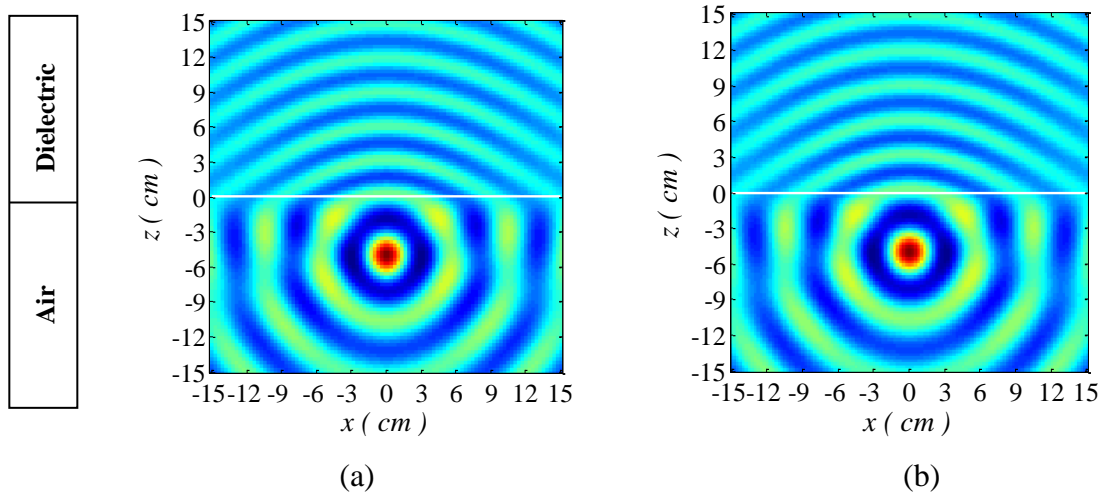


Figure 2.3. Calculated real part of  $E_z$ . (a) reference [41], and (b) implementing (15) (Case 1: top layer is dielectric, bottom layer is air).

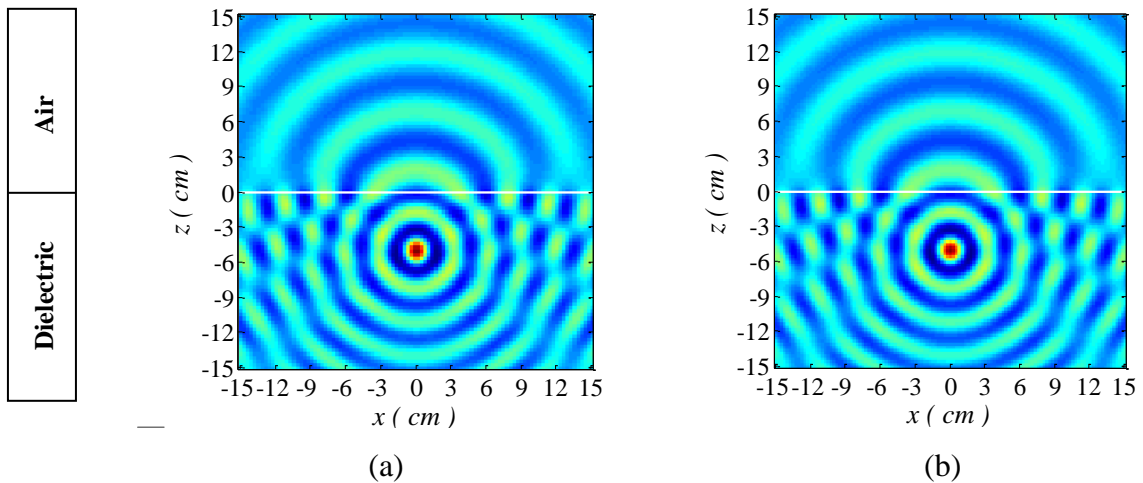


Figure 2.4. Calculated real part of  $E_z$ . (a) reference [41], and (b) implementing (15) (Case 2: top layer is air, bottom layer is dielectric).

The calculated scalar Green's function for this structure is shown in Fig. 2.5. The real, imaginary, and magnitude parts of the field are normalized and the phase distribution is in radian. By looking at the real, imaginary, magnitude, and phase of the field, one can see how the wave fronts bend passing across the boundaries. Moreover, in the layer that includes the point source (i.e.,  $m = 3$ ), superposition between the source field and the reflected backward waves from the top and bottom boundaries produce a complex interference pattern. These *multiple* reflections can create problems in the imaging procedure which will be discussed in Sections 3 and 4.

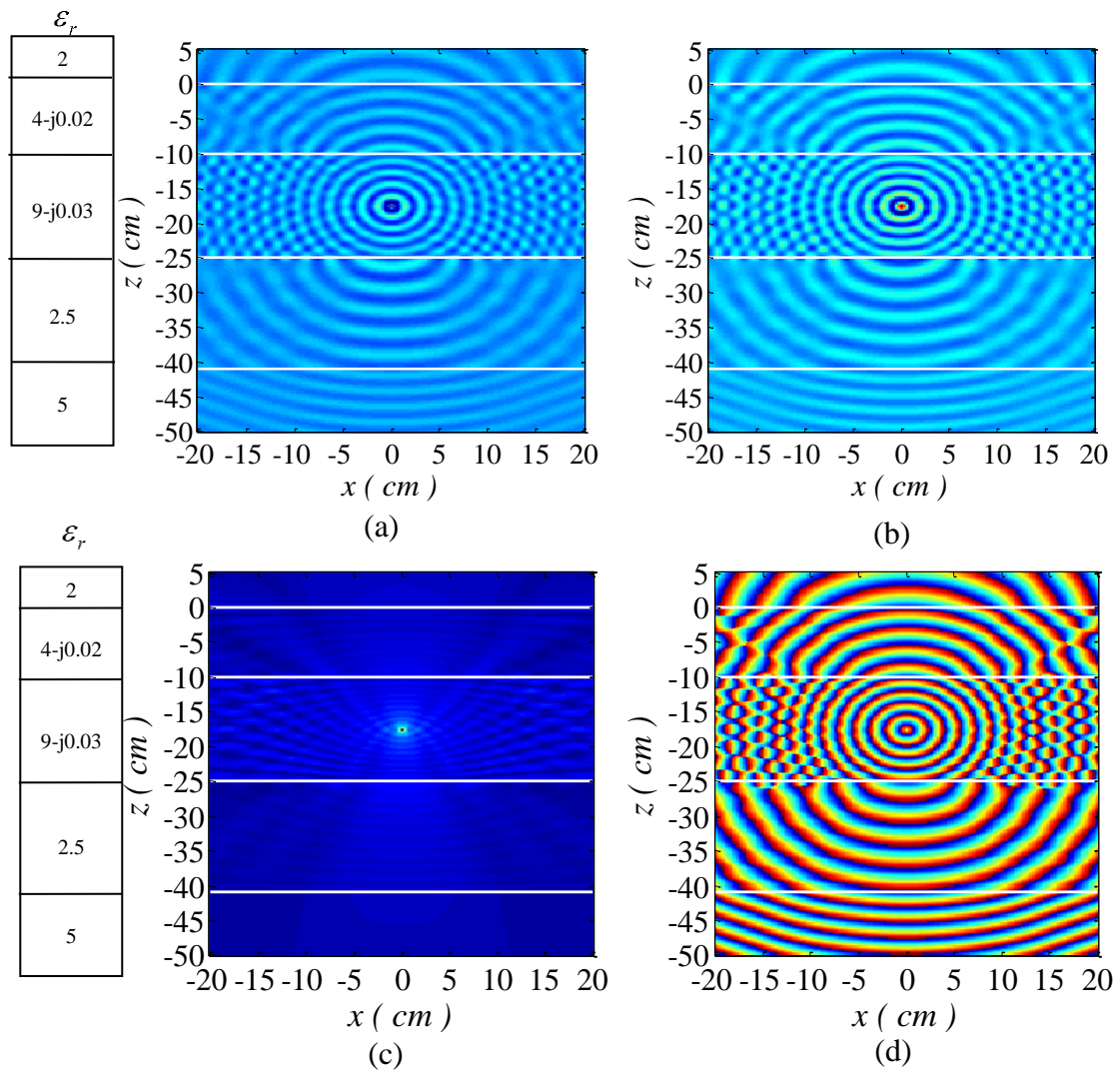


Figure 2.5. Calculated scalar Green's function for Example 2. (a) normalized real part, (b) normalized imaginary part, (c) normalized magnitude, and (d) phase (rad).

In the third example, a more general case is considered by assuming three different point sources (at TE mode) embedded in a four-layer printed circuit board (PCB) and operating at 10 GHz. These point sources are mimicking actual traces routed inside of a multilayered PCB and they are all located in the  $xz$ -plane and positioned at  $(-6, 0, -4.5)$  cm,  $(-16.5, 0, -18)$  cm, and  $(9, 0, -30)$  cm, respectively. First layer is air and it extends from  $z = 0$  to positive infinity in the  $z$ -direction. Second layer is 12 cm thick and it is assumed to be Rogers RO3203 ( $\epsilon_r = 3.02 - j0.003$ ). Third layer is 12 cm thick Arlon AR450 ( $\epsilon_r = 4.5 - j0.0135$ ). The fourth layer is 15 cm thick Rogers RO4003 ( $\epsilon_r = 3.55 - j0.01$ ). The bottom layer is Rogers RT5880 which extends to negative infinity in the  $z$ -direction and its dielectric constant is  $\epsilon_r = 2.2 - j0.001$ .

Since the layers are simple time-invariant medium, superposition rule can be readily used. Scalar Green's function per each source was calculated while two other point sources were removed. Then, the coherent summation of the calculated scalar Green's functions resulted in total scalar Green's function which is shown in Fig. 2.6. The real, imaginary, and magnitude parts of the field are normalized and the phase distribution is in radian. The field distribution (real, imaginary, magnitude, and phase) shows how the sources interact constructively and destructively in a typical layered structure.

#### 2.4. A VECTOR DISTRIBUTED SOURCE IN A LAYERED STRUCTURE

In Section 2.3, field distribution inside of a layered structure for a scalar embedded source was calculated. However, in actual situations sources must be represented by their vector representations (as it was shown in Fig. 2.2). This vector (distributed) source produces vector E- and H-fields.

To calculate E- and H-fields distributions in layered structure, expressions in [38] will be briefly explained in here. Assume that  $\vec{J}$  and  $\vec{M}$  are electric and magnetic current densities, respectively, which exist in a limited volume inside layer  $m$  of the layered structure (Fig. 2.2).

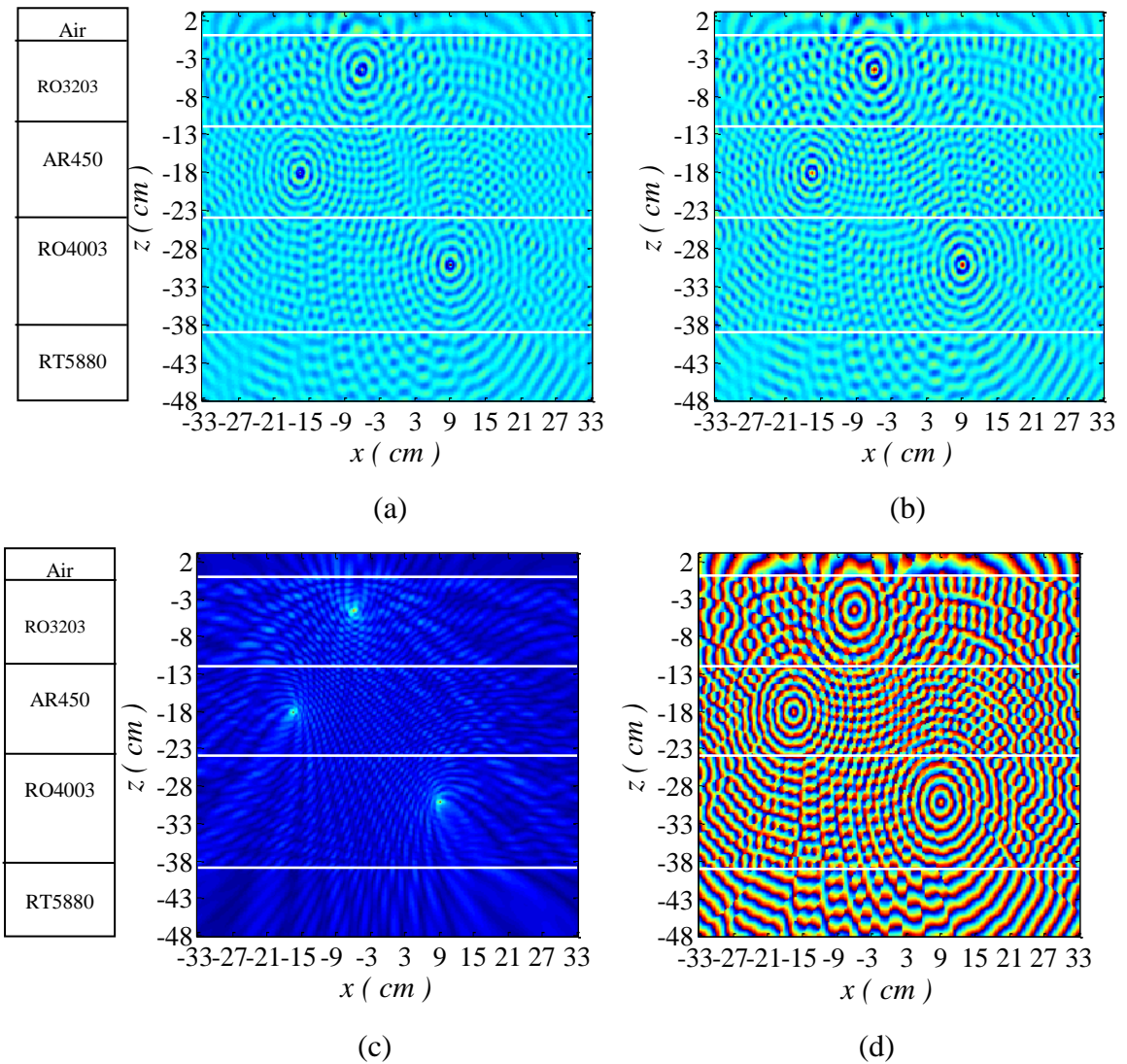


Figure 2.6. Calculated scalar Green's function for Example 3. (a) normalized real part, (b) normalized imaginary part, (c) normalized magnitude, and (d) phase (rad).

The electric and magnetic field distributions at observation point  $\vec{r} = (x, y, z)$  can be calculated from [38]:

$$\vec{E}(\vec{r}) = L_E(\vec{r}, \vec{r}') \cdot \vec{J}(\vec{r}') + \kappa_E(\vec{r}, \vec{r}') \cdot \vec{M}(\vec{r}'), \quad (16)$$

$$\vec{H}(\vec{r}) = L_H(\vec{r}, \vec{r}') \cdot \vec{M}(\vec{r}') + \kappa_H(\vec{r}, \vec{r}') \cdot \vec{J}(\vec{r}'), \quad (17)$$

where  $\vec{r}'=(x',y',z')$  is the source point. Also,  $L_E, \kappa_E, L_H, \kappa_H$  are integral operators which can be defined as [38]:

$$L_E(\vec{r},\vec{r}')=-j\omega\int d\vec{r}'\bar{\bar{G}}_e(\vec{r},\vec{r}')\mu(\vec{r}'), \quad (18)$$

$$\kappa_H(\vec{r},\vec{r}')=\mu^{-1}(\vec{r})\int d\vec{r}'\vec{\nabla}\times\bar{\bar{G}}_e(\vec{r},\vec{r}')\mu(\vec{r}'), \quad (19)$$

$$L_H(\vec{r},\vec{r}')=-j\omega\int d\vec{r}'\bar{\bar{G}}_m(\vec{r},\vec{r}')\varepsilon(\vec{r}'), \quad (20)$$

$$\kappa_E(\vec{r},\vec{r}')=-\varepsilon^{-1}(\vec{r})\int d\vec{r}'\vec{\nabla}\times\bar{\bar{G}}_m(\vec{r},\vec{r}')\varepsilon(\vec{r}'). \quad (21)$$

In these equations,  $\bar{\bar{G}}_e(\vec{r},\vec{r}')$  shows electric-type dyadic Green's function and  $\bar{\bar{G}}_m(\vec{r},\vec{r}')$  shows magnetic-type dyadic Green's function [38]. A dyad is a  $3\times 3$  matrix that transforms a vector to a vector [36].

As (16), (18) and (19) show, to calculate E-field,  $\bar{\bar{G}}_e(\vec{r},\vec{r}')$  and  $\vec{\nabla}\times\bar{\bar{G}}_e(\vec{r},\vec{r}')$  are required, whose derivations are addressed next.

**2.4.1. Calculation of  $\bar{\bar{G}}_e(\vec{r},\vec{r}')$ .** According to [38],  $\bar{\bar{G}}_e(\vec{r},\vec{r}')$  can be expressed as:

$$\bar{\bar{G}}_e(\vec{r},\vec{r}')=\bar{\bar{G}}_e^{TE}(\vec{r},\vec{r}')+\frac{1}{K_{nm}^2}\bar{\bar{G}}_e^{TM}(\vec{r},\vec{r}'), \quad (22)$$

where,  $K_{nm}=\omega^2\varepsilon_n\mu_m$ , and:

$$\bar{\bar{G}}_e^{TE}(\vec{r},\vec{r}')=(\vec{\nabla}\times\hat{z})(\vec{\nabla}\times\hat{z})g^{TE}(\vec{r},\vec{r}'), \quad (23)$$

$$\bar{\bar{G}}_e^{TM}(\vec{r},\vec{r}')=(\vec{\nabla}\times\vec{\nabla}\times\hat{z})(\vec{\nabla}\times\vec{\nabla}\times\hat{z})g^{TM}(\vec{r},\vec{r}'). \quad (24)$$

Considering the fact that  $\vec{\nabla} \times \hat{z} = \partial_y \hat{x} - \partial_x \hat{y}$ , where  $\partial$  denotes the partial operator,  $\bar{\bar{G}}_e^{TE}(\vec{r}, \vec{r}')$  can be written as [38]:

$$\bar{\bar{G}}_e^{TE}(\vec{r}, \vec{r}') = \begin{bmatrix} \partial_y \partial_{y'} & -\partial_y \partial_{x'} & 0 \\ -\partial_x \partial_{y'} & \partial_x \partial_{x'} & 0 \\ 0 & 0 & 0 \end{bmatrix} g^{TE}(\vec{r}, \vec{r}') = \begin{bmatrix} G_{e,xx}^{TE} & G_{e,xy}^{TE} & 0 \\ G_{e,yx}^{TE} & G_{e,yy}^{TE} & 0 \\ 0 & 0 & 0 \end{bmatrix}. \quad (25)$$

Then, each nonzero entries of  $\bar{\bar{G}}_e^{TE}(\vec{r}, \vec{r}')$  in (25) can be separately calculated as:

$$G_{e,xx}^{TE} = \frac{-j}{2} F_{xy}^{-1} \left( \frac{K_y^2 F^{TE}(\vec{K}_s, z, z')}{K_{mz} |\vec{K}_s|^2} \right), \quad (26)$$

$$G_{e,xy}^{TE} = \frac{j}{2} F_{xy}^{-1} \left( \frac{K_x K_y F^{TE}(\vec{K}_s, z, z')}{K_{mz} |\vec{K}_s|^2} \right), \quad (27)$$

$$G_{e,yx}^{TE} = \frac{j}{2} F_{xy}^{-1} \left( \frac{K_x K_y F^{TE}(\vec{K}_s, z, z')}{K_{mz} |\vec{K}_s|^2} \right), \quad (28)$$

$$G_{e,yy}^{TE} = \frac{-j}{2} F_{xy}^{-1} \left( \frac{K_x^2 F^{TE}(\vec{K}_s, z, z')}{K_{mz} |\vec{K}_s|^2} \right). \quad (29)$$

In order to calculate  $\bar{\bar{G}}_e(\vec{r}, \vec{r}')$ , the second term in (22),  $\bar{\bar{G}}_e^{TM}(\vec{r}, \vec{r}')$ , must be known. The entire calculation is similar to  $\bar{\bar{G}}_e^{TE}(\vec{r}, \vec{r}')$  calculation. Considering the fact that  $\vec{\nabla} \times \vec{\nabla} \times \hat{z} = \partial_x \partial_z \hat{x} + \partial_y \partial_z \hat{y} + |\vec{K}_s|^2 \hat{z}$ ,  $\bar{\bar{G}}_e^{TM}(\vec{r}, \vec{r}')$  in (24) can be written as [38]:



$$\begin{aligned}
\bar{\bar{G}}_e^{TM}(\vec{r}, \vec{r}') &= \begin{bmatrix} \partial_x \partial_x \partial_z \partial_z & \partial_x \partial_y \partial_z \partial_z & \partial_x \partial_z |\vec{K}_s|^2 \\ \partial_y \partial_x \partial_z \partial_z & \partial_y \partial_y \partial_z \partial_z & \partial_y \partial_z |\vec{K}_s|^2 \\ \partial_x \partial_z |\vec{K}_s|^2 & \partial_y \partial_z |\vec{K}_s|^2 & |\vec{K}_s|^4 \end{bmatrix} g^{TM}(\vec{r}, \vec{r}') \\
&= \begin{bmatrix} G_{e,xx}^{TM} & G_{e,xy}^{TM} & G_{e,xz}^{TM} \\ G_{e,yx}^{TM} & G_{e,yy}^{TM} & G_{e,yz}^{TM} \\ G_{e,zx}^{TM} & G_{e,zy}^{TM} & G_{e,zz}^{TM} \end{bmatrix}.
\end{aligned} \tag{30}$$

Then, each entry of  $\bar{\bar{G}}_e^{TM}(\vec{r}, \vec{r}')$  in (30) can be calculated as:

$$G_{e,xx}^{TM} = \partial_z \partial_{z'} \left( \frac{-j}{2} F_{xy}^{-1} \left( \frac{K_x^2 F^{TM}(\vec{K}_s, z, z')}{K_{mz} |\vec{K}_s|^2} \right) \right), \tag{31}$$

$$G_{e,xy}^{TM} = \partial_z \partial_{z'} \left( \frac{-j}{2} F_{xy}^{-1} \left( \frac{K_x K_y F^{TM}(\vec{K}_s, z, z')}{K_{mz} |\vec{K}_s|^2} \right) \right), \tag{32}$$

$$G_{e,xz}^{TM} = \partial_z \left( \frac{-j}{2} F_{xy}^{-1} \left( \frac{j K_x F^{TM}(\vec{K}_s, z, z')}{K_{mz}} \right) \right), \tag{33}$$

$$G_{e,yx}^{TM} = \partial_z \partial_{z'} \left( \frac{-j}{2} F_{xy}^{-1} \left( \frac{K_x K_y F^{TM}(\vec{K}_s, z, z')}{K_{mz} |\vec{K}_s|^2} \right) \right), \tag{34}$$

$$G_{e,yy}^{TM} = \partial_z \partial_{z'} \left( \frac{-j}{2} F_{xy}^{-1} \left( \frac{K_y^2 F^{TM}(\vec{K}_s, z, z')}{K_{mz} |\vec{K}_s|^2} \right) \right), \tag{35}$$

$$G_{e,yz}^{TM} = \partial_z \left( \frac{-j}{2} F_{xy}^{-1} \left( \frac{j K_y F^{TM}(\vec{K}_s, z, z')}{K_{mz}} \right) \right), \tag{36}$$

$$G_{e,zx}^{TM} = \partial_z \left( \frac{j}{2} F_{xy}^{-1} \left( \frac{jK_x F^{TM}(\vec{K}_s, z, z')}{K_{mz}} \right) \right), \quad (37)$$

$$G_{e,zy}^{TM} = \partial_z \left( \frac{j}{2} F_{xy}^{-1} \left( \frac{jK_y F^{TM}(\vec{K}_s, z, z')}{K_{mz}} \right) \right), \quad (38)$$

$$G_{e,zz}^{TM} = \frac{-j}{2} F_{xy}^{-1} \left( \frac{|\vec{K}_s|^2 F^{TM}(\vec{K}_s, z, z')}{K_{mz}} \right). \quad (39)$$

**2.4.2. Calculation of  $\vec{\nabla} \times \bar{\bar{G}}_e(\vec{r}, \vec{r}')$ .** By applying curl operator to both sides of (22), one can get [38]:

$$\vec{\nabla} \times \bar{\bar{G}}_e(\vec{r}, \vec{r}') = \vec{\nabla} \times \bar{\bar{G}}_e^{TE}(\vec{r}, \vec{r}') + \frac{1}{K_{nm}^2} \vec{\nabla} \times \bar{\bar{G}}_e^{TM}(\vec{r}, \vec{r}'). \quad (40)$$

Then, by implementing some mathematical simplifications (similar to Section 2.4.1), one can calculate  $\vec{\nabla} \times \bar{\bar{G}}_e^{TE}(\vec{r}, \vec{r}')$  as [38]:

$$\begin{aligned} \vec{\nabla} \times \bar{\bar{G}}_e^{TE}(\vec{r}, \vec{r}') &= \begin{bmatrix} \partial_x \partial_z \partial_{y'} & -\partial_x \partial_z \partial_{x'} & 0 \\ \partial_y \partial_z \partial_{y'} & -\partial_y \partial_z \partial_{x'} & 0 \\ |\vec{K}_s|^2 \partial_{y'} & -|\vec{K}_s|^2 \partial_{x'} & 0 \end{bmatrix} g^{TE}(\vec{r}, \vec{r}') \\ &= \begin{bmatrix} [\nabla \times G_e^{TE}]_{xx} & [\nabla \times G_e^{TE}]_{xy} & 0 \\ [\nabla \times G_e^{TE}]_{yx} & [\nabla \times G_e^{TE}]_{yy} & 0 \\ [\nabla \times G_e^{TE}]_{zx} & [\nabla \times G_e^{TE}]_{zy} & 0 \end{bmatrix}, \end{aligned} \quad (41)$$

where each entry of  $\vec{\nabla} \times \bar{\bar{G}}_e^{TE}(\vec{r}, \vec{r}')$  can be written as:

$$\left[ \vec{\nabla} \times G_e^{TE} \right]_{xx} = \partial_z \left( \frac{-j}{2} F_{xy}^{-1} \left( \frac{K_x K_y F^{TE}(\vec{K}_s, z, z')}{K_{mz} |\vec{K}_s|^2} \right) \right), \quad (42)$$

$$\left[ \vec{\nabla} \times G_e^{TE} \right]_{xy} = \partial_z \left( \frac{j}{2} F_{xy}^{-1} \left( \frac{K_x^2 F^{TE}(\vec{K}_s, z, z')}{K_{mz} |\vec{K}_s|^2} \right) \right), \quad (43)$$

$$\left[ \vec{\nabla} \times G_e^{TE} \right]_{yx} = \partial_z \left( \frac{-j}{2} F_{xy}^{-1} \left( \frac{K_y^2 F^{TE}(\vec{K}_s, z, z')}{K_{mz} |\vec{K}_s|^2} \right) \right), \quad (44)$$

$$\left[ \vec{\nabla} \times G_e^{TE} \right]_{yy} = \partial_z \left( \frac{j}{2} F_{xy}^{-1} \left( \frac{K_x K_y F^{TE}(\vec{K}_s, z, z')}{K_{mz} |\vec{K}_s|^2} \right) \right), \quad (45)$$

$$\left[ \vec{\nabla} \times G_e^{TE} \right]_{zx} = \frac{1}{2} F_{xy}^{-1} \left( \frac{K_y F^{TE}(\vec{K}_s, z, z')}{K_{mz}} \right), \quad (46)$$

$$\left[ \vec{\nabla} \times G_e^{TE} \right]_{zy} = \frac{1}{2} F_{xy}^{-1} \left( \frac{K_x F^{TE}(\vec{K}_s, z, z')}{K_{mz}} \right). \quad (47)$$

Similarly for  $\vec{\nabla} \times \vec{G}_e^{TM}(\vec{r}, \vec{r}')$ ,

$$\vec{\nabla} \times \vec{G}_e^{TM}(\vec{r}, \vec{r}') = \begin{bmatrix} \partial_y \partial_x \partial_{z'} & \partial_y \partial_y \partial_{z'} & \partial_y |\vec{K}_s|^2 \\ -\partial_x \partial_x \partial_{z'} & -\partial_x \partial_y \partial_{z'} & -\partial_x |\vec{K}_s|^2 \\ 0 & 0 & 0 \end{bmatrix} \cdot K_n^2 g^{TM}(\vec{r}, \vec{r}') =$$

$$\begin{bmatrix} [\vec{\nabla} \times G_e^{TM}]_{xx} & [\vec{\nabla} \times G_e^{TM}]_{xy} & [\vec{\nabla} \times G_e^{TM}]_{xz} \\ [\vec{\nabla} \times G_e^{TM}]_{yx} & [\vec{\nabla} \times G_e^{TM}]_{yy} & [\vec{\nabla} \times G_e^{TM}]_{yz} \\ 0 & 0 & 0 \end{bmatrix}, \quad (48)$$

where,

$$[\vec{\nabla} \times G_e^{TM}]_{xx} = \partial_{z'} \left( K_n^2 \frac{-j}{2} F_{xy}^{-1} \left( \frac{K_x K_y F^{TM}(\vec{K}_s, z, z')}{K_{mz} |\vec{K}_s|^2} \right) \right), \quad (49)$$

$$[\vec{\nabla} \times G_e^{TM}]_{xy} = \partial_{z'} \left( K_n^2 \frac{-j}{2} F_{xy}^{-1} \left( \frac{K_y F^{TM}(\vec{K}_s, z, z')}{K_{mz} |\vec{K}_s|^2} \right) \right), \quad (50)$$

$$[\vec{\nabla} \times G_e^{TM}]_{xz} = \left( -K_n^2 \frac{1}{2} F_{xy}^{-1} \left( \frac{K_y F^{TM}(\vec{K}_s, z, z')}{K_{mz}} \right) \right), \quad (51)$$

$$[\vec{\nabla} \times G_e^{TM}]_{yx} = \partial_{z'} \left( K_n^2 \frac{j}{2} F_{xy}^{-1} \left( \frac{K_x F^{TM}(\vec{K}_s, z, z')}{K_{mz} |\vec{K}_s|^2} \right) \right), \quad (52)$$

$$[\vec{\nabla} \times G_e^{TM}]_{yy} = \partial_{z'} \left( K_n^2 \frac{j}{2} F_{xy}^{-1} \left( \frac{K_x K_y F^{TM}(\vec{K}_s, z, z')}{K_{mz} |\vec{K}_s|^2} \right) \right), \quad (53)$$

$$\left[ \bar{\nabla} \times G_e^{TM} \right]_{yz} = \left( K_n^2 \frac{-1}{2} F_{xy}^{-1} \left( \frac{K_x F^{TM}(\vec{K}_s, z, z')}{K_{mz}} \right) \right). \quad (54)$$

Once  $\bar{G}_e^{TM}(\vec{r}, \vec{r}')$  and  $\bar{\nabla} \times \bar{G}_e^{TM}(\vec{r}, \vec{r}')$  are calculated,  $L_E$  and  $\kappa_E$  can be calculated from (18) and (19) and then E-field can be calculated from (16). Moreover, H-field can be calculated using duality [38]. Since the considered case is general, it can be used for various types of sources and configurations. As a special case, electric and magnetic field distribution for an embedded electric dipole in a layered structure are calculated next.

**2.4.3. Embedded Electric Dipole Antenna in a Layered Structure.** Consider a center-fed thin dipole antenna with a length  $L_D$  which is embedded in layer  $m$  of a layered structure and is oriented arbitrarily in the  $xy$ -plane. The electric current density is assumed to be  $\vec{J} = J_x \hat{x} + J_y \hat{y}$  where  $J_x$  and  $J_y$  are constant and the magnetic current density is zero ( $\vec{M} = 0$ ). Using (16) and after pertinent calculations, E-field can be calculated as:

$$\vec{E}(\vec{r}) = \begin{bmatrix} E_x \\ E_y \\ E_z \end{bmatrix} = \begin{bmatrix} G_x^{p,x'}(\vec{r}; \vec{r}', f) \\ G_y^{p,x'}(\vec{r}; \vec{r}', f) \\ G_z^{p,x'}(\vec{r}; \vec{r}', f) \end{bmatrix} \frac{\omega \mu_m L_D}{2} J_x + \begin{bmatrix} G_x^{p,y'}(\vec{r}; \vec{r}', f) \\ G_y^{p,y'}(\vec{r}; \vec{r}', f) \\ G_z^{p,y'}(\vec{r}; \vec{r}', f) \end{bmatrix} \frac{\omega \mu_m L_D}{2} J_y, \quad (55)$$

where,  $G_i^{p,q}$  shows path Green's function in  $i$ -direction resulted from a  $q$  directed electric current density ( $i \in (x, y, z)$  and  $q \in (x', y')$ ) and it is defined as:

$$G_x^{p,x'}(\vec{r}; \vec{r}', f) = F_{xy}^{-1} \left( \frac{K_y^2 F^{TE}(\vec{K}_s, z, z')}{K_{mz} |\vec{K}_s|^2} \right) + \frac{1}{K_{mm}^2} \left( \partial_z \partial_{z'} \left( F_{xy}^{-1} \left( \frac{K_x^2 F^{TM}(\vec{K}_s, z, z')}{K_{mz} |\vec{K}_s|^2} \right) \right) \right), \quad (56)$$

$$\begin{aligned}
G_y^{P,x'}(\vec{r};\vec{r}',f) &= F_{xy}^{-1} \left( \frac{-K_x K_y F^{TE}(\vec{K}_s, z, z')}{K_{mz} |\vec{K}_s|^2} \right) \\
&+ \frac{1}{K_{mm}^2} \left( \partial_z \partial_{z'} \left( F_{xy}^{-1} \left( \frac{K_x K_y F^{TM}(\vec{K}_s, z, z')}{K_{mz} |\vec{K}_s|^2} \right) \right) \right),
\end{aligned} \tag{57}$$

$$G_z^{P,x'}(\vec{r};\vec{r}',f) = \frac{-1}{K_{mm}^2} \left( \partial_z \left( F_{xy}^{-1} \left( \frac{jK_x F^{TM}(\vec{K}_s, z, z')}{K_{mz}} \right) \right) \right), \tag{58}$$

$$\begin{aligned}
G_x^{P,y'}(\vec{r};\vec{r}',f) &= F_{xy}^{-1} \left( \frac{-K_x K_y F^{TE}(\vec{K}_s, z, z')}{K_{mz} |\vec{K}_s|^2} \right) \\
&+ \frac{1}{K_{mm}^2} \left( \partial_z \partial_{z'} \left( F_{xy}^{-1} \left( \frac{K_x K_y F^{TM}(\vec{K}_s, z, z')}{K_{mz} |\vec{K}_s|^2} \right) \right) \right),
\end{aligned} \tag{59}$$

$$\begin{aligned}
G_y^{P,y'}(\vec{r};\vec{r}',f) &= F_{xy}^{-1} \left( \frac{K_x^2 F^{TE}(\vec{K}_s, z, z')}{K_{mz} |\vec{K}_s|^2} \right) \\
&+ \frac{1}{K_{mm}^2} \left( \partial_z \partial_{z'} \left( F_{xy}^{-1} \left( \frac{K_y^2 F^{TM}(\vec{K}_s, z, z')}{K_{mz} |\vec{K}_s|^2} \right) \right) \right),
\end{aligned} \tag{60}$$

$$G_z^{P,y'}(\vec{r};\vec{r}',f) = \frac{1}{K_{mm}^2} \left( \partial_z \left( F_{xy}^{-1} \left( \frac{-jK_y F^{TM}(\vec{K}_s, z, z')}{K_{mz}} \right) \right) \right). \tag{61}$$

## 2.5. CONCLUSION

In this section, wave propagation inside of a layered structure was studied. The currently-available wave equations in literatures were used to calculate scalar Green's function for an embedded point source inside of a layered structure. Then, the point

source was replaced with vector distributed source and the corresponding E-field and H-field equations were presented. The obtained equations can be used to model a layered structure. The model is called forward model and it can be used to analyze the layered structure with an embedded source.

### 3. SAR-BASED MICROWAVE IMAGING OF EMBEDDED ACTIVE TARGETS

#### 3.1. INTRODUCTION

There is a growing interest to use newly emerging wireless devices such as embedded sensors and radio frequency identification (RFID) tags for commercial, industrial, and medical applications [43]-[45]. Considering most practical environments, these wireless devices may be embedded in an inhomogeneous structure consisting of an arbitrary number of layers. Also, these devices usually communicate with each other or with another device by transmitting and receiving EM signals. So, they may be modeled as active sources embedded in a layered structure. In Section 2, Green's function-based forward modeling technique was outlined which may be used to analyze a planar layered structure with an embedded EM source. By using this forward model, the E- and H-field distributions can be calculated anywhere inside of the layered structure. However, there are situations where locating an embedded sensor or a tag based on the received EM radiation (from it) is of interest. Moreover, locating any EM source in a layered structure may also be important from electromagnetic interference and compatibility (EMI/EMC) point of view. For instance, in a multilayered PCB, locating the source(s) of an unwanted EM signal radiation has significant value for EMI/EMC purposes.

In general, an externally illuminated embedded passive object or an embedded active EM source whose location is desired to be estimated is referred to as active target. Since the forward model calculates field distribution for an embedded active source inside a layered structure, locating the active target is considered as the inverse problem. In fact, in this inverse problem, there is a limited knowledge about the field distribution. Actually, an area outside of the structure (and usually in air) is considered where the measurements are performed over a 2D grid (so-called sampling or scanning area), as shown in Fig. 3.1. In this measurement scenario, the probe should not perturb the field that it intends to measure [46]-[47]. The probe may consist of a moving single probe that is scanned over the 2D area, or a collection of probes distributed (in some known fashion) over the 2D area. The latter case requires a more complex measurement system and hardware [48]. Furthermore, the near-by probes cause undesired mutual coupling that must be (in some way) measured or estimated and accounted for [49].



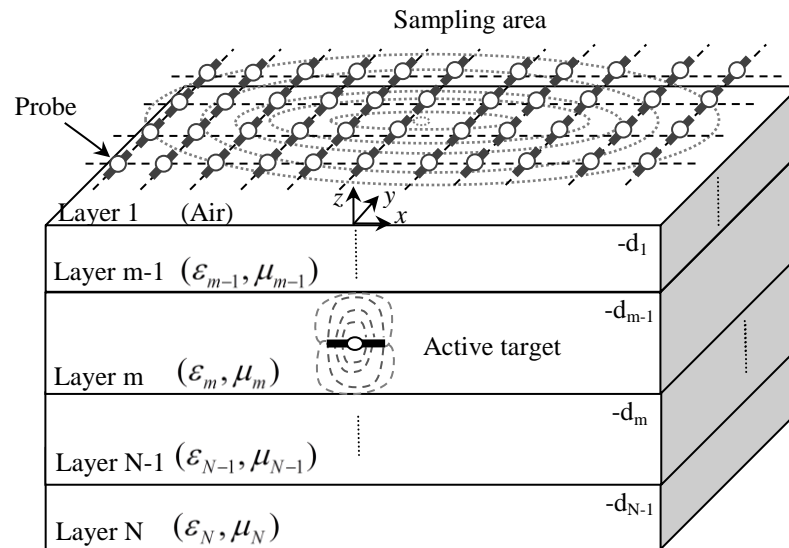


Figure 3.1. Using a collection of distributed probes to measure field distribution for an embedded active target inside of a planar layered structure.

A single scanning probe may minimally affect the measurements and can be readily scanned over the desired 2D area, while eliminating issues related to mutual coupling [2]. However, depending on the size of the sampling area and the distance between two adjacent sampling points (i.e., sampling step), the data collection time may become excessively long for many practical applications. To address the time issue, a few techniques have been developed which use nonuniform sampling and compressed sensing techniques [50]-[51].

To locate the active target, the collected sampled data must be properly processed. This processing is generally performed using (microwave) imaging technique. As mentioned earlier, there are two types of different (microwave) imaging techniques depending on the sought-for information, namely; quantitative and qualitative imaging. Quantitative imaging techniques or inverse scattering methods give the electrical and geometrical properties (distributions) of an imaged target by solving a nonlinear inverse problem. The nonlinear inverse problem is commonly solved iteratively while within each iteration the problem is linearized using Born or distorted Born approximations. This procedure is known as forward-iterative solution which requires high computational resources [9]-[16]. On the other hand, qualitative imaging techniques use migration-based

algorithms to reconstruct a qualitative (and approximate) image profile of the active target. Qualitative imaging methods usually invoke “*simplifying assumptions and approximations*” which may reduce the accuracy of the technique in comparison with quantitative methods. However, qualitative imaging techniques are usually robust and relatively fast (non-iterative). To this end, there are only a few imaging techniques introduced in literatures to image embedded objects or active targets in an arbitrary layered structure. Most of these techniques belong to quantitative imaging class which is slow, difficult to implement, and require extensive computational resources. On the other hand, synthetic aperture radar techniques are robust and fast imaging methods and have shown significant potential for many imaging applications [3],[5],[6]. Synthetic aperture radar methods assume that the background medium is homogeneous, and there exists only one reflected signal (i.e., no multiple reflections). Moreover, SAR methods assume the background medium to be lossless. These underlying assumptions limit the applications of SAR to only homogeneous and lossless (or low loss) medium.

Therefore, in this section, to address the first limitation of the SAR algorithm to image active targets embedded in a planar layered structure, a method, referred to as modified piecewise SAR (MPW-SAR) is developed, which takes into account the electrical and physical properties of each layer one at a time (hence, piecewise). The modification, over piecewise SAR [23], involves accounting for the effect of discontinuities between layers by incorporating appropriate transmission coefficients. Later, to address all of the three limitations of SAR associated with imaging sources in an arbitrary layered structures, another method is developed, which is referred to as Wiener filter-based layered SAR (WL-SAR). After mathematical manipulations a closed-form expression is derived for imaging embedded targets in an arbitrary layered structure. As will be shown, in this case the procedure to obtain an image from collected data is cast into a deconvolution procedure and then the Wiener filter-based deconvolution method, which is an efficient deconvolution technique, is selected for solving the deconvolution problem and reconstructing the image. In the following, first the qualitative image will be defined and the relationship between qualitative image and collected data will be established. Subsequently, SAR, MPW-SAR, and WL-SAR techniques will be explained in details.

### 3.2. RELATIONSHIP BETWEEN QUALITATIVE IMAGE AND COLLECTED DATA

Consider the embedded distributed (vector) current source in layer  $m$  of a planar layered structure, as shown in Fig. 2.2. As first approximation, Approximation 1, the vector source distribution is assumed to have no component in the  $z$ -direction (i.e., no component in range or depth direction). The distribution, then, is assumed to be composed of many electric Hertzian dipoles (i.e., a dipole with length  $L_D \rightarrow 0$ ). Without the loss of generality, it is assumed that the magnetic current density is zero. By using duality rules, the obtained results for the electric current density can be in turn applied to the magnetic current density case. The Hertzian dipole is very tiny (dimensionless) and the electric current density over each dipole positioned at  $\vec{r}' = (x', y', z')$  is assumed to be  $\vec{J}(\vec{r}') = J_x(\vec{r}')\hat{x} + J_y(\vec{r}')\hat{y}$ . Now, by considering the definition of dyadic Green's function, which was described in Section 2 and then using (55), E-field at the observation point  $\vec{r} = (x, y, z)$  can be calculated for each embedded Hertzian dipole as:

$$\vec{E}(\vec{r}, f) = \begin{bmatrix} E_x(\vec{r}, f) \\ E_y(\vec{r}, f) \\ E_z(\vec{r}, f) \end{bmatrix} = \begin{bmatrix} G_x^{p,x'}(\vec{r}; \vec{r}', f) \\ G_y^{p,x'}(\vec{r}; \vec{r}', f) \\ G_z^{p,x'}(\vec{r}; \vec{r}', f) \end{bmatrix} \Gamma_{x'}(\vec{r}', f) + \begin{bmatrix} G_x^{p,y'}(\vec{r}; \vec{r}', f) \\ G_y^{p,y'}(\vec{r}; \vec{r}', f) \\ G_z^{p,y'}(\vec{r}; \vec{r}', f) \end{bmatrix} \Gamma_{y'}(\vec{r}', f) \quad (62)$$

where,  $G_i^{p,q}$  (path Green's function in  $i$ -direction resulted from a  $q$  directed electric current density ( $i \in (x, y, z)$  and  $q \in (x', y')$ ) was defined in (56)-(61). Also,  $\Gamma_i(\vec{r}', f)$  is related to  $J_i(\vec{r}', f)$  as:

$$\Gamma_i(\vec{r}', f) = \frac{\omega \mu_m L_D J_i(\vec{r}', f)}{2}, \quad i \in (x', y'). \quad (63)$$

In fact,  $\Gamma_i(\vec{r}', f)$  can be considered as a qualitative image of the Hertzian dipole's projection in the  $i$ -direction ( $i \in (x', y')$ ). The vector equation in (62) can be divided into three scalar equations, for each of  $E_x$ ,  $E_y$ , and  $E_z$ . Solving any of these three equations is similar to the other one, and so, by dropping the indices (i.e.,  $x$ ,  $y$ , or  $z$ ), and defining

$s(\vec{r}, f)$  to be sampled (measured)  $E(\vec{r}, f)$  at the scanning area, then (62) can be rewritten as:

$$s(\vec{r}, f) = \Gamma_{x'}(\vec{r}', f)G^{P,x'}(\vec{r}; \vec{r}', f) + \Gamma_{y'}(\vec{r}', f)G^{P,y'}(\vec{r}; \vec{r}', f). \quad (64)$$

To solve (64), a system of two independent equations are required to solve for the two unknowns, namely;  $\Gamma_{x'}(\vec{r}', f)$  and  $\Gamma_{y'}(\vec{r}', f)$ . This system of two equations can be formed if the measuring probe can measure two components of E-field (e.g.,  $E_x$  and  $E_y$ ). However, practically speaking, instead of using E-field measurement techniques, a vector network analyzer is used for the measurement purpose. One of the VNA's ports (e.g., Port 2) is used to excite the active target and the other port (e.g., Port 1) is connected to the collector antenna (e.g., open-ended waveguide (OEW)) to collect the scattered signal. Therefore, the measured quantity is usually in term of S-parameters (i.e.,  $S_{21}$ ) and it is proportional to the received amplitude of the signal. Then, polarization loss factor (PLF) between the incoming wave and the antenna's polarization plays a major role [52]. Since dipole antenna and open-ended waveguide, as two commonly used collector antennas, are linearly polarized (in  $x$ - or  $y$ -direction), only one of the components of the E-field ( $E_x$  or  $E_y$ ) will have major contribution on the measured  $S_{21}$ . In other word,  $S_{21}$  can be interpreted as a qualitative measure of  $E_x$  or  $E_y$  depends on the polarization of the collecting antenna. So, as a measurement limitation, it is not possible to measure both components of the E-field simultaneously. Then, (64) becomes an underdetermined system which may have no or multiple solutions. Consequently, to remedy this problem, as second approximation, Approximation 2, depends on the antenna's polarization and *a priori* knowledge about the source polarization, one of the terms in the right side of (64) is removed. As a convention, term which has bigger polarization loss factor (in linear scale) with regards to the scanning antenna's polarization (or the term which is parallel to the antenna's polarization) will be kept and the other term will be eliminated.

Now, considering this fact that each layer of the planar layered structure is simple time-invariant medium, the data collected at the transceiver from a distributed vector

active target that is contained in the volume bounded by  $(x'_{\min} - x'_{\max})$ ,  $(y'_{\min} - y'_{\max})$ , and  $(z'_{\min} - z'_{\max})$  may be modeled as the superposition of E-field of Hertzian dipoles as:

$$S(\vec{r}, f) = \int_{z'=z'_{\min}}^{z'_{\max}} \int_{y'=y'_{\min}}^{y'_{\max}} \int_{x'=x'_{\min}}^{x'_{\max}} \Gamma(\vec{r}', f) G^P(\vec{r}; \vec{r}', f) dx' dy' dz', \quad (65)$$

where  $\Gamma(\vec{r}', f)$  is the qualitative image of the active target in the direction of the antenna's polarization. Also,  $G^P$  is the path Green's function calculated for this direction. Equation (65) relates the qualitative image of the embedded active target in a layered structure with the collected data. For homogenous media and by neglecting signal attenuation, (65) simplifies into a well-known equation [5]-[6]:

$$S(\vec{r}, f) = \int_{z'=z'_{\min}}^{z'_{\max}} \int_{y'=y'_{\min}}^{y'_{\max}} \int_{x'=x'_{\min}}^{x'_{\max}} \Gamma(\vec{r}', f) \exp(-jK_b R) dx' dy' dz', \quad (66)$$

where,  $K_b$  is wavenumber of homogeneous media or "background" and it is defined in (3). Also,  $R$  is the distance between the transceiver antenna and any point on the target, as defined in (2).

As indicated in (65) and (66), the unknown qualitative image ( $\Gamma$ ) is in the integrand, and hence, its direct evaluation becomes challenging. Qualitative imaging techniques for homogeneous background media attempt to simplify (65) by making reasonable assumptions that significantly reduce computational complexity. However as mentioned earlier, there are only a few reported qualitative imaging techniques in the literature pertaining to arbitrary layered structures [9]-[20]. Thus, two qualitative imaging techniques, namely; MPW-SAR and WL-SAR are introduced here and their results are compared to those of SAR images. Synthetic aperture radar algorithm is well-known, and therefore only a brief review is provided here.

### 3.3. SAR ALGORITHM

Synthetic aperture radar uses (66) and invokes the Weyl identity [36]-[38] to simplify and transform (66) into the  $xy$ -spectral domain using a 2D Fourier transform resulting in:

$$\bar{S}(K_x, K_y, z, f) = \bar{\Gamma}(K_x, K_y, z', f) \cdot \exp(-jK_z(z' - z)), \quad (67)$$

where,  $K_z$  is related to  $K_x$ ,  $K_y$ , and  $K_b$  via the dispersion relation (5). It should be noted that for the SAR algorithm,  $K_b$  is always a real number, and therefore  $K_z$  in (67) is only either real or imaginary. Only real and negative  $K_z$  (downward propagating waves) were used [5]-[6]. Then, the following expression can be used to calculate the qualitative image:

$$\Gamma(x', y', z') = \sum_f FT_{xy}^{-1} \left[ \bar{S}(K_x, K_y, z, f) \cdot \exp(jK_z(z' - z)) \right], \quad (68)$$

where,  $FT_{xy}^{-1}$  is the 2D inverse Fourier transform in  $K_x$  and  $K_y$  which is defined as:

$$FT_{xy}^{-1} \left\{ \bar{f}(K_x, K_y) \right\} = \frac{1}{(2\pi)^2} \iint \bar{f}(K_x, K_y) \exp(jK_x x) \exp(jK_y y) dK_x dK_y. \quad (69)$$

Comparing the applied definition in (69) with the one used in (6), one can see that in (6), the inverse Fourier transform uses  $(x - x')$  and  $(y - y')$  arguments in the definition. From now on, the bar will be reserved to present the spectral (Fourier) domain representation. Moreover, in [5] and [6], (68) was manipulated to utilize the three-dimensional (3D) inverse Fourier transform  $F_{xyz}^{-1}$  in  $K_x$ ,  $K_y$ , and  $K_z$  to obtain an estimate of the qualitative image, given by:

$$\Gamma(x', y', z' - z) = FT_{xyz}^{-1} \left[ \bar{S}(K_x, K_y, K_z, z) \cdot \exp(jK_z z) \right]. \quad (70)$$

Equation (70) has lower computational complexity than (68) if FFT and inverse FFT (IFFT) algorithms are used. As one can see from (68), (69), and (70), this SAR formulation only applies to homogeneous (background) medium. In order to use SAR for arbitrary layered structures, an *effective* homogenous medium may be estimated from the properties of the individual layers. As will be demonstrated later, using an effective homogeneous medium instead of the actual layered medium results in a shifted or defocused image of an embedded target, and may not be the most appropriate way to image a target in such media. This results from the fact that SAR does not consider the electrical or physical properties of the individual layers. However, in some special cases, this approximation may be useful for practical applications. The first attempt to address this problem resulted in the MPW-SAR algorithm, which is described below.

### 3.4. MODIFIED PIECEWISE SAR ALGORITHM

Piecewise SAR which was previously developed [23], incorporates additional phase to the spectrum of the collected data in a piecewise manner (i.e., one layer at a time) in order to focus on the target of interest. As such, it can account for layers of differing electrical/magnetic and physical properties (i.e., thickness). The governing expression in PW-SAR to focus on a target in layer  $m$  and at depth of  $z'$  from an antenna located at  $z$  can be written in spectral domain as:

$$\begin{aligned} \bar{\Gamma}(K_x, K_y, z', f) = & \bar{S}(K_x, K_y, z, f) \cdot \exp(jK_{z,1}(-d_1 - z)) \cdot \left[ \prod_{i=1}^{m-2} \exp(jK_{z,i}(d_i - d_{i+1})) \right] \\ & \cdot \exp(jK_{z,m}(z' + d_{m-1})), \end{aligned} \quad (71)$$

where,  $d_i$  is boundary between layer  $i$  and  $i+1$ , as shown in Fig. 3.1. Also, for  $i^{th}$  layer with relative dielectric constant of  $\varepsilon_i$  and permeability of  $\mu_i$ ,  $K_{z,i}$  is calculated using (5) where  $\varepsilon_b$  and  $\mu_b$  are replaced with  $\varepsilon_i$  and  $\mu_i$ , respectively. The qualitative image in spatial domain can be calculated using a 2D inverse FFT along  $x$  and  $y$ . However, (71) does not consider the discontinuity at the boundary between layers. To address this issue, a study was conducted to modify the piecewise SAR method in order to consider the

discontinuity between layers. The method is called modified PW-SAR or MPW-SAR. In MPW-SAR, to model and consider the boundary, the TE or TM mode Fresnel or generalized transmission coefficients  $T_{i,i+1}^{\rho,\vartheta}$  between layer  $i$  and  $i+1$  are used where  $\vartheta = \text{Generalized or Fresnel}$  ([36]-[37]) and their impacts are incorporated in (71) as:

$$\begin{aligned} \bar{\Gamma}(K_x, K_y, z', f) = & \bar{S}(K_x, K_y, z, f) \cdot \exp(jK_{z,1}(-d_1 - z)) \cdot \left[ \prod_{i=1}^{M-2} \exp(jK_{z,i}(d_i - d_{i+1})) \right] \\ & \cdot \exp(jK_{z,M}(z' + d_{M-1})) / \prod_{i=1}^{M-1} T_{i,i+1}^{\rho,\vartheta} T_{i+1,i}^{\rho,\vartheta} \end{aligned} \quad (72)$$

Since the transmission coefficients (either transverse magnetic or transvers electric) may become zero or have a very small value, (72) may become singular [20]. To overcome this problem, only the phase of transmission coefficients may be considered. Moreover, to obtain finer range resolution, a frequency sweep over a bandwidth is required. Then, the final imaging equation can be written as:

$$\Gamma(x', y', z') = \sum_f FT_{xy}^{-1} \left\{ \begin{aligned} & \bar{S}(K_x, K_y, z, f) \cdot \exp(jK_{z,1}(-d_1 - z)) \cdot \left[ \prod_{i=1}^{M-2} \exp(jK_{z,i}(d_i - d_{i+1})) \right] \\ & \cdot \exp(jK_{z,M}(z' + d_{M-1})) / \prod_{i=1}^{M-1} \exp(-j\angle(T_{i,i+1} T_{i+1,i})) \end{aligned} \right\}. \quad (73)$$

The entire procedure is summarized in a flow-chart and it is presented in Fig. 3.2. Equation (73) can be seen as a general and more complete version of equation (11) reported in [20] for through-wall imaging. Equation (73) considers properties of the layers as well as boundary discontinuities. In contrast with [20] that uses spatial domain representation, (73) uses the spectral domain representation resulting in much faster execution time and does not require explicit angular dependency (i.e.,  $\theta$  in [20]). The MPW-SAR takes proper phase shift into account from the collecting antenna at  $z$  to a focusing plane at  $z'$ , which enables obtaining correctly-positioned and focused indications of targets in the images. However, both SAR and MPW-SAR do not compensate for multiple reflections or signal attenuation. Therefore, it can be expected that if there is a large distance or a lossy material between the antenna and the object, the



object may appear dim or not appear at all. This was the motivation to seek a more comprehensive technique that addresses these problems, as will be discussed next.

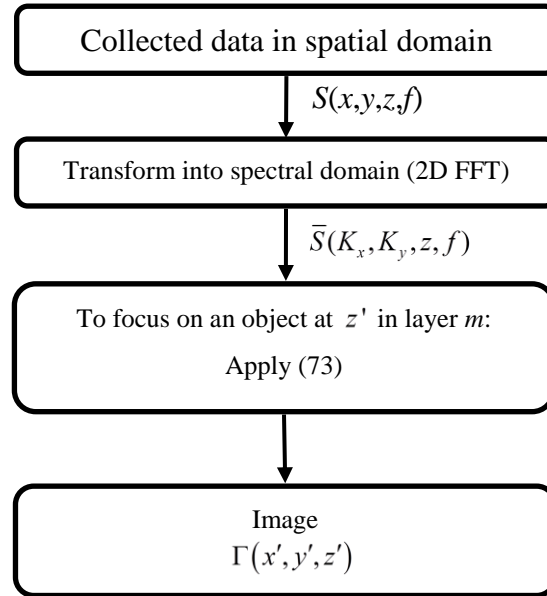


Figure 3.2. Flow-chart of MPW-SAR.

### 3.5. WIENER FILTER-BASED SAR

As it was explained earlier in Section 3.2, collected data  $S(\vec{r}, f)$  is related to the physical and electrical properties of the media and the qualitative image,  $\Gamma$ , through (65). Moreover, based on provided equations for path Green's function, it can be shown that:

$$G^P(x, y, z; x', y', z', f) = G^P(x - x', y - y', z - z', f). \quad (74)$$

By applying (74) to (65), (65) can be rewritten as:

$$S(x, y, z, f) = \int_{z'=z'_{\min}}^{z'_{\max}} \int_{y'=y'_{\min}}^{y'_{\max}} \int_{x'=x'_{\min}}^{x'_{\max}} \Gamma(x', y', z', f) \cdot G^P(x - x', y - y', z, z', f) dx' dy' dz'. \quad (75)$$

Then, by the definition of convolution, (75) can be written as:

$$S(x, y, z, f) = \int_{z'=z'_{\min}}^{z'_{\max}} \left[ \Gamma(x, y, z', f) * G^P(x, y, z, z', f) \right] dz', \quad (76)$$

where (\*) denotes the convolution operation along the  $x$  and  $y$  dimensions. Obtaining the reflectivity function from (76) requires solving integral equations which are computationally intensive and case-dependent. Consequently, instead of solving (76) directly, it may be simplified by assuming the qualitative image has nonzero values only on the plane  $z'$  (i.e., the target only exists on the plane of  $z'$ ). This assumption, Approximation 3, is similar to the assumption used in [5] and [6] where the SAR algorithm for free-space was developed. Therefore, (76) can be simplified as:

$$S(x, y, z, f) = \Gamma(x, y, z', f) * G^P(x, y, z, z', f) + \nu(x, y, z, f). \quad (77)$$

Considering actual measurements, noise and other sources of interference also contribute to the measured data. To account for these as well, one extra term, namely;  $\nu(x', y', z', f)$  was added into (77) to represent additive noise. Equation (77) is the final imaging expression written in convolution form. Finding the qualitative image from (77) requires a deconvolution. Although convolution techniques are robust and well-studied, deconvolution techniques are usually case-dependent. After a thorough literature search, the Wiener filter-based deconvolution was selected to perform the deconvolution in the presence of additive noise. This deconvolution technique, can estimate an unknown input signal from known output and known transfer function of the system. The Wiener filter has been used for many applications such as blurred image restoration, image reconstruction for aperture synthesis radiometers, digital seismic signal processing, improving time-resolution and signal-to-noise ratio (SNR) of ultrasonic nondestructive testing signals, noise reduction in SAR interferometry, and de-speckling of SAR images [53]-[59]. As a more specific example, the Wiener filter was used to estimate the impulse response of a possible tumor in breast tissue [60]. However, using Wiener filter-based

deconvolution for the SAR-based imaging of a layered structure has not been reported before. Applying the Wiener filter deconvolution to (77) gives:

$$\Gamma(x', y', z', f) = FT_{xy}^{-1} \left\{ \frac{\bar{S} \cdot (\bar{G}^P)^H}{\bar{G}^P \cdot (\bar{G}^P)^H + \delta^2} \right\}, \quad (78)$$

where,  $(H)$  represents the complex conjugate operator. Also,  $\bar{S}$  and  $\bar{G}^P$  are spectral domain representations of  $S$  and  $G^P$ , respectively, and both are function of  $K_x, K_y, K_z, z$ , and  $f$ . Moreover,  $\delta^2$  is noise desensitization factor and is defined as:

$$\delta^2 = \frac{PSD_v}{PSD_\Gamma}, \quad (79)$$

where,  $PSD_v$  and  $PSD_\Gamma$  are noise and qualitative image power spectral densities, respectively [54]. It is clear that the Wiener filter requires *a priori* knowledge about the noise and reflectivity functions. However, it is not practical to know the power spectral density of qualitative image ahead of time. Therefore, by modification of the proposed criteria in [54], an approximate value for  $\delta^2$  can be set as:

$$\delta^2 = \alpha \left| \bar{G}^P(K_x, K_y, z, f) \right|_{\max}^2, \quad (80)$$

where,  $\left| \bar{G}^P \right|_{\max}^2$  shows maximum value of the  $\left| \bar{G}^P \right|^2$  over the range of  $z$  corresponding to the imaging volume. Also,  $\alpha$  is a coefficient that may be adjusted or “tuned” and its value is case-dependent (i.e., ranging between  $10^{-1}$  to  $10^{-12}$ ). In [54], it is suggested to set  $\alpha$  to a fixed value (i.e., 0.01), however, as it will be seen, this approximate value does not work for all the cases. Based on the available data in the literatures, it was found that there is no closed-form expression for calculating this coefficient. In fact, in (78),  $\delta^2$  was used as a regularization parameter that takes care of cases where  $\left| \bar{G}^P \right|^2$  has zero values

(i.e., singularity) indicating non-propagating waves. Moreover, as distance between the focusing plane and the scanning antenna increases, the signal power decreases, which is proportional to  $|\bar{G}^P|^2$ . The amount of attenuation strongly depends on the distance and signal loss in the propagation path. The longer the distance and the higher the loss is, the smaller  $|\bar{G}^P|^2$  will be. Therefore,  $\delta^2$  is used to regulate not only zero valued  $|\bar{G}^P|^2$  but also small  $|\bar{G}^P|^2$ . In fact,  $\delta^2$  can be seen as a selection criterion for minimum power threshold. As a rule of thumb, by only having an approximate knowledge about the region of interest, one may calculate  $|\bar{G}^{RT}|_{Region}^2 / |\bar{G}^{RT}|_{max}^2$  for that region and then use the calculated value to estimate  $\alpha$  for imaging purposes. Additional explanation is provided later when the simulation results are discussed. To gain finer range resolution, as in the case of SAR, frequency may be swept within a prescribed bandwidth [3],[5],[6]. Thus, the final image is simply the sum of all the estimated qualitative images per each discrete frequency. Consequently, this can be expressed as:

$$\Gamma(x', y', z') = \sum_f \Gamma(x', y', z', f). \quad (81)$$

The entire imaging procedure is summarized in the flow-chart shown in Fig. 3.3.

In the following, simulations and measurements are used to show the advantages and limitations of SAR, PW-SAR, MPW-SAR, and WL-SAR image reconstruction algorithms for the specific purpose of imaging embedded active targets in an arbitrary planar layered structure.

### 3.6. SIMULATIONS

In this part, the efficacy of the proposed imaging techniques is examined through some simulations. For each example, physical and electrical properties of layers, scanning area, and frequency range must be known.

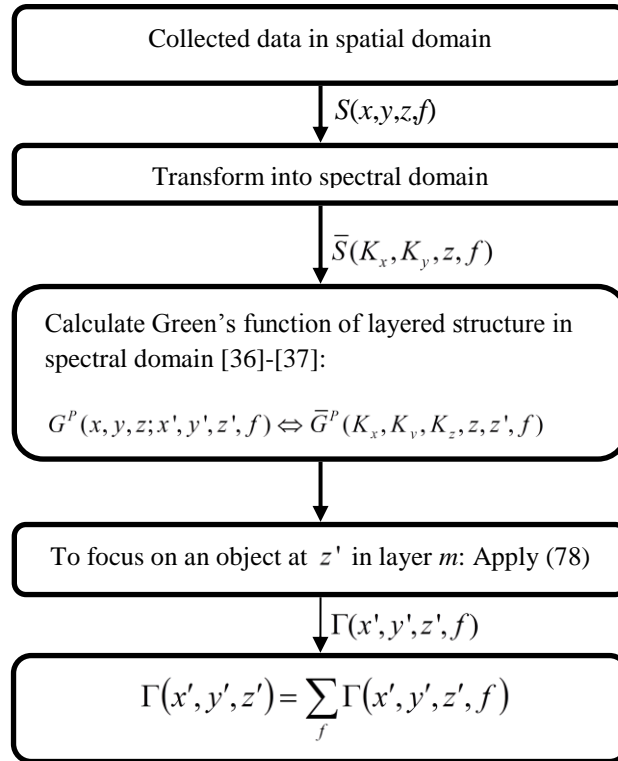


Figure 3.3. Flowchart of the WL-SAR algorithm.

The selection of scanning antenna is also important. Finer cross-range resolution is achieved through a wide beamwidth and a large synthetic aperture (scanning area), and finer range resolution is achieved through wider transmitted signal BW [24]. However, for imaging of active targets, the bandwidth of operation is dictated by the frequency range of active target radiation. In the simulations, the antenna and the active target are assumed to be isotropic to simplify the simulations by using forward modeling which was explained in Section 2. By using the forward model, the complex electric field distribution over the scanning area can be calculated. Having calculated the complex field distribution, one can sample it at the prescribed scanning antenna positions and use the sampled data as collected data (i.e., representing measured electric field).

In the experiments, an open-ended rectangular waveguide is used since it provides a relatively wide beamwidth, supports a relatively wide bandwidth, and has been the workhorse of probes for nondestructive testing-based imaging [4]. To collect measured data, an automated scanning table is used in conjunction with an HP8510C VNA to scan

an OEW over the sample under test and collect the complex transmission scattering coefficient  $S_{12}$ , serving as the collected data. Also, since the equations were derived for an isotropic scanning antenna, using an OEW for active target imaging may introduce some undesired issues since the antenna pattern and directivity are not incorporated in the equations. However, since the OEW has a fairly wide beamwidth, this issue may not be considered so critical for the purpose of demonstrating the efficacy of these imaging techniques [24].

All of the simulations are performed at X-band (i.e., 8.2-12.4 GHz) with frequency step size of 100 MHz unless otherwise mentioned. The simulation and image formation are performed on a 64-bit PC with 8 GB of RAM and Core2 Quad CPU of 2.66 GHz.

Also, as mentioned in Section 3.1, locating embedded sensors, RFID tags, radiating traces in a multilayered PCB, or generally any EM signal leakage in a structure has practical value, and therefore will be addressed here. In simulations, the sensors, RFID tags, radiating traces, pre-illuminated passive objects or any EM source of leakages will be simply modeled using a point source. This simple modeling of physical source with a scalar point source may not be accurate and comprehensive; however, it can serve as the initial study to pave a road for future works.

**3.6.1. Finding a Radiating Trace in a Single Layer PCB.** In the first simulation (Simulation 1), a situation is mimicked where a trace which is routed inside of a RogersRT6006 dielectric substrate ( $\epsilon_r = 6.5 - j0.018$ ) is radiating an unwanted signal. From EMI/EMC point of view, it is desired to find the location of the trace. To model the trace, an isotropic source is used at a depth of 2 cm from surface of the substrate. The mode of wave propagation inside the layered structure is also assumed to be TM mode (which is required for scalar Green's function calculations). The dielectric substrate is assumed to be 4 cm thick (thinner substrates can be tested by increasing the frequency). Moreover, an isotropic scanning antenna is in the first (top) layer at a distance of 2 cm from the substrate. The bottom layer (third layer) is assumed to be extended to infinity in the  $z$ -direction. The 2D configuration of the structure and scanning setup is shown in the  $xz$ -plane in Fig. 3.4. The scanning was performed linearly along the  $x$ -direction from -7.5 cm to 7.5 cm with a step size of 0.3 cm.

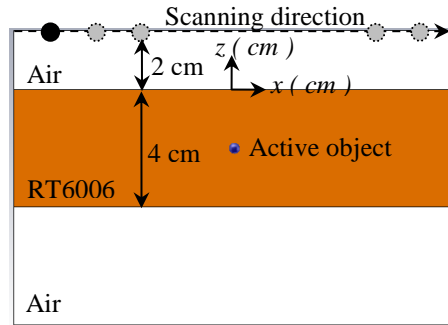


Figure 3.4. Configuration of Simulation 1.

By implementing the TM mode scalar Green's function using (15) for the layered structure, the 2D complex electric field distribution was calculated per frequency. For frequency of 10 GHz, the real, imaginary, magnitude, and phase parts of the electric field are shown in Fig. 3.5. The real, imaginary, and magnitude parts of the field are normalized and the phase distribution is in radian.

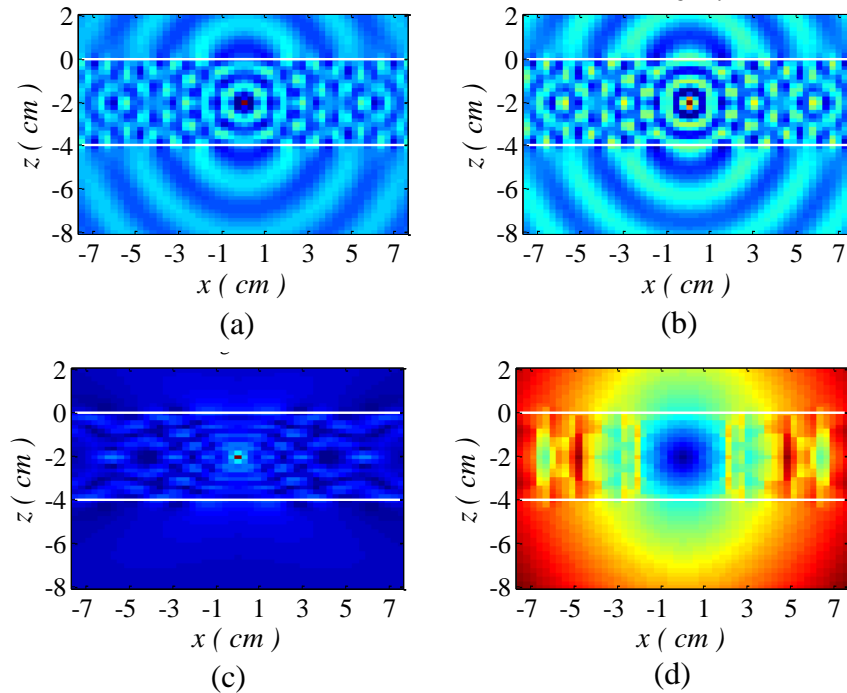
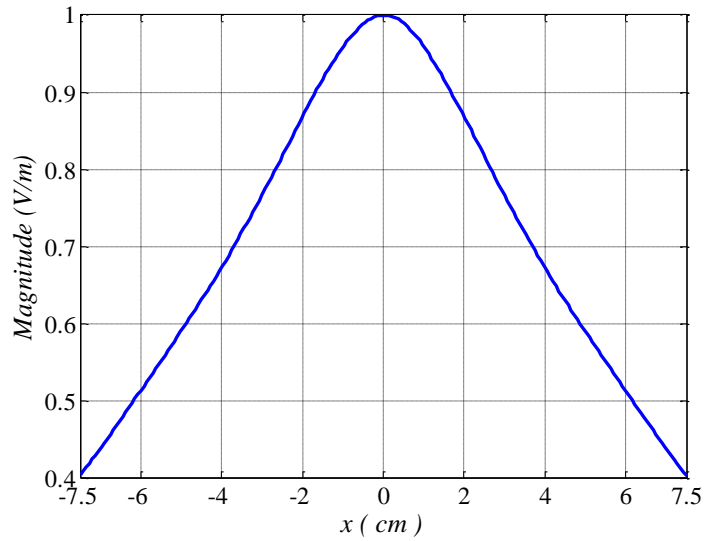
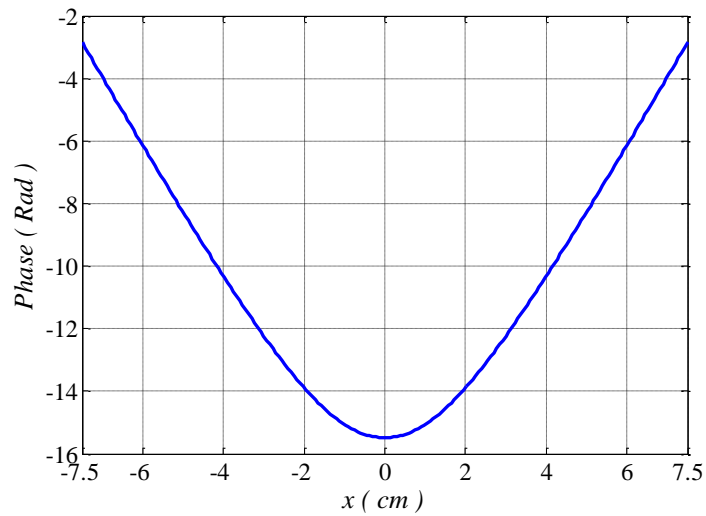


Figure 3.5. Calculated electric field distribution. (a) real, (b) imaginary, (c) magnitude, and (d) unwrapped phase (rad).

The sampled complex electric field at  $z = 2$  cm (the scanning antenna's position) is used as the collected data ( $S$ ). For frequency of 10 GHz the collected data is shown in Fig. 3.6. The collected data is then processed using the imaging techniques discussed earlier so that the results may be directly compared.



(a)



(b)

Figure 3.6. Collected data at 10 GHz (a) normalized magnitude (V/m), and (b) phase (rad).



For SAR, the effective homogeneous background medium can be calculated in different ways. The layer with the lowest dielectric constant or the highest dielectric constant can be used as background medium. Alternatively a simple geometric average of permittivity may be used to estimate the permittivity of the background medium. However, for demonstration purposes this average suffices since it will be seen in the results that this approach to SAR does not work well, regardless. Based on this idea, the effective relative dielectric constant for a layered structure can be considered as:

$$\varepsilon_{r,b} = \frac{\text{Real} \left[ \sum_{i=1}^N \varepsilon_{r,i} t_i \right]}{\sum_{i=1}^N t_i}, \quad (82)$$

where,  $t_i$  is thickness of  $i^{\text{th}}$  layer. Thickness of first layer was assumed to be equal to the distance of the antenna from the second layer (i.e., 2 cm). For the  $N^{\text{th}}$  layer (i.e., bottom layer), the thickness was selected to be larger than the distance between the deepest target and the boundary between layer  $N$  and layer  $N-1$  (if there is any target in  $N^{\text{th}}$  layer). This results in  $\varepsilon_{r,b} = 3.2$ , which as anticipated, is not a good representative of the layered structure. Subsequently, the produced image using SAR algorithm is shown in Fig. 3.7 (a). To indicate the boundaries between layers, the white horizontal lines were added to all images in Fig. 3.7. The SAR image shows a focused but shifted indication of target. Moreover, there is a weak and false defocused indication of target appearing in an incorrect depth. For the sake of comparison, the SAR images using lowest and highest dielectric constants were also calculated and shown in Fig. 3.7 (b)-(c), respectively. As one can see, indication of the target is defocused and misplaced. As anticipated, the inaccurate modeling of the layered structure is the root of the problems for SAR. Therefore, estimating the background medium with an effective material is not an appropriate way to compensate for phase shifts, which leads to unfocused and shifted indications of actual target(s) in SAR images. In contrast, Fig. 3.7 (d) shows the image resulting from the MPW-SAR, indicating focused and correctly located target. This was expected since the MPW-SAR applies correct phase shift to the collected data. The

resolution limitations caused the size of indication of target which is a point source to look bigger.

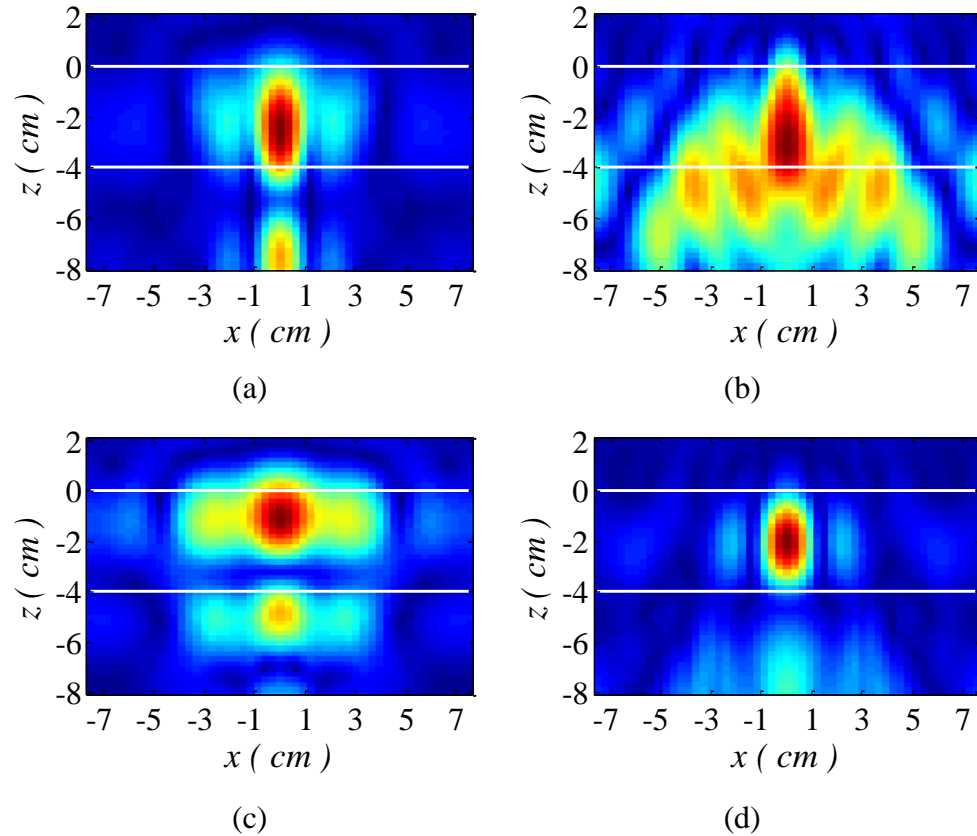


Figure 3.7. Image for Simulation 1. (a) SAR ( $\varepsilon_{r,b} = 3.2$ ), (b) SAR ( $\varepsilon_{r,b} = 1$ ), (c) SAR ( $\varepsilon_{r,b} = 6.5$ ), (d) MPW-SAR.

The same collected data is then used in conjunction with the WL-SAR algorithm to produce an image of the embedded target. The rule of thumb method, which was explained earlier, was used to select  $\alpha$  for the Wiener filter. First, it was assumed that there is *a priori* knowledge concerning the region of interest. In fact, it was assumed that the target is only located inside the substrate (i.e., second layer). Then, for two selected focusing planes in the second layer (e.g.,  $z' = -0.6 \text{ cm}$  and  $z' = -3 \text{ cm}$ ),  $|\bar{G}^{RT}|_{\text{Region}}^2 / |\bar{G}^{RT}|_{\text{max}}^2$  was calculated and plotted in Fig. 3.8 (in dB scale) for operating frequency of 10 GHz.

The maximum value of the plots over  $K_x$  was used to select  $\alpha$ . Therefore, a value in the range of approximately -15 dB (or  $10^{-1.5}$ ) to -50 dB (or  $10^{-5}$ ) for  $\alpha$  may be a good choice.

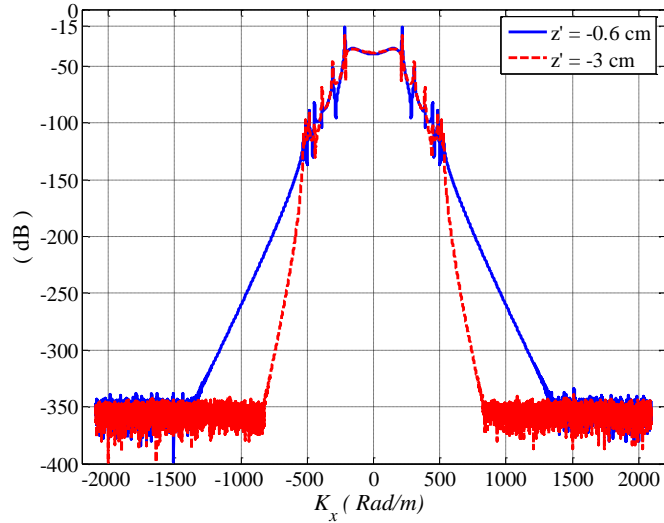


Figure 3.8. Calculated  $|\bar{G}^{RT}|_{Region}^2 / |\bar{G}^{RT}|_{max}^2$  for two different values of  $z' = -0.6\text{ cm}$  and  $z' = -3\text{ cm}$  at 10 GHz.

The produced images using the WL-SAR algorithm with  $\alpha$  of -15dB, -35dB, -50 dB, and -70dB are shown in Fig. 3.9, respectively. For  $\alpha = -15\text{ dB}$ , target is focused and correctly positioned. However, there are some defocused artifacts at the bottom of the image (Fig. 3.9 (a)). By reducing  $\alpha$  to -35 and then -50 dB, those artifacts disappear (Fig. 3.9 (b)-(c)). However, by reducing  $\alpha$  (e.g., to -70 dB), small defocused images in the third layer is significantly intensified (Fig. 3.9 (d)). In fact, the WL-SAR algorithm seems to emphasize deeper focusing planes from antenna rather than closer planes and the region of interest will change to third layer. Therefore, by decreasing  $\alpha$ , the indication of small artifacts in deeper layers becomes stronger while the indication of target becomes weaker. This example proved that a choice of  $\alpha$  in the range of -15 dB to -50 dB which was estimated by rule of thumb, results in relatively clean and focused indications of target in the image.

From performance point of view, the produced WL-SAR image with  $\alpha = -50\text{dB}$  contains much less artifacts in the bottom of the image in comparison with SAR and the MPW-SAR (Fig. 3.7). However, the processing time for WL-SAR was about 5 minutes while it was only 1 second for SAR and MPW-SAR each.

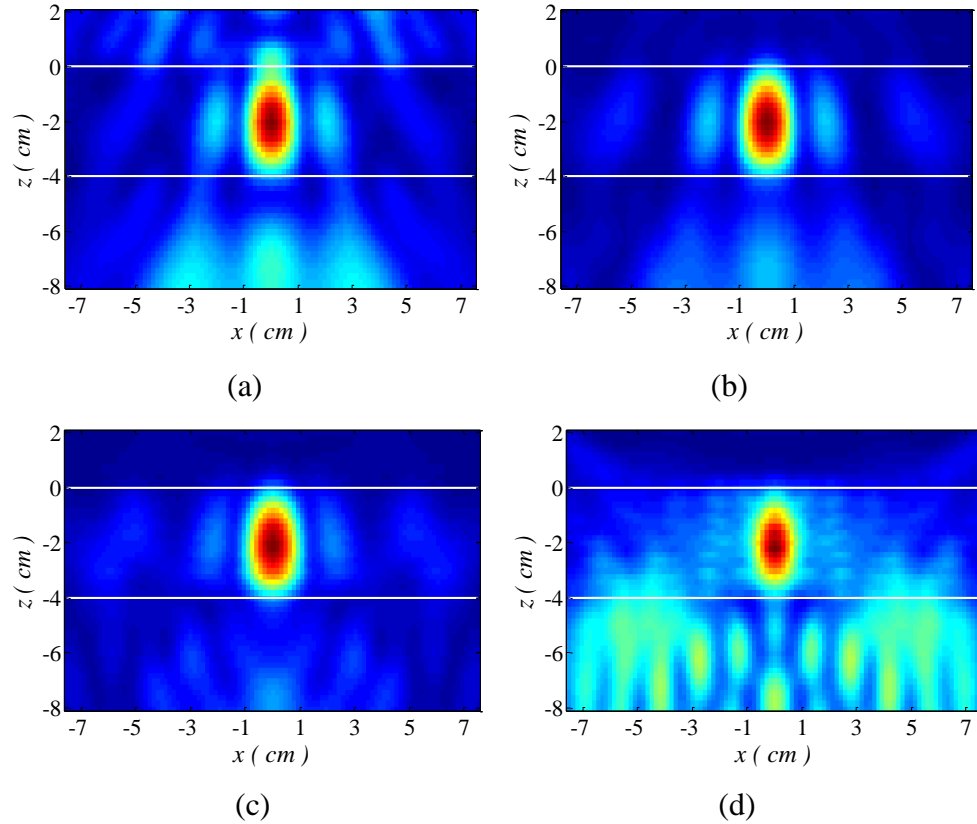


Figure 3.9. Images for Simulation 1 using WL-SAR. (a)  $\alpha = -15\text{dB}$  , (b)  $\alpha = -35\text{dB}$  , (c)  $\alpha = -50\text{dB}$  , and (d)  $\alpha = -70\text{dB}$  .

**3.6.2. Locating Radiating Traces in Multilayered PCB.** In the second example, a more general case is considered by assuming three different point active targets embedded in a complex four-layer PCB which operate in TM mode. The configuration is selected to be similar to the third example in Section 2. The scanning isotropic antenna is located in air (top layer) at a distance of 30 cm from the PCB and linearly scans in the  $x$ -direction from -33 cm to +33 cm with a step size of 0.3 cm. First layer is air and it

extends from  $z=0$  to infinity in the  $z$ -direction. Second layer is 12 cm thick Rogers RO3203 ( $\epsilon_r = 3.02 - j0.003$ ). Third layer is 12 cm thick Arlon AR450 ( $\epsilon_r = 4.5 - j0.0135$ ). The fourth layer is 15 cm thick Rogers RO4003 ( $\epsilon_r = 3.55 - j0.01$ ). The bottom layer is Rogers RT5880 which extends to infinity in the other  $z$ -direction and its dielectric constant is  $\epsilon_r = 2.2 - j0.001$ . The three active point targets (i.e., Target 1, Target 2, and Target 3) are all located in the  $xz$ -plane and positioned at  $(-6, 0, -4.5)$  cm,  $(-16.5, 0, -18)$  cm, and  $(9, 0, -30)$  cm, respectively (Fig. 3.10). Using the scalar Green's function-based forward model and following the same procedure as in Simulation 1, the complex electric field distribution was collected and fed to the proposed algorithms and the corresponding reconstructed images are shown in Fig. 3.10 (b)-(c). For SAR, the effective background medium was calculated using (82) to be  $\epsilon_{r,b} = 3.26$ . The SAR image of Targets 1 and 2 are defocused while Target 3 is correctly imaged (Fig. 3.10 (b)). Almost same explanation which was provided for Simulation 1 can be used to explain these results. On the other hand, as Fig. 3.10 (c) shows, image resulting from MPW-SAR, indicates focused and correctly imaged objects.

The same collected data is fed into the WL-SAR algorithm while the region of interest was selected to include RO3203, AR 450, and RO3003 substrates (i.e., layers 2, 3, and 4). The rule of thumb was used to select  $\alpha$  based on the region of interest. For three selected focusing planes in the region of interest (e.g.,  $z' = -1$  cm,  $z' = -14$  cm, and  $z' = -38$  cm),  $|\bar{G}^{RT}|_{Region}^2 / |\bar{G}^{RT}|_{max}^2$  was calculated and plotted in Fig. 3.11 (in dB scale) for frequency of 10 GHz. The maximum values of the plots over  $K_x$  are used to select  $\alpha$ . Therefore, a value in the range of approximately -18 dB (or  $10^{-1.8}$ ) to -40 dB (or  $10^{-4}$ ) for  $\alpha$  may be a good choice. The produced images using the WL-SAR algorithm with  $\alpha$  of -20 dB, -40 dB, -70 dB, and -110 dB are shown in Fig. 3.12. The rule of thumb estimated range for  $\alpha$  resulted in a focused indication of all three targets. By decreasing  $\alpha$  to a value lower than minimum value of the estimated range (e.g.,  $\alpha = -110$  dB), the indications become unfocused and artifacts become stronger.

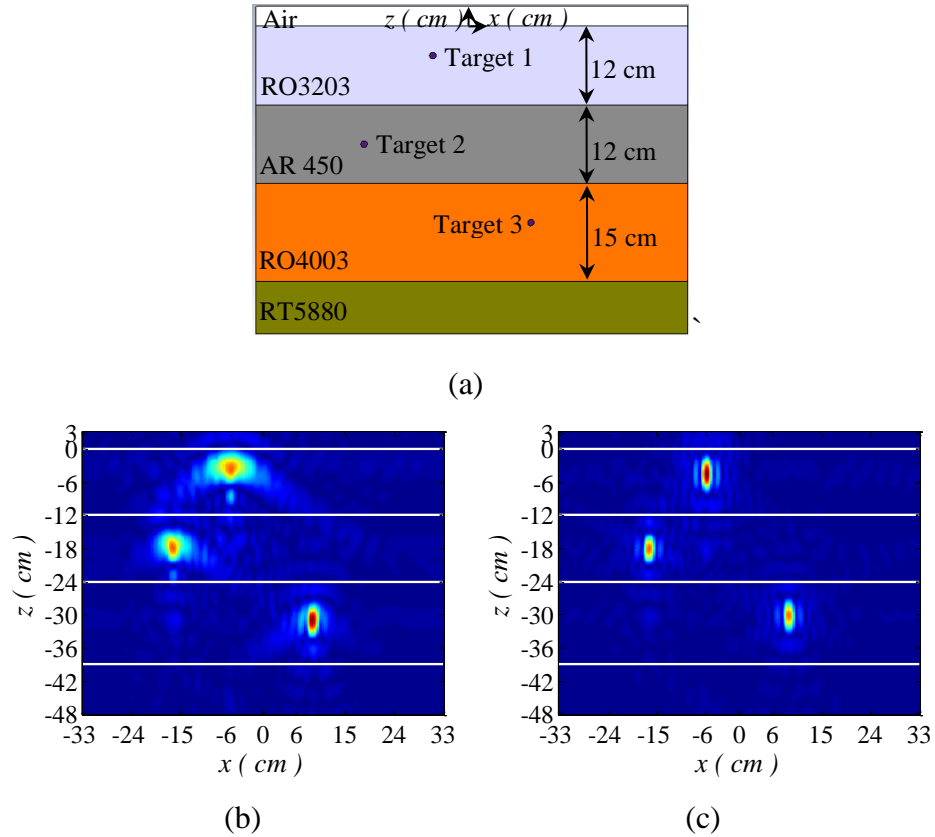


Figure 3.10. Simulation 2. (a) configuration, (b) SAR image ( $\varepsilon_{r,b} = 3.26$ ), (c) MPW-SAR image.

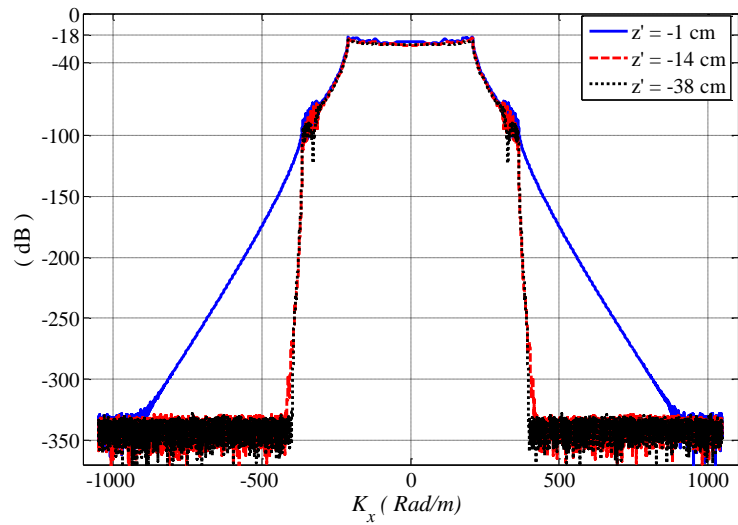


Figure 3.11. Calculated  $\left| \bar{G}_{Region}^{RT} \right|^2 / \left| \bar{G}_{max}^{RT} \right|^2$  for three different values:  $z' = -1\text{ cm}$ ,  $z' = -14\text{ cm}$ , and  $z' = -38\text{ cm}$ .

Moreover, a direct comparison between results of SAR and MPW-SAR (Fig. 3.10) with the produced image using WL-SAR with  $\alpha = -40\text{dB}$ , shows that two deeper targets (Targets 2 and 3) are more stronger in Fig. 3.12 (b).

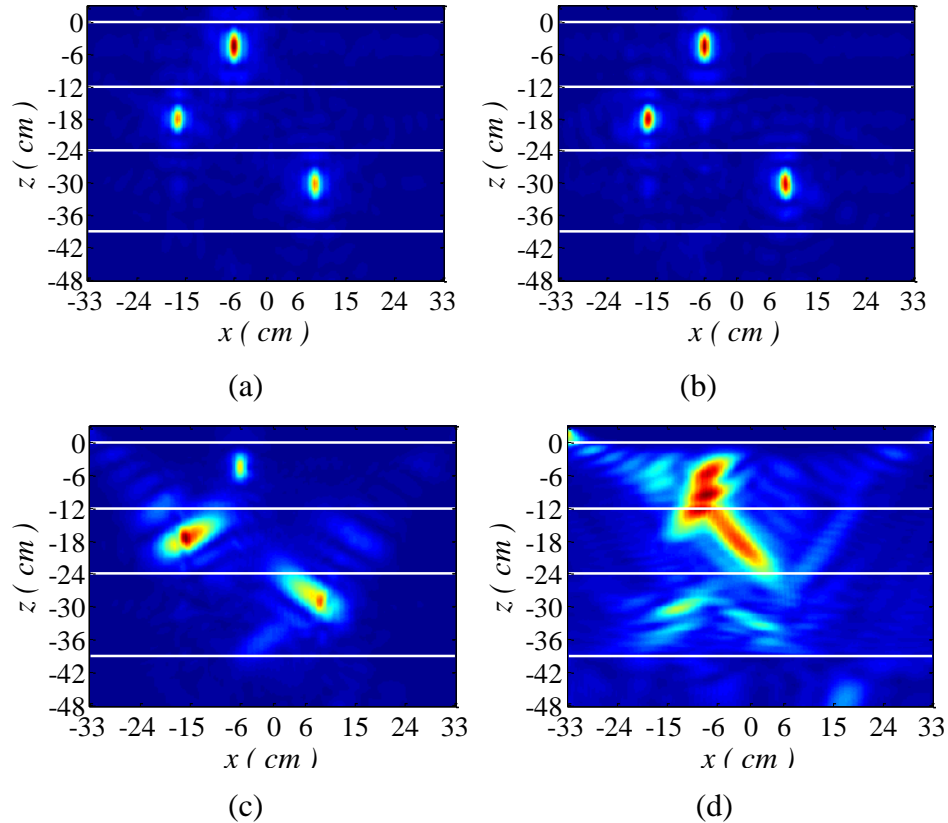


Figure 3.12. Reconstructed images for Simulation 2 using WL-SAR. (a)  $\alpha = -20\text{dB}$ , (b)  $\alpha = -40\text{dB}$ , (c)  $\alpha = -70\text{dB}$ , and (d)  $\alpha = -110\text{dB}$ .

As an extra step, and to show the limitation/ability of the techniques, the same example is repeated by changing the dielectric constant of the third layer (i.e., Arlon AR 450) to be  $\epsilon_r = 4.5 - j0.2$ . Then, the same scanning configuration was used for data collection and the collected data was fed into the three imaging algorithms. The produced images are shown in Fig. 3.13. Increasing the loss significantly degraded the performance of the SAR and the MPW-SAR. Targets 2 and 3 are shown to be faint, while the WL-SAR shows superior performance and correctly imaged all three targets.

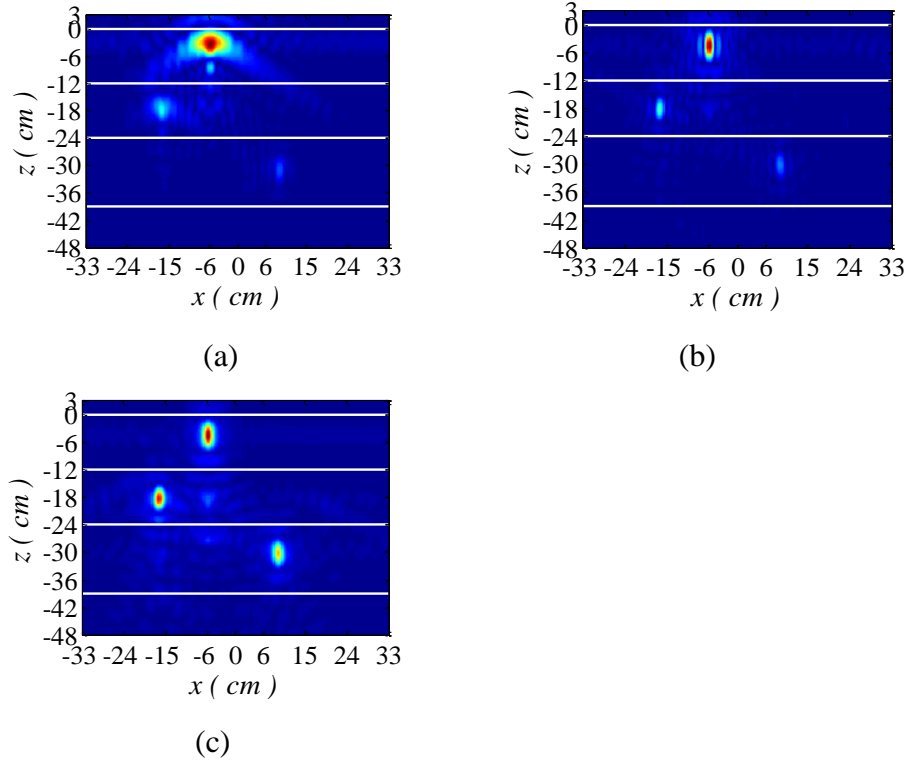


Figure 3.13. Reconstructed images for Simulation 2 after introducing extra loss. (a) SAR, (b) MPW-SAR, and (c) WL-SAR with  $\alpha = -40\text{dB}$  .

**3.6.3. Experimental Result.** In this experiment (Experiment 1), finding an EM source such as active RFID tag or wireless sensor which is located behind a refractory brick is considered. Two dipole antennas each with a length of approximately 1 cm were used as active targets, which were connected to Port 2 of the VNA using a 3-dB power divider, as shown in Fig. 3.14. The dipoles were slightly tilted and were positioned at two slightly different depths below the structure. The first layer is air and it extends from  $z=0$  to infinity in the  $z$ -direction. The second layer is a 7.8 cm thick clipper DP refractory brick ( $\epsilon_r = 3.73 - j0.05$ ) [61]. The bottom layer is air which extends to infinity in the other  $z$ -direction. A Ku-band (12.4-18 GHz) open-ended rectangular waveguide used as the scanning antenna which was installed on the scanner at a distance of 7.8 cm above surface of the refractory brick. The antenna was moved while linearly scanned from  $x = -10$  cm to 10 cm with a step size of 0.2 cm. The antenna is polarized in  $y$ -direction. The  $S_{21}$  measurements were performed at Ku-band with frequency step size of



500 MHz. The collected data was fed into SAR (with  $\varepsilon_{r,b} = 1.77$  from (82)), PW-SAR, and MPW-SAR. The indication of dipoles in the produced image using SAR is focused but slightly shifted down (Fig. 3.15). The indication of dipoles in the produced images using PW-SAR is focused and correctly positioned (Fig. 3.15 (b)). For MPW-SAR, to model the discontinuity between layers, TE/TM mode Fresnel/generalized transmission coefficients, can be used. After trying all four different cases, it was observed that the produced image using any of these cases is only slightly different from the other one. Therefore, only the results for TM mode Fresnel coefficient are shown in Fig. 3.15 (c). A comprehensive study will be provided in next section (Section 4) which compares different discontinuity modeling methods.

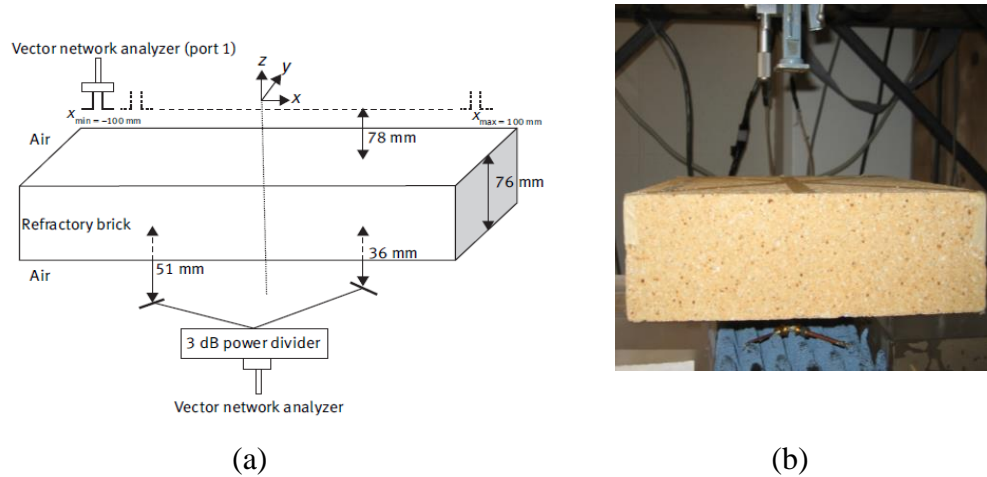


Figure 3.14. Measurement setup for Experiment 1.

Later, the same collected data (measured  $S_{21}$ ) was fed to WL-SAR. Since the scan was linear and only in  $x$ -direction, then wavenumber in  $y$ -direction does not exist (i.e.,  $K_y = 0$ ). Also, the open-ended waveguide is polarized in  $y$ -direction, which means that  $E_y$  component of the radiated field by the dipoles has major contribution on the measured  $S_{21}$ . These two facts result in selection of:  $\Gamma = \Gamma_y$  and

$$G^P = G_y^{p,y'} = F_{xy}^{-1} \left( \frac{F^{TE}(\vec{K}_s, z, z')}{K_{mz}} \right) \text{ in (76).}$$

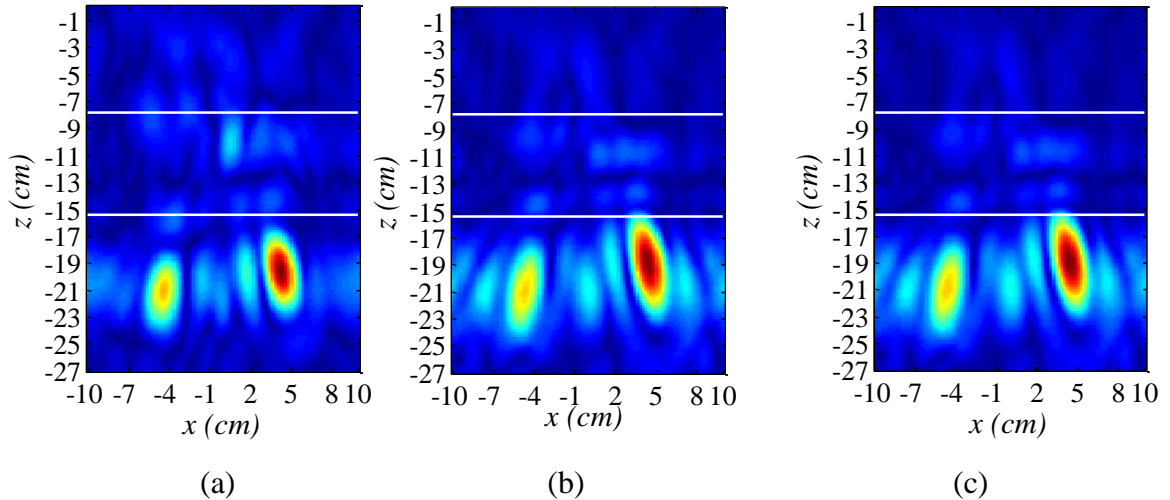


Figure 3.15. Image for Experiment 1. (a) SAR ( $\epsilon_{r,b} = 1.77$ ), (b) PW-SAR, and (c) TM mode MPW-SAR with Fresnel transmission coefficients.

Moreover, the third layer was set as the region of interest, and then the appropriate value of  $\alpha$  for the Wiener filter was estimated to be -35 dB or  $10^{-3.5}$ . The WL-SAR image shows indication of both dipoles (Fig. 3.16) and there is not any significant difference between this image and the image produced using TM mode MPW-SAR with Fresnel transmission coefficients (Fig. 3.15 (c)).

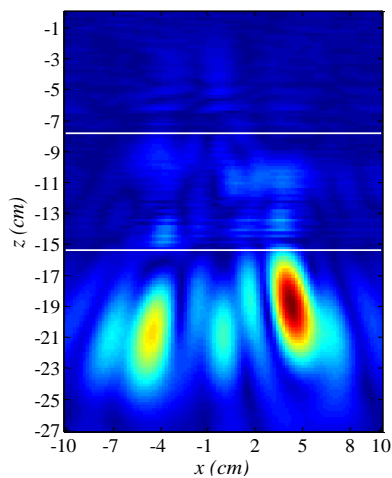


Figure 3.16. Reconstructed image for Experiment1 using WL-SAR( $\alpha = -35$  dB).

### 3.7. CONCLUSION

In this section, it was aimed to image an embedded active source (target) in a layered structure. Initially, the idea of scanning an area over the layered structure using one single antenna to collect data was explained. Then, a new concept namely qualitative image was defined and its relationship with the collected data was established and derived using dyadic Green's function of the layered structure. Later, the most well-known qualitative imaging technique, SAR method, was briefly explained and its limitations to produce image from the collected data for an embedded active target in a layered structure was discussed. To address the first limitation of SAR, which is the homogeneous background assumption, previously developed PW-SAR was modified in a way to not only consider physical/electrical properties of each layer between the scanning antenna and the target but also incorporate the discontinuity between layers. The modified PW-SAR (MPW-SAR) uses TE/TM mode Fresnel/generalized transmission coefficients to incorporate the discontinuity between layers. MPW-SAR is robust, easy to implement, and fast. However, this method does not consider multiple reflections or signal attenuation due to loss (second and third limitations of SAR). To address loss and multiple reflection issues, a comprehensive method namely WL-SAR was developed. Based on the established relationship between the layered structure, collected data, and the image, extra mathematical manipulations were then invoked to cast the imaging problem into a deconvolution procedure where Wiener filter deconvolution was used to solve the problem. Several simulations and one experiment were conducted to prove the efficacy and limitations of the proposed methods for imaging embedded active targets in a layered structure.

## 4. MONOSTATIC SAR-BASED MICROWAVE IMAGING OF EMBEDDED PASSIVE OBJECTS

### 4.1. INTRODUCTION

Microwave imaging techniques have been used by those involved in NDT&E, applied physics and radar and remote sensing for the purpose of detecting and evaluating embedded (passive) objects in a structure [3]-[7],[62]-[63]. New applications such as imaging the interior structure of a wall (i.e., intra-wall imaging [64]), breast cancer detection, through-wall imaging, and structural health monitoring have all accelerated the demands for robust microwave imaging techniques applicable to inhomogeneous media [18]-[22]. Most of these applications involve planar structures that are considered homogeneous in the spatial extent direction while inhomogeneous (i.e., layered) in the transverse (depth or range) direction. Although these cases have been studied in past two decades, only a few quantitative imaging techniques have been developed properly addressing all of their unique attributes [6]-[19]. As it was mentioned in Sections 1 and 3, these techniques require high computational resources. In [9], a qualitative imaging technique is proposed that uses a SAR migration algorithm to image embedded objects in a planar layered structure. However, the efficacy of the algorithm is only demonstrated for a 2D two-layer medium consisting of air and ground. Moreover, for applications such as through-wall imaging, a few modified version of SAR algorithm is introduced which incorporate transmission coefficients for the air-to-wall discontinuity in the SAR image formation in spatial domain [17], [20], [22]. Moreover, since these algorithms are developed in spatial domain their implementation is rather cumbersome requiring significant processing time.

Therefore, there is a lack of robust and fast qualitative imaging techniques for embedded passive objects and active targets inside layered structures. In Section 3, this problem was addressed for an active target by introducing two novel methods (i.e., MPW-SAR and WL-SAR). With some appropriate modifications the underlying idea behind the concepts of the methods in Section 3 can be used to develop imaging methods for embedded passive objects in a layered structure. In fact, a passive object has to be illuminated and then the reflected/scattered EM wave can be collected and used to reconstruct the image of the object. As it was mentioned in Section 3, a stationary EM

source can be used to illuminate the object while a moving antenna (scanning antenna) can collect a portion of the reflected/scattered EM signal by the object (i.e., the bistatic case). As an alternative and to reduce the complexity, the scanning antenna may send the EM signal and then also collects the reflected/scattered EM signal (i.e., operating as transceiver). This type of data collection is known as “monostatic” case. Since the bistatic case somehow was studied in Section 3, the monostatic case will be investigated in this section.

In the following, SAR, MPW-SAR, and WL-SAR will be modified for monostatic imaging of embedded passive objects in an inhomogeneous (layered) structure. Then, simulations and measurements will be used to demonstrate the efficacy and limitations of these methods.

#### 4.2. MONOSTATIC SAR AND MPW-SAR

The governing equations for monostatic SAR and MPW-SAR are similar to the previously-derived SAR and MPW-SAR algorithms for active targets, respectively (i.e., equations (68), (69), (70), (71), (72), and (73)). However, since in monostatic case the wave undergoes a round-trip travel path from the transceiver to the target, the dispersion relation in (5) must be modified as:

$$4K_b^2 = K_z^2 + K_x^2 + K_y^2. \quad (83)$$

#### 4.3. MONOSTATIC WL-SAR

The expressions introduced in Section 3.5 for WL-SAR for imaging an embedded active target can now be used for imaging a passive object by only modifying the total signal path in the Green’s function. In fact, to consider round-trip path,  $G^P(x, y, z; x', y', z', f)$  in (74), (75), (76), and (77) should be replaced with the round-trip Green’s function  $G^{RT}$ :

$$G^{RT}(x, y, z; x', y', z', f) = G^P(x, y, z; x', y', z', f) \cdot G^P(x', y', z'; x, y, z, f). \quad (84)$$

Then, (77) should be modified as:

$$S(x, y, z, f) = \Gamma(x, y, z', f) * G^{RT}(x, y, z, z', f) + v(x, y, z, f). \quad (85)$$

Therefore, the final imaging expression in (78) can be modified as:

$$\Gamma(x', y', z', f) = FT_{xy}^{-1} \left\{ \frac{\bar{S} \cdot (\bar{G}^{RT})^H}{\bar{G}^{RT} \cdot (\bar{G}^{RT})^H + \delta^2} \right\}, \quad (86)$$

then, the proposed rule-of-thumb method for calculating  $\delta^2$  can be used by replacing  $\bar{G}^P$  with  $\bar{G}^{RT}$  in (80).

#### 4.4. SIMULATION AND MEASUREMENT SETUP

In here, the efficacy of the monostatic MPW-SAR and WL-SAR methods to image embedded passive objects in a layered structure will be tested through simulations and measurements. As it was mentioned in Section 3.6, for each example, physical and electrical properties of layers, scanning area, and frequency range must be known. For scanning, an open-ended rectangular waveguide antenna is considered. All of the simulations and measurements are performed at X-band with frequency step size of 100 MHz unless otherwise specifically mentioned. Since this is a monostatic measurement, reflection coefficient (i.e.,  $S_{11}$ ) is recorded at the antenna aperture using a calibrated HP8510C VNA. Also, since the equations were derived for an isotropic scanning antenna, and as it was mentioned in Section 3.6, using an OEW may introduce some issues to be considered. First, the antenna pattern and directivity are not incorporated in the equations. Since the OEW has a fairly wide beamwidth, this issue was not considered to be critical [24]. Second, the antenna-to-air boundary creates a reflection that is ever-present in the recorded reflection coefficient and may mask weaker/smaller reflections

from the structure under the test. For the monostatic case this may become a significant issue since the reflection coefficient of the OEW radiating into air is relatively high (i.e., in range of -12 dB [65]) while the reflection from the embedded object(s) can be relatively much lower (e.g., -60 dB). However, since the reflection coefficient of the OEW is the same for each point over the scanning area, one can calculate the average of the collected data for monostatic case (i.e.,  $S_{11}$ ) over the scanning area per frequency and then coherently subtract this average from the collected data as:

$$S(x, y, f) = S_{11}(x, y, f) - \sum_y \sum_x S_{11}(x, y, f) / (N_y N_x), \quad (87)$$

where  $N_x$  and  $N_y$  are the number of samples in the  $x$ - and  $y$ -directions, respectively. In a linear scan case, averaging is only required in the scanning direction (i.e.,  $x$  or  $y$ ). Also, the origin of coordinate system is always assumed to be on the boundary between the first and the second layer.

Since the antenna has a certain polarization and supports propagating mode(s) in the vicinity of the antenna, the dominant wave propagation in the layered structure can be TE mode, TM mode, or a combination of both modes. Moreover, the transmission coefficient between layers  $i$  and  $i+1$  can be calculated using Fresnel equations which assumes that layer  $i$  and  $i+1$  extend to infinity [36]-[37]. To increase the accuracy, the transmission coefficient between layers  $i$  and  $i+1$  can be calculated by considering all the other layers to exist as well (generalized transmission coefficient) [36]-[37]. The computational complexity for calculation of the generalized transmission coefficient is higher than Fresnel coefficient. Then, for the MPW-SAR, five different cases were studied as: TM mode with Fresnel transmission coefficients (TMFMPW-SAR), TE mode with Fresnel transmission coefficients (TEFMPW-SAR), TM mode with generalized transmission coefficients (TMGMPW-SAR), TE mode with generalized transmission coefficients (TEGMPW-SAR), and coherent summation of produced images using TEFMPW-SAR and TMFMPW-SAR (TEMFMPW-SAR).

For simulation purposes and to mimic practical situations, the full-wave simulation tool CST Microwave Studio<sup>®</sup> is used in conjunction with MATLAB<sup>®</sup> to simulate the collected (or measured) data. MATLAB is used to update the scanning

antenna position for the CST program which in turn simulates the structure and determines the reflection coefficient ( $S_{11}$ ). Later, MATLAB is used to store this information and subsequently update and repeat the process for each antenna position. For more details concerning the MATLAB-CST linkage, the reader is referred to [66]. The simulation and image formation were performed on a 64-bit PC with 8 GB of RAM and Core2Quad CPU of 2.66 GHz.

Measured data is collected using an automated 2D scanning table in conjunction with an HP8510C VNA to scan an OEW over the sample and collect the complex reflection coefficient ( $S_{11}$ ) calibrated to the aperture of the waveguide. After scanning, the spatial mean value of  $S_{11}$  is coherently subtracted, as per (87).

#### 4.5. SIMULATION RESULTS

The efficacy of monostatic SAR, MPW-SAR, and WL-SAR for applications such as structural health monitoring, intra-wall imaging, and through-wall imaging has been investigated through several simulations which are discussed here.

##### 4.5.1. Detecting Corrosion in Reinforcing Steel Bars in Concrete Structures.

Corrosion in steel reinforced concrete structures is the main cause of deterioration in concrete structures. In the U.S. alone, the cost associated with structural repair and maintenance due to such corrosion problems is about \$276 billion per year [67]. Therefore, early detection of corrosion is of paramount importance.

In this example (Simulation 1), two long rebars are buried inside mortar (concrete without coarse aggregates), as shown in Fig. 4.1. The radius of the rebar ( $r_o$ ) before corrosion is 0.79 cm. For comparison, corrosion and rust are added to the left rebar while the right rebar is left untouched. The radius of rebar after corrosion ( $r_{met}$ ) and outer radius of rust ( $r_{oxi}$ ) are shown for a corrosion ratio of  $N_c$ . To model corrosion and rust, provided equations in [67] are used as:

$$r_{met} = r_o \sqrt{1 - N_c}, \quad (88)$$

and,



$$r_{oxi} = r_o \sqrt{1 + 3N_c}. \quad (89)$$

For this example, the corrosion type is assumed to be black rust ( $\epsilon_r = 12.5 - j2.3$  [68]) and  $N_c = 0.2$ . The radius  $r_{met} = 0.70$  cm and  $r_{oxi} = 1.0$  cm are calculated from (88) and (89), respectively. The antenna distance from mortar surface is 13.7 cm and mortar with  $\epsilon_r = 4 - j0.2$  [69] is assumed to be 12.5 cm thick, as shown in Fig. 4.1. Moreover, the polarization of the antenna is orthogonal to the length of rebars. Scanning is performed linearly along  $x$  from -6.5 cm to 6.5 cm with a step size of 0.1 cm. To include the effect of using OEW instead of isotropic antenna, the collected complex reflection coefficients are applied into (87) to produce the collected data ( $S$ ). The collected data is then processed using the monostatic SAR, PW-SAR, and MPW-SAR imaging techniques. For SAR, the effective background medium was calculated using (82) to be ( $\epsilon_{r,b} = 2.43$ ). As can be seen in Fig. 4.1 (d) the SAR image of rebars is defocused and it has an incorrectly placed and strong indication of presumably an object in a location between the two rebars. The coherent addition of incorrectly phase-compensated data is the main reason for the defocused and incorrectly located rebars.

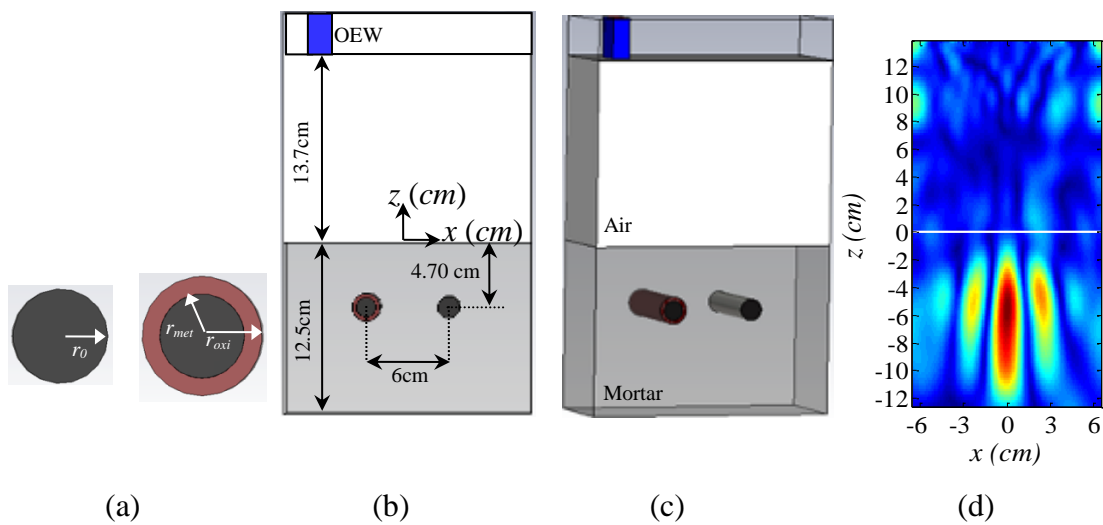


Figure 4.1. Simulation 1. (a) rebar before and after corrosion, (b) cross-section view and (c) perspective view, and (d) reconstructed image using SAR ( $\epsilon_{r,b} = 2.43$ ).

On the other hand, PW-SAR and MPW-SAR produce artifacts corresponding to the air-to-mortar boundary and one of the rebars is not visible. This happens since the corroded rebar is a relatively weak EM scatterer and is placed relatively deep inside the lossy mortar and PW-SAR and MPW-SAR do not compensate for signal attenuation. Since the antenna is an open-ended waveguide radiating to a layered structure, incident wave and the reflected back wave can excite TE, TM, or a combination of TE and TM modes [65] (this was not a case with isotropic antenna). In contrast with SAR and PW-SAR which do not incorporate the boundaries, and do not depend on propagation mode, MPW-SAR is a function of propagation mode. In fact, the mode of propagation is required for Fresnel or generalized transmission coefficients calculations. As mentioned earlier in this section, some of the more common situations were considered, studied, and the results are compared with PW-SAR, as shown in Fig. 4.2. As one can see, inclusion of the discontinuity by only using transmission coefficients does not aid in improving the results significantly. Processing time for SAR, PW-SAR, and MPW-SAR is about 2 seconds, each.

The same collected data is used in conjunction with WL-SAR. Since the scan was linear and only in the  $x$ -direction, then wavenumber in the  $y$ -direction becomes zero (i.e.,  $K_y = 0$ ). Also, the open-ended waveguide is polarized in the  $x$ -direction, which means that  $E_x$  component of the radiated field by the objects contributes most prominently to the measured  $S_{11}$ . These two facts result in selection of:  $\Gamma = \Gamma_{x'}$  and

$$G^{RT} = (G^p)^2 = \left( \frac{1}{K_{mm}^2} \partial_z \partial_{z'} F_{xy}^{-1} \left( \frac{F^{TM}(\vec{K}_s, z, z')}{K_{mz}} \right) \right)^2 \text{ in (85).}$$

Moreover, it is assumed that there is *a priori* knowledge concerning the region of interest and mortar is set as the region of interest. Then, for two selected focusing planes in the second layer (i.e., mortar) at  $z' = -2.5 \text{ cm}$  and  $z' = -8.5 \text{ cm}$ ,  $|\bar{G}^{RT}|_{\text{Region}}^2 / |\bar{G}^{RT}|_{\text{max}}^2$  was calculated at 10 GHz and plotted in Fig. 4.3 (in dB scale).

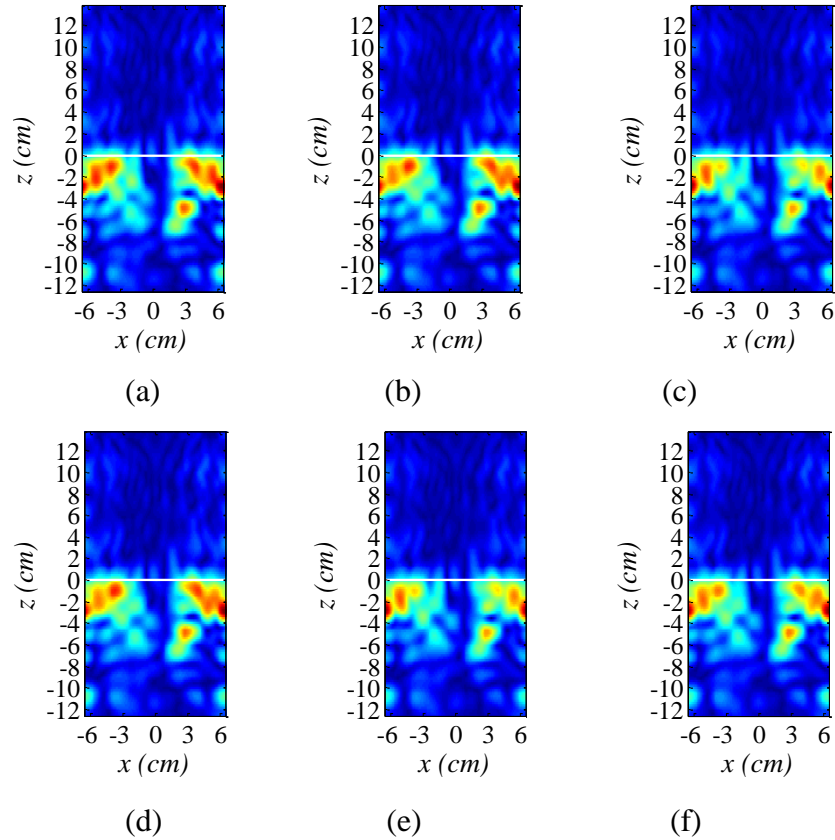


Figure 4.2. Image for Simulation 1. (a) PW-SAR, (b) TMFMPW-SAR, (c) TEFMPW-SAR, (d) TMGMPW-SAR, (e) TEGMPW-SAR, and (f) TEMFMPW-SAR.

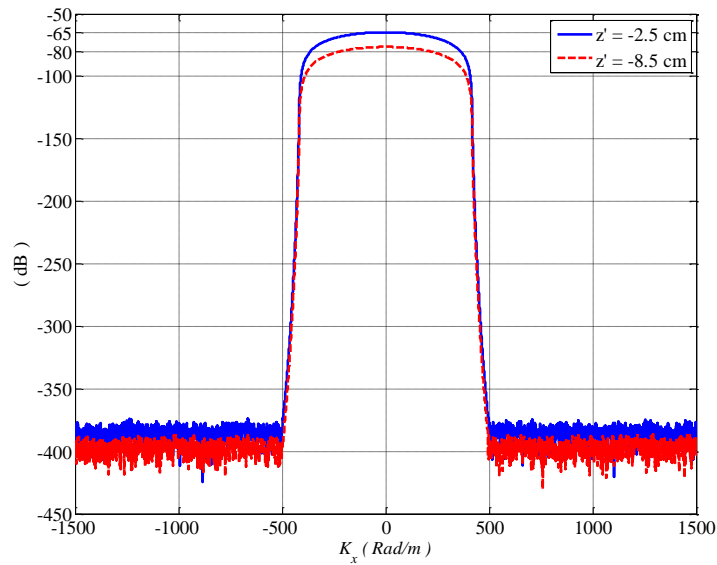


Figure 4.3. Calculated  $|\bar{G}^{RT}|_{Region}^2 / |\bar{G}^{RT}|_{max}^2$  for two different values  $z' = -2.5\text{ cm}$ , and  $z' = -8.5\text{ cm}$  at 10 GHz.

The maximum value of the plots over  $K_x$  is used to select  $\alpha$ . Therefore, a value in range of approximately -60 dB (or  $10^{-6}$ ) to -80 dB (or  $10^{-8}$ ) for  $\alpha$  may be a good choice. The produced images using WL-SAR algorithm with  $\alpha$  of -50 dB, -70 dB, -90 dB, and -100 dB are shown in Fig. 4.4. For  $\alpha = -50$  dB, both rebars can be seen and distinguished, as shown in Fig. 4.4 (a). However, there are artifacts in the vicinity of the boundary between air and mortar. By decreasing  $\alpha$ , WL-SAR algorithm emphasizes the deeper ranges as opposed to the shallower ranges (referring to provided explanations for  $\alpha$  selection in Section 3.5). Therefore, by decreasing  $\alpha$ , the indication of artifacts becomes weaker while the indication of rebars becomes stronger. A choice of  $\alpha = -70$  dB results in relatively clean and focused indications of both rebars in the image (Fig. 4.4 (b)). This image correctly shows a weaker indication of the left rebar in comparison with the strong indication of the right rebar. This happens because rust on the left rebar is lossy and scatters less compared to metal. The ability of WL-SAR to distinguish between these two rebars is very important from a corrosion detection point of view. Moreover, by decreasing  $\alpha$ , defocused indications of rebars (which are farther away from the antenna) are more emphasized in comparison with the focused indication of rebars. Therefore, these indications become brighter in the image, as shown in Fig. 4.4 (c)-(d). Processing time for WL-SAR is about 130 seconds.

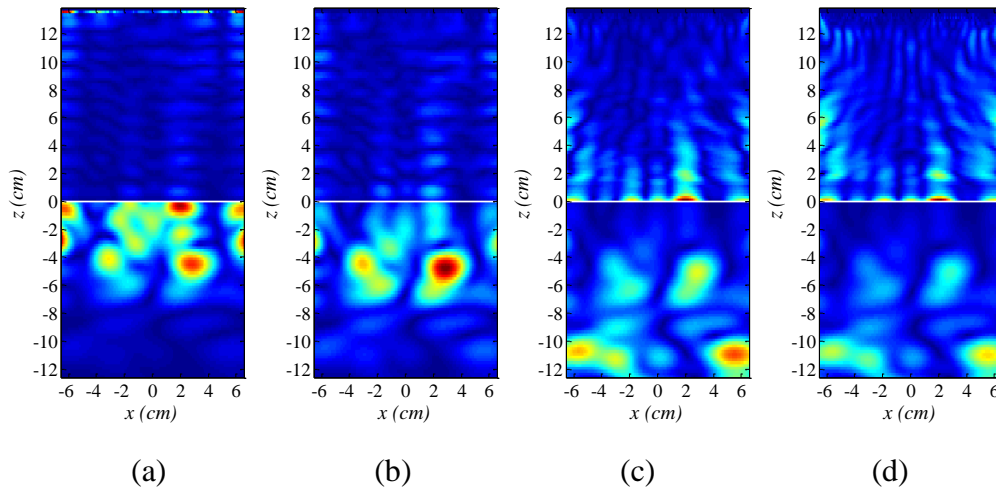


Figure 4.4. Images for Simulation 1 using WL-SAR. (a)  $\alpha = -50$  dB, (b)  $\alpha = -70$  dB, (c)  $\alpha = -90$  dB, and (d)  $\alpha = -100$  dB.

It is worthy to note that using  $\partial_z(\partial_{z'})$  operator introduces  $+jK_z(-jK_z)$  as a coefficient into the  $G^{RT}$  equations. Since  $K_z$  can be a very small value (or even zero), then it can force  $G^{RT}$  to a very small or zero value. Considering imaging equation (86), this can intensify the singularity problem. As an approximation, operator  $\partial_z(\partial_{z'})$  was eliminated and  $G^{RT} = (G^P)^2 = \left( F_{xy}^{-1} \left( \frac{F^{TM}(\vec{K}_s, z, z')}{K_{mz}} \right) \right)^2$  was used for WL-SAR image formation. Based on rule of thumb,  $\alpha = -50\text{dB}$  was estimated and the corresponding produced image is shown in Fig. 4.5. The comparison between the achieved images before dropping  $\partial_z(\partial_{z'})$  and after dropping  $\partial_z(\partial_{z'})$  shows that eliminating  $\partial_z(\partial_{z'})$  did not change the image significantly. However, dropping  $\partial_z(\partial_{z'})$  helped to reduce the complexity of the implementation procedure. In SAR algorithm development for free-space in [6], similar assumption was used where  $+jK_z$  was removed from the final SAR equation.

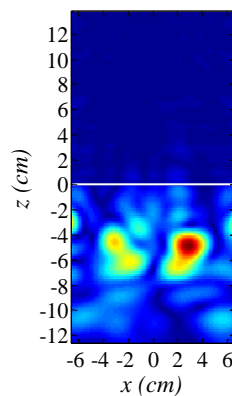


Figure 4.5. Image for Simulation 1 using modified WL-SAR with  $\alpha = -50\text{dB}$ .

In comparison with the image produced using MPW-SAR (Fig. 4.2 (b)-(f)), the indications of rebars in the WL-SAR image with  $\alpha = -70\text{dB}$  (Fig. 4.4 (b)) are focused and properly positioned. Moreover, as it was explained for  $\alpha$  selection, WL-SAR

emphasizes the region of interest while de-emphasizing the air-to-mortar boundary (in this case) in contrast to MPW-SAR.

**4.5.2. Intra-Wall Imaging.** Imaging the interior structure of a wall (i.e., intra-wall imaging) can be used for practical applications such as finding routed wires and investigating embedded rebars or plumbing pipes [64], [70]. Therefore, the second simulation (Simulation 2) is devoted to this topic. To mimic a practical situation, a typical wall is modeled using layers of drywall, insulation, and mortar. Considering the fact that the antenna is in the air, this constitutes a four-layer structure (Fig. 4.6). Thickness of drywall and insulation are chosen to be 1.2 cm and 5 cm, respectively. Air and mortar layers are assumed to extend to positive and negative infinity in  $z$ -direction, respectively. Based on literature search and previous experiences, dielectric constants of layers are selected as: air ( $\epsilon_r = 1$ ), drywall ( $\epsilon_r = 2.19 - j0.02$ ), insulation ( $\epsilon_r = 1.1 - j0.001$ ), and mortar ( $\epsilon_r = 4 - j0.2$ ) [67]-[69]. There are two embedded objects considered in this structure placed at different depths. The first object (Object 1) is a metallic cylinder located at  $(-7, 0, -4)$  cm with radius of 0.3 cm that extends to positive and negative infinity in  $y$ -direction. This object mimics a wire routed inside the insulation layer. The second object (Object 2) is a metallic cylinder located at  $(3, 0, -9.7)$  cm with a radius of 1 cm that extends to infinity in  $y$ -direction. This object mimics rebar or plumbing pipe embedded inside mortar. The X-band open-ended waveguide antenna is in the top layer at a distance of 2 cm above the drywall (Fig. 4.6 (a)).

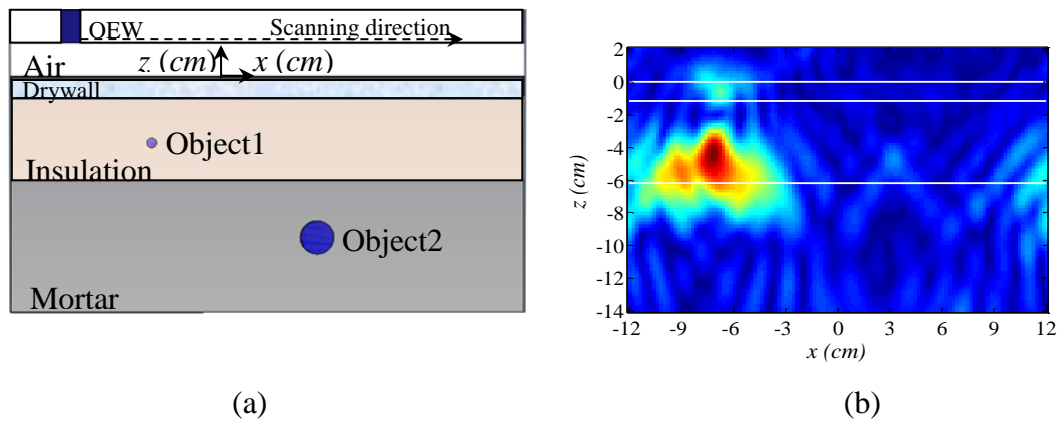


Figure 4.6. Simulation 2. (a) configuration, (b) reconstructed image by SAR ( $\epsilon_{r,b} = 2.58$ ).

The EM wave polarization is orthogonal to the length of both objects. Moreover, scanning is performed linearly along  $x$ -direction from -12 cm to 12 cm with a step size of 0.2 cm. To include the effect of using OEW instead of isotropic antenna, the collected complex reflection coefficients are applied into (87) to produce the collected data ( $S$ ). The collected data is then processed using the monostatic SAR, PW-SAR, and MPW-SAR imaging techniques. For SAR, the effective homogeneous background medium is calculated using (82) to be  $\varepsilon_{r,b} = 2.58$ . The produced image using SAR algorithm is shown in Fig. 4.6 (b). The image shows a defocused indication of Object 1 while Object 2 is completely undetected. As anticipated, this inaccurate model of the layered structure is the root of the problems for SAR. In addition, ignoring the discontinuity at the insulation-to-mortar boundary contributes to the problem. To account for the correct phase shift and model discontinuities, MPW-SAR is used while different modes (TE/TM) and discontinuity modeling (Fresnel/generalized) situations as it was explained for Simulation 1 were investigated, and the results are compared with PW-SAR in Fig. 4.7.

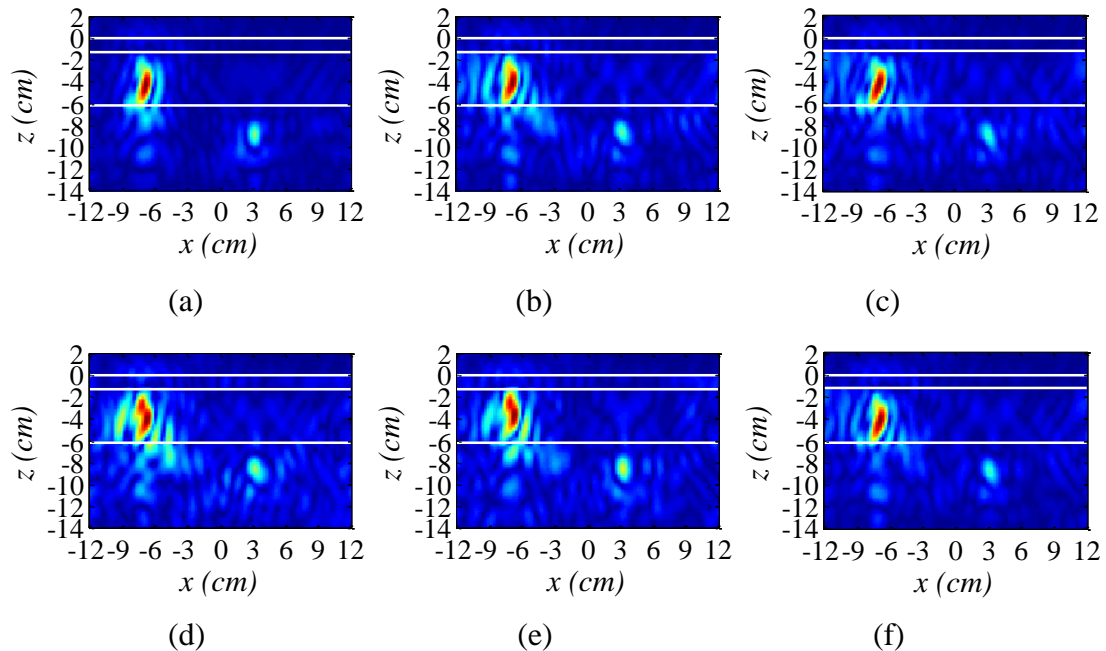


Figure 4.7. Produced images for Simulation 2. (a) PW-SAR, (b) TMFMPW-SAR, (c) TEFMPW-SAR, (d) TMGMPW-SAR, (e) TEGMPW-SAR, (f) TEMFMPW-SAR.

As Fig. 4.7 (a) shows, in PW-SAR produced image, indication of objects are focused and properly positioned, however, the indication of Object 2 is not strong. Adding Fresnel TM mode or TE mode transmission coefficients to the PW-SAR did not improve the results (Fig. 4.7 (b)-(c)). While the produced image using TMGMPW-SAR is not showing any improvement (Fig. 4.7 (d)), the produced image using TEGMPW-SAR shows a slight improvement over PW-SAR image where the indication of Object 2 is relatively stronger (Fig. 4.7 (e)). However, there are small artifacts in the image in comparison with PW-SAR produced image. Also, the produced image by coherent summation of calculated images using Fresnel TE and TM modes transmission coefficients (Fig. 4.7 (f)) is not showing any improvement in comparison with PW-SAR produced image. In fact, modeling the discontinuity between different layers with the transmission coefficients (either Fresnel or generalized) is a simple approximation which may not be accurate for complex layered structures. Maybe PW-SAR and TEGMPW-SAR can be seen as the most appropriate imaging methods for this example.

Later, the same collected data is fed to WL-SAR. Since the scan was linear and only in  $x$ -direction, and a 2D imaging scenario was considered, then wavenumber in  $y$ -direction does not exist (i.e.,  $K_y = 0$ ). Also, the open-ended waveguide is polarized in  $x$ -direction, which means that  $E_x$  component of the radiated field by the objects have major contribution on the measured  $S_{11}$ . These two facts result in selection of:  $\Gamma = \Gamma_x$ , and

$$G^{RT} = (G^p)^2 = \left( \frac{1}{K_{mn}^2} \partial_z \partial_{z'} F_{xy}^{-1} \left( \frac{F^{TM}(\vec{K}_s, z, z')}{K_{mz}} \right) \right)^2 \text{ in (85).} \quad \text{As it was explained for}$$

Simulation 1, for the simplicity of the implementation, operator  $\partial_z (\partial_{z'})$  will not be considered. Moreover, it is assumed that there is *a priori* knowledge concerning the region of interest. In fact, it is assumed that the objects are only located in third and fourth layers. Then, for a selected focusing plane in the third layer ( $z' = -3\text{ cm}$ ) and fourth layer ( $z' = -12\text{ cm}$ ),  $\left| \bar{G}^{RT} \right|_{\text{Region}}^2 / \left| \bar{G}^{RT} \right|_{\text{max}}^2$  was calculated at 10 GHz and plotted in Fig. 4.8 (in dB scale).



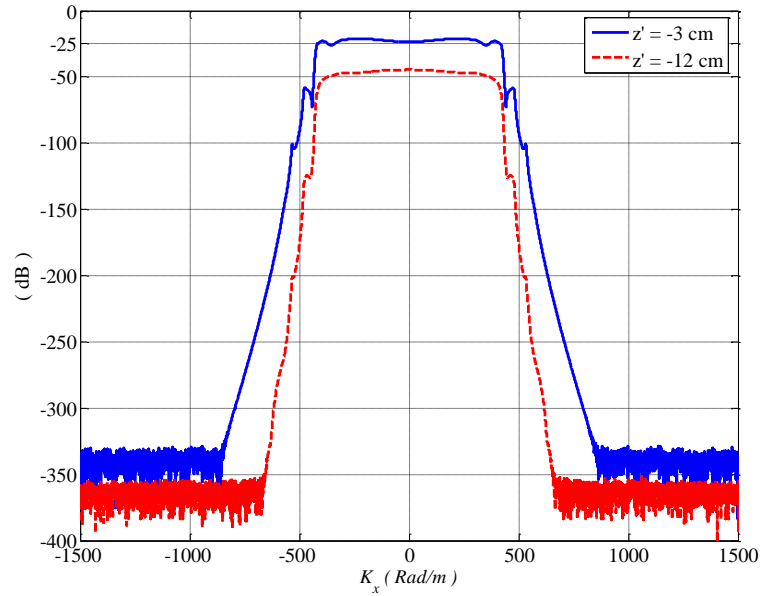


Figure 4.8. Calculated  $\left| \bar{G}^{RT} \right|_{\text{Region}}^2 / \left| \bar{G}^{RT} \right|_{\text{max}}^2$  for two different values  $z' = -2 \text{ cm}$ , and  $z' = -12 \text{ cm}$  at 10 GHz.

The maximum values of the plots over  $K_x$  are used to select  $\alpha$ . Therefore, a value in range of approximately -25 dB (or  $10^{-2.5}$ ) to -50 dB (or  $10^{-5}$ ) for  $\alpha$  may be a good choice. The produced image using WL-SAR algorithm with  $\alpha$  of -30 dB is shown in Fig. 4.9. In this image, indication of both objects can be seen and distinguished. In comparison with produced images using PW-SAR and TEGMPW-SAR, the indication of Object 2 in the produced image using WL-SAR is slightly brighter.

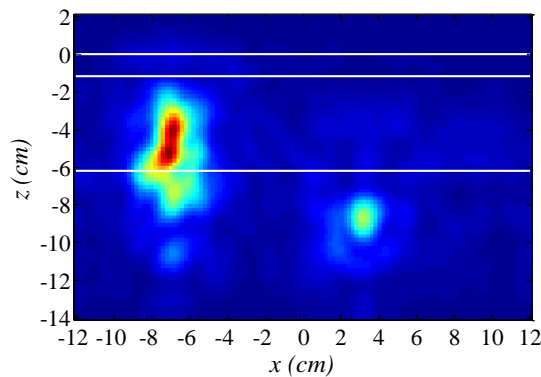


Figure 4.9. Produced image for Simulation 2 using WL-SAR with  $\alpha = -30 \text{ dB}$ .

**4.5.3. Through-Wall Imaging.** There is a high demand for imaging interior of a building to identify and detect the interior objects. This is known as through-wall imaging. The EM waves have this ability to penetrate through nonmetallic building materials such as drywall, cinder blocks, mortar and concrete blocks, brick, fiberglass, and glass [17]. So, EM signals have this potential to be used for through-wall imaging applications. Therefore, Simulation 3 is devoted to through-wall imaging topic. In this simulation, two walls separated by of 4.5 cm are considered. A mortar block (similar to Simulations 1 and 2) is used to represent the wall (simplified wall). Moreover, thickness of the walls is 2 cm and 1 cm, respectively (Fig. 4.10). The selected values of thicknesses are not practical, however, by scaling the frequency down to lower frequency band, one can increase the thickness of the walls and the results should be comparable. Considering the fact that the antenna is in the air, this constitutes a five-layer structure (Fig. 4.10 (a)).

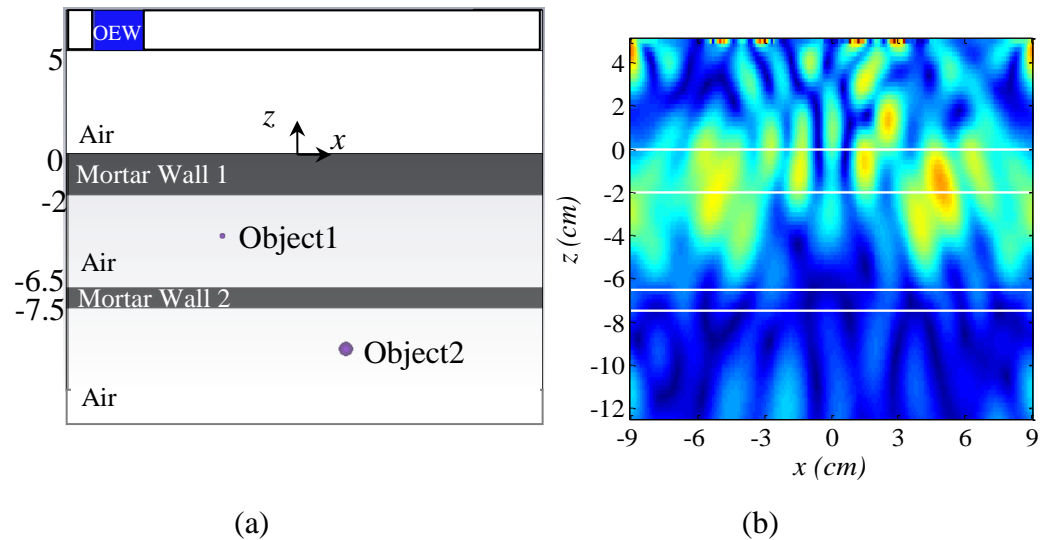


Figure 4.10. Simulation 3. (a) configuration, (b) reconstructed image using SAR ( $\epsilon_{r,b} = 1.52$ ).

The scanning X-band antenna is located 5 cm from the first layer of mortar. Two metallic spheres are added to the scene: one with radius 0.15 cm located at (-4, 0, -4) cm and the other with radius of 0.35 cm located at (2, 0, -9.5) cm, as shown in Fig. 4.10 (a).

Scanning is performed linearly along the  $x$ -direction from -9 cm to 9 cm with step size of 0.1 cm. For SAR, an effective relative dielectric constant of  $\varepsilon_{r,b} = 1.52$  was calculated using (82). The produced image using SAR is shown in Fig. 4.10 (b). As it was expected, the SAR image of objects is defocused. Incorrect phase compensation and not including the discontinuity between layers in the calculations can be the root of the problem. On the other hand, PW-SAR and MPW-SAR with all of the explained cases in Simulation 3 are investigated (Fig. 4.11). As Fig. 4.11 (a) shows, in PW-SAR produced image, indications of objects are focused and properly positioned, however, the strong reflection of the boundary of the closets wall (i.e., Wall 1) to the antenna masks both objects. Adding Fresnel TM mode or TE mode transmission coefficients to the PW-SAR improves the results slightly (Fig. 4.11 (b)-(c)) while adding generalized TM mode or TE mode transmission coefficients increases the amount of artifacts in the images (Fig. 4.11 (d)-(e)). The coherent summation of calculated images using Fresnel TE and TM modes transmission coefficients does not improve the images in comparison with produced images using TEFMPW-SAR or TMFMPW-SAR. This may be explained by considering the fact that the objects have spherical shapes which their reflections are not polarization-dependent. Moreover, the size of the sphere is smaller than the wavelength. In all the images, a strong indication of reflection at the boundary between air and Wall 1 exists. This happens because modeling the discontinuity between layers only by considering Fresnel or generalized reflection coefficient is not complete and accurate.

The same collected data is fed to WL-SAR and since the scan was linear and only in  $x$ -direction, then wavenumber in  $y$ -direction is set as zero (i.e.,  $K_y = 0$ ). Also, similar to Simulations 1 and 2, the open-ended waveguide is polarized in  $x$ -direction, which means that  $E_x$  component of the radiated field by the objects have major contribution on the measured  $S_{11}$ . These two facts result in selection of:  $\Gamma = \Gamma_x$ , and

$$G^{RT} = (G^p)^2 = \left( \frac{1}{K_{mm}^2} \partial_z \partial_z F_{xy}^{-1} \left( \frac{F^{TM}(\vec{K}_s, z, z')}{K_{mz}} \right) \right)^2 \text{ in (85).}$$

With the same reason explained for Simulations 1 and 2, the operator  $\partial_z(\partial_z \cdot)$  is removed. The WL-SAR method produced an image with focused and correctly placed indication of the spheres (Fig. 4.12).

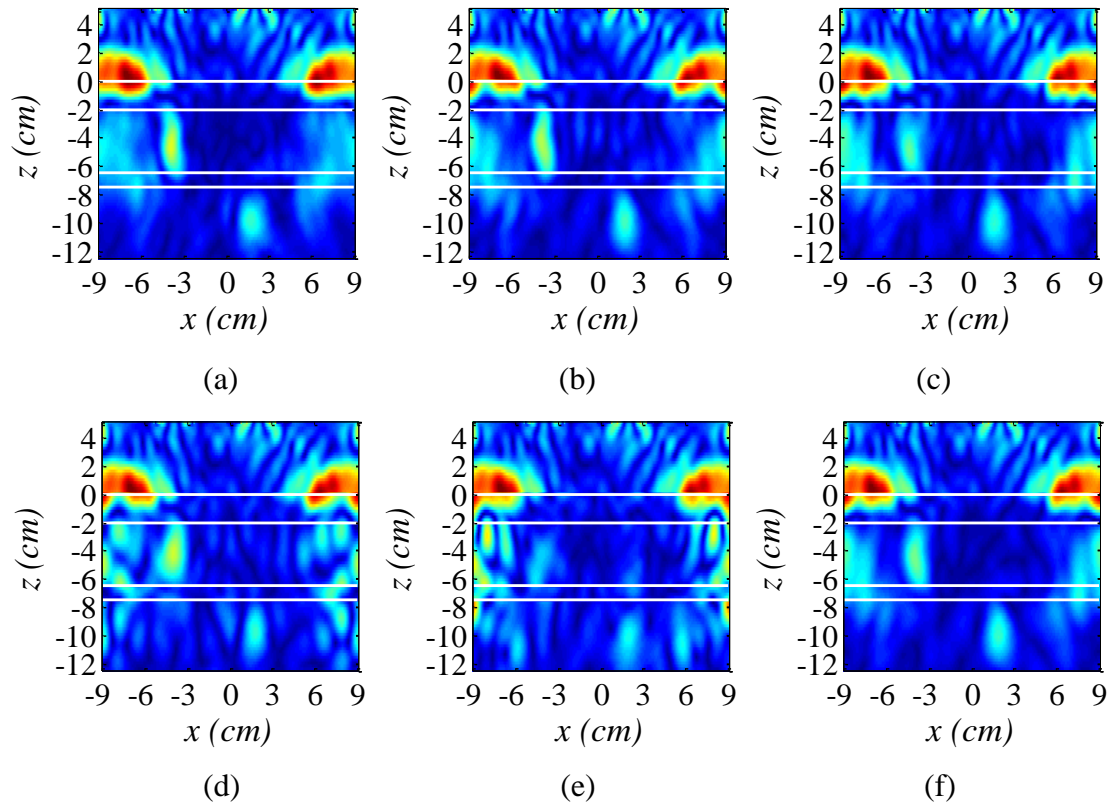


Figure 4.11. Produced images for Simulation 3. (a) PW-SAR, (b) TMFMPW-SAR, (c) TEFMPW-SAR, (d) TMGMPW-SAR, (e) TEGMPW-SAR, (f) TEMFMPW-SAR.

Moreover, the simple model which was used in MPW-SAR to incorporate the boundary is not complete. It should be noted that by setting the region of interest to only include layers 3, 4, and 5, a similar procedure that was explained in Simulations 1 and 2 was used to estimate  $\alpha$  for the Wiener filter as  $-35$  dB or  $10^{-3.5}$ .

#### 4.6. EXPERIMENTAL RESULTS

Two mortar samples were previously constructed in the Applied Microwave Nondestructive Testing Laboratory (*amntl*) at the Missouri University of Science and Technology (Missouri S&T) to investigate corrosion in steel reinforced concrete structures [71]. These samples will be used in the following experiments to illustrate the performance of the imaging algorithms.

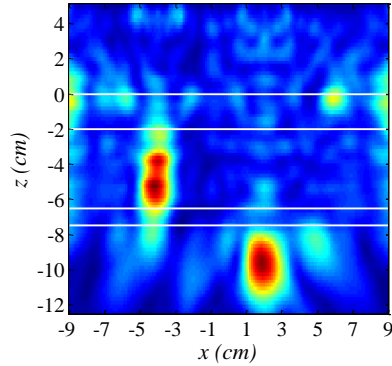


Figure 4.12. Produced image for Simulation 3 using WL-SAR with  $\alpha = -35$  dB.

In Experiment 1, a mortar specimen with four rebars, hereafter referred to as R4, is investigated, as shown in Fig. 4.13. The dimensions of the sample are 30 cm by 30 cm by 12.5 cm containing four different embedded rebars. Two 1.6 cm-diameter rebars have ground out regions with diameters 0.8 cm and 1.5 cm to represent different degrees of recession due to corrosion (i.e., thinning), as shown in Fig. 4.13 (a). Two other rebars with diameter of 0.95 cm are also embedded adjacent to each other to show the ability to distinguish thinner rebars with less separation. The spacing between the two thick rebars and the two thin rebars is approximately 6 cm and 1 cm, respectively. All four rebars are located at a depth of about 2 cm from the top surface of the sample [71]. The measurement setup is shown by the schematic in Fig. 4.13 (c). A linear scan is performed over the ground out regions denoted by the red arrow in Figs. 4.13 (a)-(c). The linear scanning dimension is from  $x = -11.5$  cm to 11.5 cm with a step size of 0.1 cm.

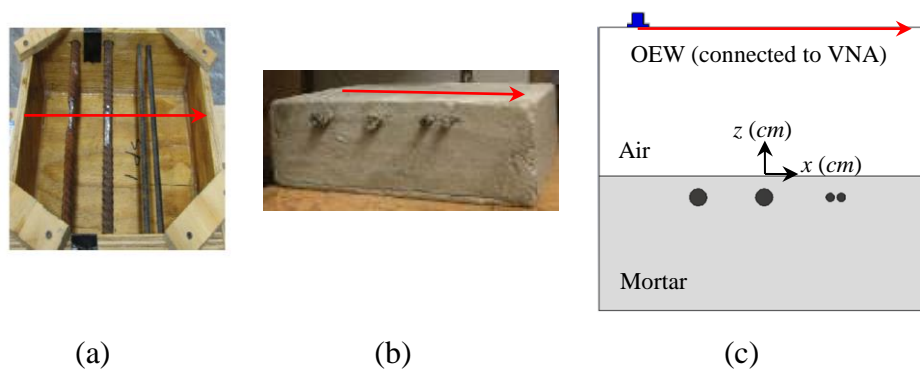


Figure 4.13. Sample R4. (a) rebars, (b) mortar block, and (c) measurement setup (red arrow indicates scanning direction).

The resulting images are shown in Fig. 4.14. As Fig. 4.14 (a) shows, SAR with  $\varepsilon_{r,b} = 2.39$  is not able to correctly image the rebars. In fact, the final image has many unfocused and shifted false indications of possible objects, as explained for the previous cases. Moreover, the reflection from the air-to-mortar boundary is not incorporated or compensated in SAR, which further contributes to incorrect indications of the rebars. On the other hand, the image produced by PW-SAR and TEFMPW-SAR are significantly better, as shown in Fig. 4.14 (b)-(c). However, some faint artifacts corresponding to the air-to-mortar boundary still exist. This may stem from the simple modeling of the air-to-mortar boundary using Fresnel transmission coefficients.

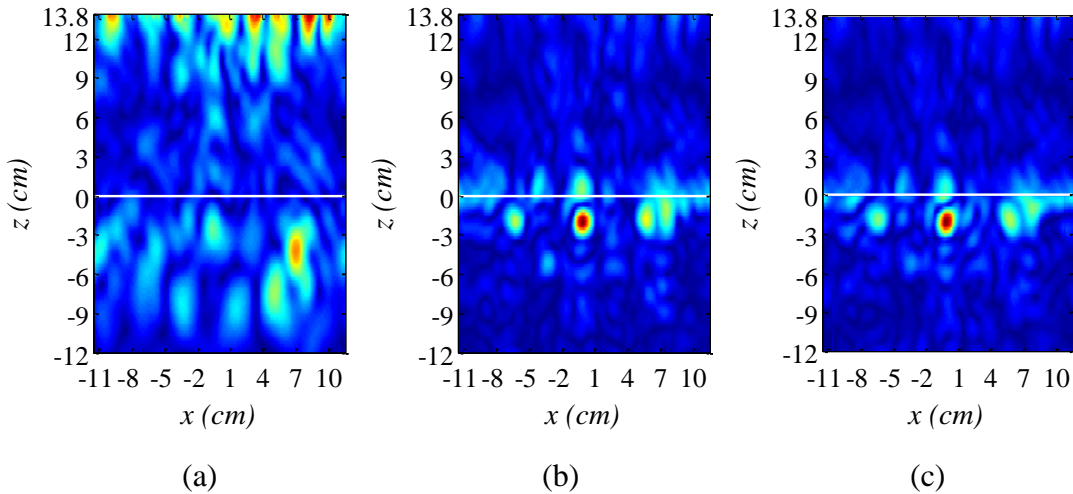


Figure 4.14. Image for Experiment 1. (a) SAR ( $\varepsilon_{r,b} = 2.39$ ), (b) PW-SAR, and (c) TEFMPW-SAR.

The same collected data is fed to WL-SAR and since the scan was linear and only in  $x$ -direction, and the open-ended waveguide is polarized in  $x$ -direction,  $\Gamma = \Gamma_x$ , and

$$G^{RT} = (G^p)^2 = \left( \frac{1}{K_{mn}^2} \partial_z \partial_{z'} F_{xy}^{-1} \left( \frac{F^{TM}(\vec{K}_s, z, z')}{K_{mz}} \right) \right)^2 \text{ in (85).}$$

With the same reason explained for Simulations 1 and 2, the operator  $\partial_z (\partial_{z'})$  will be removed. Moreover, it is assumed that the objects are only located in second layer (i.e., mortar). The image produced by the

WL-SAR with  $\alpha = -40\text{dB}$  (Fig. 4.15) is improved in comparison with the image produced using PW-SAR and TEFMPW-SAR (Fig. 4.14 (b)-(c)). The indications of rebars in the image are focused and properly positioned. Moreover, as it was explained for  $\alpha$  selection, WL-SAR emphasizes the region of interest while de-emphasizing the air-to-mortar boundary (in this case) in contrast to TEFMPW-SAR.

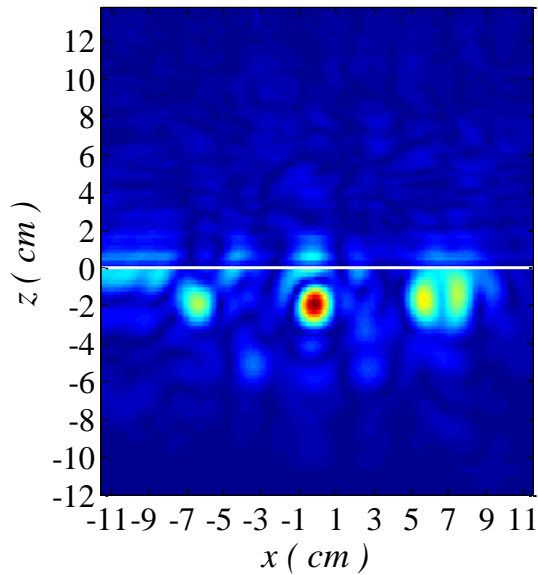


Figure 4.15. Produced image for Experiment 1 using WL-SAR with  $\alpha = -40\text{dB}$ .

In Experiment 2, a mortar specimen with two rebars, hereafter referred to as R2 is investigated. The dimensions of the sample are about 30 cm by 19 cm by 12.5 cm with two 1.6 cm-diameter rebars located at a depth of about 4.5 cm from the top surface of the sample, as shown in Fig. 4.16. One of the rebars has a ground out region. To model relatively severe corrosion, rust powder was collected from corroded rebars (left in ambient moist environment for a long period of time), and then the ground region is covered and filled with this rust powder and wrapped with plastic sheet and tape [71]. Since the rebars are deep inside lossy mortar, this example can show the performance of these different techniques in the presence of loss. The measurement setup is shown in Fig. 4.16 (d).

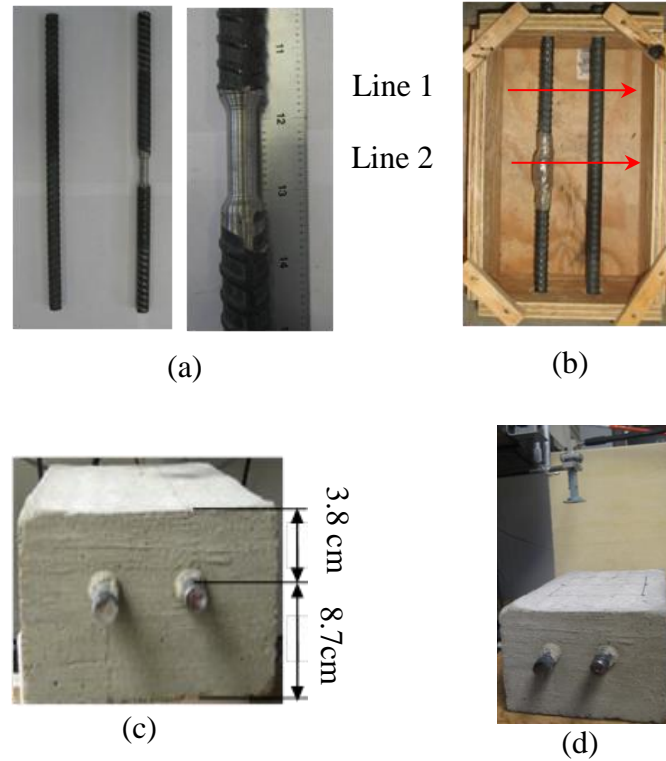


Figure 4.16. Sample R2: (a) rebars with and without corrosion, (b) two different scanning lines, (c) sample, and (d) measurement setup.

The scan is performed over two different lines. Under line 1, both rebars are whole, while under line 2, one of the rebars has corrosion (Fig. 4.16 (b)). Scanning is performed from  $x = -6.5$  cm to  $6.5$  cm with step size of  $0.1$  cm. Simulation 1, as explained earlier, is immediately comparable to the scan under line 2. The collected data is fed into all three algorithms. For SAR, a background medium with  $\epsilon_{r,b} = 2.42$  was assumed. The produced SAR images are shown in the left column of Fig. 4.17. There are many false indications of objects and defocused artifacts in the images. The same explanation as it was provided for Experiment 1 can explain these observations. The PW-SAR and TMFMPW-SAR produced images have unexpected artifacts, as depicted in the middle column of Fig. 4.17 (a)-(b). Actually, loss plays a more significant role in this experiment in comparison with Experiment 1.



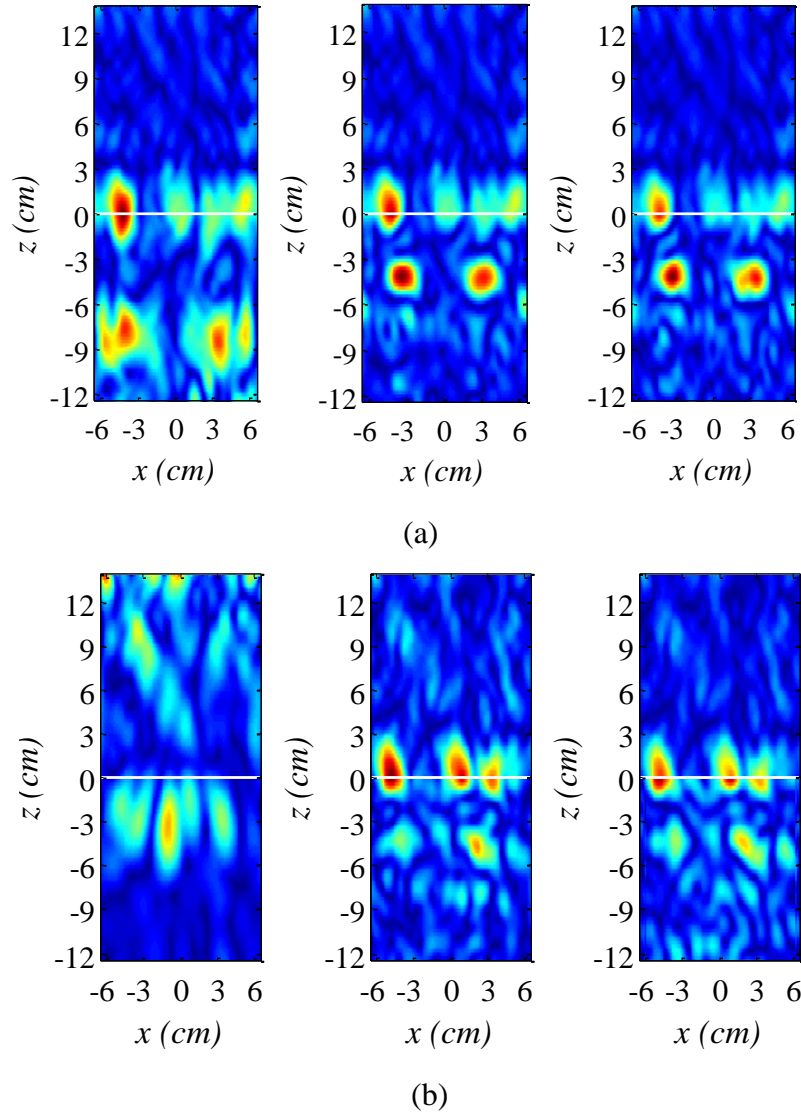


Figure 4.17. Reconstructed images for R2 for different scans. (a) line 1, and (b) line 2 (left column: SAR, middle column: PW-SAR, right column TMFMPW-SAR).

With the same reason which was provided for Experiment 1, it is assumed that

$$\Gamma = \Gamma_{x'}, G^{RT} = (G^p)^2 = \left( \frac{1}{K_{mm}^2} \partial_z \partial_{z'} F_{xy}^{-1} \left( \frac{F^{TM}(\vec{K}_s, z, z')}{K_{mz}} \right) \right)^2, \text{ and later, the operator } \partial_z (\partial_{z'})$$

is removed. Moreover, it is assumed that the objects are only located in second layer (i.e., mortar). The produced image using WL-SAR for scan line 1 and line 2 with  $\alpha = -50\text{dB}$ , are presented in Fig. 4.18. There are false indications of objects and defocused artifacts in the TMFMPW-SAR images. While MPW-SAR compensates for the phase shift of each

layer properly, it does not compensate for loss. Moreover, as it was mentioned for Experiment 1, the discontinuity is not properly modeled. With regard to these facts, WL-SAR is expected to show better performance. The image produced by WL-SAR (Fig. 4.18 (a)-(b)) is much sharper where the indications of rebars are focused and properly positioned. Comparing the images from lines 1 and 2, the indication of the left object in line 2 is weaker, corresponding to the presence of rust. Also, it should be noted that a comparison between Fig. 4.4 (b) and Fig. 4.18 (b) verifies that the produced images using simulated data are in a reasonable agreement with the produced images using measured data.

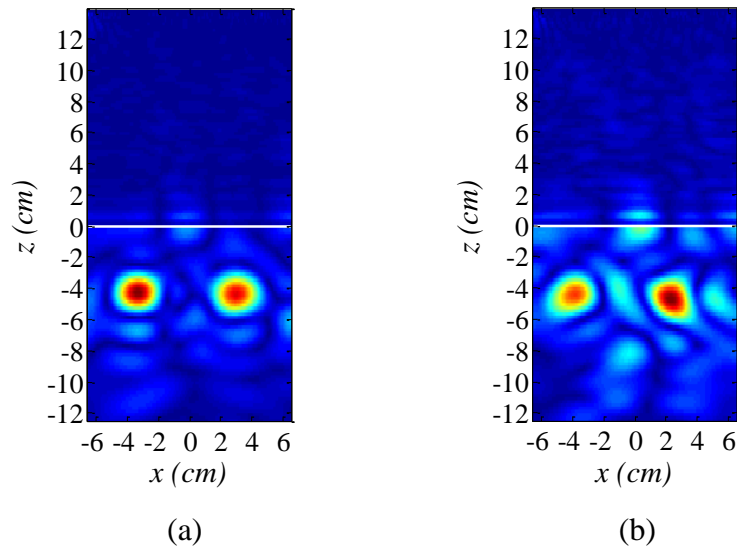


Figure 4.18. Reconstructed images for R2 using WL-SAR ( $\Gamma_x$ ) ( $\alpha = -50\text{dB}$ ). (a) line 1, and (b) line 2.

#### 4.7. 3D IMAGE RECONSTRUCTION

The proposed MPW-SAR and WL-SAR methods can be used to analyze wideband and 2D scanned areas to produce three dimensional images. To show the efficacy of the methods to generate 3D images, two experiments (Experiment 3 and Experiment 4) were performed.

In Experiment 3, to show the ability of the introduced techniques to produce 3D image from embedded objects in a lossy media, R4 was flipped and scanned, as shown in Fig. 4.19. The antenna and measurement setup are the same as before except that now an area is scanned with dimensions  $x = -11$  cm to 11 cm with step size of 0.2 cm and  $y = -10.5$  cm to 10.5 cm with step size of 0.4 cm. The antenna is 13 cm away from the top surface of mortar sample.

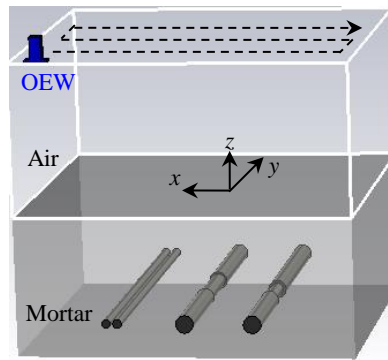


Figure 4.19. Measurement setup for flipped R4 sample to be used for 3D image reconstruction (Experiment 3).

The 3D image produced by TMFMPW-SAR coefficients shows artifacts at the boundary between mortar and air. These artifacts exist because the method does not properly model the boundary. Moreover, it does not compensate for the loss. Then, the collected data is fed into WL-SAR method. Since the scan is performed in 2D at  $x$ - and  $y$ -directions,  $K_x$  and  $K_y$  both exist. Also, the scanning standard X-band open-ended waveguide is polarized in  $x$ -direction, which means that  $E_x$  component of the radiated field by the objects has major contribution on the measured  $S_{11}$ . Based on these facts and the provided explanation in Sections 3.2 and 4.3, as an approximation, it should be decided that the major contribution on the collected data is coming from  $\Gamma_x$  or  $\Gamma_y$ . In here, to be consistent with the antenna's polarization,  $\Gamma_x$  is selected. Therefore,  $\Gamma = \Gamma_x$ .

$$\text{and } G^{RT} = (G^p)^2 = \left( F_{xy}^{-1} \left( \frac{K_y^2 F^{TE}(\vec{K}_s, z, z')}{K_{mz} |\vec{K}_s|^2} \right) + \frac{1}{K_{mn}^2} \partial_z \partial_{z'} F_{xy}^{-1} \left( \frac{K_x^2 F^{TM}(\vec{K}_s, z, z')}{K_{mz} |\vec{K}_s|^2} \right) \right)^2 \text{ in (85).}$$

As another approximation and to simplify the computer-based implementation, the second term on the right side of the equation is removed and only TE mode related term is used. The produced 3D image using the WL-SAR is shown in Fig. 4.20 which in contrast with TMFMPW SAR produced image, does not contain the artifacts since the boundary is properly modeled and the region corresponding to the rebar is emphasized. The value  $\alpha = -85$  dB was estimated using the rule of thumb method and used to produce this image.

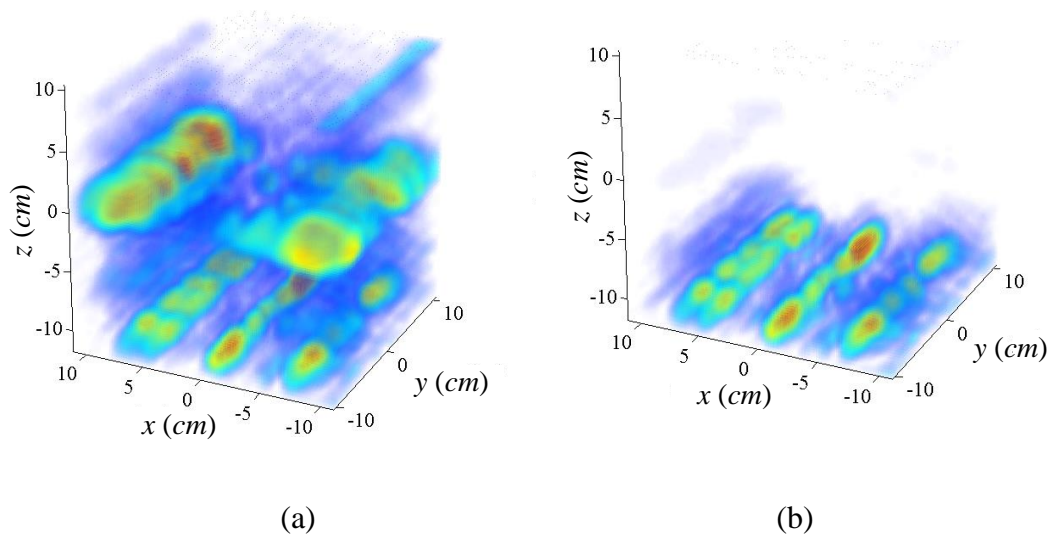


Figure 4.20. Reconstructed 3D images for R4 flipped at X-band. (a) TMFMPW-SAR, and (b) WL-SAR.

Moreover, to provide a cross-section view, one slice of the 3D images corresponding to the layer containing the rebars (i.e.,  $z = -9.5$  cm) is selected and shown in Fig. 4.21. It can be seen that both TMFMPW-SAR and WL-SAR produce a focused image of the rebars. Although the image produced by WL-SAR shows the thinner rebars slightly cleaner, the results of both techniques are comparable. Therefore, for this case, WL-SAR has a distinct advantage over MPW-SAR for volume images but is only

marginally better for a slice of the volume images at the plane of the rebars. The processing time for MPW-SAR was about 3 seconds and for Wiener filter was about 30 minutes. Thus, MPW-SAR has a distinct time performance advantage over WL-SAR. The WL-SAR method requires calculation of the layered structure Green's function which is a time and memory consuming procedure. Therefore, WL-SAR algorithm is much slower than PW-SAR algorithm.

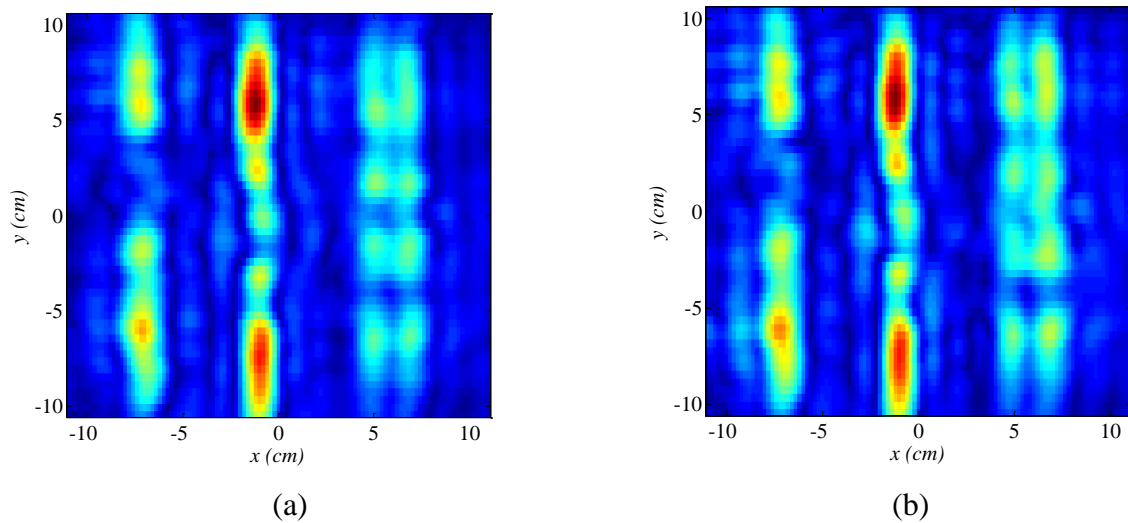


Figure 4.21. One slice at  $z = -9.5\text{cm}$  of the produced volumetric image for flipped R4 sample. (a) TMFMPW-SAR, and (b) WL-SAR.

The frequency of operation determines cross-range resolution of the final produced image [6]. Higher the frequency is, finer the cross-range resolution can achieve. To show this point, in Experiment 4, R4 sample is scanned with a K-band OEW. The measurement setup and scanning dimensions are the same as Experiment 3. However, the antenna is only 0.8 cm away from the top surface of mortar sample and in  $y$ -direction, scanning step size is reduced to 0.2 cm. The produced 3D images are shown in Fig. 4.22. The 3D image produced by TMFMPW-SAR shows artifacts at the boundary between mortar and air. On the other hand, the 3D image produced by WL-SAR ( $\alpha = -65\text{dB}$ ) does not contain these artifacts since the boundary is properly modeled and the region corresponding to the rebars is emphasized. Moreover, since the measurement frequency is higher, the

resolution is much finer and more details of the rebars can be seen in the images in comparison with Experiment 3. This was expected because the resolution is directly proportional to the measurement frequency. The corroded sections on thick rebars can be easily seen and distinguished in the produced images from whole rebars.

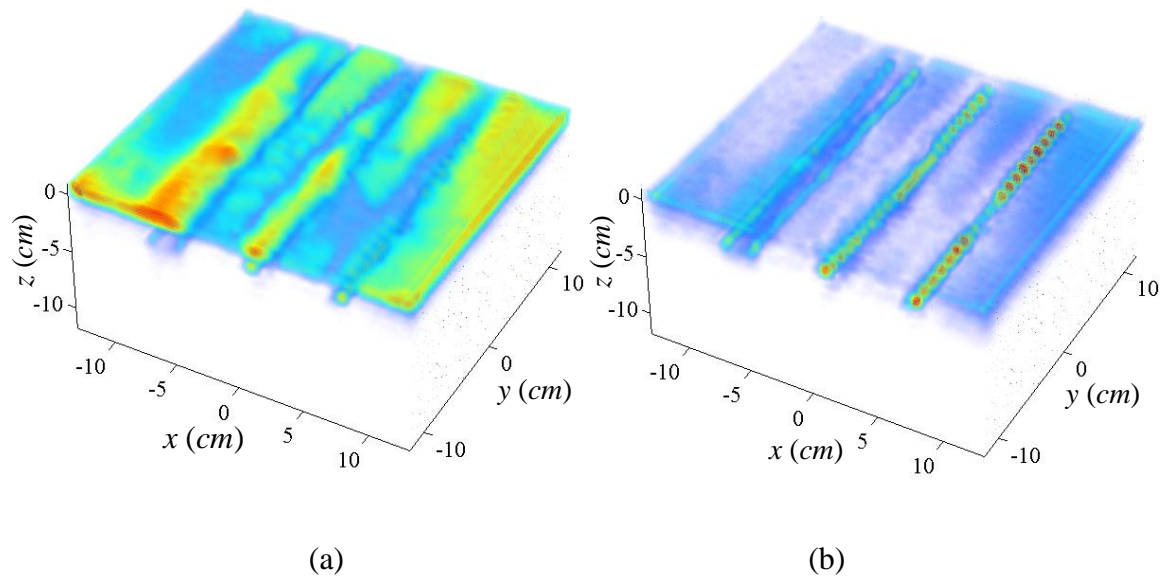


Figure 4.22. Reconstructed 3D images for R4 at K-band. (a) TMFMPW-SAR, and (b) WL-SAR.

To provide a cross-section view, one slice of the 3D images corresponding to the layer containing the rebars (i.e.,  $z = -1.8$  cm) is selected and shown in Fig. 4.23. Similar to Experiment 3, the 2D slices are very similar to each other, however, the thinner rebars are imaged slightly better using WL-SAR. Moreover, both images show the corrosion on the two thicker rebars. This is very important from corrosion detection point of view.

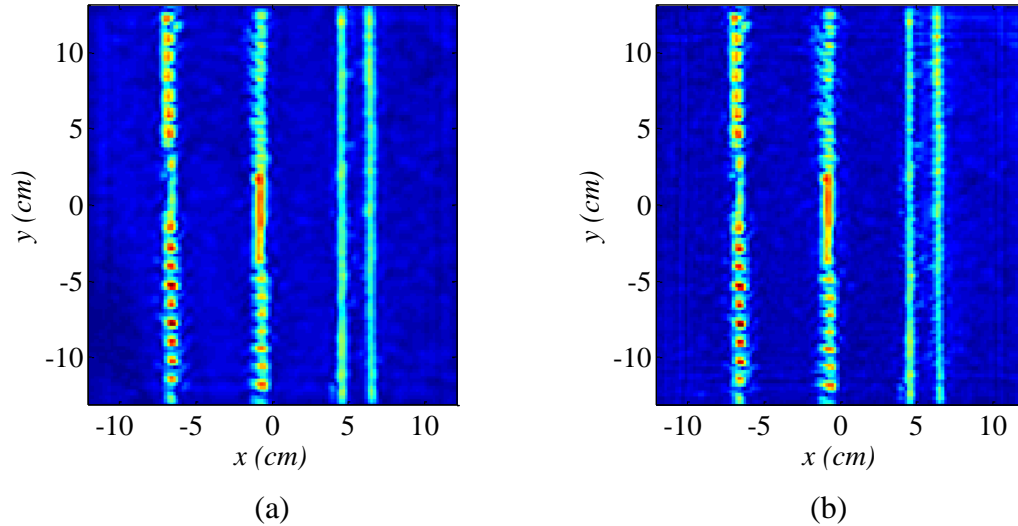


Figure 4.23. One slice at  $z = -1.8$  cm of the produced volumetric image for R2 sample. (a) TMFMPW-SAR, and (b) WL-SAR.

#### 4.8. CONCLUSION: COMPARING PERFORMANCE OF DIFFERENT IMAGING METHODS

In this section, SAR, MPW-SAR and WL-SAR imaging methods which were developed in Section 3 for imaging embedded active targets in a layered structure were manipulated to be used for passive objects, as well. It was shown that monostatic SAR as a robust and fast qualitative imaging technique is suitable for imaging objects in a homogenous background but it is not appropriate for imaging embedded objects in layered structures. Monostatic MPW-SAR as a modification over previously developed PW-SAR method was introduced to improve PW-SAR performance to image high contrast layered structures; however, the investigation showed that MPW-SAR could not provide a significant improvement over PW-SAR. Simple modeling of the boundary between layers by incorporating Fresnel or generalized transmission coefficient in the MPW-SAR equations could be seen as major root of the problem. Moreover, MPW-SAR similar to PW-SAR and SAR techniques has problem imaging an embedded object inside of a lossy material. To overcome these issues, a comprehensive method namely WL-SAR was developed. Firstly, the relationship between the layered structure, collected data, and the image was established using the Green's function of layered structures. Mathematical





## 5. ANTENNA DESIGN FOR HARDWARE PART OF MICROWAVE IMAGING SYSTEM

### 5.1. INTRODUCTION

Antenna is an essential part of any microwave imaging system which is used in conjunction with a measurement and recording tool to collect data from a sample under test (Fig. 1.1). When interested in 3D SAR imaging, wider beamwidth and larger bandwidth are required to have finer cross-range and range resolutions, respectively [24]. Moreover, if the object of interest is embedded in an unknown medium, having an antenna whose characteristics (e.g., operating frequency band, polarization, and pattern) can be dynamically modified is critically useful. This requires that antenna cover a wide range of characteristics, or one whose important characteristics can be appropriately tuned. Among these characteristics, the operating frequency and the bandwidth associated with the antenna play significant roles. These two parameters are not necessarily independent of each other since bandwidth is commonly measured by a certain percentage of the operating frequency.

One would expect that using a multiband antenna or one with a very wide bandwidth may be the best option [72]-[74]. However, multiband, wideband or ultra wideband (UWB) antennas may not be optimum for communications or imaging systems where the frequency and bandwidth of the transceiver may need to be dynamically changed. In past decades, there have been extensive efforts to develop wideband and ultra wideband antenna design techniques for different applications such as: high resolution microwave imaging, short range wireless communication systems, wireless body area network (WBAN), wireless personal area networks (WPAN), and electromagnetic compatibility measurements [75]-[77]. However, interference issues along with relative form-factor (i.e., overall dimensions and bulkiness), limit the utility of wideband/UWB antennas for the imaging and long distance communication purposes [25]-[28]. Alternatively, multiband antennas were introduced which operate in more than one frequency band at a time [78]. However, these antennas still require receivers with effective out-of-band noise rejection filters in their front-end circuitry [25]. Moreover, covering a wide range of distinct frequency bands using multiband antennas is quite a challenge.

On the other hand, the growing interest in wireless communication market toward integrating more and more radios into a single chip (or single platform) significantly accelerated the demand for an antenna with multiple radiation characteristics [25]. However, reconfigurable antennas are capable of addressing many of these issues [25],[26],[79]. A reconfigurable (dynamic) antenna can electronically or mechanically switch among different configurations to provide for a set of desired characteristics.

Despite many advantages offered by reconfigurable antennas, the topic is fairly recent, and there is not a robust and methodical design procedure for compact reconfigurable antennas. Since the reconfigurable antennas show a significant potential for microwave imaging systems and currently growing multiradio communication devices, this section and next section will be devoted to this topic. Moreover, considering the current demand for small and miniaturized antennas, “compact reconfigurable antenna design” can be seen as an attractive topic. To address this requirement, a good knowledge about the currently-available miniaturization techniques may be required in conjunction with a deep understating of current progress in reconfigurable antenna design.

Therefore, in this section, a review of miniaturization techniques is provided which is followed by a discussion on currently-available miniaturized wideband antennas. Limitations and problems will be addressed and then, currently-available reconfigurable antennas will be discussed. In Section 6, a methodical design procedure for reconfigurable antennas will be introduced. Then, this method will be used to design a novel compact reconfigurable antenna.

## **5.2. SUMMARY OF ANTENNA MINIATURIZATION TECHNIQUES**

Antenna miniaturization has been the subject of numerous studies for almost 70 years [80]-[83]. The early studies showed that as the antenna size decreases, so do the bandwidth and efficiency [80]. The fundamental miniaturization limitation was introduced by Chu [80] and later was re-examined by McLean [83]. This fundamental limitation relates the quality factor (Q) of an antenna to the bandwidth of the antenna. The higher the Q is, the narrower the operating bandwidth will be.

Recently, many new investigations have been conducted to reduce the form-factor (or the overall size) of the antenna. These miniaturization techniques are generally founded on changing the electrical and physical properties of the antenna. In fact, two major categories of miniaturization technique exist, namely: a) topology-based, and b) material-based miniaturization techniques, as described below.

**5.2.1. Topology-Based Miniaturization Techniques.** Geometry, the current (either electric or magnetic) density distribution, and electrical dimensions of an antenna determine its characteristics. Based on this underlying concept, some methods and techniques have been developed which manipulate and optimize the shape and geometry of the antenna in order to achieve the desired radiation characteristics with the smallest possible dimensions. In the following, some of these methods and techniques will be reviewed.

**5.2.1.1 Fractal antennas.** Mandelbrot introduced fractal, to describe a family of complex shapes that have an inherent self-similarity or self-affinity in their geometrical structure [84]. Fractal means broken or irregular fragments and fractal structures can be found in nature such as: coastlines, snowflakes, trees, ferns, etc. [84]. Fractals are space-filling geometries that can be used to fit a long length in a small area. This underlying concept was considered by antenna engineers as fractal geometry was incorporated into antenna design to create a new class of antennas named “*fractal antennas*” versus traditional Euclidean geometry-based antennas [84].

Fractal antennas can provide radiation pattern and input impedance similar to a larger antenna, while occupying a much smaller area as a result of their self-similarity property. Koch dipole, from Koch curve family, is smaller than a wire dipole both resonating in same frequency. A Koch curve generation is an iterative process [85], as shown in Fig. 5.1.

The total length of Koch curve at the  $n^{\text{th}}$  iteration is  $(4/3)^n$  of  $0^{\text{th}}$  iteration length (straight line). This means, a Koch dipole that starts and ends in same positions as ordinary dipole, provides a longer length and hence a lower resonant frequency. This enables a miniaturized design procedure.

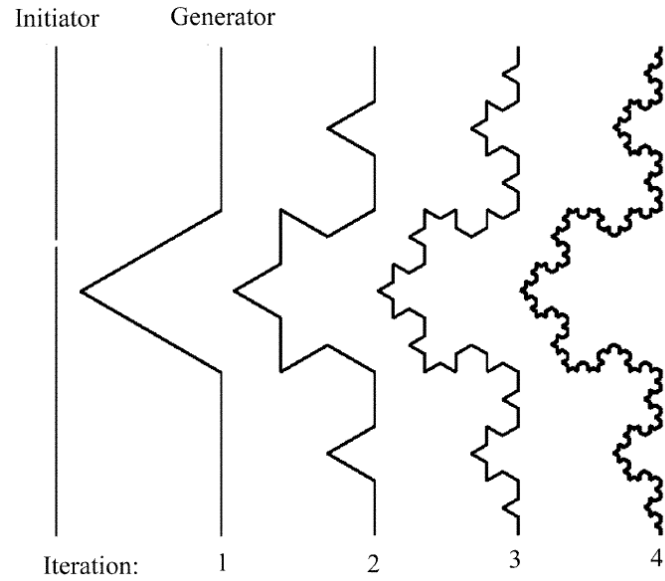


Figure 5.1. Koch curve generations [29].

Koch snowflake/island [86]-[87], Sierpinski gasket [84],[88], and Minkowski island fractal [89], are among well-known fractal shapes for antenna application. Some of these fractal shapes are shown in Figs. 5.2-5.4.

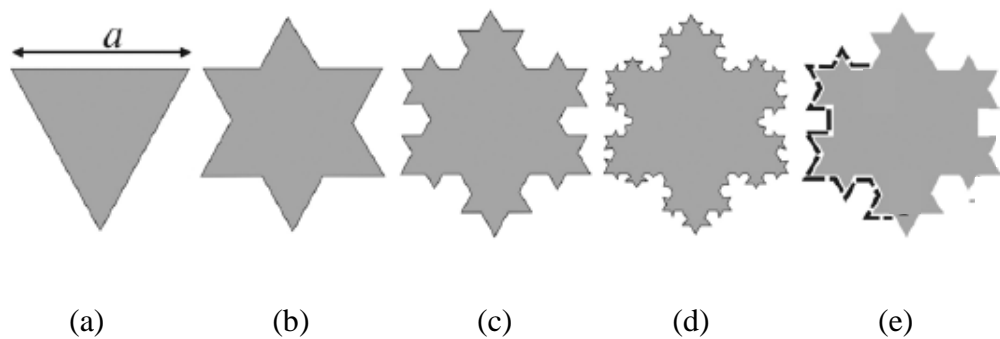


Figure 5.2. Koch snowflake geometry in different iterations. (a) basic geometry, (b) first iteration, (c) second iteration, (d) third iteration, and (e) modified second iteration [87].

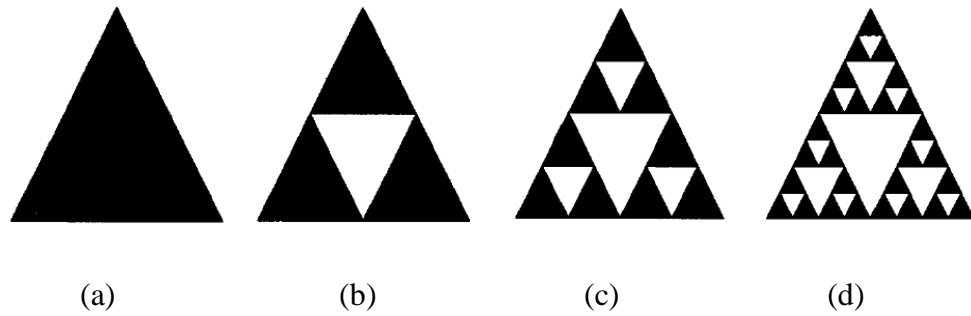


Figure 5.3. Sierpinski gasket geometry over different iterations. (a) basic geometry, (b) first iteration, (c) second iteration, and (d) third iteration [84].

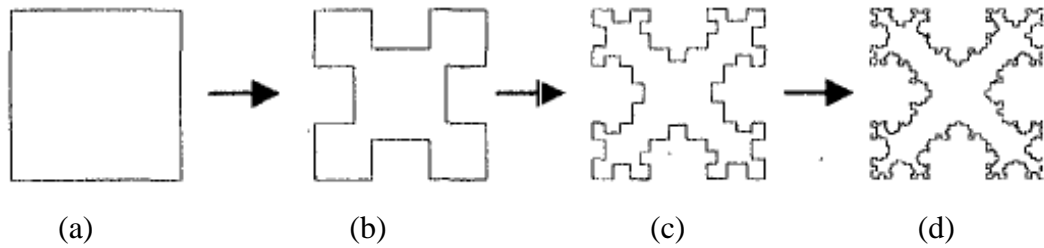


Figure 5.4. Minkowski island fractal geometry over different iterations. (a) basic geometry, (b) first iteration, (c) second iteration, and (d) third iteration [89].

In [87], a compact coplanar waveguide (CPW)-fed modified Koch fractal slot antenna is designed for 2.4/5.2/5.8 GHz wireless local area network (WLAN) and 2.5/3.5/4.5 GHz worldwide interoperability for microwave access (WiMAX) applications. Initially, a CPW antenna with a triangular slot was used. Then, Koch snowflake geometry, which was shown in its different iteration stages in Fig. 5.2, was modified and used instead of the triangular slot (Fig. 5.5). The study showed that replacing the triangular slot shape with the modified Koch snowflake reduced the operating frequency of the antenna. This resulted in a compact antenna ( $25.8 \times 33.5 \text{ mm}^2$ ) with enhanced bandwidth (Fig. 5.5 (b)). The dimension of the antenna is  $0.228\lambda_0 \times 0.268\lambda_0$  where  $\lambda_0 = 125 \text{ mm}$  is the wavelength at the lowest operating frequency (i.e., 2.4 GHz).

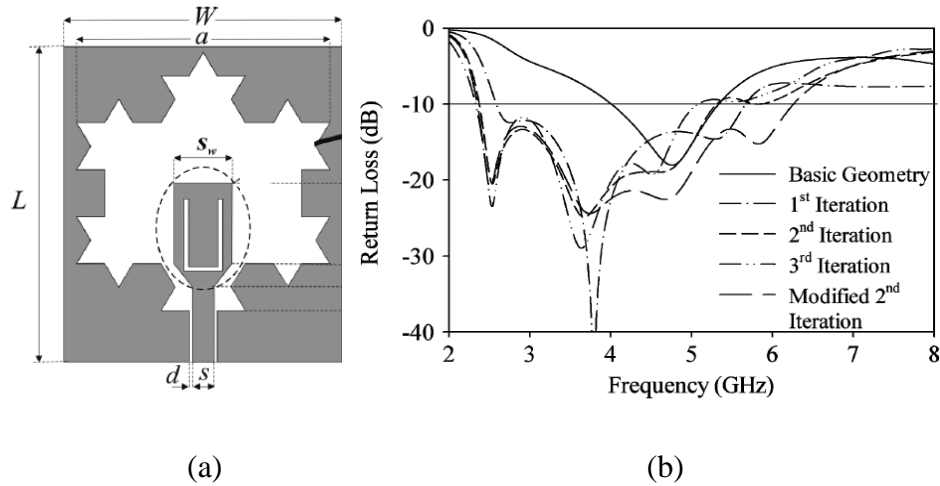


Figure 5.5. CPW-fed modified Koch fractal slot antenna. (a) configuration, and (b) simulated return loss for different iteration of the slot [87].

**5.2.1.2 Reactively loaded antennas.** By adding the appropriate inductance or capacitance per unit length to a transmission line, its electrical length can be increased [90]. On the other hand, an antenna can be effectively modeled as a transmission line so that transmission line theory can be applied to antenna analysis and design [90]. Therefore, a smaller antenna can be created by properly loading it with an inductance or capacitance. Actually capacitive or inductive loading increases the (wave) propagation constant, resulting in a slow wave structure [90]. In order to slow down guided wave and to create a slow wave structure, in [90] a periodically-load printed antenna with shunt lumped capacitance is proposed. Slow wave enhancement factor is defined as the “ratio of the loaded to the unloaded propagation constants of the wave in the antenna”. It is shown that this ratio directly influences antenna miniaturization factor [90]. Loading parameters (e.g., type (inductive, capacitive), value, and spacing) may be obtained based on the desired size reduction. A planar inverted F antenna (PIFA) and a high-frequency (HF) slot-loop antenna were miniaturized based on this loading technique [90]. The size of both antennas is reduced approximately by factor of 10 in comparison with their unloaded counterparts [90]. The configuration of the proposed capacitor-loaded PIFA and photograph of the fabricated antenna is shown in Fig. 5.6. The overall size of this antenna is about  $0.013\lambda_0 \times 0.018\lambda_0$  at the operating frequency (i.e., 374 MHz or

$\lambda_0 = 80\text{cm}$ ) which shows more size reduction in comparison with the former capacitor-loaded planar inverted-F antenna reported in [91] for mobile telephone handsets. The simulation and measurement results for this antenna with and without the loading capacitors are compared in Fig. 5.7 [90]. This figure clearly shows the role of capacitive loading in reducing the resonant frequency. However, the maximum gain of the antenna is only  $-22.6\text{ dBi}$  which is very small.

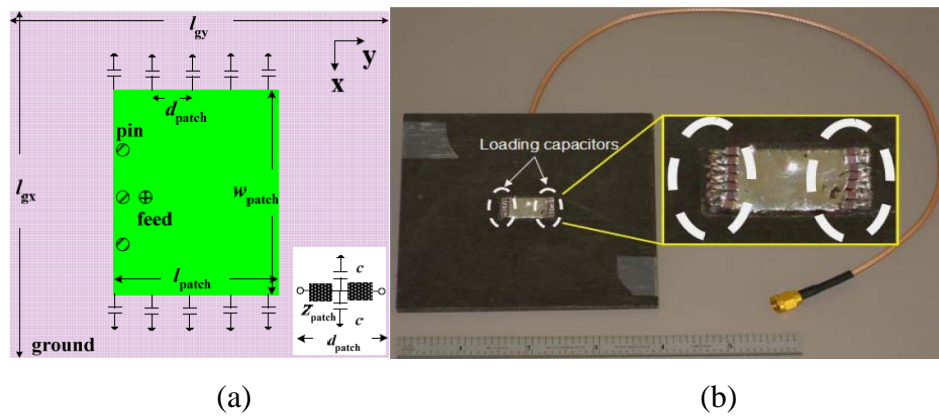


Figure 5.6. Capacitor-loaded PIFA, (a) schematic view, and (b) fabricated antenna [90].

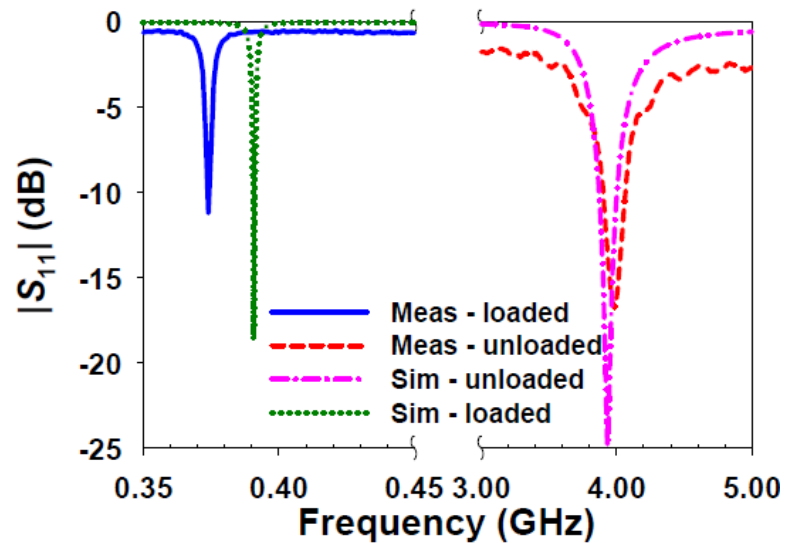


Figure 5.7. Measurement and simulation results for loaded and unloaded PIFA [90].

On the other hand, the designed HF slot loop antenna gives a bandwidth of 0.38% for a voltage standing wave ratio smaller or equal 2 ( $VSWR \leq 2$ ). To improve the bandwidth, [90] proposed an L-section matching network which is derived from filter design techniques. This matching section helped in increasing the bandwidth by 1.78%. The configuration of the HF slot loop antenna and photograph of the fabricated antenna is shown in Fig. 5.8 [90]. The overall size of this antenna is about  $0.031\lambda_0 \times 0.017\lambda_0$  at the operating frequency (i.e.,  $\sim 24$  MHz or  $\lambda_0 = 12.5$  m) and it provides a very low gain of -34.9 dBi [90]. The simulation and measurement results for this antenna with and without L-section matching are compared in Fig. 5.9 [90].

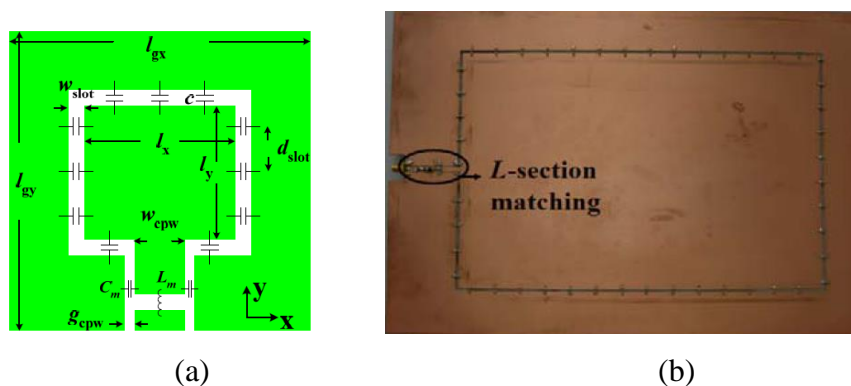


Figure 5.8. Capacitive loaded HF slot loop antenna. (a) schematic view, and (b) fabricated antenna [90].

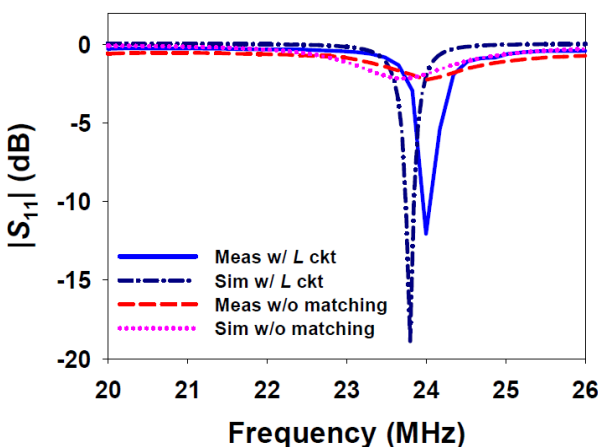


Figure 5.9. Measurement and simulation results for HF slot loop antenna with/without L-section matching circuit [90].



In [92], antenna miniaturization based on transmission line resonator idea is proposed. Transmission line resonator is created by loading one end of quarter wavelength transmission line with a short circuit while leaving the other end open. A quarter-wave resonant slot antenna is miniaturized based on this idea [92]. Although, shorting a slot line can be easily implemented, but, making an open circuit on a slot line without reaching the edge of the structure is difficult. To create an open circuit, a spiral slot of a quarter-wavelength long and short-circuited at the other end was used. This spiral slot is a quarter-wavelength long at the resonant frequency and transforms the short circuit to an open circuit at the resonant frequency (Fig. 5.10) [92]. A size reduction of 50 percent was reported using this topology [92]. Further size reduction was achieved by bending the radiating section in a way such that no section carries a magnetic current in opposite direction of any other sections (Fig. 5.10). This method provides miniaturized antenna as small as  $0.05\lambda_0 \times 0.05\lambda_0$  (where  $\lambda_0 = 50\text{ cm}$ ) and with a fairly high efficiency of about  $-3\text{dBi}$  [92]. An open-ended quarter-wavelength microstrip line under the slot is used to feed it. The reactive part of the antenna input impedance can be cancelled out by changing the length of feeding line. The reflection coefficient ( $S_{11}$ ) of the antenna is shown in Fig. 5.11 showing a resonance at 0.6 GHz with a narrow bandwidth.

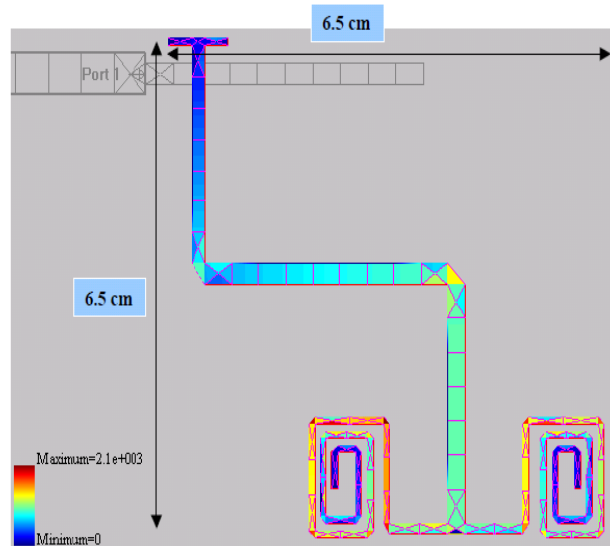


Figure 5.10. Miniaturized resonant slot antenna [92].

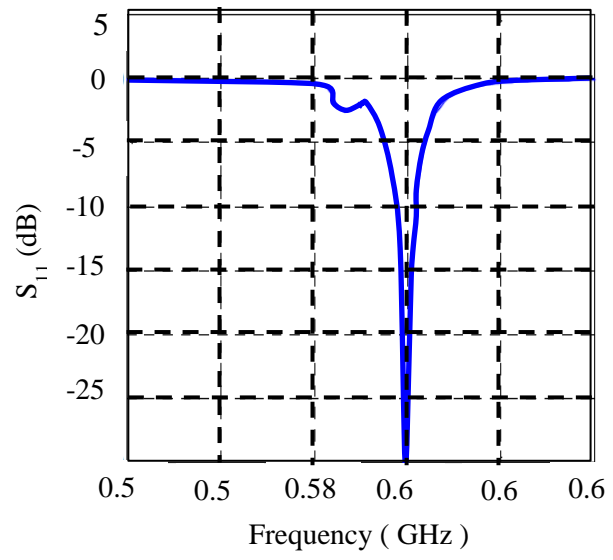


Figure 5.11. S<sub>11</sub> for miniaturized resonant slot antenna [92].

Also, [93] proposed miniaturize slot antenna using symmetric inductive loading (Figs. 5.12, 5.13).

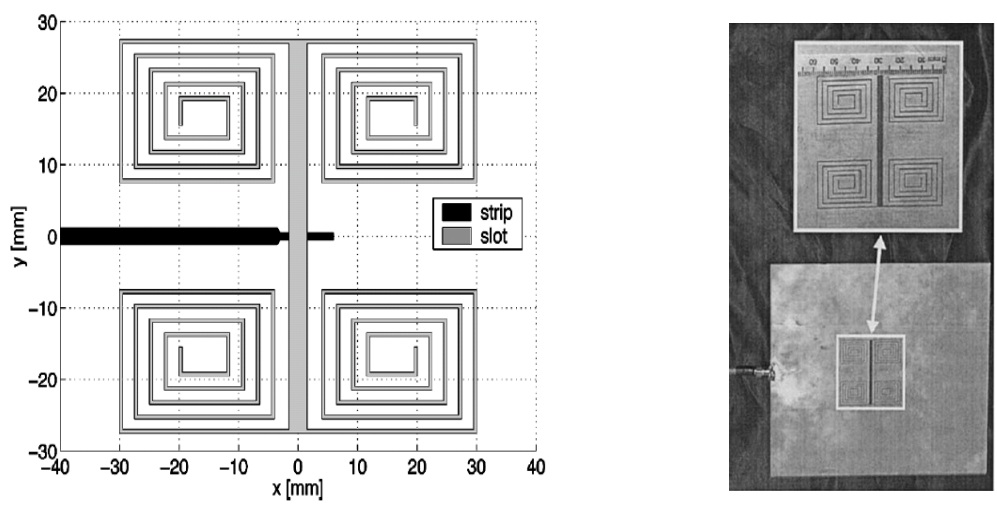


Figure 5.12. Symmetrically loaded slot antenna and its feed designed to operate at 300 MHz [93].

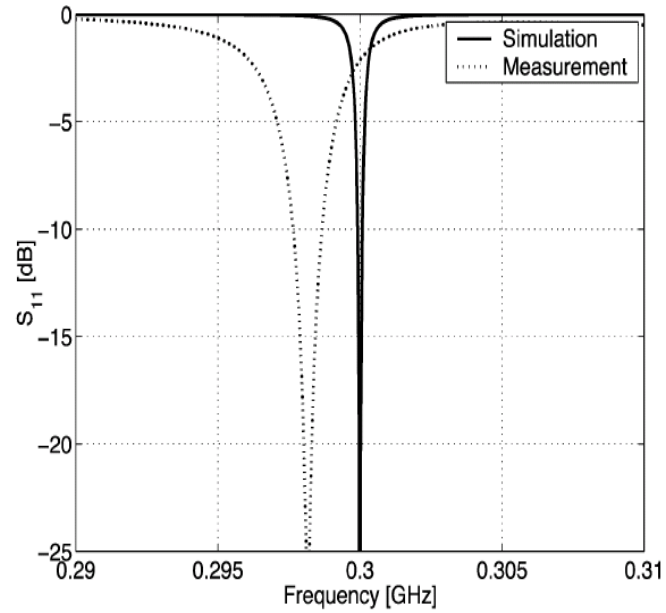


Figure 5.13. Simulated and measured  $S_{11}$  for symmetrically loaded slot antenna [93].

To enhance bandwidth of this antenna, miniaturized folded-slot topology is proposed in [94] (Fig. 5.14). For this topology, bandwidth defined for 10 dB return loss, shows 0.34% to 0.93% increase over the original antenna introduced in [92].

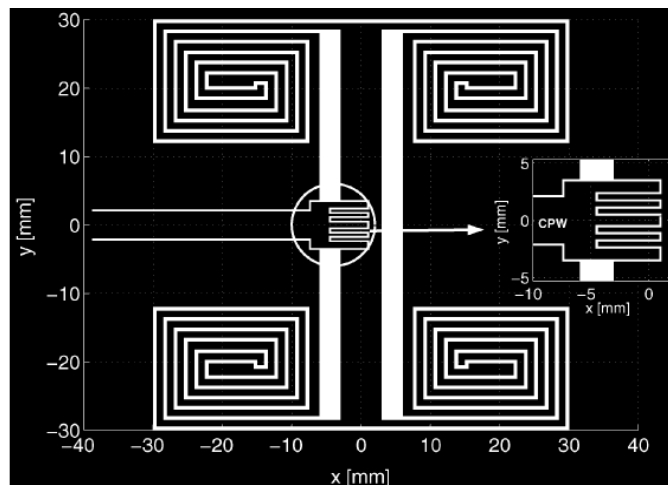


Figure 5.14. Miniaturized folded-slot antenna fed by capacitively coupled CPW line [94].

**5.2.1.3 Antenna with engineered ground plane.** Engineering the ground plane (GND) of a planar antenna has also shown to improve the antenna characteristics. Electromagnetic band gap (EBG) structures in general and defected ground structures (DGS) as one-dimensional EBG have been used for these purposes [95]-[96]. As a limitation, these approaches only work for planar antennas but still cover a wide range of antennas including microstrip antennas. Microstrip patch antennas as a well-known member of this family with light weight, low profile, and ability to be integrated with monolithic microwave integrated circuit (MMIC) designs have been utilized in many applications such as handheld wireless devices (e.g., cellular phones), aircraft, and satellite [97]. In [95], dielectric EBG rods were used to realize a thin high directivity microstrip patch antenna. In [96], DGS was used to suppress cross-polarized radiation from a microstrip patch antenna. Recently, EBG and DGS structures have been used for antenna miniaturization purpose [97]-[98]. In [97], two four-arm spiral-shaped DGS were used to reduce size (by about 50 percent) and achieve multiband operation capability (Fig. 5.15). Adding a slot in the ground plane can increase the length of return current path and make the antenna look electrically larger.

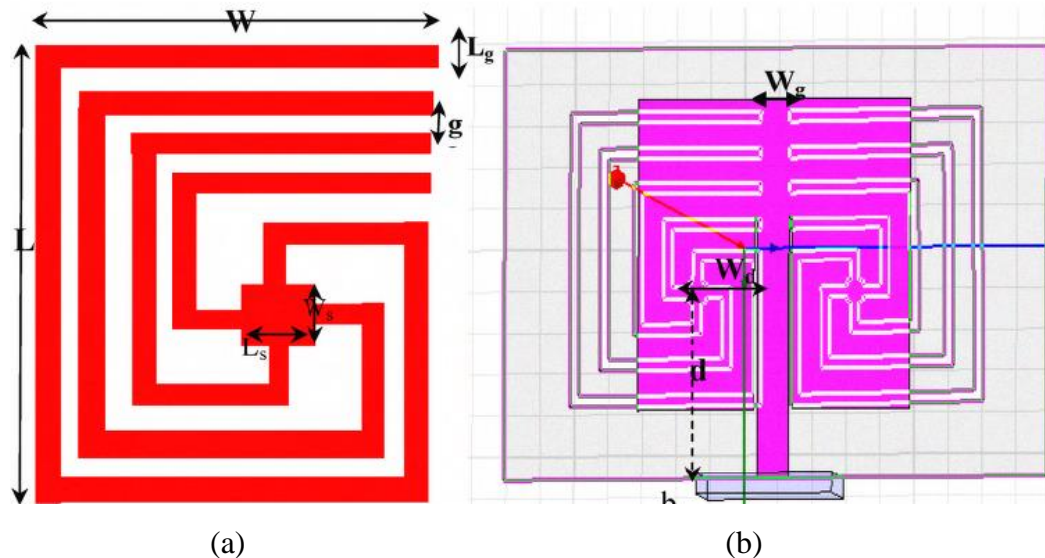


Figure 5.15. Antenna with DGS. (a) spiral cell DGS, and (b) patch antenna with two spiral shaped DGS [97].

Also, [98] used dumbbell shaped slots in the ground plane of a microstrip antenna to reduce its size by 60 to 65 percent in comparison with the conventional microstrip antennas (Fig. 5.16).

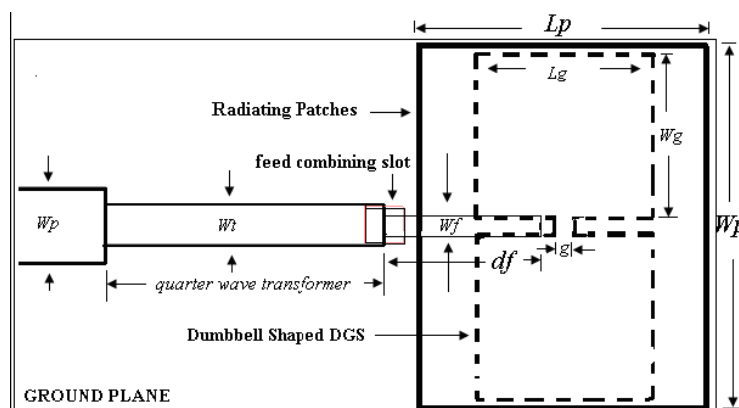


Figure 5.16. Miniaturized microstrip antenna with dumbbell shaped DGS [98].

The reflection coefficient of the antenna with DGS is compared with conventional antenna with same size but without DGS (Fig. 5.17) [98]. As Fig. 5.17 shows, the antenna with DGS resonates at  $\sim 1.8$  GHz while the antenna without DGS resonates at  $\sim 5$  GHz.

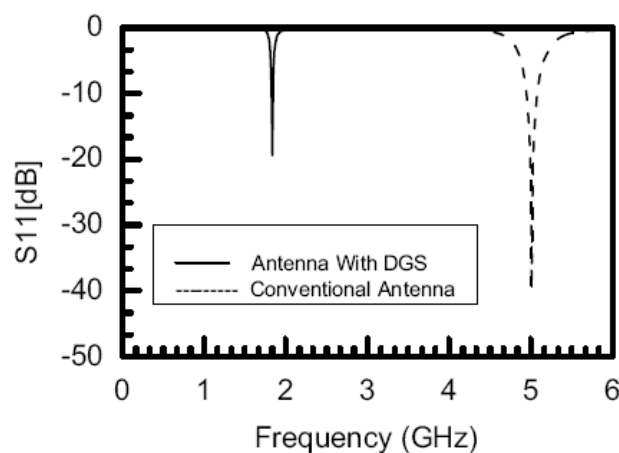


Figure 5.17. A comparison between return loss of the antenna with DGS and conventional antenna without DGS [98].

**5.2.1.4 Meander antennas.** Meander antenna was firstly introduced in 1991 [99]. Meandering technique aims to fill space and bend long straight lines in order to occupy smaller lengths (somewhat similar to fractal). In [100], a solid microstrip patch antenna was transformed into a rectangular wire-mesh. Then, the rectangular meshes were squeezed by using a sinusoidal meandering scheme to reduce the size of the antenna by 72 percent in comparison with a conventional corner-truncated square microstrip antenna [101] while both antennas provide circular polarization. The different steps for a compact meandered-grid microstrip antenna which radiates at  $\sim 2.32$  GHz are shown in Fig. 5.18.

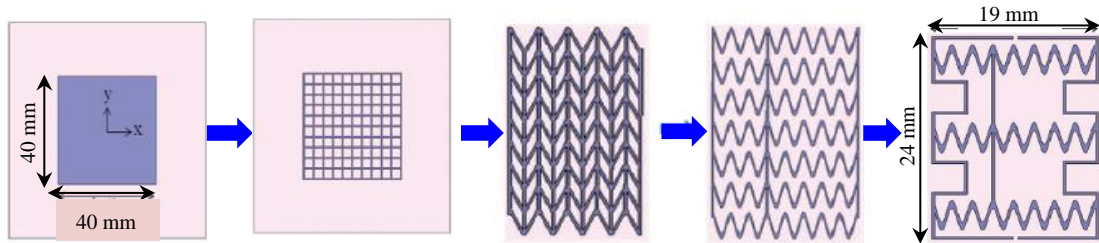


Figure 5.18. Evolution of a circularly polarized compact meandered-grid microstrip antenna from a solid microstrip antenna.

Nowadays, meandering techniques are widely used to design miniaturized ultra high frequency (UHF) RFID tags [45],[102]-[104]. A commercial RFID tag namely ALEN ALN-9540 “squiggle” is shown in Fig. 5.19 which uses meandering line idea.

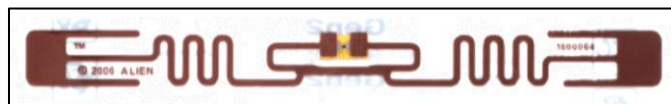


Figure 5.19. ALEN ALN-9540 squiggle RFID tag [104].

In [105], a spiral meander line antenna was introduced and optimized using Genetic Algorithm (GA). The final optimized antenna for operating frequency of 956

MHz ( $\lambda_0 = 313\text{mm}$ ) is shown in Fig. 5.20. The dimension of the antenna is  $27\text{mm} \times 11\text{mm}$  ( $(0.035 \times 0.086)\lambda_0$ ).

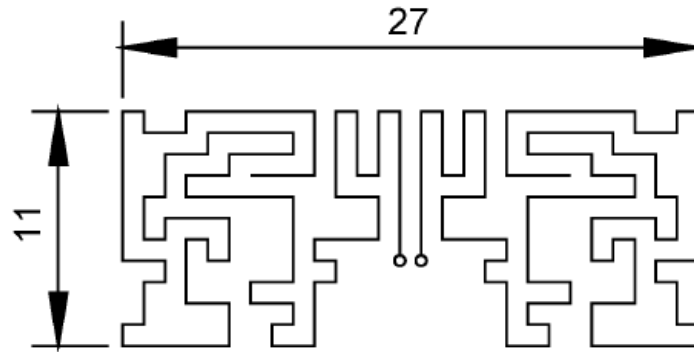


Figure 5.20. Optimized miniaturized spiral meander line antenna (unit: mm) [105].

In [106] a good theoretical discussion is provided to analyze and model meander lines. The model is based on geometry and it is frequency-independent.

**5.2.2. Material-Based Miniaturization Techniques.** This family includes miniaturization methods and techniques which manipulate and optimize materials in the antenna structure. In the following some of these methods are reviewed from literatures.

**5.2.2.1 Application of high dielectric constant substrate.** In the planar antennas which are usually implemented on a dielectric substrate, antenna size is reversely proportional to the square root of dielectric constant [106]. In [107], the effect of increasing substrate dielectric constant on the resonant frequency is studied and an integrated slot spiral antenna etched on a high permittivity material (i.e.  $\epsilon_r = 197$ ) is reported. Two different types of these antennas, namely; double twin spiral and twin spiral are shown in Fig. 5.21. The overall dimension of the squares is  $10\text{mm} \times 10\text{mm}$ .

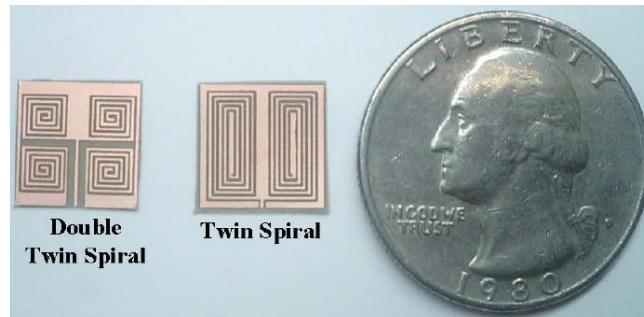


Figure 5.21. Two different slot spiral antennas (twin and double twin slots) etched on high permittivity dielectric material [107].

Measured reflection coefficients of these two antennas for two different values of dielectric constant (i.e., 2.6 and 197) showed that by increasing the dielectric constant, the resonant frequency reduces (Fig. 5.22). In this figure, dotted line is used to represent results for substrate with dielectric constant of 2.6 and solid line is used for dielectric constant of 197. The bandwidth of the antennas is very narrow and gain is very low (-42 dBi). Actually high dielectric constant can cause stronger electromagnetic coupling between the patch and the ground. Then, substrate can absorb most of the power and trap it rather than allowing the energy to propagate into free-space [107]. Moreover, high dielectric constant material with some amount of loss can dissipate energy in the form of heat. So, the overall radiation efficiency of the antenna decreases [108]. Narrow bandwidth and expected low antenna efficiency are two major drawbacks of this method.

To overcome part of the problem of microstrip antennas with thick and high permittivity materials, [109] proposed the idea of substrate perforation in order to lower the effective dielectric constant of the substrate surrounding the patch. The substrate is divided into two parts. The part which is under the patch is left unperturbed, thus, the size reduction is achieved. The surrounding part, however, is manipulated to lower its effective dielectric constant to create a smoother transition to the edge of the antenna and air. To lower the dielectric constant of the surrounding substrate, substrate was perforated. Actually, an array of small and closely-spaced holes is used for perforation purpose [109]. The perforation helped to mitigate the unwanted interference pattern of edge diffraction or scattering and leaky waves [109].



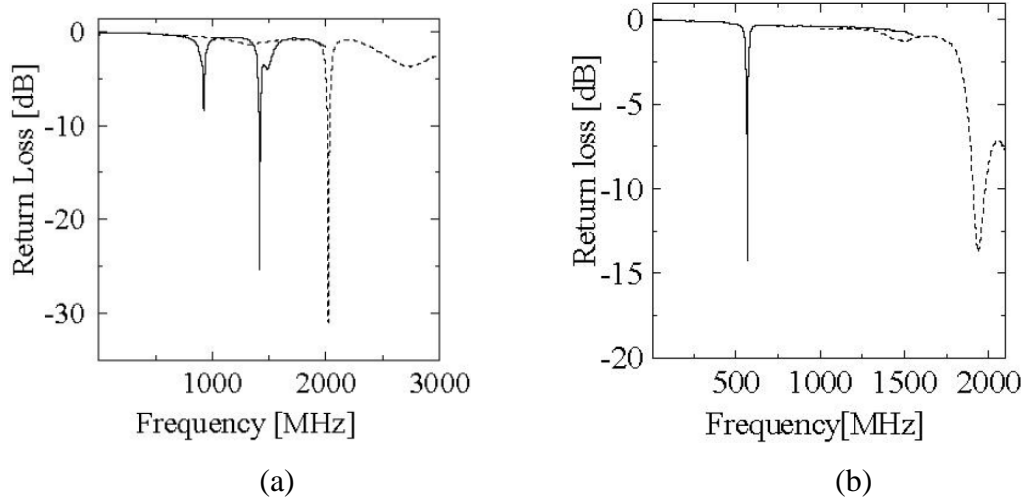


Figure 5.22. Measured return loss for: (a) double twin slot, and (b) twin slot [107].

**5.2.2.2 Metamaterial - based miniaturization techniques.** It was mentioned in Section 5.2.2.1 that the size of antenna is reversely proportional to the square root of the dielectric constant of the substrate material (for planar structures). In general, antenna miniaturization factor (or antenna form-factor) is inversely related to refraction index ( $n_i$ ) which is defined as:

$$n_i = \sqrt{\mu_r \epsilon_r}. \quad (90)$$

While intrinsic impedance is defined as:

$$\eta_i = \sqrt{\mu_r / \epsilon_r}. \quad (91)$$

Therefore, for material with high permittivity and permeability as long as  $\eta_i$  is close to  $\eta_i$  of air, EM wave does not concentrate inside of the substrate and so efficiency does not degrade. To address this issue, magneto-dielectric metamaterials were used that provide high reflection index with low intrinsic impedance [110]. In [92], initially a rectangular patch antenna (13.33 mm by 16.67 mm) on a finite size substrate (50 mm by 50 mm) with  $\epsilon_r = 25$ , loss tangent of 0.001, and thickness of 3.33 mm was designed to resonate at

1.56 GHz ( $\lambda_0 = 19.2$  cm). The dimension of the patch was about 1/10 of the free-space wavelength ( $\lambda_0$ ) (Fig. 5.23). However, the achieved bandwidth was 0.64 percent (relative to center frequency) and efficiency was 77 percent. To address the bandwidth and efficiency problems, a magneto-dielectric metamaterial with  $\epsilon_r = 5$  and  $\mu_r = 5$  was used to improve the performance. Since the refraction index still is 5, the antenna with the same size as before can resonate at 1.56 GHz. However, since air and substrate have same intrinsic impedance, only a small portion of EM is trapped in the magneto-dielectric material and the bandwidth is enhanced to 7.94 percent and antenna's efficiency increased to about 99 percent.

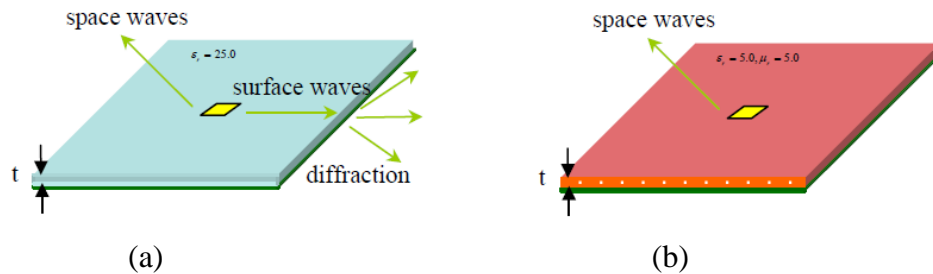


Figure 5.23. Rectangular patch antenna. (a) dielectric substrate, (b) magneto-dielectric substrate [92].

### 5.3. SUMMARY ON MINIATURIZED WIDEBAND ANTENNAS

Today's wireless communication systems demand not only a compact antenna but also an antenna which can cover a wide bandwidth. An antenna with wide bandwidth is sometimes referred to as broadband antenna [111]. The term “broadband” is relative of course. Up to now, it was assumed that the bandwidth is a certain percentage of the center frequency ( $BW_p$ ) and is defined as [111]:

$$BW_p = \frac{f_U - f_L}{f_C} \times 100\%, \quad (92)$$

where  $f_U$ ,  $f_L$ , and  $f_c$  are the upper, lower, and center frequency of operation, respectively. Now, it is worth mentioning that there is another way to express the bandwidth of an antenna as the ratio of the upper to the lower frequencies as [111]:

$$BW_r = \frac{f_U}{f_L}. \quad (93)$$

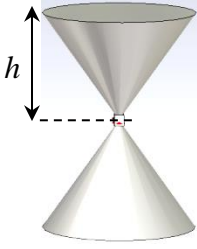
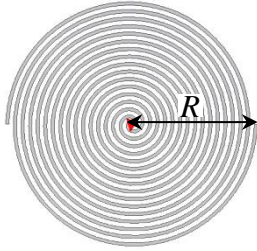
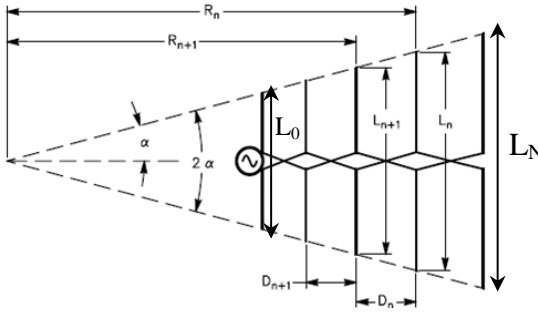
The bandwidth of a narrow band antenna (e.g., a resonant antenna) is usually expressed as a percentage using (92) while for a broadband or ultra wideband antenna (e.g., a traveling wave antenna), (93) is preferred. Based on a conventional definition which is provided in [111], “*if the impedance and the pattern of an antenna do not change significantly over about an octave ( $BW_r=2$ ) or more, the antenna is classified as broadband antenna*”.

Based on the conventional definition, helix, finite bicone, discone, and sleeve dipole antennas can be categorized as broadband antenna [111],[52]. Moreover, in some literatures (e.g., [111]), another definition is used to distinguish between antennas with  $BW_r$  higher than 10. Based on the definition provided in [111], “an antenna with a bandwidth of about 10:1 or more is referred as a ***frequency-independent antenna***”. Infinite biconical, equiangular spiral, Archimedean spiral, conical equiangular spiral, and log-periodic antennas belong to this category [111]. A self-scaling behavior is the most distinguishing feature of these antennas [111]. In fact, the wideband behavior (either broadband or frequency-independent) can be achieved if the antenna (1) emphasizes on angles rather than lengths (e.g., helix and spiral); (2) has self-complementary structures (e.g., equiangular spiral); (3) has thick metal (fatter is better) (e.g., bow-tie antenna or biconical antenna are two ultimate fat dipoles) [111].

Although the broadband or frequency-independent antennas can cover enough operating frequency bandwidth for many applications, but, they all suffer from size/bulkiness problem. To show this problem, three different antennas from the broadband category, namely; finite biconical antenna, spiral antenna, and log-periodic dipole array (LPDA) antenna were selected and studied. The required dimensions for these antennas to operate in a certain bandwidth from  $f_L$  to  $f_U$  (equivalently  $\lambda_U$  to  $\lambda_L$ ) are

compared in Table 5.1. More specifically, the dimensions of these antennas were calculated and listed in the fourth row of table for  $f_L = 50$  MHz in very high frequency (VHF) band. As the table shows, these antennas are not size efficient and their size will be too big and bulky if the lower frequency extends to VHF bands. To address the size issue, miniaturized broadband/ultra wideband antenna topic has been studied in recent years. Most of these techniques try to apply miniaturization approaches on wideband antennas to reduce their size. In the following a review of miniaturized/compact broadband antenna designs will be provided.

Table 5.1. Comparing sizes of three different classical broadband antennas to cover a bandwidth from  $\lambda_U$  to  $\lambda_L$  (moreover, size for  $f_L=50$  MHz is listed in fourth row)

Finite biconical	Spiral	LPDA
		
$h = \frac{\lambda_L}{4}$	$R_s = \frac{\lambda_L}{2\pi}$	$L_N = \frac{\lambda_L}{2} \quad ; \quad L_0 = \frac{\lambda_U}{2}$
$h = 150 \text{ cm}$	$R_s = 95 \text{ cm}$	$L_N = 300 \text{ cm}$

**5.3.1. Miniaturization of LPDA Antenna Using Fractal Tree.** Table 5.1 shows that by decreasing the frequency, LPDA antenna size grows and it becomes too big for low frequencies (e.g., 50 MHz). To address this problem, in [112], fractal geometry was applied to LPDA and the final antenna is referred as fractal tree LPDA. In this antenna, printed rectangular arms of LPDA were replaced with fractal tree structure in order to reduce overall size of the antenna (Fig. 5.24). A size reduction of about 61% in lateral size of the proposed antenna is reported in [112] while keeping designed antenna radiation characteristics and bandwidth approximately constant. This antenna has VSWR of less than 2 from 0.4-2 GHz (Fig. 5.25).

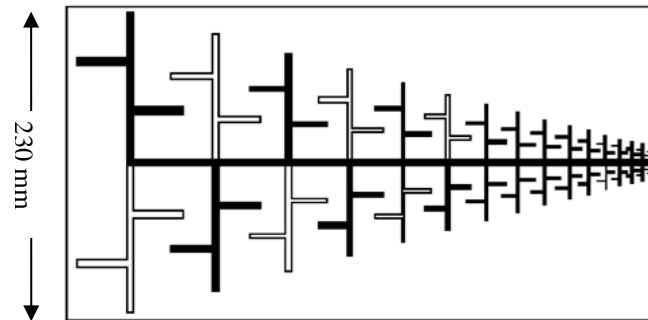


Figure 5.24. Fractal tree log-periodic dipole antenna [112].

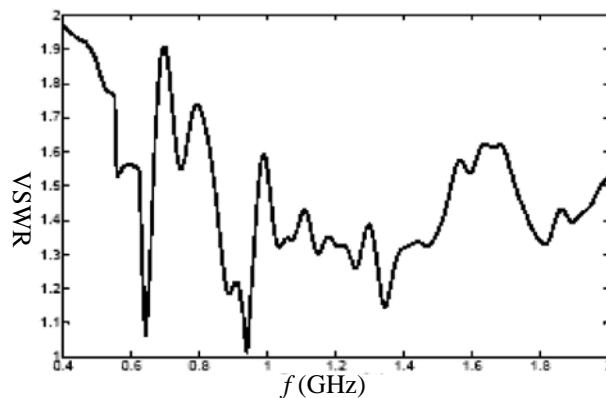


Figure 5.25. VSWR of the fractal tree log periodic dipole antenna [112].

One disadvantage of the antenna is its low gain particularly at lower frequencies which is approximately 2 dB. To increase the gain of this antenna, [113] improved radiating element by adding cap to the end of tree branches (Fig. 5.26). Overall size is same as before but gain value is improved (Fig. 5.27).

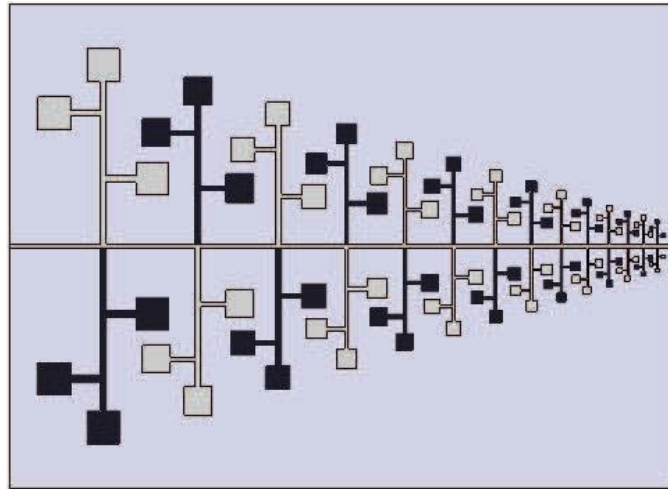


Figure 5.26. Configuration of improved fractal tree LPDA [113].

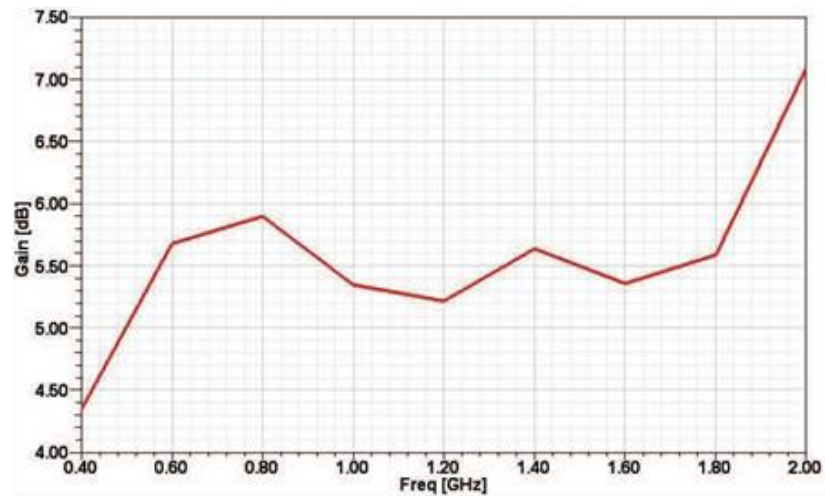


Figure 5.27. The gain of improved fractal tree LPDA [113].

**5.3.2. Meander Wide Band Antennas.** meandering technique, as mentioned in Section 5.2.1.4, aims to fill space and bend long straight lines in order to occupy smaller lengths. Application of this idea on wideband antennas, for size reduction, has been promising with only a small effect on antenna parameters. In [114], a meandered arm method is introduced to miniaturize Archimedean spiral antennas (Fig. 5.28). The outer radius of the meandered Archimedean spiral antenna is 70 mm (12.8% less than the classic (conventional) Archimedean spiral antenna), and it operates from 0.8 GHz to 4 GHz while the classical Archimedean spiral antenna operates only from 0.8 GHz to 2.3 GHz (Fig. 5.29). A simple calculation shows that for  $f_L=50$  MHz, the antenna radius should be 112 cm.

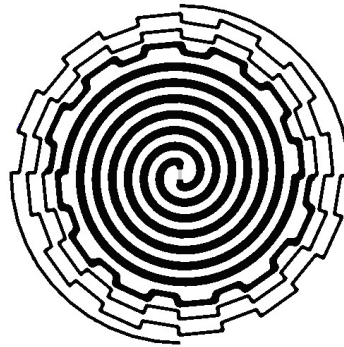


Figure 5.28. Optimized meander Archimedean spiral antenna [114].

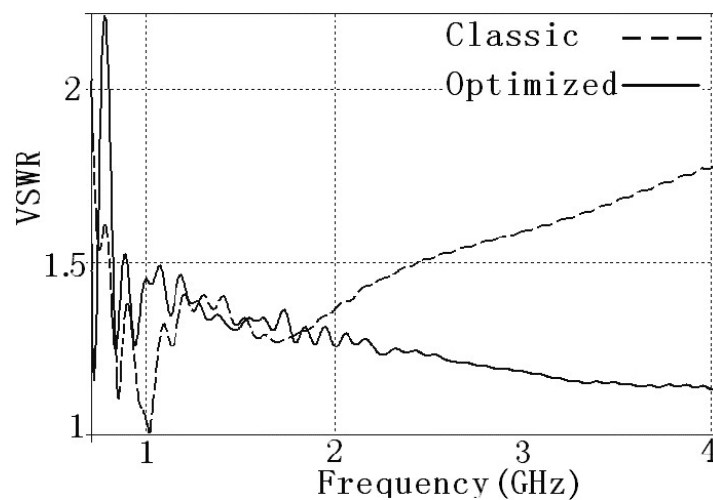


Figure 5.29. VSWR of meander Archimedean spiral antenna and classic one [114].

In [115], lowest frequency of operation of a compact dual-linear polarization tapered antenna was further reduced by tapering the inductive arms (i.e., replacing straight arms with zigzag arms). The diameter and height of the antenna are 38.1 cm and 15.24 cm, respectively (Fig. 5.30). The reported measured reflection coefficient for the antenna is shown in Fig. 5.31. The antenna operates with a minimum realized gain of -15 dBi from 100 MHz to 2000 MHz. If the operating frequency of the antenna was to start from 50 MHz, its dimensions could be as big as 76.2 cm (diameter) and 30.48 cm (height). As another disadvantage, this antenna is volumetric and bulky.

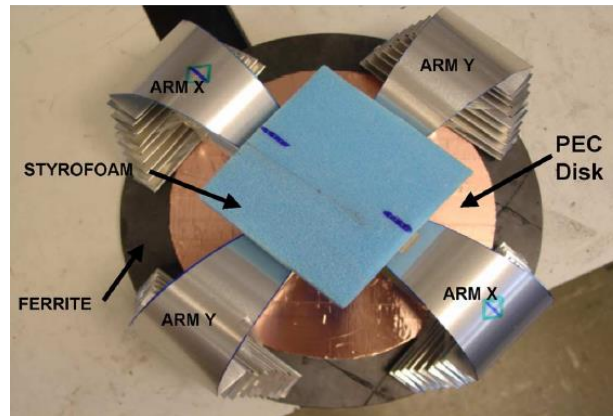


Figure 5.30. UWB tapered horn antenna with zigzag arms to improve performance at low frequencies [115].

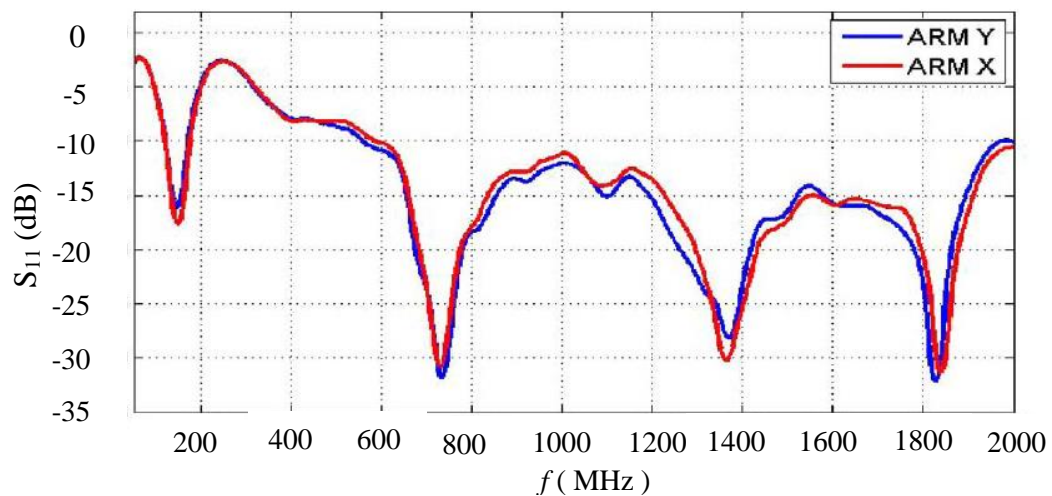


Figure 5.31. Measured  $S_{11}$  of the fabricated horn antenna with zigzag arms [115].



**5.3.3. Corrugation.** Corrugation technique has been used to improve antenna characteristics such as directivity, radiation efficiency and bandwidth [116]-[117]. This technique is also useful for antenna size reduction applications. In [118], an omnidirectional UWB antenna was miniaturized by applying corrugation to its radiator and ground plane. First an UWB antenna was designed (Fig. 5.32) and then parts of the outer structure were trimmed and removed. The resulted trimmed antenna has smaller dimension (Fig. 5.32 (b)) in comparison with the original antenna (Fig. 5.32 (a)). This trimming action will cause antenna matching problems (Fig. 5. 33). To overcome this, [118] proposed radiator and ground plane corrugation (Fig. 5.32 (c)). Corrugation helped to reduce lower end frequency (Fig. 5.33). The surface area of the antenna was reduced from  $18\text{ mm} \times 19.5\text{ mm}$  (Fig. 5.32 (a)) to  $10.4\text{ mm} \times 16\text{ mm}$  (Fig. 5.32 (c)) which is about a %50 size reduction. Moreover, the miniaturized antenna size, normalized to the wavelength at lowest frequency (i.e.,  $\sim \lambda_L = 30/3 = 10\text{ cm}$ ), is  $0.104\lambda_L \times 0.16\lambda_L$ . Therefore, the size of this antenna for  $f_L = 50\text{ MHz}$  could be as small as  $0.6\text{ m} \times 0.96\text{ m}$ .

Although the introduced miniaturization techniques could help reducing the size of wideband antennas, the overall size becomes very large when the operating frequency decreases (e.g., VHF band).

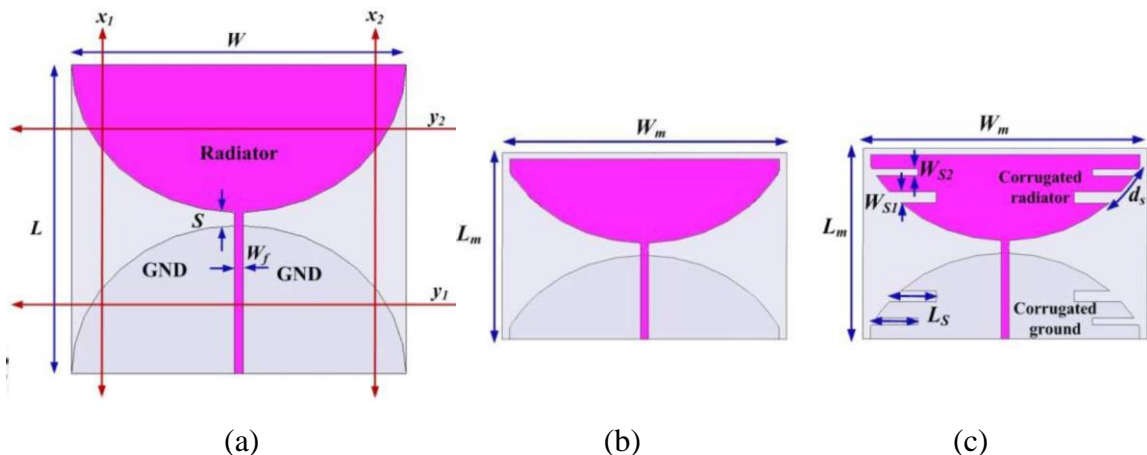


Figure 5.32. The introduced UWB antenna in [118]. (a) before minimization, (b) after trimming, (c) final (trimmed and corrugated).

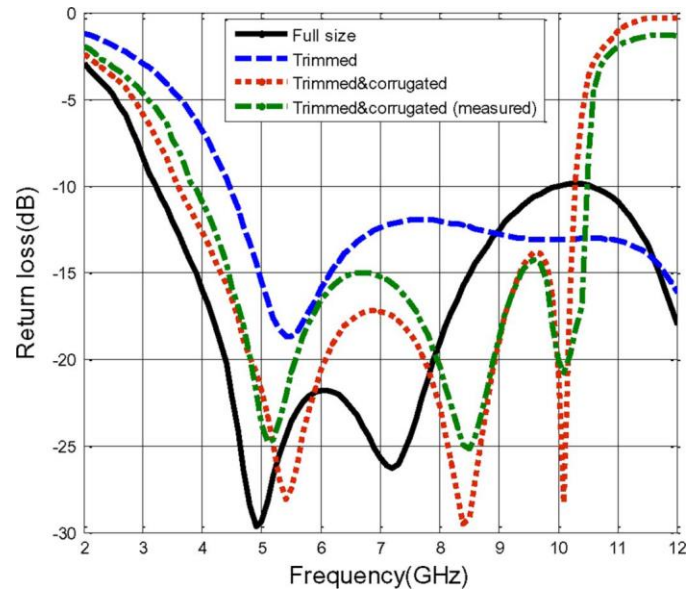


Figure 5.33. Return loss for different configurations shown in Fig. 5.30 [118].

On the other hand, in many applications not all of the designed bandwidth is utilized, and only a pre-selected discrete set of frequencies and their associated bandwidths are used. These discrete frequencies may be distributed over a wide range. Therefore, an alternative to wideband antennas is one that is designed to operate over these distinct frequencies rather than the entire bandwidth. Consequently, reconfigurable antenna and multiband antenna concepts were introduced to address this issue. However, the noise and interference issues become critical for multiband antennas when the number of desired bands and the overall covered frequency range increases. However, reconfigurable antennas are capable of operating at one frequency band at a time and hence alleviating this problem. To demonstrate the advantages of reconfigurable antennas over multiband antennas, an example is provided in [25]. In this example, a global positioning system (GPS) receiver was subjected to a jamming signal. Then, two setups were considered. In the first step, the receiver was connected to a multiband antenna which simultaneously covers GPS and 2.4 GHz WLAN band. However, in the second setup, the receiver was connected to a frequency reconfigurable antenna which supports either the GPS or the WLAN services at any given time based on the reconfiguration. The antennas had identical gain and their received signals were guided through same GPS front-end (e.g., same stringent filtering). So, the resulting carrier-to-noise ratios (C/Ns) of

the received GPS in both setups were expected to be the same. Later, a signal generator connected to a horn antenna operating at 2.4 GHz with the power of 20 dBm was used to emulate the WLAN radio. The performance of the second setup with the reconfigurable antenna in terms of C/Ns did not show any pronounced degradation while a drop of over 8 dB C/N was measured for the multiband antenna (Fig. 5.34) [25]. This example clearly demonstrates the poor out-of-band rejection characteristics of the multiband antenna in comparison with the reconfigurable antenna.

This work is focused on reconfigurable antennas and in the following, a brief review of currently-available reconfigurable antennas will be provided and limitations and capabilities of each one will be discussed.

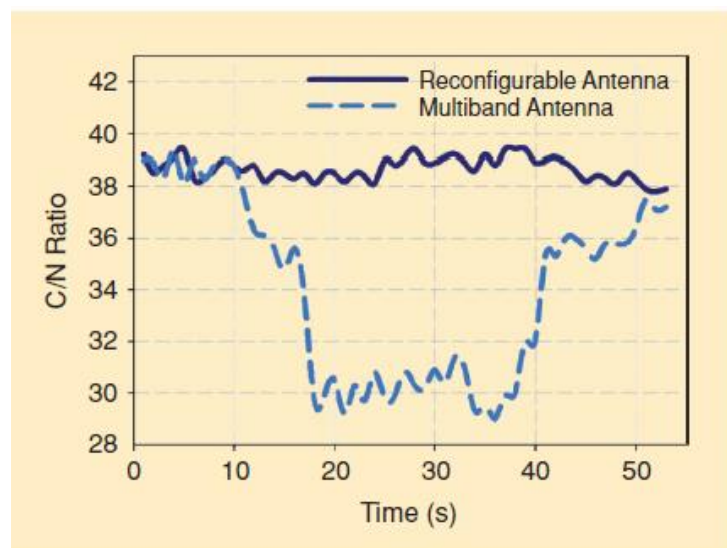


Figure 5.34. Carrier-to-noise ratios for a GPS module connected to multiband and reconfigurable antennas with a 2.4 GHz jamming signal injected for a limited time [25].

#### 5.4. RECONFIGURABLE ANTENNAS

Term “to reconfigure” means to rearrange/reorganize important properties of something in order to achieve a desired goal [119]. For instance and as it relates to patch antenna design, patch shape, substrate parameters (e.g., material and thickness), type and

location of the feed are essential to configure a microstrip antenna in order to satisfy a desired characteristic. Then, if the desired characteristic of the antenna change, the antenna should be reconfigured to satisfy new specifications [119]. From a practical point-of-view, a reconfigurable patch antenna has the ability to change its electrical characteristics by altering the current density on the patch. Changing the current density can be accomplished using mechanically movable components, electronic switches (e.g. PIN diode, MEMS, FET), phase shifters, attenuators, tunable materials, or active materials [119]. A reconfigurable antenna can be a single antenna or it can be made of an array of antennas. Reconfigurable antennas may be classified based on functionality as: frequency reconfigurable (where operating frequency changes), radiation pattern reconfigurable (where the direction of maximum radiation changes), polarization reconfigurable (where polarization changes), or a combination of these classes.

In the following, a brief review of currently-available reconfigurable antennas will be provided. These antennas are distinguished based on the applied technology to change the configuration of the antenna.

**5.4.1. Reconfigurable Antenna Based on Different Switch Technologies.** By changing the current (either magnetic or electric) distribution on antenna structure, its electrical and radiation characteristics can be changed. When this is done intelligently, then one obtains a desired radiation characteristic. To change the current distribution, switches may be used.

An ideal switch acts as an open circuit when there is no actuation (e.g., voltage) applied and a short circuit when an actuation (e.g., voltage) is applied. However, practically, switches usually show a resistive behavior when they are ON and some capacitive behavior when they are OFF. Some important characteristics of a switch which can affect its performance may be listed as [119]:

- 1) Characteristic impedance: shows how well the switch is matched to a line,
- 2) Bandwidth: some switches are low pass and some others are band pass filters,
- 3) Insertion loss and isolation: is defined as the ratio between the output and input powers when the switch is ON and OFF,
- 4) Switching speed: indicates how quickly a switch can change its state from ON to OFF after the control pulse reaches 50% of its level,

- 5) Expected life time: is the measure of the number of switch activations until switch fails,
- 6) Power handling: indicates how much passing signal power can be handled by the switch.

Different switch technologies have been developed in past decades such as: electromagnetic switches (e.g., reed switch), semiconductor switches (e.g., optical, FET and PIN diode), and Microelectromechanical system (MEMS) switches, to name a few. Among these switch design technologies, PIN diode, FET family, and MEMS have attracted the highest attention for being used for reconfigurable antenna applications. In Table 5.2, a comparison between PIN diode, FET, and MEMS switches are provided. As the table shows, MEMS switches, as an advantage over PIN diode and FET switches, have the highest isolation and lowest insertion loss. However, MEMS requires a high actuation voltage and its switching time is long. On the other hand, PIN diode and FET switches are relatively easier to be implemented on a PCB board.

Next, the application of these switches (i.e., MEMS, FET, PIN diode, and reed) for reconfigurable antennas design is shown in term of a few examples.

In [122], a reconfigurable ground-slotted patch antenna is introduced which uses PIN diode-loaded slots on the ground plane in order to achieve dual-frequency operation (Fig. 5.35). When the PIN diodes are OFF, the presence of slots in the ground plane increases the electrical length of the antenna (because the return current should turn around the slots). Therefore, the antenna operates at the lower desired band (i.e., 1.75-1.87 GHz). However, by turning ON the PIN diodes, the slots are shorted and removed from the return current path (current can use the PIN diode pass as a shortcut instead of truing around the slots). Therefore, the electrical length of the ground plane decreases and the antenna operates at higher frequency band (i.e., 2.3-2.4 GHz).

Table 5.2. A comparison of PIN diode, FET, and MEMS switches [119]-[121]

Parameter	PIN diode	FET	RF MEMS
Voltage (V)	$\pm 3-5$	3-5	20-80
Current (mA)	3-20	0	0
Consumption (mW)	5-100	0.05-0.1	0.05-0.1
Isolation (1-10 GHz)	High	Medium	Very High
Isolation (10-40 GHz)	Medium	Low	Very High
Isolation (40-60 GHz)	Medium	N/A	High
Insertion Loss (1-100 GHz) dB	0.3-1.2	0.4-2.5	0.05-0.2
Lower frequency limit	DC	DC	DC
Typical ON resistance	1.7 ohm	1.5 m-ohm	1.5 m-ohm
Typical OFF capacitance	0.05 pF	0.4 pF/mm	2-4 fF
Switching time	1-100 ns	1-100 ns	1-300 $\mu$ s

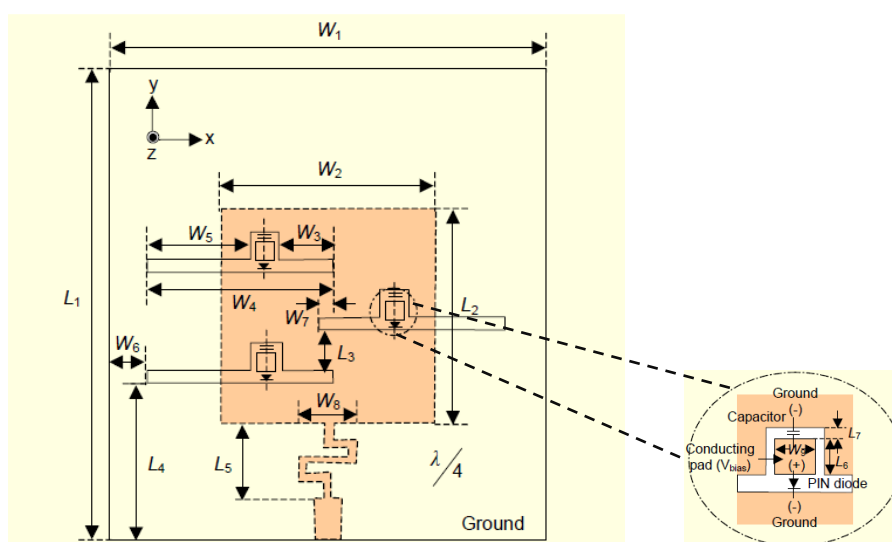


Figure 5.35. Reconfigurable ground-slotted patch antenna loaded with PIN diode switches [122].

In [123], instead of carving the slots on the ground plane, the radiating patch itself is loaded with slots while slots are controlled by PIN diode to switch between right-hand circular polarization (RHCP) and left-hand circular polarization (LHCP) (Fig. 5.36).

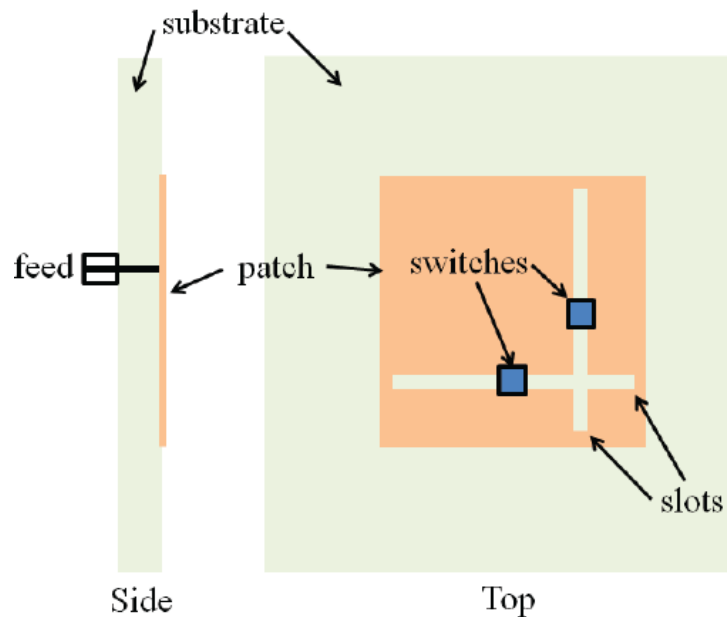


Figure 5.36. Polarization reconfigurable PIN diode-loaded slotted-patch antenna [119],[123].

Since the late 1990s, MEMS technology has been used to add reconfigurability to antennas [119], [124]. In [125], two UWB coplanar waveguide-fed elliptical patch monopoles with a reconfigurable band notch in the WLAN frequency range (5.15-5.825 GHz) are introduced. In the first antenna, a U-shaped slot was embedded on the elliptical patch and it was loaded with MEMS (Fig. 5.37). The U-shaped slot is approximately  $\lambda/2$  (where  $\lambda = 5.17$  cm) long and it resonates at 5.8 GHz if the MEMS is open. When the slot resonates, the currents in the inner and outer side of the slot flow in opposite directions and cancel out each other. This contributes to a notch in the operating frequency of the UWB elliptical patch antenna. However, if the MEMS switch is closed, the length of the slot is cut in half. Therefore, the slot no longer resonates at 5.8 GHz and its existence does not affect the performance of the antenna.

In the second case, two symmetrically placed inverted-L shaped open stubs were connected to the elliptical patch using MEMS switches (Fig. 5.37 (b)). By closing the MEMS switches, a current will flow on the inverted-L shaped stubs at the resonant frequency (when the stub length is  $\lambda/4$ ). This current will cancel out the current flowing on the nearby edge of the elliptical patch and so, the radiated fields cancel each other and a notch will be introduced in the frequency response. However, when the MEMS switches are open, the antenna operates over the whole UWB range (i.e., 3.1-10.6 GHz).

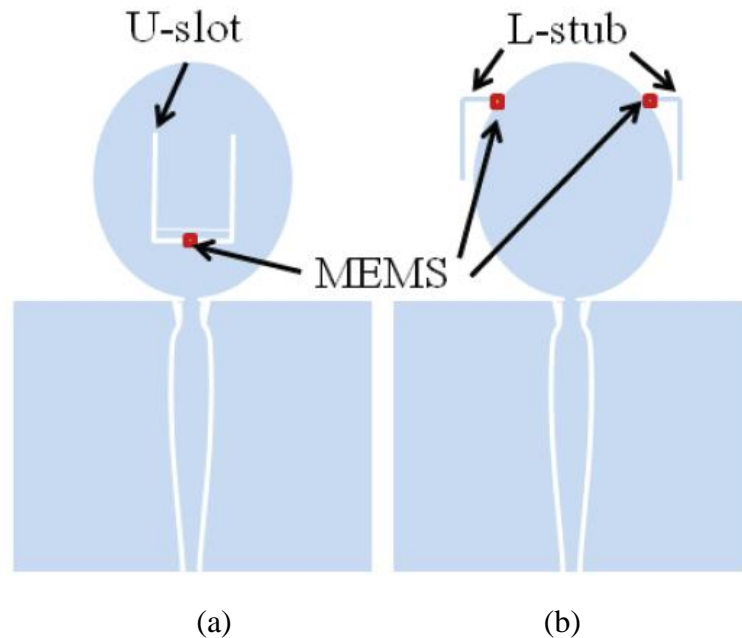


Figure 5.37. Reconfigurable UWB antenna using MEMS [119],[125].

In [126], reed switch is used to add reconfigurability to patch antenna. The reed switch was invented in Bell Telephone Laboratories in 1936 and it can be controlled by a magnetic field generated by a coil (Fig. 5.38) [126]. Since the reed switch does not require placing DC bias and control lines in the immediate vicinity of the radiating element, its impact on the antenna characteristics (e.g., radiation pattern) may be small.



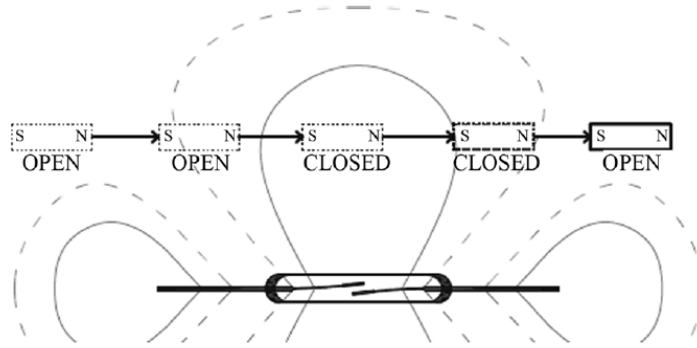


Figure 5.38. Open/closure domains for Reed switch in the switch plane [126].

The prototype hexagonal patch antenna with reed switch is shown in Fig. 5.39. The antenna operates at  $\sim 2.4$  GHz when the switch is OFF and at  $\sim 1.9$  GHz when the switch turns ON and adds an extra metallic section to the hexagonal patch.

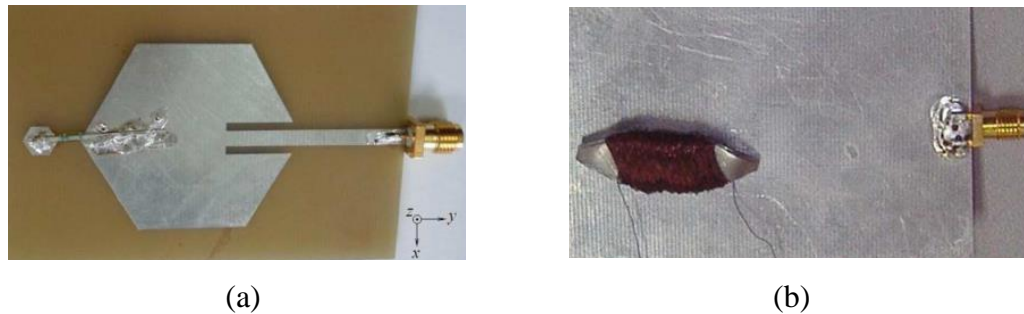


Figure 5.39. Prototype reconfigurable hexagonal patch antenna with reed switch. (a) top view, (b) bottom view [126].

**5.4.2. Reconfigurable Antenna Design Using Varactor Diode.** A varactor diode acts like a capacitor when it is inverse biased. The amount of the capacitance is inversely proportional to the square root of the applied voltage [119]. A variable capacitor can be useful for loading an antenna and changing its resonant frequency. Thereby, varactors have found a vast application for tuning the antenna frequency response. In [27], a slot antenna is loaded with a varactor at a certain location along the slot to achieve dual-band frequency response (Fig. 5.40). For a fixed location of the varactor, increasing the

applied voltage on the varactor and so decreasing the capacitor results in increasing the first and second resonance frequencies of the slot antenna. However, since the first and second resonance frequencies change unequally, a dual-band antenna with 1.2-1.65 frequency ratio tuning range (i.e., center frequency of higher band/center frequency of lower band) could be obtained. The capacitance range of the varactor was 0.5-2.2 pF.

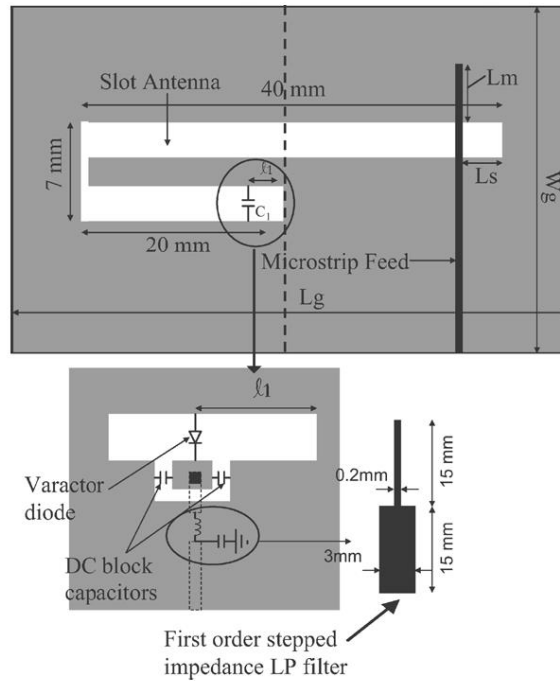


Figure 5.40. Reconfigurable dual-band slot antenna using varactor loading [27].

In [127], a varactor diode tuned elliptical slot antenna at K-band (18-26.5 GHz) is introduced (Fig. 5.41). Commercially available GaAs constant gamma flip-chip varactor diode MA46H120 was used to tune an optimally designed elliptical slot antenna. In order to test the antenna, it was installed on a rectangular waveguide and the reflection coefficient of the antenna was measured. This antenna was then successfully used to produce single-frequency and wideband multi-frequency synthetic aperture radar-based images of sample under test.

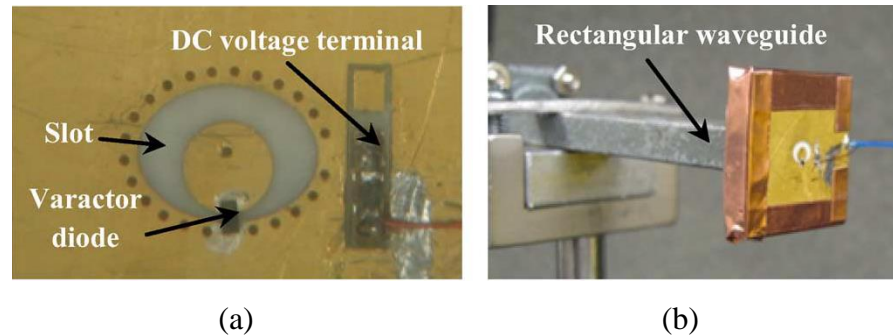


Figure 5.41. The varactor diode-loaded resonant elliptical slot antenna. (a) closed-up view, (b) testing setup using rectangular waveguide [127].

**5.4.3. Reconfigurable Antenna Using Tunable Materials.** New technologies have introduced new materials with tunable electrical, magnetic, and mechanical properties. The application of these tunable materials into antenna realm may help to add reconfigurability to the antenna characteristics [119].

As an example, conductivity of a semiconductor material (e.g., silicon) can be altered by changing temperature, DC bias, or light [119]. The tunable conductivity of the semiconductor can be benefited for reconfigurable antenna design. In [128]-[129], a patch antenna is modified by adding a thin strip of silicon and a thin metal extension on the right edge (Fig. 5.42). An infrared source is embedded below the silicon strip and based on the provided infrared radiation, the conductivity of the silicon changes (Fig. 5.42 (b)). The patch resonates at 2 GHz when the illumination is off. By increasing the illumination, the conductivity of silicon increases to 1000 S/m which causes the patch to resonate at 1.78 GHz.

In [130], tunable permeability ferrite is used to achieve a tunable coaxial-fed microstrip antenna. The microstrip antenna is built on ferrite substrate (i.e., Trans-Tech G-113 YIG) with operating frequency of 4.6 GHz. Then, a DC magnetic bias field is applied to the ferrite substrate to change its permeability and achieve bandwidth tuning of 40%.

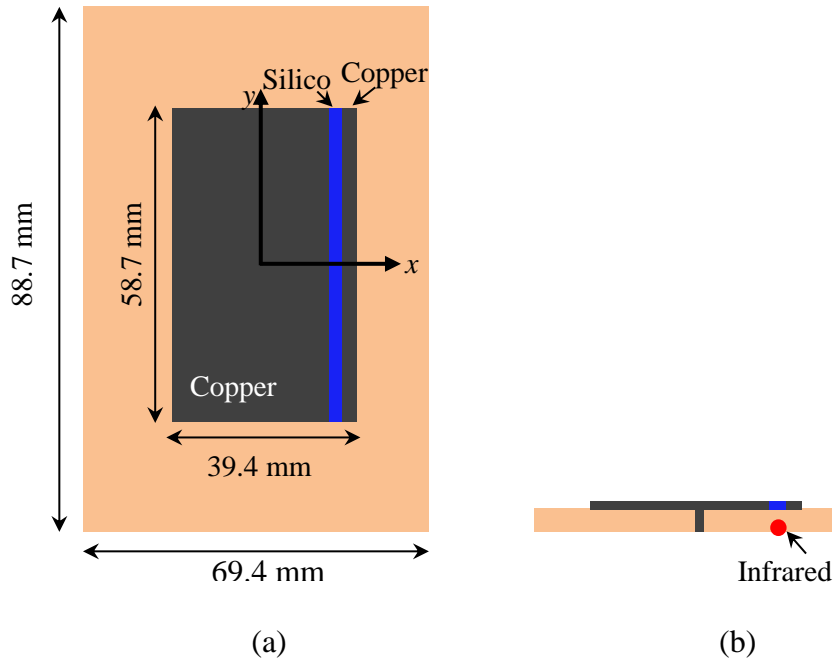


Figure 5.42. Reconfigurable patch antenna using tunable conductivity silicon [128]-[129].

## 5.5. CONCLUSION

In this section, an overview on currently available miniaturized antenna design methods was provided. The miniaturization techniques can be classified as topology-based and material-based miniaturization methods. For the first class (i.e., topology-based methods), fractal, reactively loaded, engineered ground plane, and meander antennas were discussed. In the second class, planar antennas with high dielectric constant substrates and antennas using metamaterial were discussed. Table 5.3 summarizes these techniques and compare them based on size, frequency response and gain. For size comparison, for each method, the smallest reported dimensions were normalized to the longest operating wavelength in free-space (i.e.,  $\lambda_0$ ).

As one disadvantage, the bandwidth of most of these miniaturized antennas is narrow. To address narrow bandwidth problem, later, miniaturization techniques for wideband antennas were discussed. A few miniaturized wideband antennas such as: LPDA with fractal tree, meandered Archimedian antenna, tapered horn with zigzag arms, and corrugated antennas were discussed.

Table 5.3. Comparison of miniaturized antenna design techniques

Technique	Typical Size	Frequency Response	Typical Gain
Fractal	$(0.23 \times 0.23)\lambda_0$	Multi/wide-band	Reasonable
Reactive loaded	$(0.013 \times 0.018)\lambda_0$	Very Narrow-band	Low
Engineered ground-plane	$\sim (0.3 \times 0.3)\lambda_0$	Multi-band	Reasonable
Meandering	$(0.035 \times 0.086)\lambda_0$	Narrow-band	Reasonable
High dielectric constant substrate	$(0.016 \times 0.016)\lambda_0$	Narrow-band	Very low
Metamaterial	$(0.26 \times 0.26)\lambda_0$	Narrow-band	Reasonable

It was shown that the size of the miniaturized wideband antennas still can be so big for the antenna to operate at low frequency bands (e.g., VHF). On the other hand, larger the bandwidth is, more significant the noise, and interference issues can be. Moreover, in many applications, a wide continuous frequency range is not required and, instead, distributed discreet bands over the wide range may be sufficient. Therefore, multiband or reconfigurable antennas may show a better performance in comparison with wideband antennas. However, it was shown that the reconfigurable antenna has superior performance over multiband antenna in term of immunity to noise and interference. Then, it was shown that a reconfigurable antenna may be achieved using switch (e.g., PIN diode or MEMS), varactor, or tunable materials. Then, a few examples were provided for each of these techniques. Despite this fact that there are many recently published literatures discussing reconfigurable antennas, but, most of them only introduce a specific prototype antenna which is designed for a specific application. Actually, there is a lack of methodical design procedure for reconfigurable antennas. This was the motivation to seek a methodical design procedure to design reconfigurable antennas which will be introduced in next section.

## **6. DESIGN AND IMPLEMENTATION OF RECONFIGURABLE ANTENNAS**

### **6.1. INTRODUCTION**

Based on the provided discussion in Section 5, reconfigurable antennas have shown great potential for use in many applications including microwave imaging and multiradio/multifunction communication devices. There are different ways to incorporate reconfigurability into an antenna. Among these, using switches to add reconfigurability to the antenna has been collected the highest interest. Despite of this fact, there is not a methodical and organized method for designing reconfigurable antennas using switch technology and most of the reported works have been devoted to specific prototype antennas.

Therefore, in this section, a methodical approach to designing a reconfigurable antenna for operating at several pre-selected frequency bands will be introduced. Then, the design of such a prototype compact reconfigurable antenna will be presented. In the initial design only three frequency bands will be considered. Later, using miniaturization techniques another operating band is added at a lower frequency (at ~100 MHz). As an important aspect of this design, the goal is to reduce the operating frequency associated with the lowest operating band. Consequently by implementing several ideas it will be shown how this frequency can be moved to below 100 MHz (to ~60 MHz). Full-wave simulations, implementation of the antenna and the measurement results will be provided for each design in this comprehensive process.

### **6.2. APPROACH AND METHODOLOGY FOR DESIGNING RECONFIGURABLE ANTENNAS**

In general, defining goals, requirements, and constraints is considered as first step in antenna design and implementation procedure. These goals, requirements, and constraints may include desired antenna characteristics, physical sizes, mechanical and manufacturing constraints, etc. In second step, an initial appropriate antenna type should be selected [52], [111], [131]. For regular static (i.e., non-reconfigurable) antennas with fixed electrical and geometrical characteristics, the design procedure is usually straightforward. In this case, the antenna type may be selected based on the requirements.

For instance, a microstrip antenna is a good choice if the requirements dictate that the antennas should be narrowband, have linear polarization, be compact and conform to a planar structure. However, by changing one of the requirements (e.g., bandwidth), the microstrip structure may no longer be the optimum choice. After selecting the antenna type, analytical or numerical design equations (e.g., [52], [111],) or full-wave numerical electromagnetic solvers such as CST Microwave Studio or HFSS [132] may be used to simulate the antenna characteristics. This is then followed by implementing the antenna and comparing its critical characteristics with those obtained by the simulations and ultimately with the design requirements. This design methodology for regular antennas is summarized in a flowchart and it is shown in Fig. 6.1.

Since the optimization is a necessary step for both regular and reconfigurable antennas, the optimization procedure is also presented in a flow-chart in Fig. 6.2. This optimization procedure is based on using a combination of full-wave software and an optimizer. The optimizer can be selected from deterministic class (e.g., conjugate gradient method) or from stochastic class (e.g., Particle Swarm Optimization (PSO), Genetic Algorithm (GA), Ant Colony Optimization (ACO)). The procedure defines the antenna parameters (e.g., dimensions or substrate material) as unknowns. It assumes an initial value for unknowns and then starts simulating antenna with initial guesses in the full-wave software. After the simulation is completed, the optimizer gives pertinent simulation results (e.g.,  $S_{11}$ ). Later, a cost or error function is formed based on the difference between the pre-defined goals and the simulation results. If the difference is larger than a pre-set criteria (threshold), then the optimizer uses its own algorithm to update the unknowns. Any optimizer has its own unique way of updating the parameters and thus each optimizer has its advantages and disadvantages. To benefit from advantages of more than one technique, a combination of these optimization techniques may also be used [133]. After updating the unknown parameters, the entire procedure is repeated until the cost (or error) function becomes less than the pre-set criteria. It should be noted that there are different ways to define cost function and the definition can affect the optimization speed and convergence [134]-[135]. Here, the utilized cost function is simply defined as the magnitude of the difference between the goal and the simulation

results. A flow-chart representation of the optimization procedure is presented in Fig. 6.2.

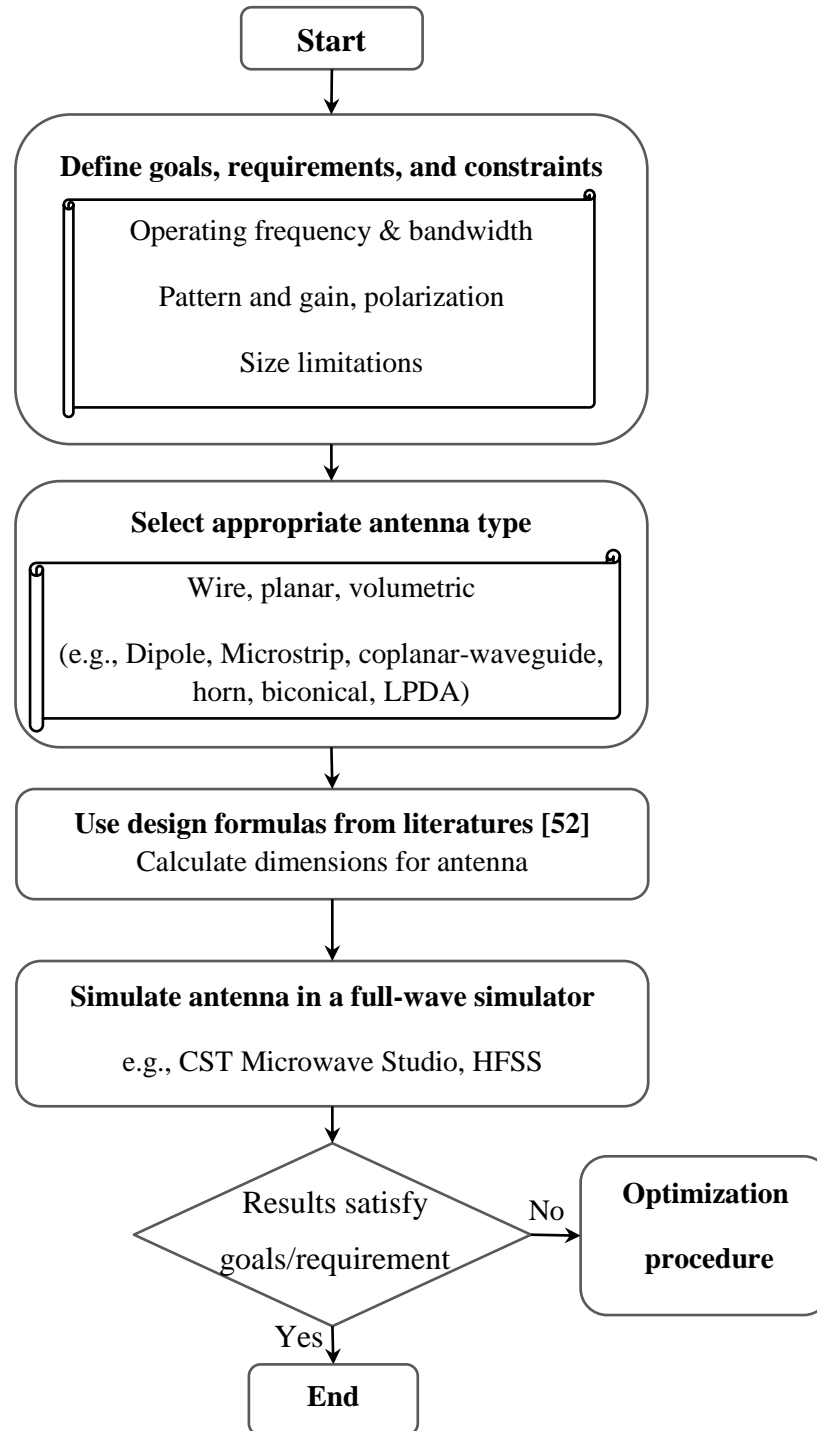


Figure 6.1. Flow-chart for designing a regular antenna.



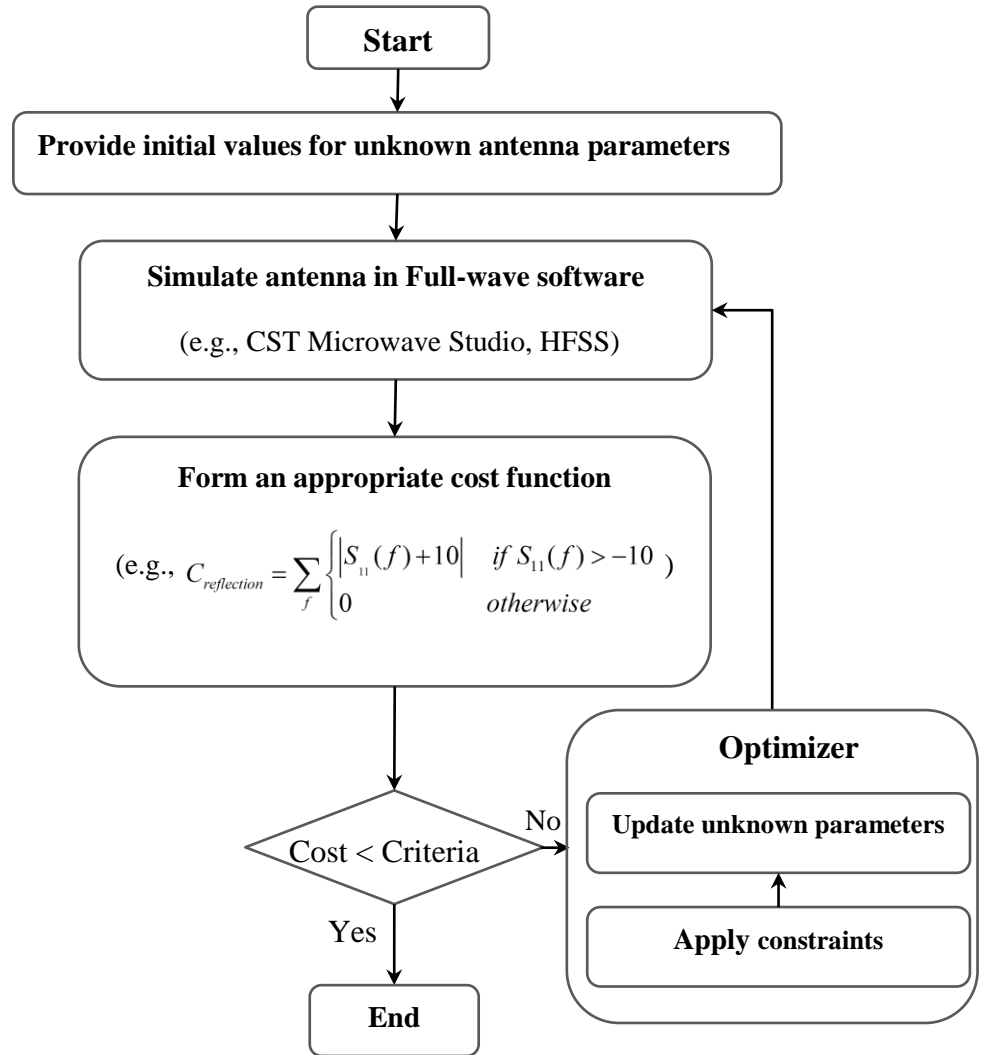


Figure 6.2. Flow-chart for optimization procedure which may be used in antenna design.

Designing a reconfigurable antenna whose characteristics may change is not as straightforward as a static antenna design procedure. To address this issue, a design methodology for frequency reconfigurable antennas is proposed in the following.

Similar to the regular antenna design procedure, one must define design objectives, requirements, and constraints as the initial step of the design procedure for reconfigurable antennas. In second step, a number of pre-selected frequency bands,  $N_B$ , should be sorted in an ascending order of operating frequency. It is more convenient to designate the bands from 1 to  $N_B$  where the band with the lowest center frequency is

designated to as Band 1 and the band with the highest center frequency is designated as Band  $N_B$ . Subsequently, the procedure begins by designing an antenna which covers the Band  $N_B$ . Similar to regular antenna design procedure, an appropriate antenna type should be selected and the design procedure should be followed to achieve an antenna that covers the highest band. Meanwhile, the antenna type should be selected in a way to provide sufficient flexibility for, as will be seen, required additional modifications. This is a critical issue for reconfigurable antenna design, making it distinguishable from regular antenna design. Antennas such as microstrip and coplanar waveguide provide a good flexibility for the designer to manipulate the ground plane or the signal path in order to change antenna characteristics. On the other hand, antennas like helix provide less flexibility. For future references, the designed antenna to cover Band  $N_B$  is called Antenna  $N_B$ . As the third step, Antenna  $N_B$  should be modified in an appropriate way to cover Band  $N_B-1$ . For a CPW-based antenna, this can be performed by adding slots to the ground plane. The slots can alter the current flow path and subsequently the desired characteristics of the antenna. By optimizing the location and dimension of such slots, the antenna “*may*” cover Band  $N_B-1$ . This antenna is called Antenna  $N_B-1$ . Then, the same procedure is used to design Antenna  $N_B-2$ ,  $N_B-3, \dots, 1$  to cover Band  $N_B-2$ ,  $N_B-3, \dots, 1$ , respectively. As an important design point, it should be possible to switch between characteristics of Antenna  $n_1$  and characteristics of Antenna  $n_2$  (where  $n_1$  and  $n_2 \in \{1, 2, \dots, N_B\}$ ) by a few short or open circuits. These shorts and opens can be electronically/mechanically realized using switches. The entire design procedure is summarized in the flow-chart shown in Fig. 6.3.

Addition of switches to change antenna characteristics makes it a reconfigurable antenna. Therefore, one reconfigurable antenna provides  $N_B$  different configurations and at each of these configurations (e.g., Configuration  $n_1$ ), it mimics the behavior of corresponding antenna (e.g., Antenna  $n_1$ ). However, since the Antenna  $n_1$  and Configuration  $n_1$  are not exactly the same, there is a possibility of a slight difference between their characteristics.

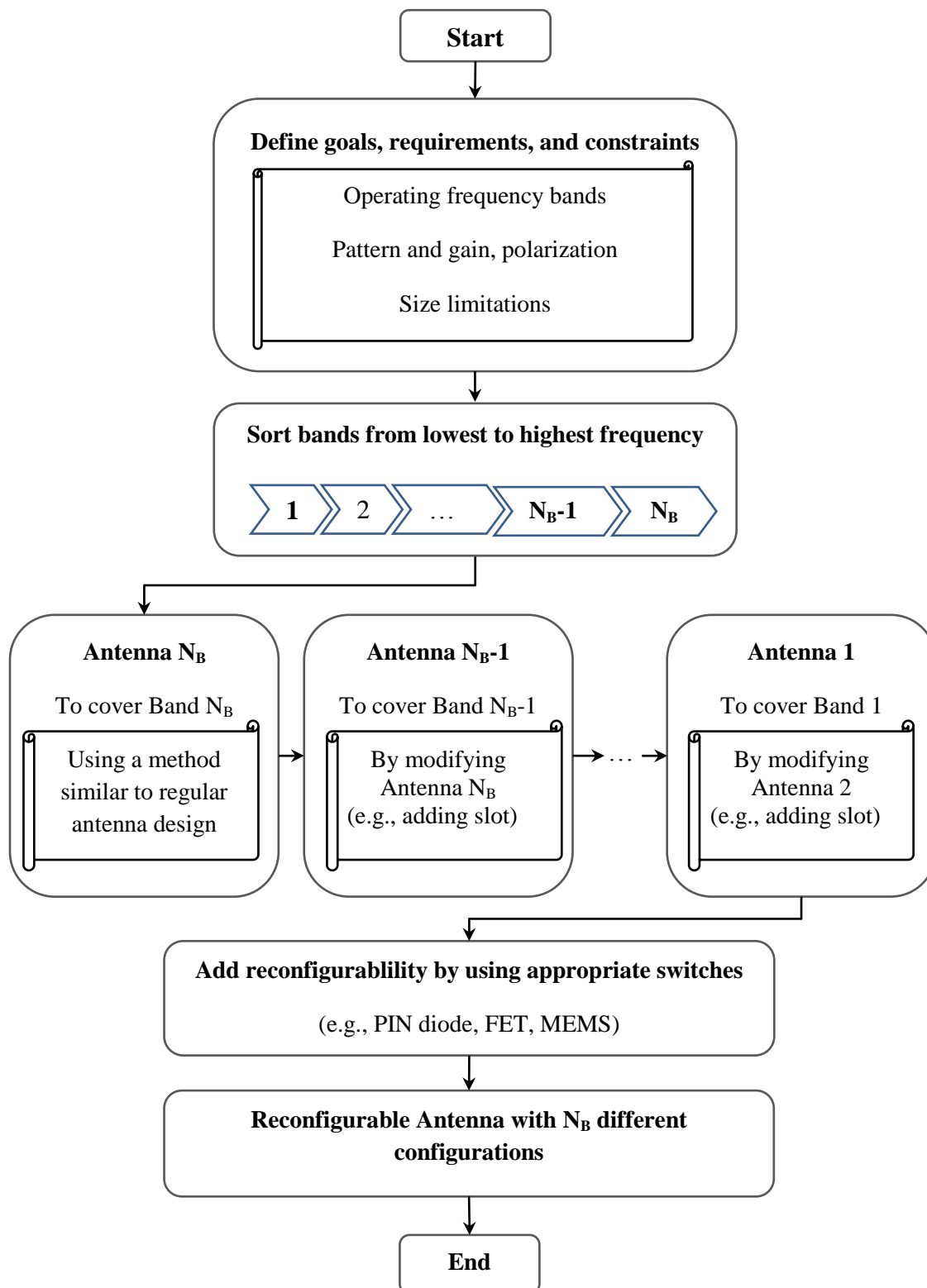


Figure 6.3. Flow-chart for designing a reconfigurable antenna using switching methodology.

To address this problem, the achieved reconfigurable antenna may be optimized by using optimization procedure. Since the individual Antennas 1 to  $N_B$  were optimized to achieve the goals, the characteristics of the reconfigurable antenna should not be far from the goals. Therefore, the optimization procedure should not take long time.

In the following, to verify the ability of the proposed reconfigurable antenna design method, a prototype reconfigurable multiband antenna is designed. Three different designed versions of the antenna will be discussed.

### **6.3. DESIGN AND IMPLEMENTATION OF A PROTOTYPE RECONFIGURABLE ANTENNA**

There are applications such as wireless sensor networking which require a compact and planar antenna to cover selected frequency bands in VHF, UHF, and L bands with a reasonable gain and a near-omnidirectional pattern. Since the required bandwidth of operation is wide, the size is limited, and the noise and interference also should be minimized, reconfigurable antenna as a good candidate may be used. For the design, the proposed procedure in Section 6.2.1 is used. The requirements (e.g., frequency bands) will be defined and the entire design, implementation, and measurement procedures will be explained.

#### **6.3.1. Design 1: Reconfigurable Antenna Covering Three Bands at UHF / L .**

As first design example, it is desired to have an antenna which can work at three bands at UHF/L frequency regions which include commercially licensed/united state public safety (PS) bands [136]. The first band is from  $\sim(300-320)$  MHz, second band is from  $\sim(390-490)$  MHz, and third band is from  $\sim(800-1200)$  MHz. It is desired for the antenna to have a reasonable gain at these bands (e.g., -5 to 0 dBi in lowest band and 3 to 5 dBi in highest band). Moreover, maximum dimension of the antenna is limited to  $20\text{cm}\times 20\text{cm}\times 5\text{cm}$ .

Before using the proposed reconfigurable antenna design method, many different antennas were considered and investigated. In the first attempt, a conventional bow-tie antenna [111] (Fig. 6.4) was manipulated in different ways to improve its bandwidth of operation (Fig. 6.4 (b)-(d)) and then it was decided to use switch addition idea to add reconfigurability to the best case (Fig. 6.4 (e)). It was determined that the designed

reconfigurable antenna could operate in the three different frequency bands but the bandwidth characteristics were not satisfactory (i.e., the bandwidth is less than desired). The other problem encountered was that the antenna size was in range of  $0.5\lambda$  (where  $\lambda$  is wavelength at the lowest operating frequency). This antenna dimension (which is  $\sim 50\text{cm} \times \sim 50\text{cm}$  at 300 MHz) is violating the maximum dimension constraint.

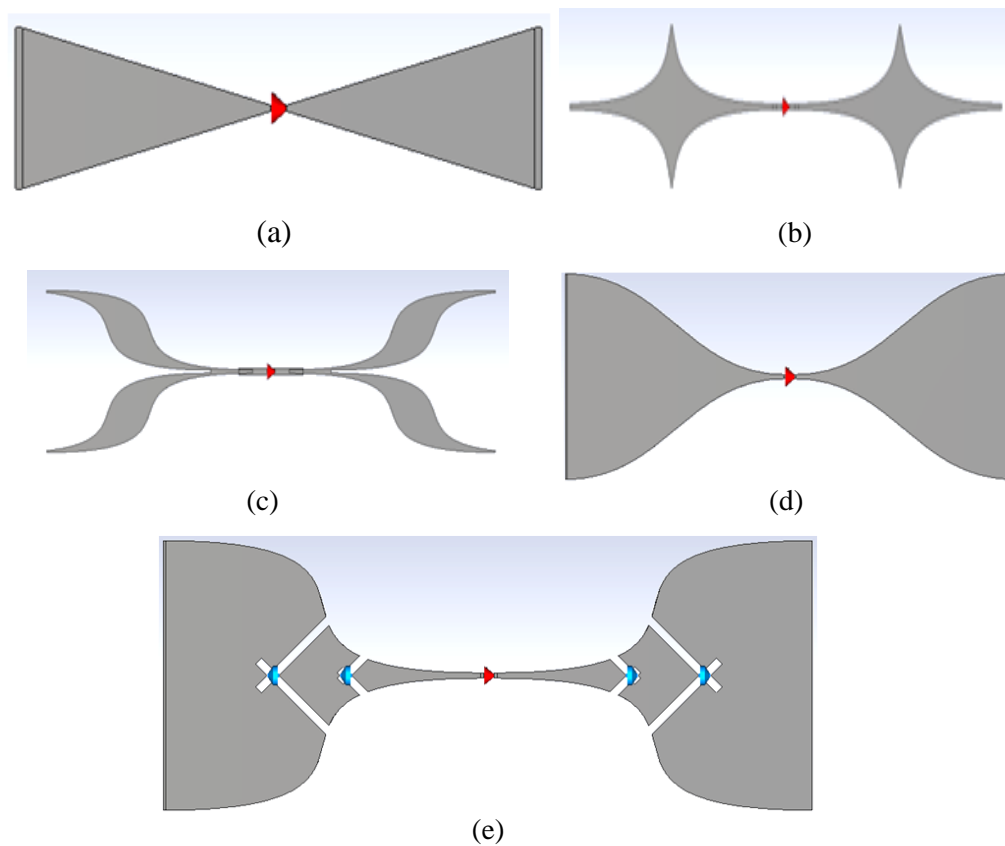


Figure 6.4. Investigated bow-tie antenna and several of its investigated modified versions (red arrow shows excitation source and blue arrow shows PIN diode).

To remedy the size problem, the bow-tie antenna was modified by dividing it into small sections and an optimization procedure was performed to find the length and width of each section to achieve miniaturization (Fig. 6.5). The overall size was subsequently reduced to  $0.2\lambda$  (where  $\lambda$  is wavelength at the lowest operating frequency). But, the problem with lack of sufficient bandwidth persisted.

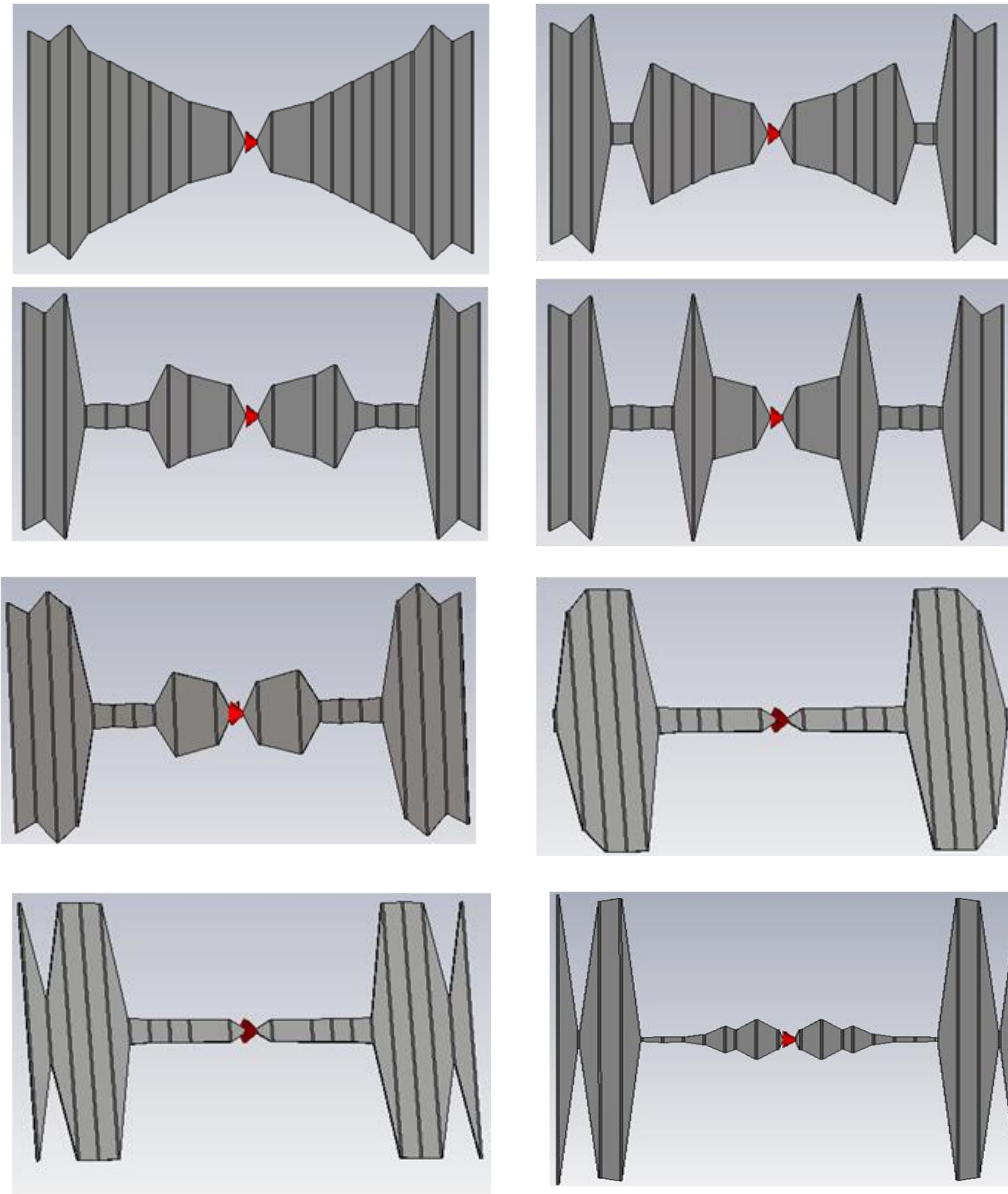


Figure 6.5. Different versions of nonuniform bow-tie antenna (red arrow shows excitation source).

To address the bandwidth issue, a coplanar waveguide structure, which is known to improve bandwidth characteristics in comparison with the microstrip type structures, was selected. Initially a circular slot loop CPW (Fig. 6.6) was investigated. Many simulations with different ideas were tried to find an appropriate antenna which can satisfy the design specifications. The major problem with this antenna was found to be its

low gain and limited bandwidth. Moreover, the antenna could not support the highest desired band (i.e., 800-1200 MHz).

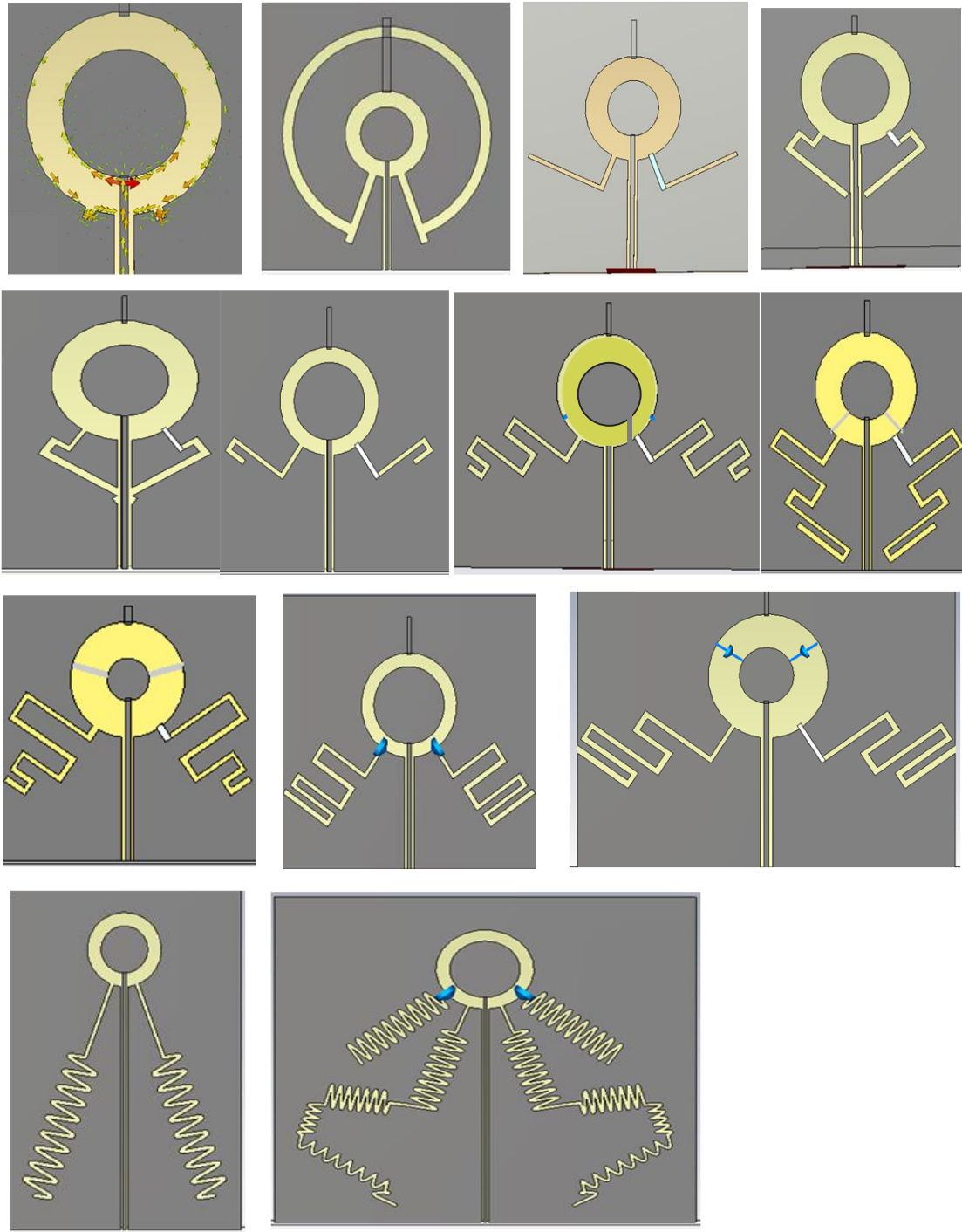


Figure 6.6. Some of the modified versions of ring slot antenna with slot line loading.

As another improvement, the circular slot was replaced with square slot and a tuning stub was added and its shape was optimized to cover the third band while trying to keep the antenna size reasonably small (Fig. 6.7). The results of this investigation showed that, a square slot with an elliptical tuning stub offered the best performance in term of bandwidth. This can be explained by noticing this fact that the elliptical tuning stub, creates a tapered slot transmission line. The gradual change in the characteristic impedance of the line can provide improved operating bandwidth in comparison with uniform transmission lines [137].

Therefore, at this point, a specific antenna with potential to cover the band with the highest frequency with large bandwidth was obtained. The procedure to incorporate reconfigurability to the antenna, to extend its operating frequency range, is explained next.

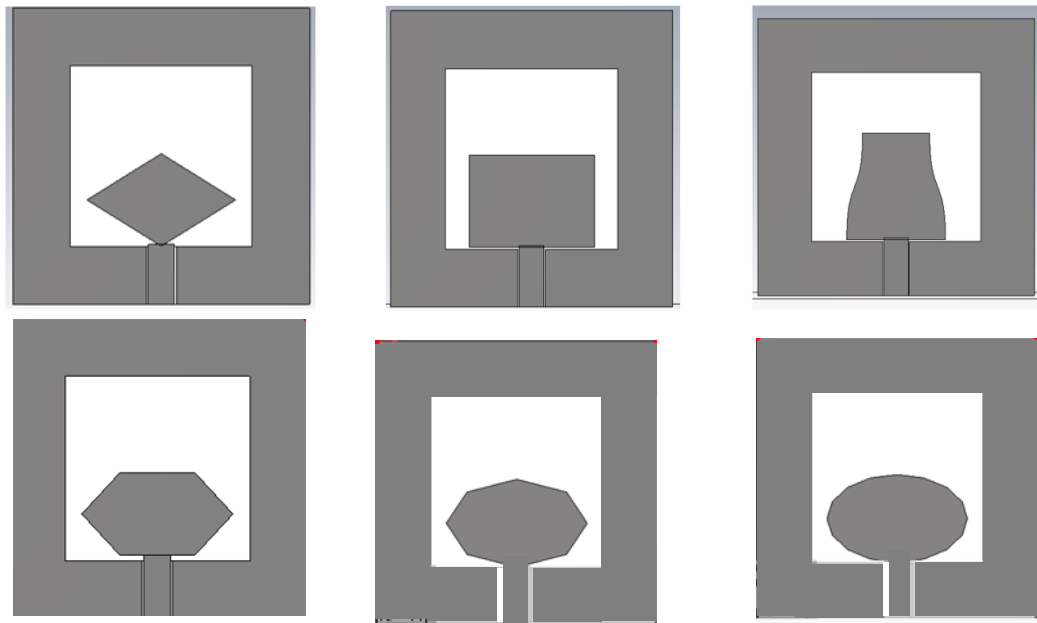


Figure 6.7. Investigated CPW-fed square slot antenna with different tuning stubs.



**6.3.1.1 Adding reconfigurability to the antenna.** For the current design, there are only three desired frequency bands (i.e.,  $N_B=3$ ). Then, based on the design procedure which was explained in Fig. 6.3, three different antennas should be designed (corresponding with each band). Later, these antennas will be implemented as one reconfigurable antenna. These steps are explained in details in the following.

Step1: In this step, the selected geometry of the CPW-fed slot antenna with an elliptical tuning stub is optimized using the optimization algorithm shown in Fig. 6.2. The reported work in [138] was used to find the initial values for the various antenna dimensions. Subsequently, using the Particle Swarm Optimization algorithm available in CST Microwave Studio, the antenna dimensions were tuned to improve/optimize its characteristics (i.e., reflection coefficient and gain pattern). The resulting optimum dimensions of the antenna (referred to as Antenna 3 to be consistent with Band 3), are listed in Table 6.1. The geometry of the antenna is shown in Fig. 6.8. Moreover, in Fig. 6.8 (b), the current distribution over the antenna at 900 MHz is shown which indicates that the current is mostly concentrated at the corners of the square slot. This observation will be used in Step 2 of the design procedure where Antenna 3 has to be manipulated to cover Band 2.

The calculated reflection coefficient for Antenna 3 using CST Microwave Studio is shown in Fig. 6.9. As the results indicate, the antenna operates from 840 MHz to above 1200 MHz which more than sufficiently covers Band 3.

Table 6.1. Optimally-calculated dimensions of Antenna 3

Parameter	$W$	$W_s$	$a$	$b$	$I$	$U_1$	$V_1$	$U_2$	$V_2$	$V_3$	$U_3$
(cm)	20	9.592	4.097	2.452	0.122	3.525	3.525	2.19	1.48	2.1	4.1

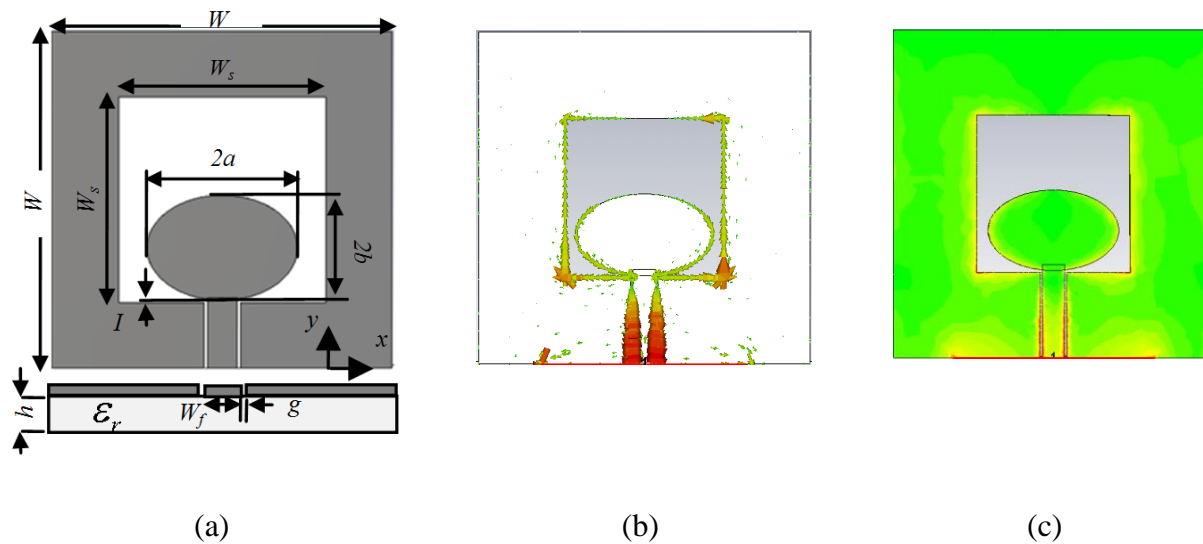


Figure 6.8. Optimally designed Antenna 3. (a) top view, (b) vector current distribution at 900 MHz, (c) magnitude of current distribution at 900 MHz.

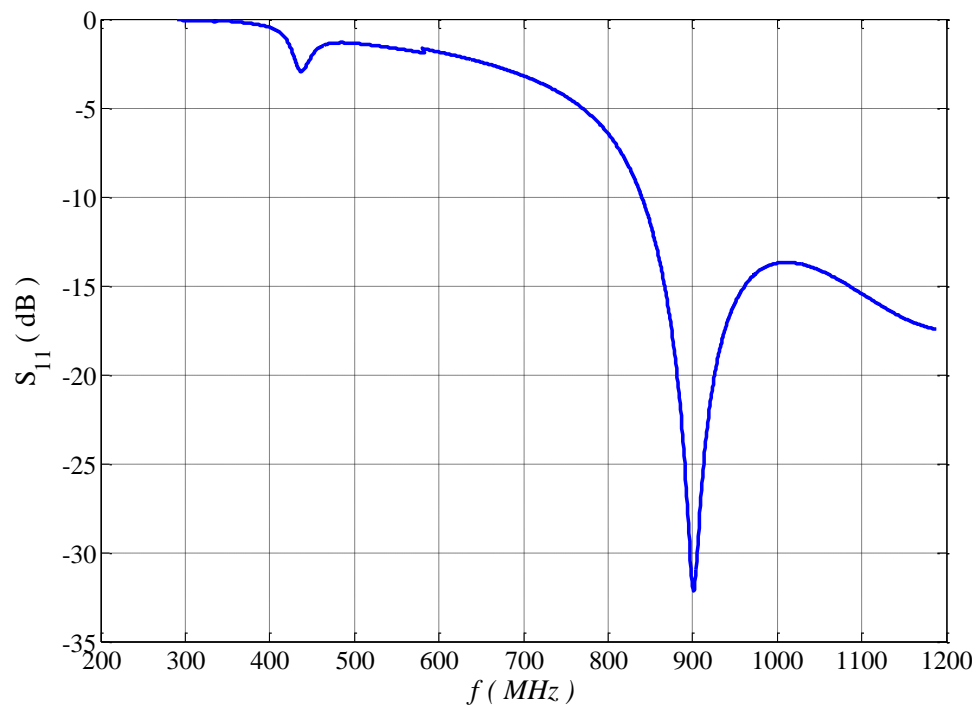


Figure 6.9. Simulated  $S_{11}$  for Antenna 3 using CST Microwave Studio.

Step 2: In this step, to cover Band 2, Antenna 3 should be manipulated or modified. The main idea is to keep the dimensions of Antenna 3 unchanged while trying to add (or remove) some portions of the antenna in order to reduce its frequency response. The addition/removal procedure should be in a way that later, it can be performed using electronic switches (e.g., PIN diodes). Moreover, it is well-known that current (both electric and magnetic) density distribution dictates the frequency response of the antenna (i.e. input impedance matching). Therefore, if one can change the current distribution of the antenna strategically and control it electronically, it is possible to electronically change its frequency response. The current distribution of Antenna 3 (Fig. 6.8 (b)-(c)) shows that the current is mostly concentrated at the corners. Then, one appropriate way to effectively manipulate the current distribution is by adding some extra shorted slots to the corner(s) of the square slot. As long as the length of slots are smaller than quarter of the operating wavelength, they behave as inductive loads. To use the antenna space efficiently, slots have to fit in the ground plane area. Some of the attempted configurations/cases are shown in Fig. 6.10. After a comprehensive investigation, it was concluded that one big square slot per each corner can make the antenna operate in the second desired frequency band (Fig. 6.11). The square slot was added to slot loop and the antenna is called Antenna 2 for future references. The added slot dimensions were optimized as before. The current distribution for the Antenna 2 (to be consistent with Band 2) is shown in Fig. 6.11 (b).

All of the added slots are similar and the calculated dimensions of them ( $U_1, V_1$ ) are listed in Table 6.1. The simulated reflection coefficient for the Antenna 2 is shown in Fig. 6.12. As the results indicate, the antenna operates from 400 to 554 MHz which covers the desired Band 2.

Step 3: In this step, to cover Band 1, Antenna 1 should be manipulated or modified. Same idea as it was explained in Step 2 was used to manipulate Antenna 2 strategically to achieve good matching in the first frequency band (Band 1). Again, the current distribution which was shown in Fig. 6.11 (b) was considered and it was concluded that the corner of the newly added slots have the highest current density. Therefore, some extra slots were added to these corners and the antenna is called Antenna 1 (to be consistent with Band 1).

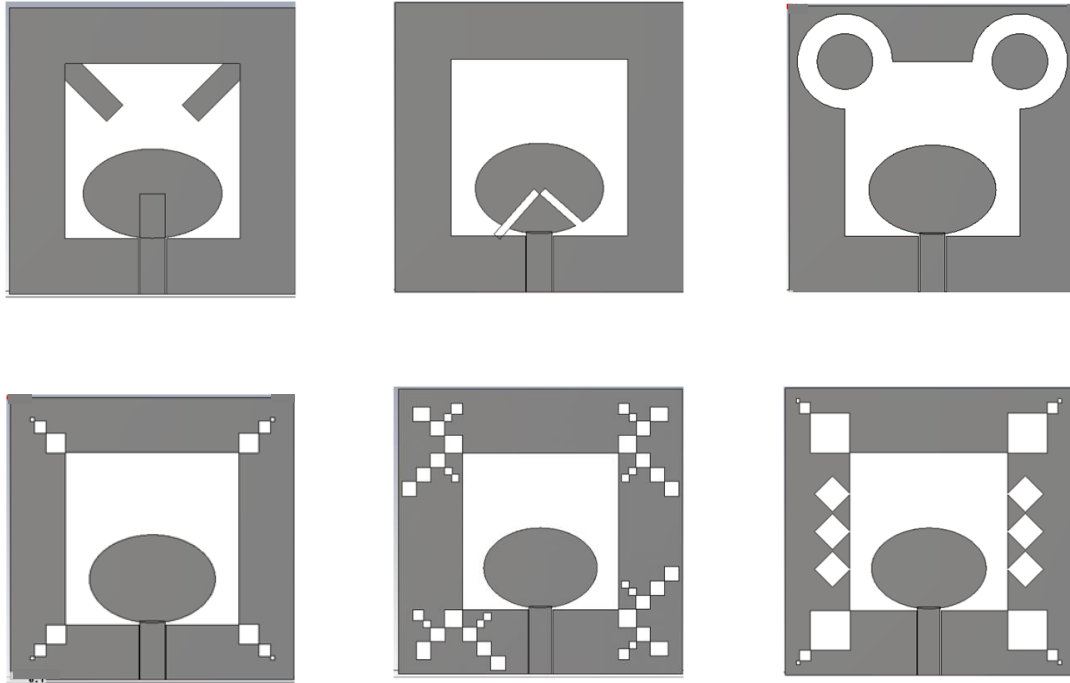


Figure 6.10. Some of the investigated ideas on Antenna 3 to reduce its resonant frequency.

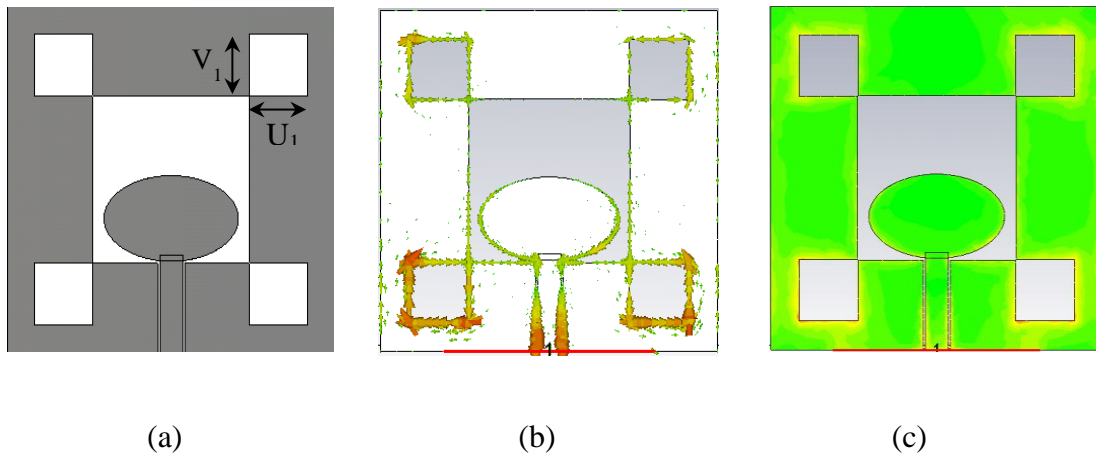


Figure 6.11. Optimally-designed Antenna 2. (a) top view, (b) vector current distribution at 460 MHz, (c) magnitude of current distribution at 460 MHz.

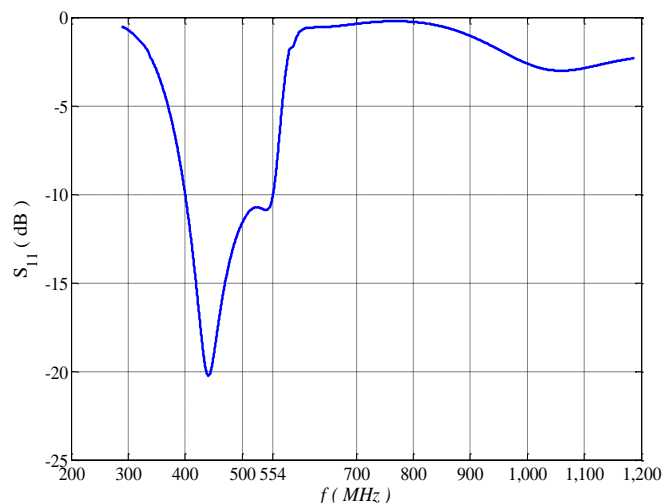


Figure 6.12. Simulated  $S_{11}$  of Antenna 2 using CST Microwave Studio.

After trying different cases, it was concluded that the two extra slots per each corner is required to cover Band 1. Then, the dimensions of these slots were optimally calculated using the explained optimization procedure. The final design is shown in Fig. 6.13 where the current distribution is shown in Fig. 6.13 (b)-(c).

Two type of slots (i.e.,  $(U_2, V_2)$  and  $(U_3, V_3)$ ) were used in the corners with their dimensions listed in Table 6.1. The simulated reflection coefficient for Antenna 1 is shown in Fig. 6.14. As the results indicate, the antenna operates from 295 to 320 MHz which covers the desired Band 1.

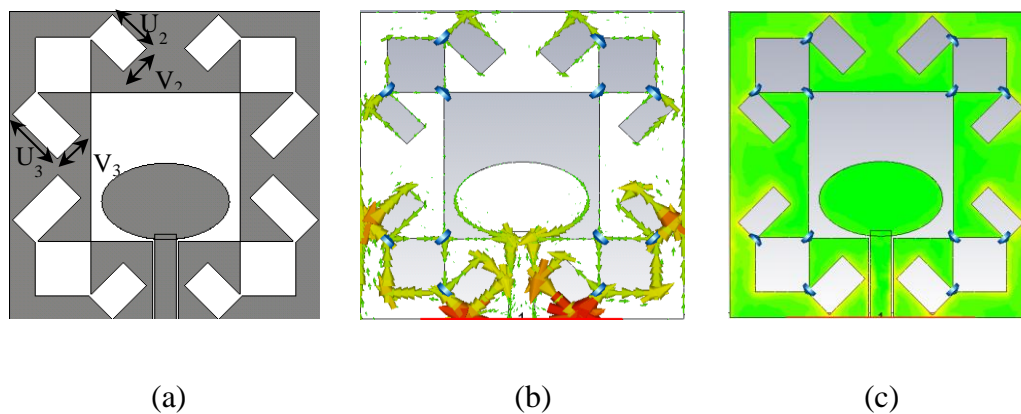


Figure 6.13. Optimally designed Antenna 1. (a) top view, (b) vector current distribution at 315 MHz, (c) magnitude of current distribution at 315 MHz.

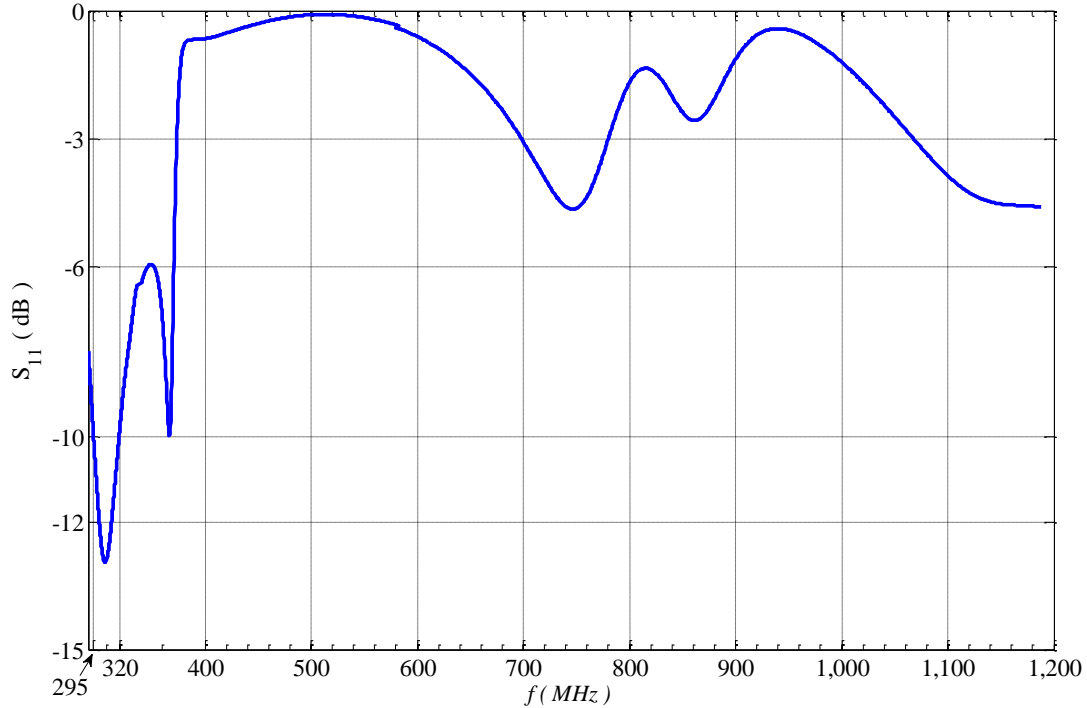


Figure 6.14. Simulated  $S_{11}$  of Antenna 1 using CST Microwave Studio.

As the design flowchart shows, to add reconfigurability to Antenna 1, PIN diodes may be utilized to incorporate the added slots. As shown in Fig. 6.15, three PIN diodes are necessary at each corner which can be electronically switched (i.e., turned ON and OFF). The selected PIN diode is Microsemi GC270 which behaves like a  $1.5\Omega$  resistance when it is ON and a  $0.2\text{ pF}$  capacitance when it is OFF. To model the PIN diode in CST Microwave Studio, an equivalent circuit may be used. As an equivalent model, the forward-biased (or turned ON) PIN diode can be replaced with a series combination of a resistor (i.e.,  $r_D$ ) and an inductor (i.e.,  $L_D$ ) (Fig. 6.16). However, since the data sheet for PIN diode usually provides the series resistor and the operating frequency is not very high,  $L_D$  is assumed to be zero. On the other hand, a reversed-biased (or turned OFF) PIN diode can be replaced with a series combination of a resistor, an inductor and a capacitor (Fig. 6.16). Again, in the frequency range that the PIN diode is going to be used (i.e., lower than  $1.5\text{ GHz}$ ), the capacitor (i.e.,  $C_R$ ) can be seen as the dominant element and the other elements may be ignored.

Three different configurations can be produced by turning the PIN diodes ON and OFF namely: when all the PIN diodes are OFF (Configuration 1), PIN diodes D1 are OFF and others are ON (Configuration 2) and all PIN diodes are ON (Configuration 3). These configurations are listed in Table 6.2.

Based on the simulation results, it was observed that the lower band resonant frequency slightly shifted after adding the PIN diodes, as one would expect since the lumped elements associated with the diodes change the overall impedance of the antennas. The optimization process was used to slightly modify the dimensions of the added slots in order to improve the return loss characteristics. The final optimally calculated dimensions are listed in Table 6.3.

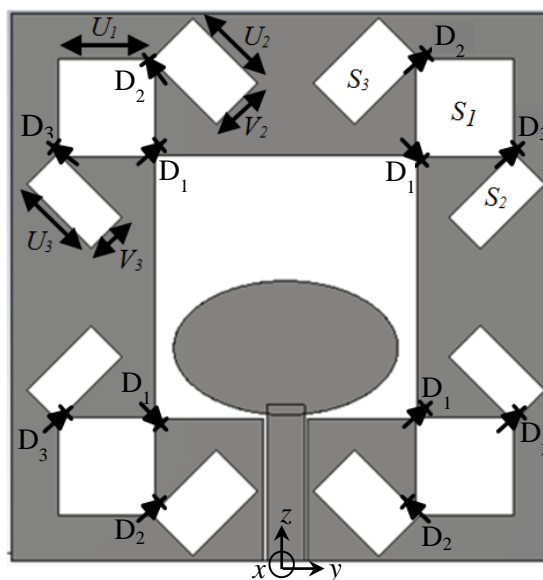


Figure 6.15. The final antenna design with PIN diode-loaded slots.

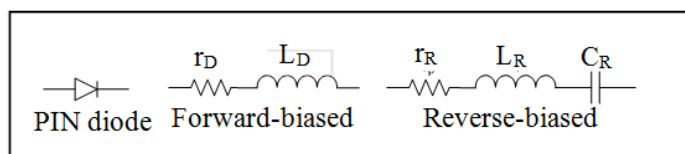


Figure 6.16. PIN diode with its forward-biased and reversed-biased equivalent circuit models.

Table 6.2. Generating three different configurations by turning PIN diodes ON and OFF

Configuration	1			2			3		
Diode	D <sub>1</sub>	D <sub>2</sub>	D <sub>3</sub>	D <sub>1</sub>	D <sub>2</sub>	D <sub>3</sub>	D <sub>1</sub>	D <sub>2</sub>	D <sub>3</sub>
State	OFF	OFF	OFF	OFF	ON	ON	ON	ON	ON

Table 6.3. Optimally calculated dimensions of reconfigurable antenna (Design 1)

Paramet.	$W$	$W_s$	$a$	$b$	$I$	$U_1$	$V_1$	$U_2$	$V_2$	$V_3$	$U_3$
(cm)	20	9.592	4.097	2.452	0.122	3.525	3.525	3.25	2.02	1.5	3.22

The final reconfigurable antenna was subsequently simulated using CST Microwave Studio. The results in Fig. 6.17 show that the proposed reconfigurable antenna can effectively cover all the three desired bands. The simulation frequency was intentionally extended to 2 GHz to show the capability of this antenna to cover frequencies beyond the desired bands. As the results indicate, all of the three configurations have a good matching characteristics at frequencies higher than 1.2 GHz.

The antenna shows maximum gain of  $G = -2.5, 0,$  and  $3.35$  dB at  $f = 315, 460,$  and  $900$  MHz, respectively. Moreover, the simulated antenna gain patterns at these frequencies are plotted in Fig. 6.18. For the first and the second bands, the XY-plane ( $\theta = 90^\circ$ ) pattern is almost omnidirectional while at the third band it is somewhat directive. The XZ-plane ( $\phi = 0^\circ$ ) pattern does not change much for different bands.

At this stage, the design phase is completed and then, the antenna was built and tested. Fabrication, test, and measurement results will be discussed next.



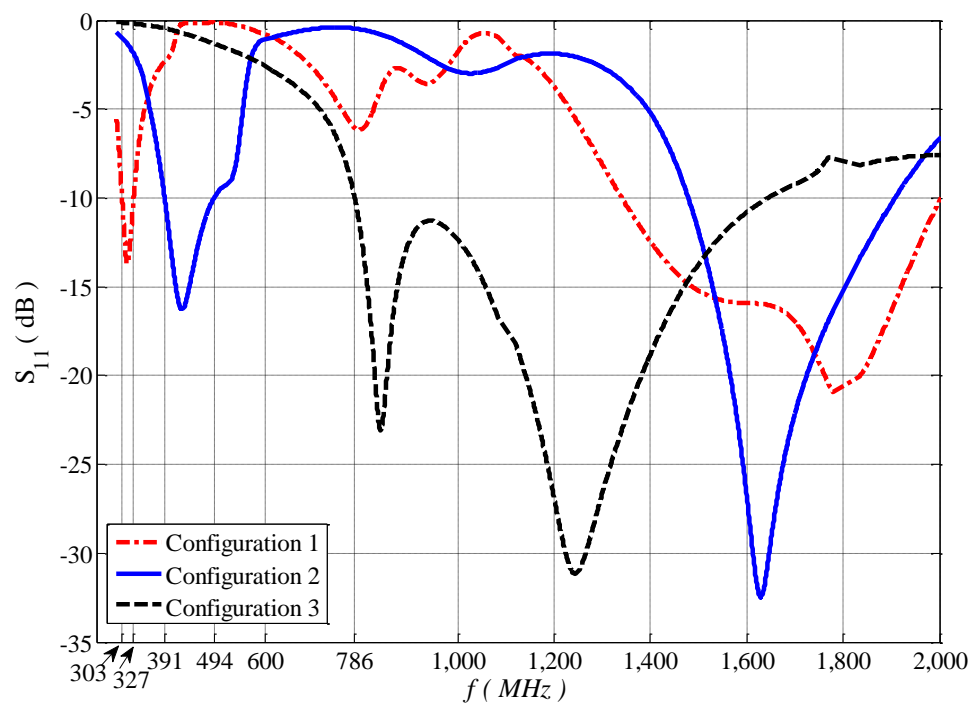


Figure 6.17. Simulated  $S_{11}$  of the proposed frequency reconfigurable antenna (with PIN diodes incorporated into the design) operating at three bands (Design 1).

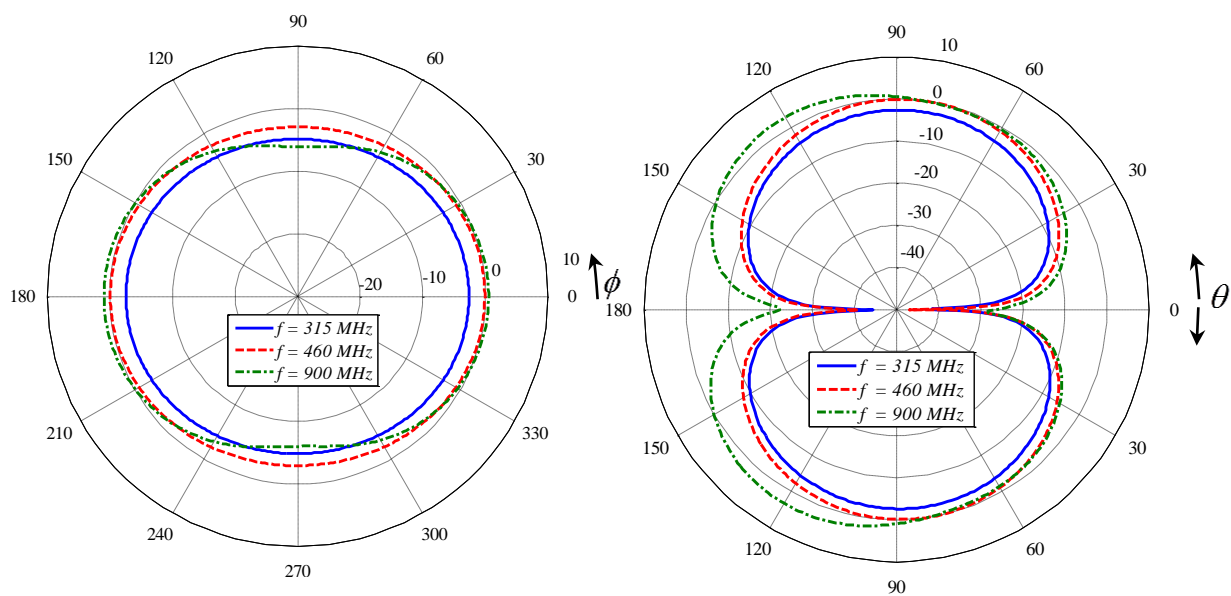


Figure 6.18. Gain pattern of the proposed reconfigurable antenna. (a) XY-plane, (b) XZ-plane.

**6.3.1.2 Fabrication, test, and measurement.** The proposed antenna was built on FR4 substrate which has a thickness of 62 mil (Fig. 6.19).

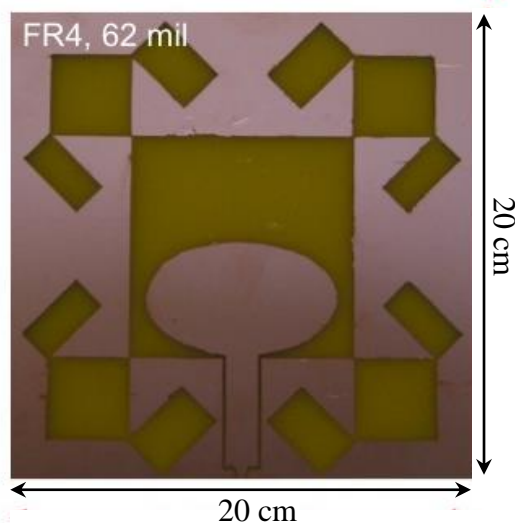


Figure 6.19. The built designed antenna (Design 1) on 62 mil FR4 substrate (bare board).

To install the PIN diodes, a suitable biasing network is required and the PIN diode leads and the ground plane must be DC decoupled (or isolated) but AC coupled (or connected). To address this issue, two small pieces of very thin PCB were soldered onto the ground plane at places where the PIN diode sits on the antenna board. Then, the PIN diode was soldered between these two pads. To create a low-impedance path between the PIN diode leads and the ground plane, bypass capacitors were installed between each lead of the PIN diode and the ground plane. The capacitance should be selected in a way that its impedance at the lowest operating frequency is very low (e.g.,  $0.1\Omega$ ) to connect both leads of the PIN diode to the ground plane. In Fig. 6.20, the proposed idea for a general slot between two ground traces is shown. Later, this idea was implemented on the manufactured antenna (Fig. 6.21). Then, a test setup was built to measure the reflection coefficient of this antenna (Fig. 6.22). To feed the PIN diodes, output DC voltage from National Instruments multifunction DAQ (NI USB-6009 [139]) was used (Fig. 6.22). This DAQ is connected to computer and all three configurations were tested by using a

simple computer program developed by National Instruments namely *Measurement and Automation* [140].

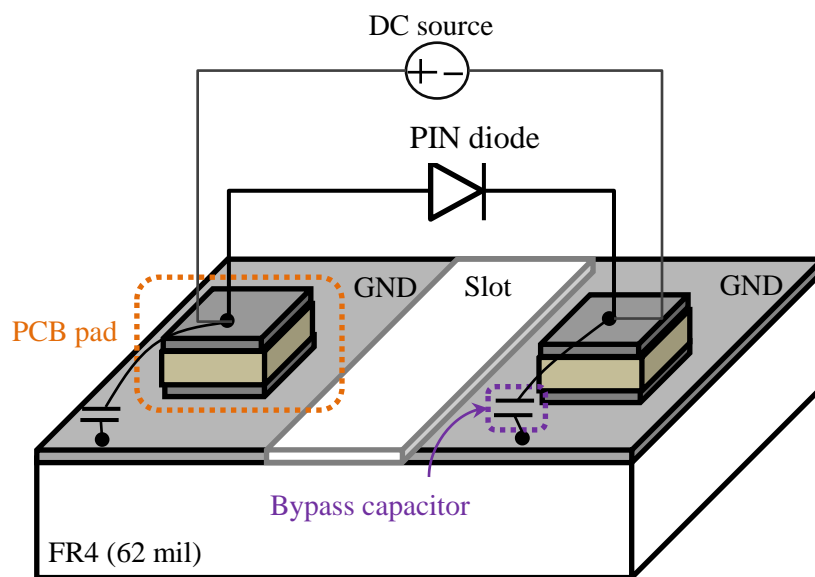


Figure 6.20. DC biasing network for the PIN diode installation over a slot trace.

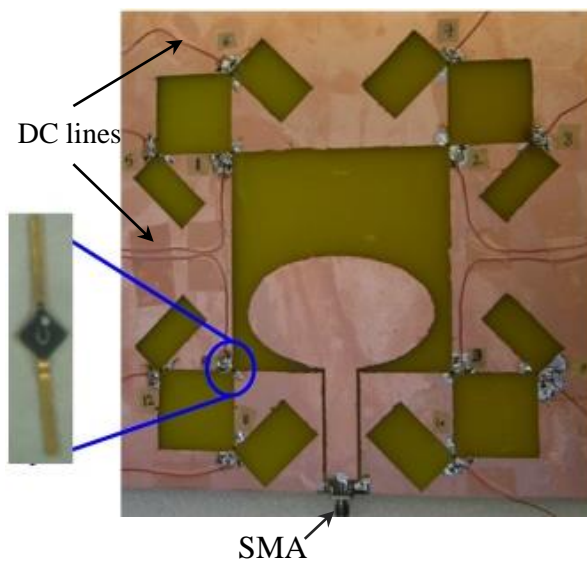


Figure 6.21. Built designed antenna (Design 1) on 62 mil FR4 substrate with the PIN diodes and DC biasing lines.

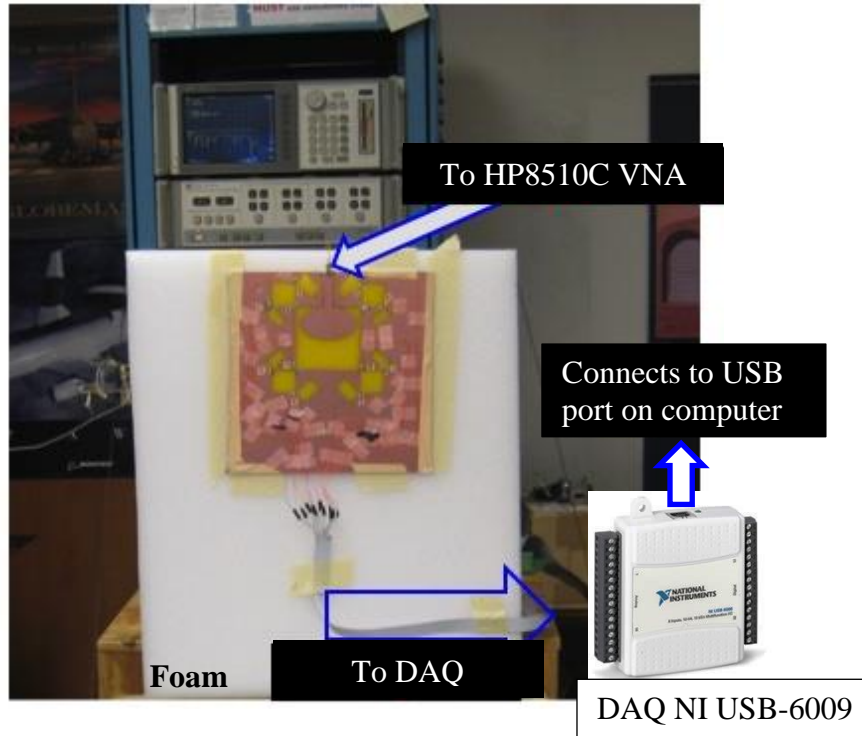


Figure 6.22. Implemented antenna (Design 1) installed on the measurement setup.

The measured  $S_{11}$  for different configurations are shown in Fig. 6.23. The measurement results are in a good agreement with the simulation results (Fig. 6.17). The implemented and tested antenna covers all the three bands but there is a slight shift in the frequency response compared to the simulation results, as shown in Table 6.4. To show this difference, a new term as error between measured and simulated results at lower and upper end of the band ( $\varepsilon_{MvS}$ ) is defined as:

$$\varepsilon_{MvS} = 100 \times \frac{|f_i^{Me} - f_i^{Si}|}{f_i^{Me}}, \quad (94)$$

where  $i \in \{L, U\}$  and then  $f_i^{Si/Me}$  shows lower and upper frequencies of the simulated (Si) and measured (Me) bands. The calculated  $\varepsilon_{MvS}$  is also listed in the fourth column of Table 6.4 which shows that the error between the measured and simulated results is less

than 6 percent for Band 1 and 2. This error for Band 3 which covers higher frequencies is higher at the lower edge of the band (i.e., ~ 10 percent). At the upper edge of the band, the error significantly increases. Manufacturing inaccuracies and substrate material tolerances might have caused the measured frequency response to shift slightly within Band 1, 2, and 3. However, for Band 3, and for the frequencies up to desired frequency of 1200 MHz, both the simulated and the measured  $S_{11}$  results are less than -10 dB. By increasing the frequency above 1200 MHz (where it was not included in the design procedure), the simulated and measured results will not follow each other well. This may be explained by considering this fact that in full-wave simulations, a wave port was used to model the excitation while in the measurement, a subminiature version A (SMA) connector which was connected to a SMA cable was used to excite the antenna. The wave port model may not be accurate enough for high frequencies. However, despite the shift, all of the three desired bands are covered by the designed and the implemented antenna.

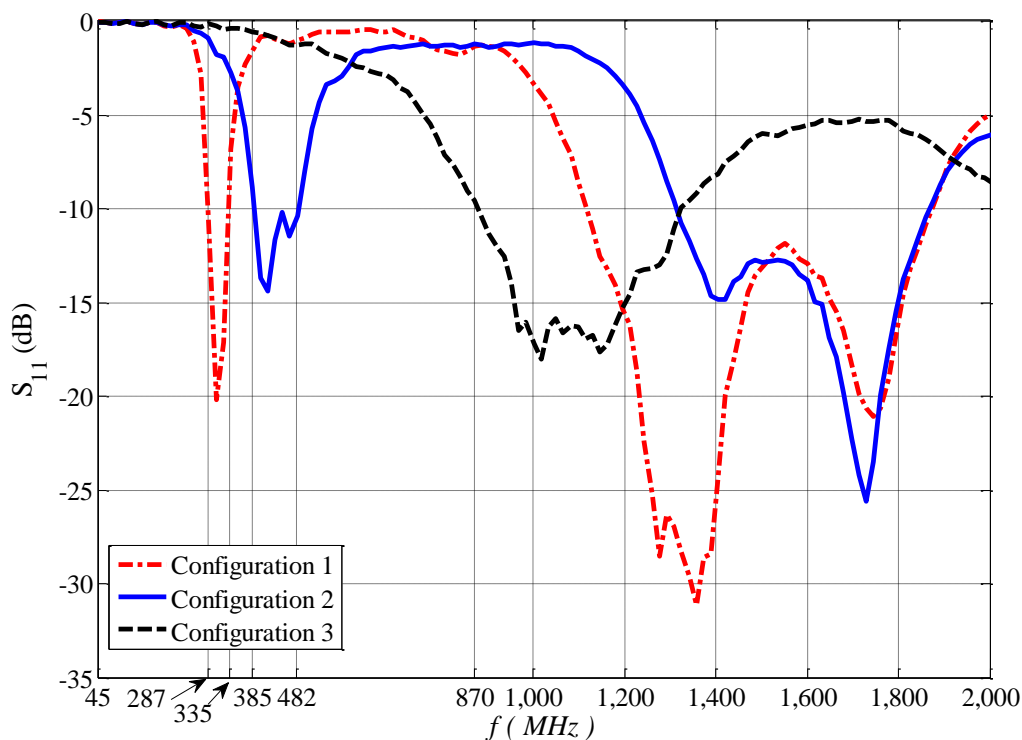


Figure 6.23. Measurement results for all three configurations (Design 1).

Table 6.4. Comparing simulation and measurement results for Design 1 (criteria:  $S_{11} \leq -10$  dB)

Band No.	Simulation Results ( MHz )	Measurement Results ( MHz )	$\varepsilon_{MvS}$ (Percentage)
1	303-327	287-335	5.58-2.4
2	391-494	385-482	1.56-2.5
3	786-2000	870-1300	9.6-50

**6.3.2. Design 2: Reconfigurable Antenna Covering Four Different Bands at VHF/UHF/L.** As it was previously shown, the proposed reconfigurable CPW-fed square slot antenna operates successfully at all of the three desired bands. However, in some applications, it is desired to reduce the frequency of operation into VHF band. For imaging, by reducing the operating frequency, the ability of the wave to penetrate inside the material increases. Therefore, in a continuing effort to lower the operating frequency, it was attempted to add another band to the proposed antenna. This would be the lowest possible frequency band attainable with this antenna, while keeping the other bands intact. This may be achieved by manipulating the current path in a way that the antenna operates in low frequency. A comprehensive study was conducted in an attempt to manipulate the Design 1 and achieve this goal. Some of the attempted configurations are show in Fig. 6.24.

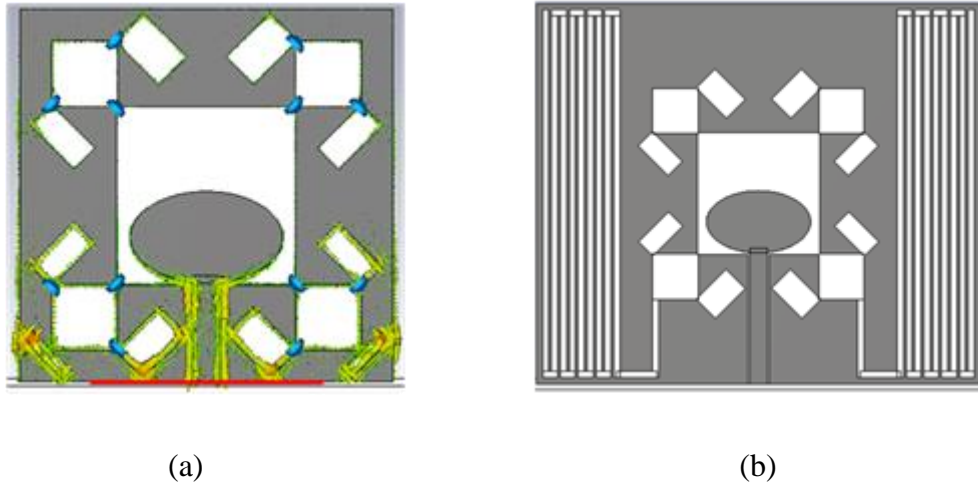


Figure 6.24. Two investigated ideas to reduce the lowest operating frequency of the proposed reconfigurable antenna in the first design.

During this investigation, revisiting the current distribution helped to realize that the additional top slots do not play a major role in the antenna frequency response (the current distribution on the added top slots, compared with the bottom slots, is relatively insignificant), as shown in Fig. 6.13. Consequently, these top slots were removed to free up more space on the ground plane. Subsequently, many different ideas were considered on this modified antenna to reduce the lowest operating frequency while trying to keep the already achieved bands intact. Some of the investigated cases are shown in Fig. 6.25. In all of these efforts, increasing the electrical length of the antenna, by loading it with extra slots, was the main objective.

Later, loading the slots with lumped elements, such as capacitors, was investigated as well. A capacitively- or inductively-loaded slot line results in a slow-wave structure which makes the slot electrically longer for the wave (Section 5.2.1.2). Based on this idea, a set of new antennas were considered, as shown in Fig. 6.26. A capacitively-loaded slot loop was incorporated into the antenna. The slot loop can be easily added/removed with an electronic switch (e.g. PIN diode) into different sections of the modified antenna. A few of the possibilities are shown in Fig. 6.26 (a)-(d).

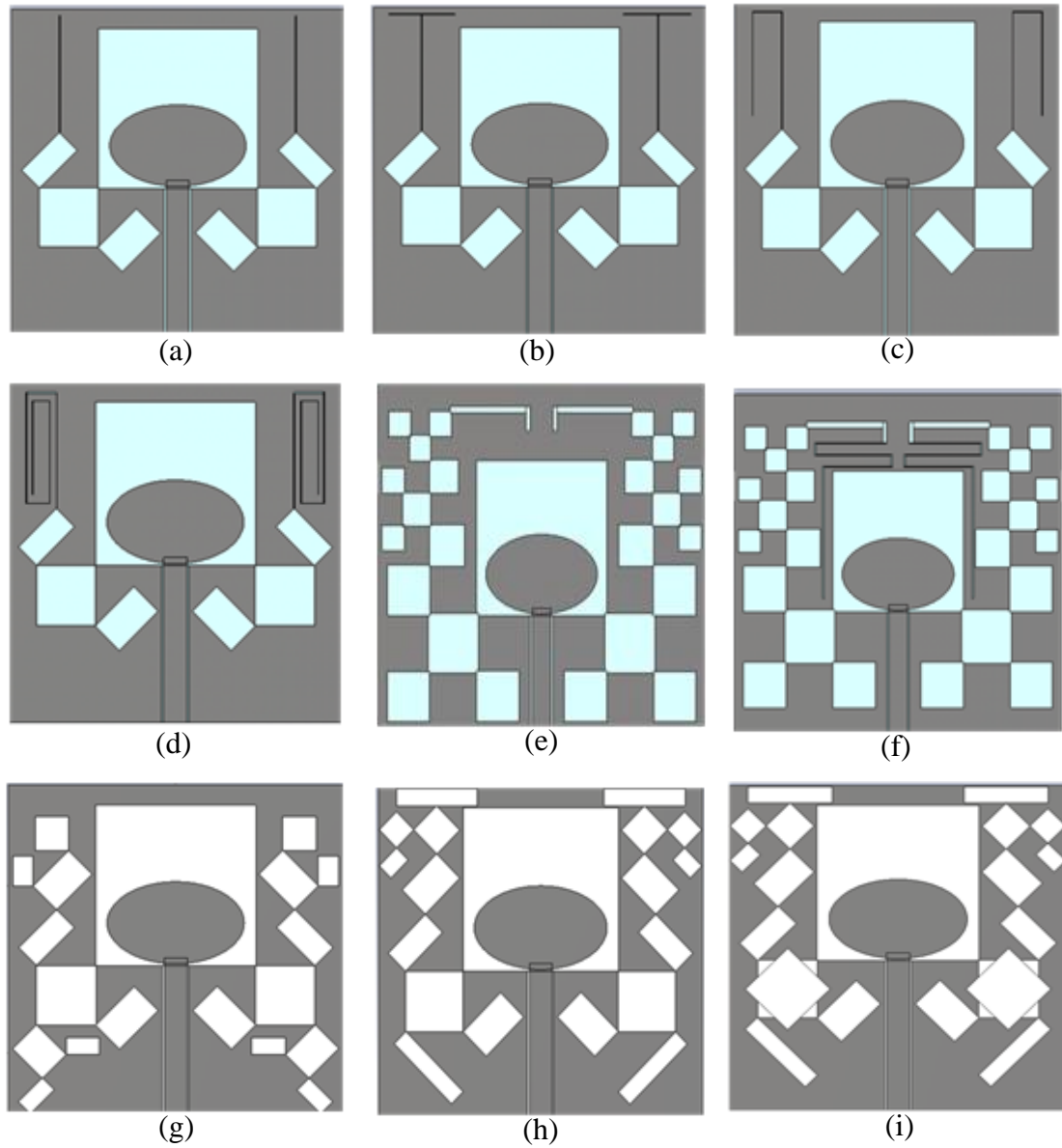


Figure 6.25. Some of the considered configurations with Design 1 to achieve the lowest possible operating frequency.



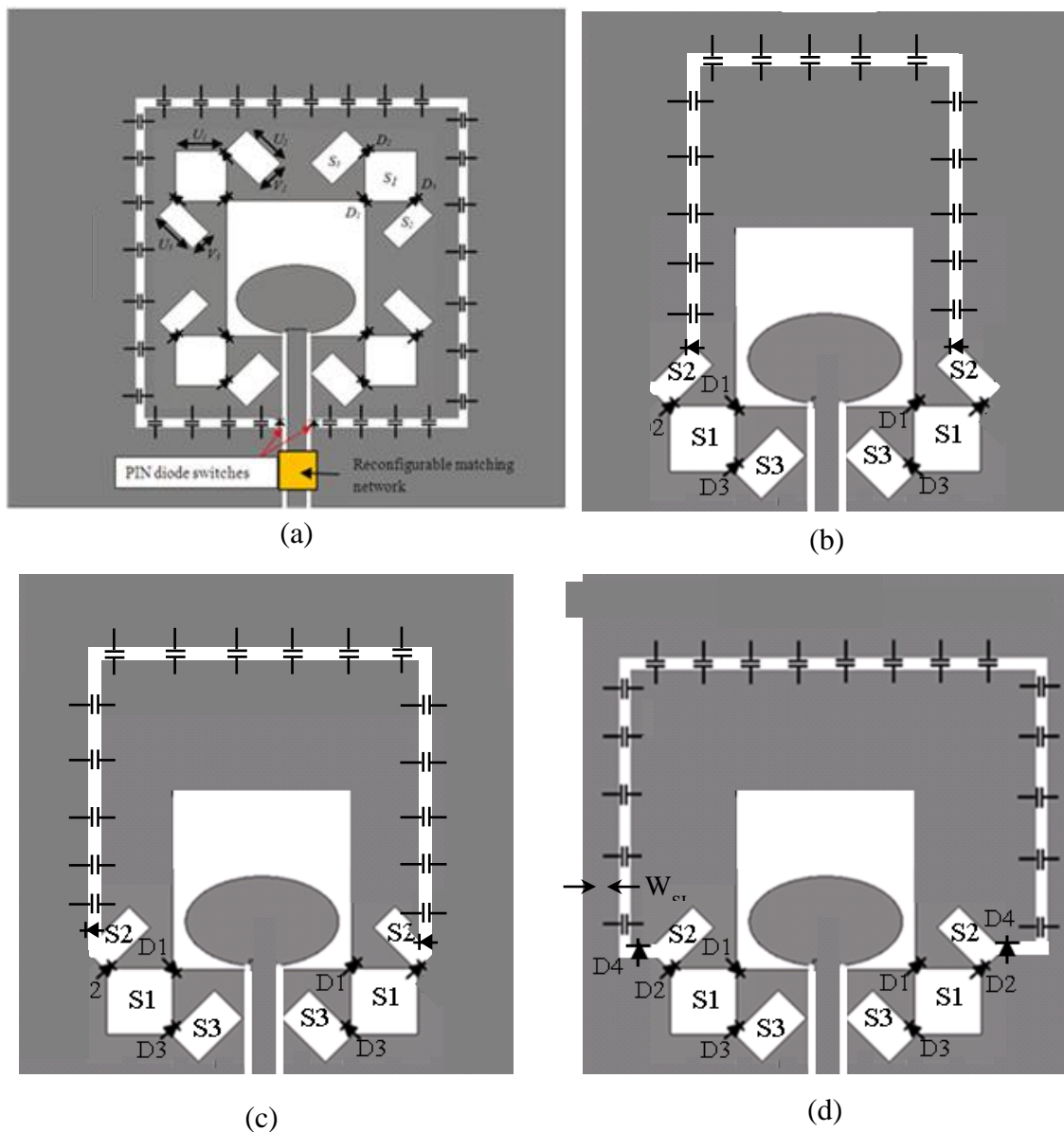


Figure 6.26. Different ways of incorporating capacitively-loaded slot loop to the modified proposed antenna.

Among these options, the configuration shown in Fig. 6.26 (d) showed the best performance. This antenna with all of the PIN diodes, capacitors, and required dimensions is shown in Fig. 6.27, which is called Design 2 for the future references. Moreover, it was assumed that the dimensions of the antenna can be extended to  $25\text{ cm} \times 27\text{ cm}$ . In order to continue the design, it is necessary to define the desired lowest

band. Considering the fact that the modified antenna, before adding slot loop antenna, was operating at 303 MHz as its lowest operating frequency, the desired lowest frequency is now set as 100 MHz. Later, a comprehensive set of simulations were performed to estimate the placement and values of the loading capacitors and the width of the added slot loop ( $W_{SL}$ ). An appropriate value for the capacitors was estimated to be 10 pF and the width of the slot loop was calculated to be 0.2 cm. Moreover, the spacing between the capacitors was calculated to be 2 cm.

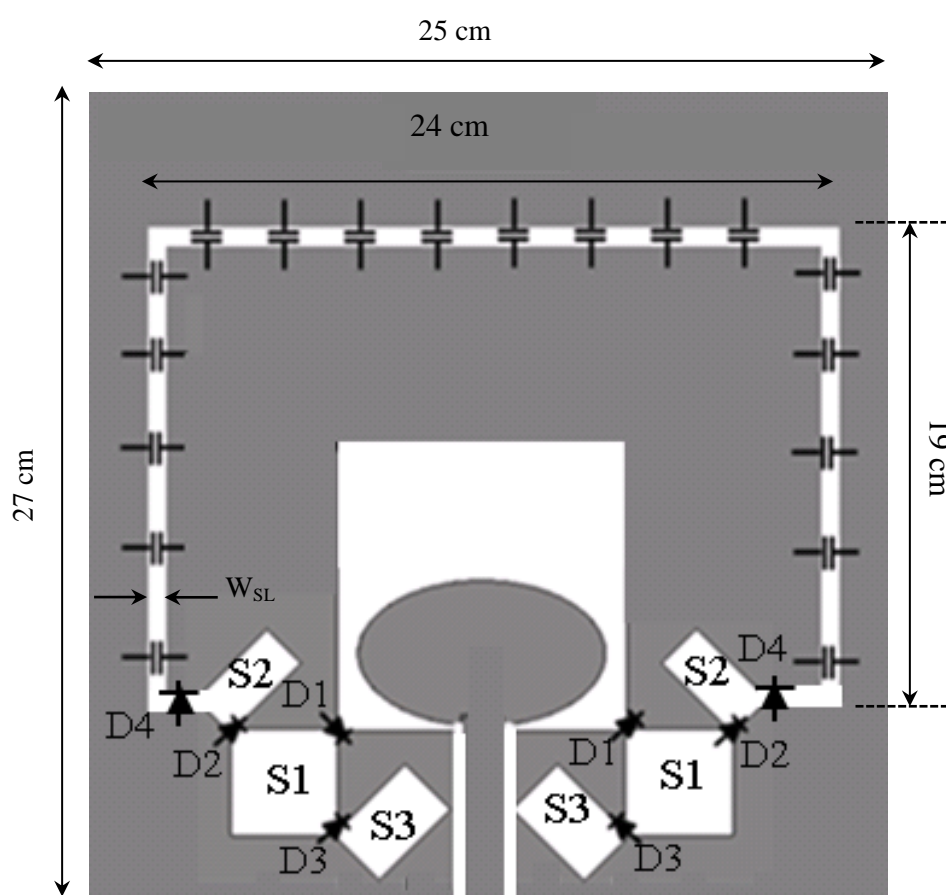


Figure 6.27. Schematic view of the proposed reconfigurable antenna to cover four bands at VHF/UHF/L (Design 2).

Based on the PIN diodes states, four different configurations can be defined for this antenna. These configurations are listed in Table 6.5. The applied PIN diodes are similar to Design 1 and so, they are modeled in a similar way in CST Microwave Studio. The simulation results for all the four different configurations (i.e., Configuration 1, 2, 3, and 4) are plotted in Figs. 6.28, 6.29, 6.30, and 6.31. In Configuration 1, antenna shows a good matching performance ( $S_{11} < -10$  dB) at 100 MHz, however, the antenna presents a multiband performance (Fig. 6.28). It means that the antenna at Configuration 1, not only covers 100 MHz, but also it covers some other frequencies. This may not be considered a good point when issues related to noise are considered. The antenna with Configuration 2 covers a range from 305-320 MHz which is in a good agreement with the desired Band 2 (Fig. 6.28). However, again, the antenna shows a multiband performance covering other frequencies. In Configuration 3, the antenna only covers from 418-482 MHz which is almost the desired Band 3 (Fig. 6.29). In configuration 4, the antenna covers from 950-1500 MHz. The lower edge of the band is moved higher in comparison with the Design 1 (Fig. 6.30).

Table 6.5. Generating four different configurations by turning PIN diodes ON and OFF

Conf.	1				2				3				4			
Diode	D <sub>1</sub>	D <sub>2</sub>	D <sub>3</sub>	D <sub>4</sub>	D <sub>1</sub>	D <sub>2</sub>	D <sub>3</sub>	D <sub>4</sub>	D <sub>1</sub>	D <sub>2</sub>	D <sub>3</sub>	D <sub>4</sub>	D <sub>1</sub>	D <sub>2</sub>	D <sub>3</sub>	D <sub>4</sub>
State	OFF	OFF	OFF	OFF	OFF	OFF	OFF	ON	OFF	ON	ON	ON	ON	ON	ON	ON

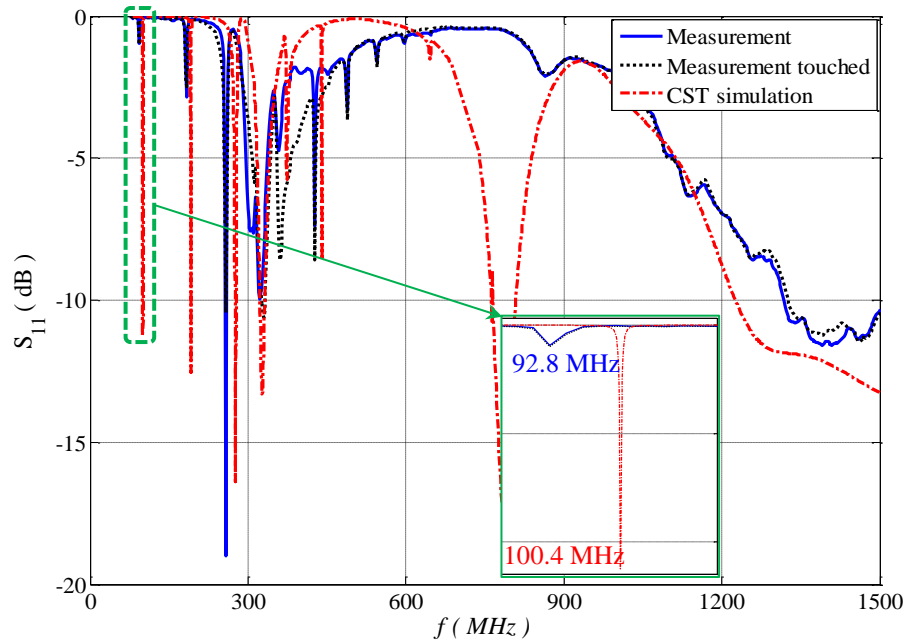


Figure 6.28. Reflection coefficient for antenna Design 2 (Configuration 1): measurement with and without touching versus simulations with CST Microwave Studio.

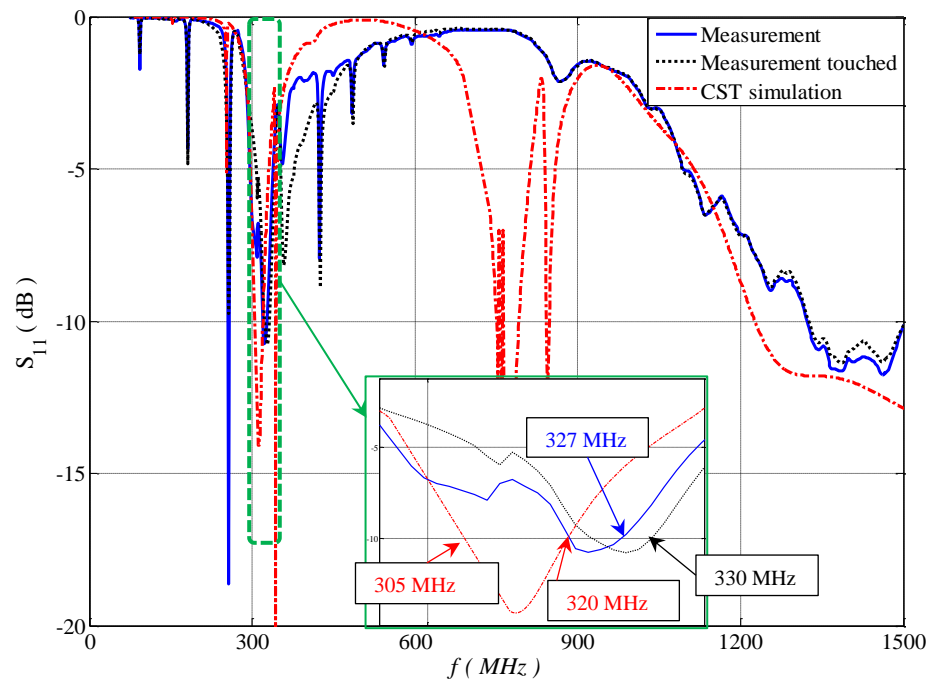


Figure 6.29. Reflection coefficient for antenna Design 2 (Configuration 2): measurement with and without touching versus simulations with CST Microwave Studio.

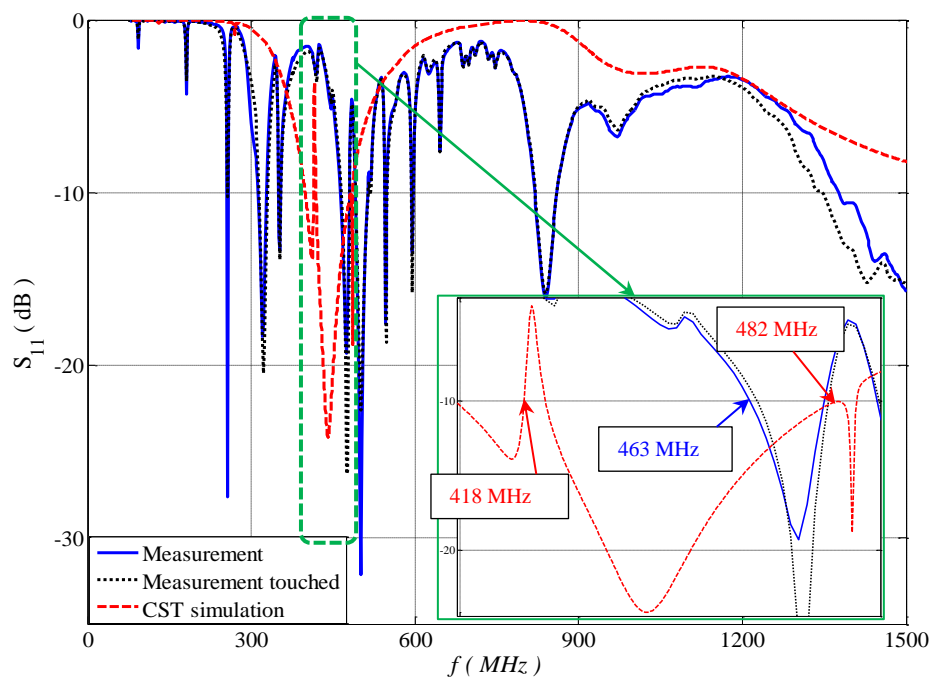


Figure 6.30. Reflection coefficient for antenna Design 2 (Configuration 3): measurement with and without touching versus simulations with CST Microwave Studio.

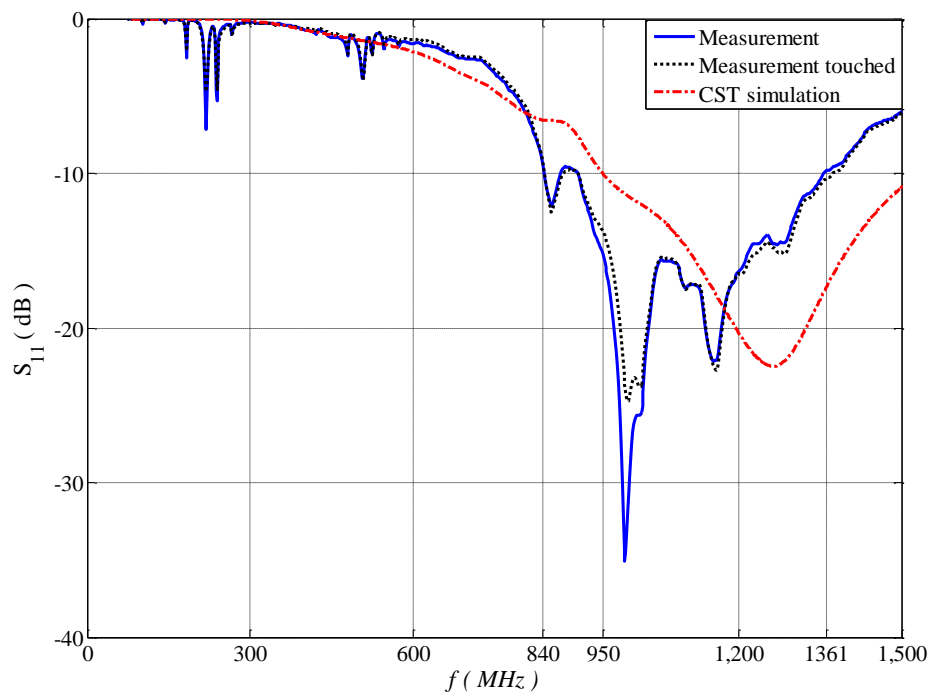


Figure 6.31. Reflection coefficient for antenna Design 2 (Configuration 4): measurement with and without touching versus simulations with CST Microwave Studio.

Later, the modified antenna (Design 2) was built and tested (Fig. 6.32). The measurement result for each configuration is added to the pertinent plot which has the simulation result (Figs. 6.28, 6.29, 6.30, 6.31). As one can see, the simulation and measurement results are not in a good agreement. Moreover, during the test, it was noticed that by touching the coaxial cable which feeds the antenna, its response changed. This may have occurred because of the unbalanced current flowing on the outer shield of the coaxial cable. Also, the close vicinity of the slots and the edge of the antenna may have contributed to this problem. To address the former problem, an extension was added to the ground plane where the cable connects to the antenna Fig. 6.32 (b)-(c). It was noticed that by increasing the width of the extension, the “touching” effect becomes less significant. The measured  $S_{11}$  for two different ground plane extensions (i.e., small (~ 9 cm) and large (~ 18 cm) (Fig. 6.32 (b)-(c))) are compared with the simulated results in Figs. 6.28, 6.29, 6.30, 6.31.

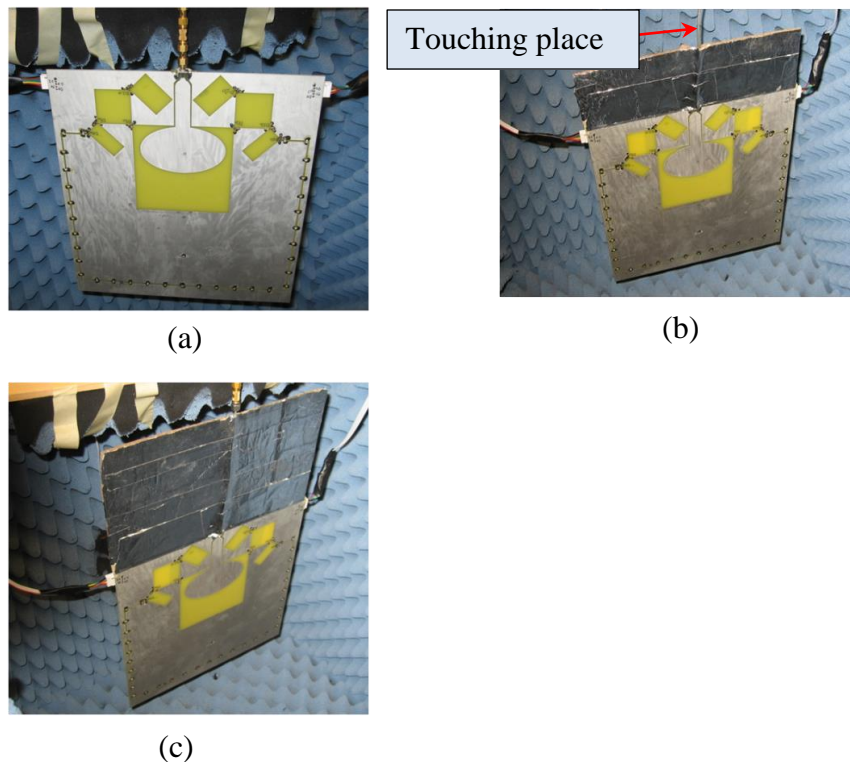


Figure 6.32. Built antenna Design 2. (a) without any ground plane extension, (b) with a small ground plane extension, and (c) with a large ground plane extension.

During the investigation to find the reason for disagreement between the simulation and measurement results, it was noticed that a symmetric plane was used in CST Microwave Studio simulations for Design 2 which was not used for Design 1. By using this symmetric plane, CST Microwave Studio assumes that tangential H-field to be zero ( $H_t = 0$ ) on this plane and it only meshes and performs the calculations for half of the structure (Fig. 6.33). This way, the entire calculation procedure speeds up. However, for the current structure, this assumption is not valid because by removing the plane, the simulation results may change.

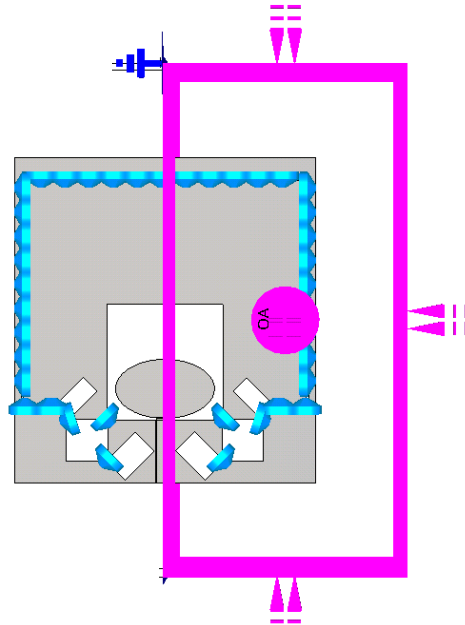


Figure 6.33. Modified antenna (Design 2) simulated in CST Microwave Studio with the symmetric plane ( $H_t = 0$ ) assumption.

**6.3.3. Design3: Reconfigurable Antenna Covering Four Different Bands at VHF/UHF/L.** In Section 6.3.2 an attempt was made to reduce the lowest operating frequency of the proposed reconfigurable CPW-fed slot antenna and a new design namely Design 2 was introduced. However, because of an invalid assumption in the simulations, the measurement and simulation results did not follow each other well. After removing the symmetry plane in the simulation, it was noticed that the antenna is no longer able to cover the bands. Then, different ideas were tried and eventually one of these ideas showed very promising results. Based on this idea, the proposed antenna in Design 1 may be manipulated by adding two shorted slot lines to each side of the antenna while the whole size of the antenna was changed to 30cm×30cm (Fig. 6.34). Moreover, by considering the positive impact of the ground plane extension in Design 2 for the touching effect reduction, a ground plane extension of 2.7 cm (i.e.,  $L_{\text{gext}} = 2.7$  cm) was added to the bottom edge where the coaxial feed line connects (Fig. 6.34).

The added slot lines are meandered and loaded with capacitors to increase the electrical length of the arms. The final shape for meandered line which is shown in Fig. 6.34 was achieved after extensive simulations. It should be noted that for this design, the simulation results showed that the top slots contribute effectively to the characteristics of the antenna, and thus they were kept.

With the new design, it was noticed that the input impedance of the antenna when all the PIN diodes are OFF can be tuned to be  $Z_{in} = R_{in} - jX_{in}$  where  $|R_{in} - 50| < \sim 50$  at (or in the vicinity of) a resonant frequency below 100 MHz. Then, if the imaginary part of the input impedance can be cancelled, a good impedance matching is achieved. As a solution, a lumped element which provides  $jX_{in}$  at (or in the vicinity of) the resonant frequency may be used. However, to keep the other bands intact, this lumped element should not be visible to other higher bands. Then, to address this issue, a type of reconfigurable serial matching circuit is embedded onto the CPW feeding line of the antenna, as shown in Fig. 6.34. This matching network is made of a series air gap which is loaded with serial inductor and switches. By considering this matching network in the design procedure, an optimization procedure can be performed to calculate width of the slot line, value of the series inductor, value of the capacitors, and their positions in order to have a deep resonance at a desired frequency below 100 MHz.



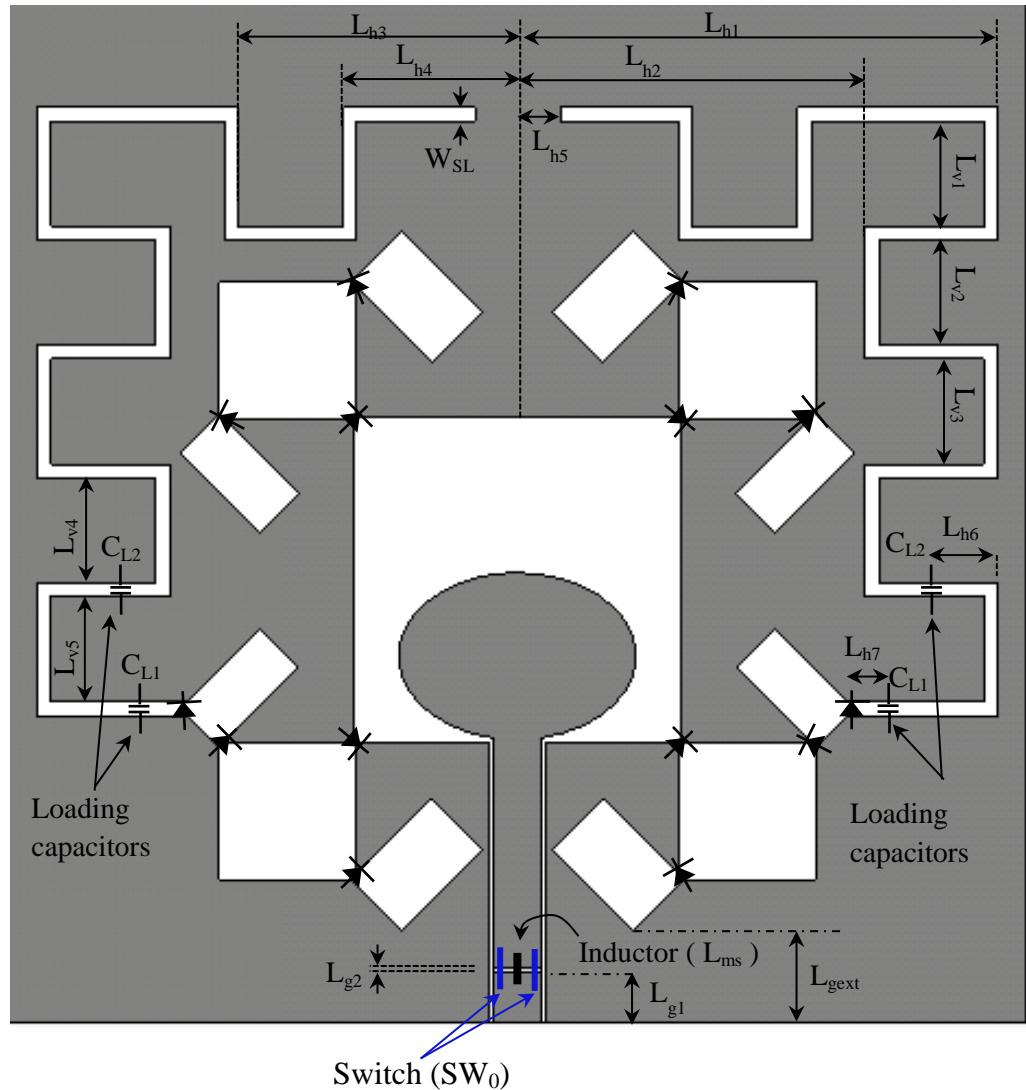


Figure 6.34. Schematic view of the proposed reconfigurable antenna to cover four bands at VHF/UHF/L (Design 3).

To continue the design, the desired lowest frequency is set to be  $\sim 50$  MHz (which is a public safety frequency [136]). Moreover,  $L_{g1}$  was selected in a way that the matching network is sufficiently away from the edge of the feeding line (i.e.,  $L_{g1}=1.5$  cm). Moreover, for the matching section, the gap size was selected to be reasonably small (i.e.,  $L_{g1}=0.1$  cm) in order to make its impact as small as possible on the higher bands. This matching circuit should only be effective for lowest band (i.e., Band 1) and it should

be “invisible” for other bands. Therefore, the smaller the gap is, it is easier to short the gap using a switch when covering the higher bands (i.e., Band 2, 3, 4). Later, based on an optimization procedure using PSO algorithm of CST Microwave Studio, the unknown parameters were calculated and are listed in Table 6.6. Moreover, the value for the capacitors was calculated as  $C_{L1} = C_{L2} = 27$  pF. Also, the inductor value in the matching network was estimated to be  $L_{ms} = 820$  nH.

Four different configurations are generated by turning ON and OFF PIN diodes and switch SW0 (Table 6.7). Since the switch SW0 is serial and on the signal trace, it is not practical to use PIN diode as switch. Instead, a switch which does not require DC biasing is preferred. Then, reed switch (876-KSK-1A04-1015 Mouser Electronics [141]) was selected to be used.

The simulation results for different configurations are shown in Fig. 6.35. As the figure shows, the antenna covers four different bands by switching between the configurations.

Table 6.6. Optimally calculated dimensions of reconfigurable antenna ( Design 3 )

Param.	$L_{h1}$	$L_{h2}$	$L_{h3}$	$L_{h4}$	$L_{h5}$	$L_{h6}$	$L_{h7}$	$L_{v1}$	$L_{v2}$	$L_{v3}$	$L_{v4}$	$L_{v5}$	$W_{SL}$
( cm )	14.15	10.25	8.25	5.15	1.25	3.1	1.6	3.3	3.3	3.3	3.3	3.3	0.2

The lowest band (Band 1), covers a frequency range from 48.33-48.53 MHz which means  $BW_p = 0.4$ . The second band (i.e., Band 2) covers from 342-362 MHz ( $BW_p = 5.68$ ). Band 3 covers from 414-496 MHz ( $BW_p = 18.02$ ). The highest band (i.e., Band 4) covers from 787-846 MHz and from 1082-1335 MHz.

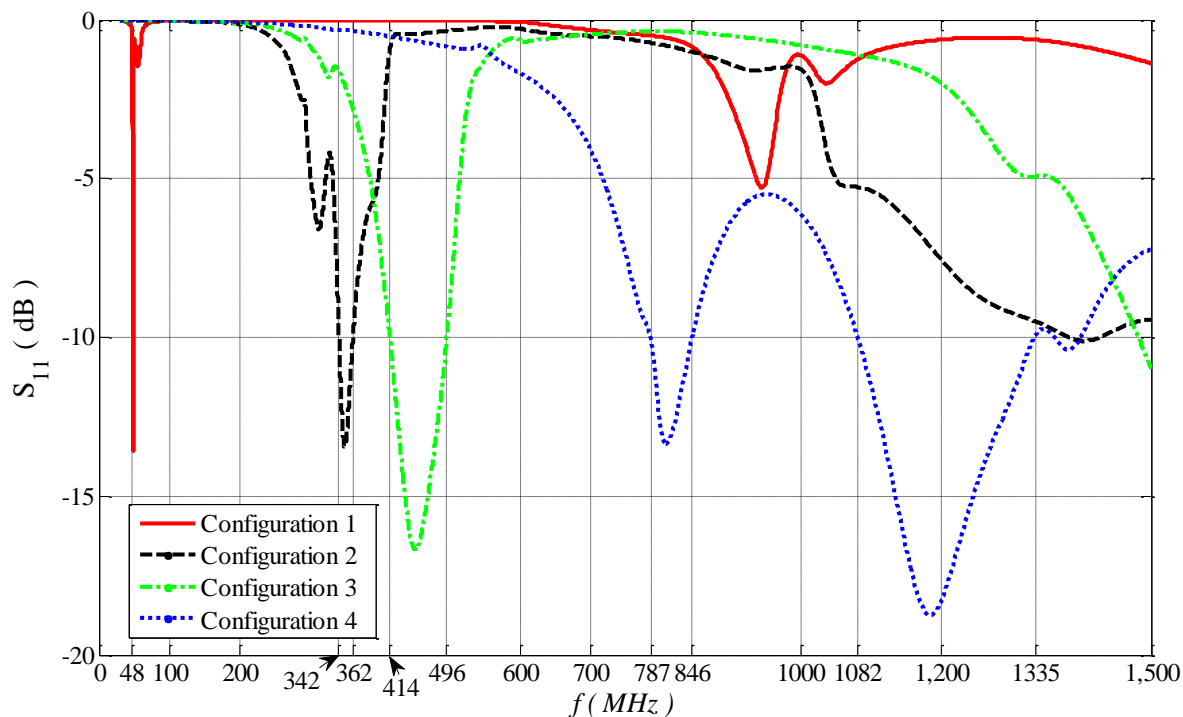


Figure 6.35. Simulation results for all the four different configurations of Design 3.

Table 6.7. Generating four different configurations by turning PIN diodes and SW0 ON and OFF ( Design 3 )

Conf.	1				2				3				4			
Diod e	D <sub>1</sub>	D <sub>2</sub>	D <sub>3</sub>	D <sub>4</sub>	D <sub>1</sub>	D <sub>2</sub>	D <sub>3</sub>	D <sub>4</sub>	D <sub>1</sub>	D <sub>2</sub>	D <sub>3</sub>	D <sub>4</sub>	D <sub>1</sub>	D <sub>2</sub>	D <sub>3</sub>	D <sub>4</sub>
Swi.	OFF				ON				ON				ON			
State	OF F	OF F	OF F	OF F	OF F	OF F	OF F	O N	OF F	O N	O N	O N	O N	O N	O N	O N

To provide a good insight about the role of matching network, the simulation result for Configuration 1 with the matching network is compared with the case where the matching network is replaced with a short circuit. The calculated input impedances at the place where the matching network starts (i.e., an  $L_{g1}$  distance from the feeding edge of

the antenna) for these two cases are plotted in Fig. 6.36. As the results show, without the matching network, the input impedance has a very large reactive part which creates matching problem. However, by adding an appropriate series inductor as the matching network, the reactive part is significantly reduced at around 48 MHz.

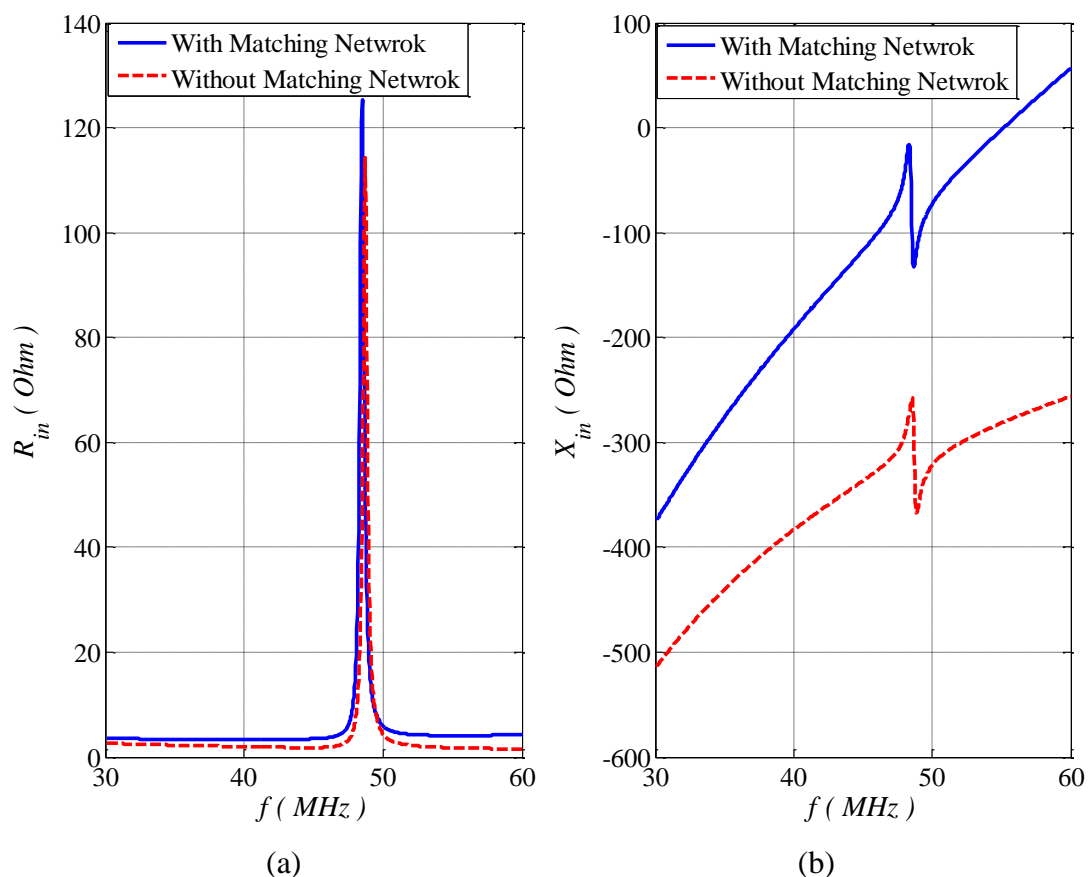


Figure 6.36. Input impedance of antenna (Design 3) with and without matching network presence. (a) real part, and (b) imaginary part.

The antenna (Design 3) was then implemented on FR4 PCB with the thickness of 62 mil. Similar biasing network as it was explained in Section 6.3.1.2 is used to install and feed the PIN diodes. The implemented antenna which has the loading capacitors and matching section is shown in Fig. 6.37. Moreover, an SMA connector is soldered to the feeding line. The antenna was then tested in anechoic chamber available in Electromagnetic Compatibility (EMC) lab at Missouri University of Science and

Technology (Fig. 6.38). Different configurations are produced by turning ON and OFF the PIN diodes using the NI DAQ and the computer. Instead of using the reed switch which was ordered but not available at the measurement time, copper tape was used. Therefore, to mimic the case where SW0 is ON, copper tape was used and when it was required to have open (i.e., SW0 in OFF state), copper tape was removed.

For the first configuration, the measured reflection coefficient is shown in Fig. 6.39. CST Microwave Studio simulation results are also shown in this figure for comparison. In the magnified plot (which is embedded inside the original plot), one can clearly see that the measured  $S_{11}$  has a resonant frequency at  $\sim 59.55$  MHz while the simulation result predicts a resonance at 48.33 MHz.

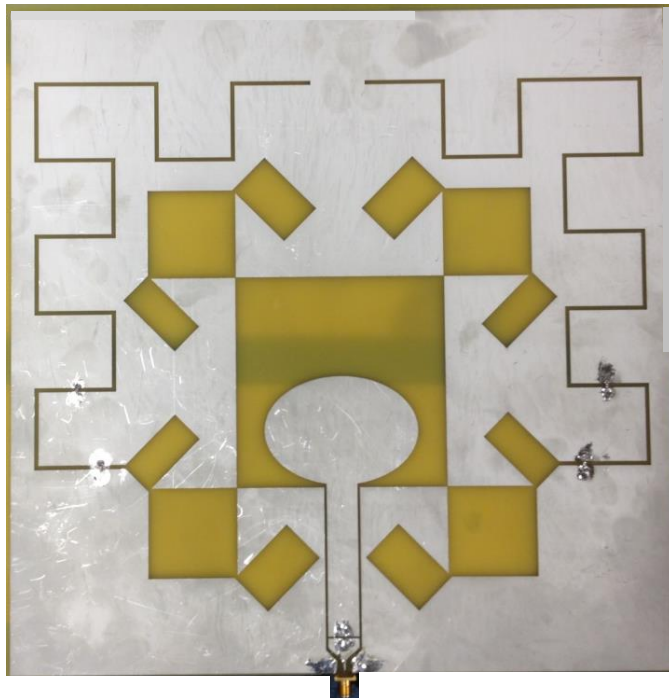


Figure 6.37. Implemented designed antenna (Design 3) on 62 mil FR4 substrate.



Figure 6.38. Antenna Design 3 with all the PIN diodes and DC bias lines installed (placed on a stand inside anechoic chamber).

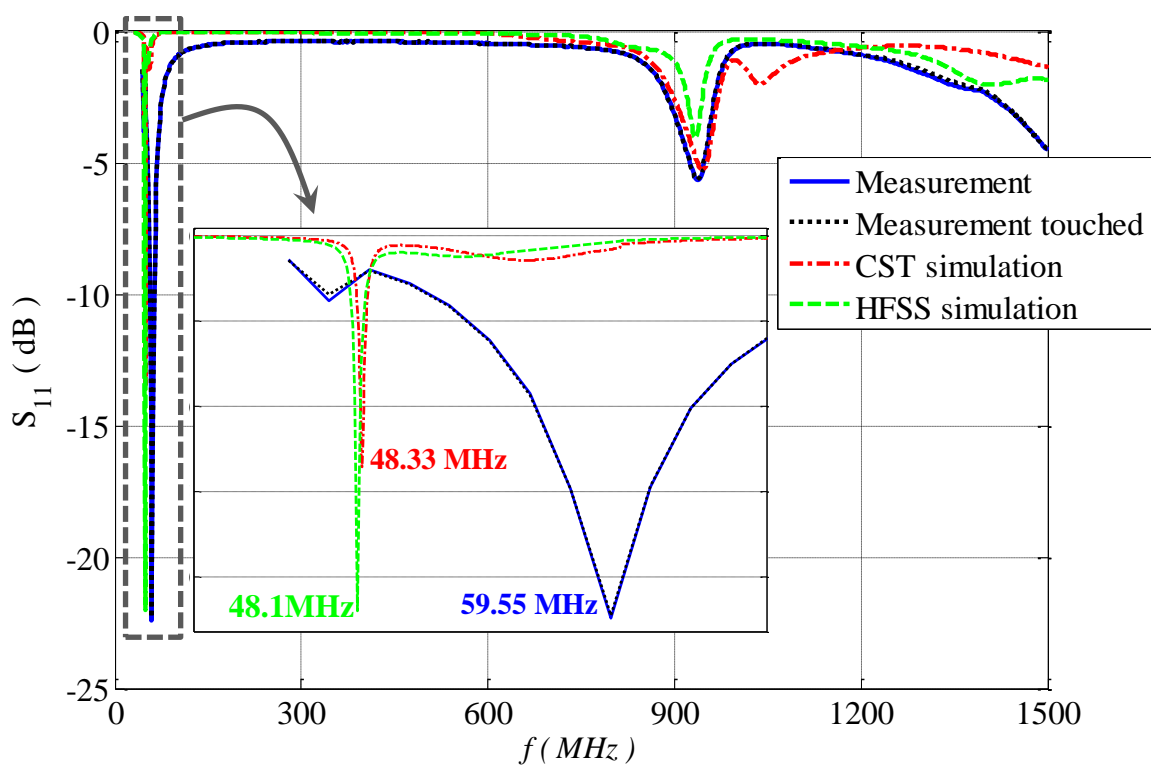


Figure 6.39. Reflection coefficient for antenna Design 3 (Configuration 1): measurement with and without touching versus simulations with CST Microwave Studio and HFSS.

For the second configuration, the measured reflection coefficient is shown in Fig. 6.40. Based on this result, antenna Design 3 at Configuration2 covers from 314-398 MHz (Band 2). CST Microwave Studio simulation result is also repeated in this figure for comparison. The simulation and measurement results are in good agreement. Moreover, the measured reflection coefficient while the feeding SMA cable was touched shows a negligible effect.

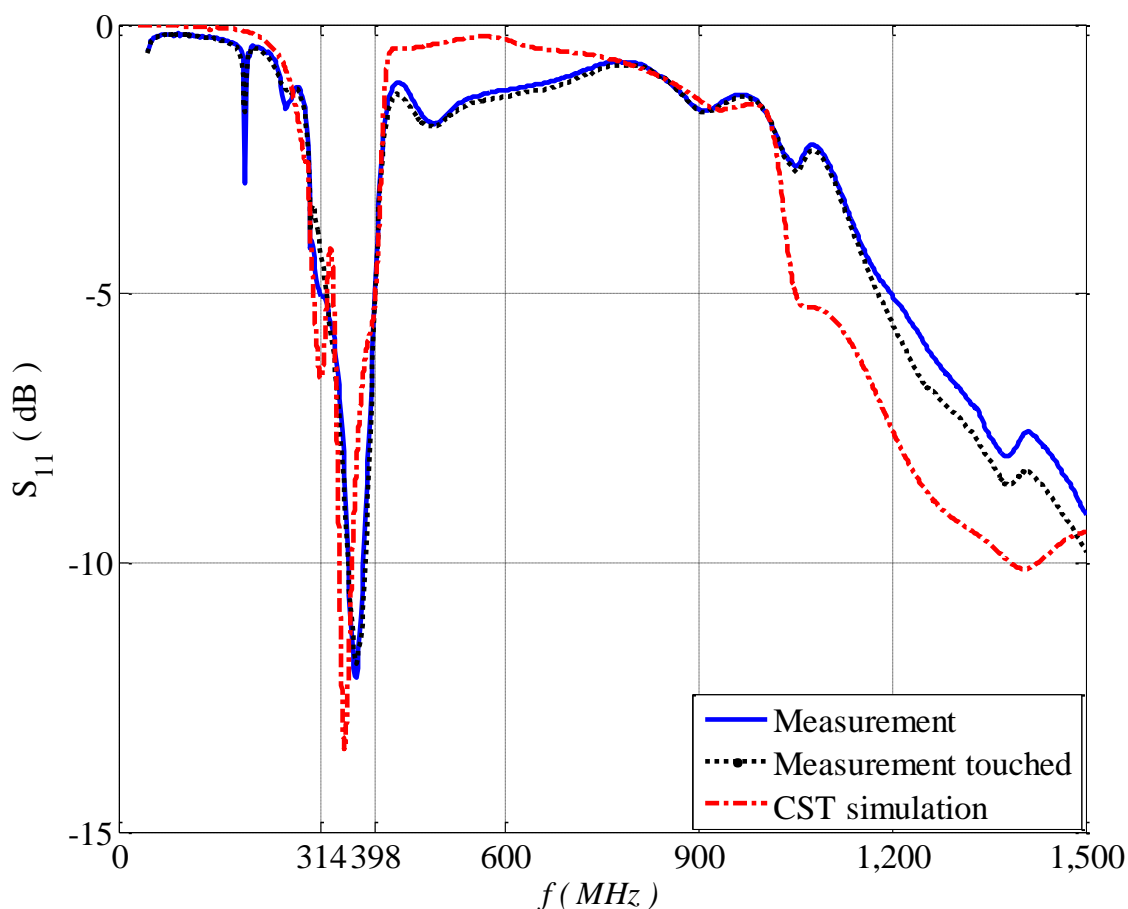


Figure 6.40. Reflection coefficient for antenna Design 3 (Configuration 2): measurement with and without touching versus simulations with CST Microwave Studio.

For the third configuration, the measured reflection coefficient is shown in Fig. 6.41 which shows that the covered band (Band 3) is from 430-496 MHz. CST Microwave Studio simulation results are also shown in this figure for comparison. Rather than a very

slight frequency shift in the beginning and end of Band 3, the simulation and measurement results are in good agreement. Moreover, the measured reflection coefficient with touched feeding SMA cable proves that the touching effect is negligible.

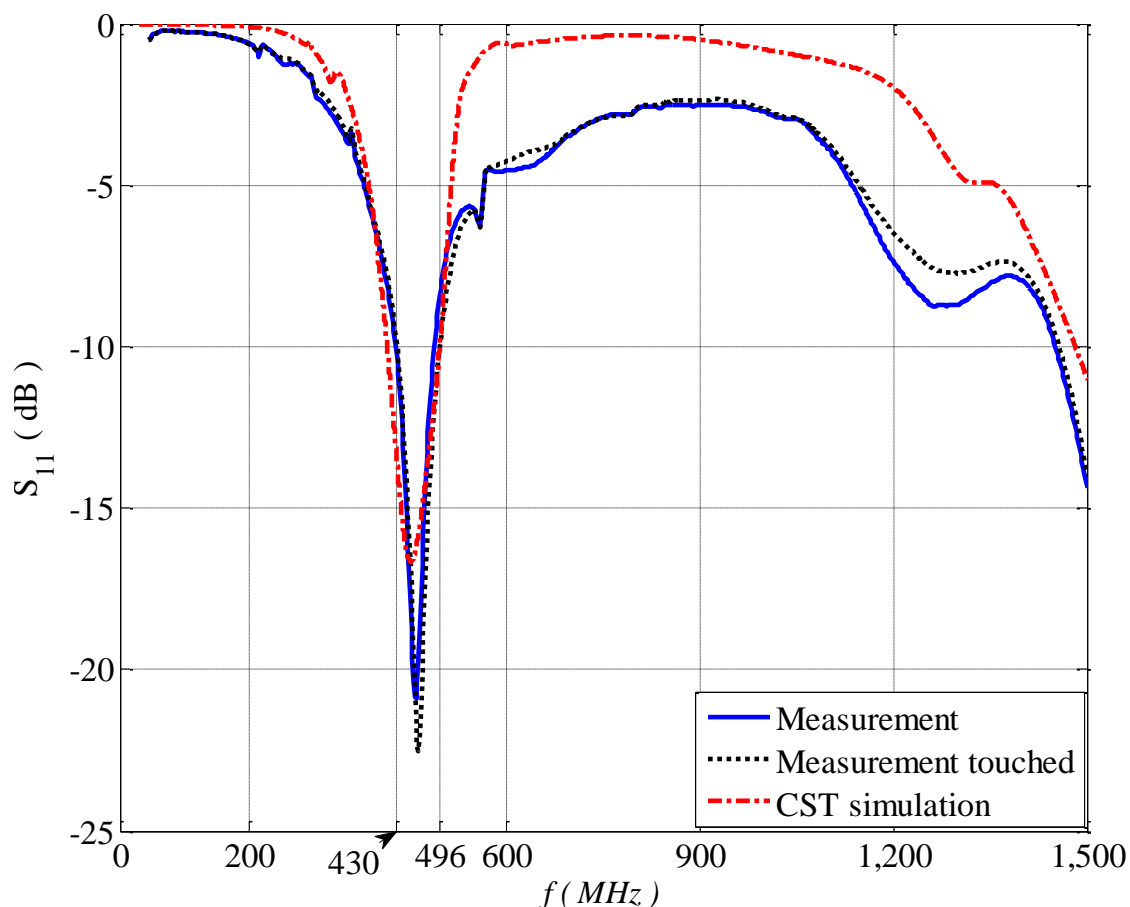


Figure 6.41. Reflection coefficient for antenna Design 3 (Configuration 3): measurement with and without touching versus simulations with CST Microwave Studio.

For the fourth configuration, the measured reflection coefficient is shown in Fig. 6.42 which shows that the covered band (Band 4) is from 792-950 MHz. CST Microwave Studio simulation results are also shown in this figure for comparison. It is clear that both simulation and measurement results are in good agreement in the beginning of Band 4, however, as the frequency increases, the simulated and measured frequency responses begin to differ. In the simulations, the feeding line was considered rectangular and a



waveguide port was used to excite the antenna in CST Microwave Studio. However, practically to install the SMA connector on the trace, it is required to taper the line (Fig. 6.43 (a)-(b)). To test the effect of tapering, another simulation was performed while the tapered trace was used. The results which are also presented in Fig. 6.42 do not show any improvement over the first simulation (i.e., without tapering) in comparison with the measurement result. As it was mentioned for Design 1, modeling a coaxial connector with a waveguide port in CST Microwave Studio can be a source of this difference. This was not an issue at the lower frequencies. It should be mentioned that touching does not change the antenna response and so it is not reported.

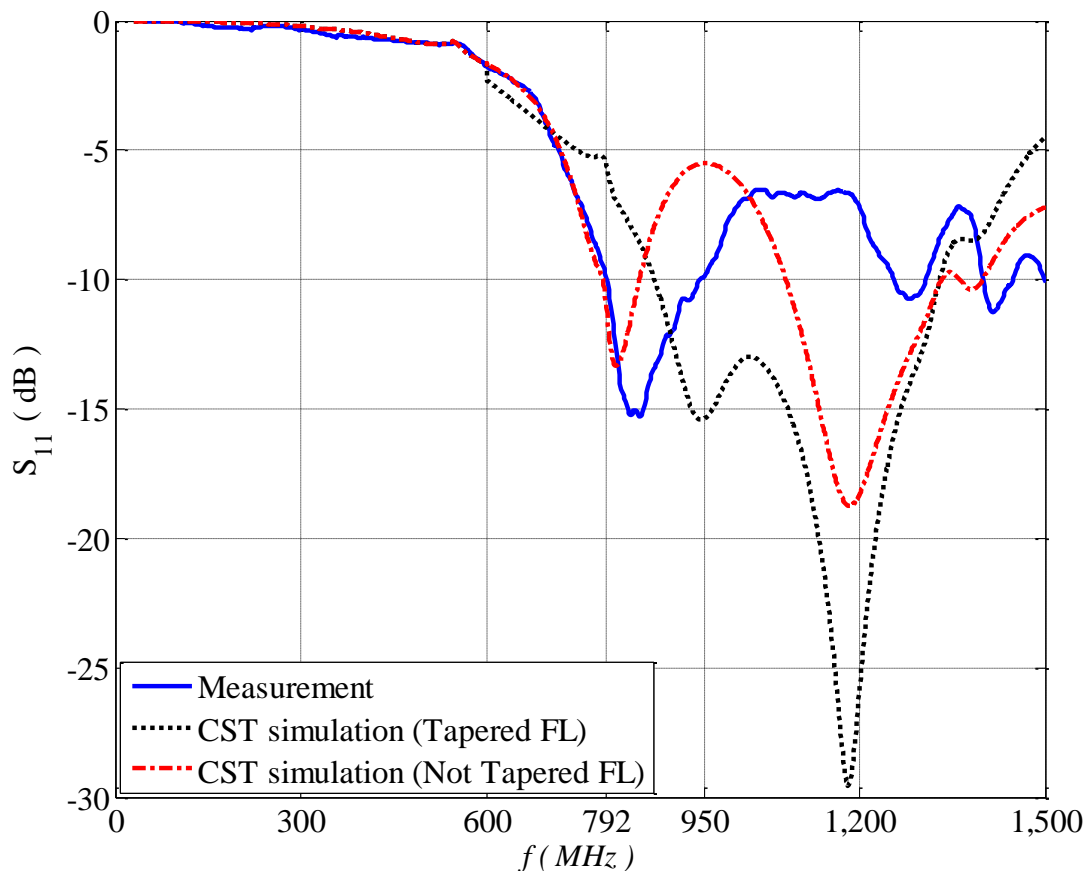


Figure 6.42. Reflection coefficient for antenna Design 3 (Configuration 4): measurement versus CST simulations with and without tapered feed line (FL).

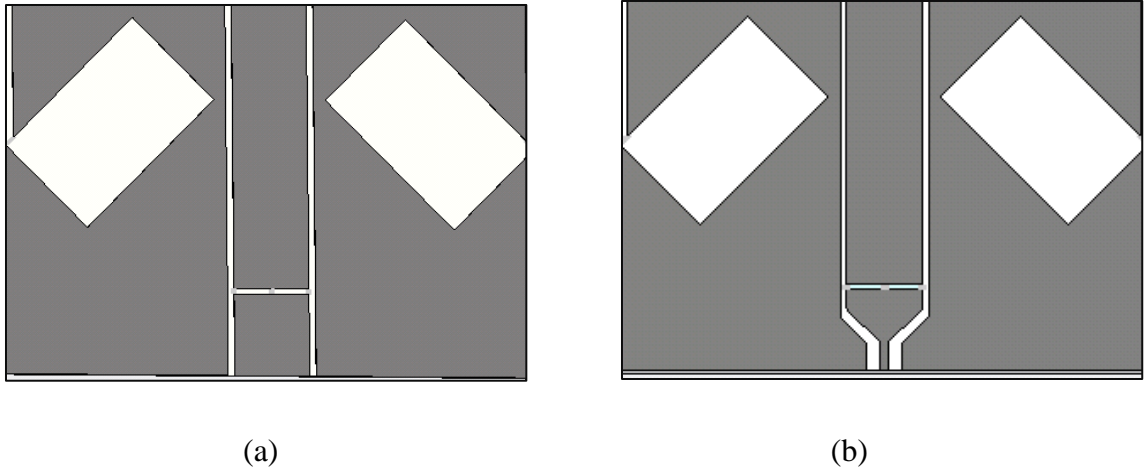


Figure 6.43. Feeding line for the antenna Design 3. (a) without any tapering, and (b) tapered.

**6.3.4. Gain Pattern Measurement.** To perform pattern and gain measurements, the anechoic chamber in EMC lab was used. Since Design 3 is considered as an evolved version of Designs 1 and 2, this antenna was selected and its pattern and gain were measured.

For the gain measurements, a reference antenna with a known gain and pattern is usually required. This reference antenna should provide a reasonable gain at the measurement frequency band. Here, since the antenna covers a wide frequency range from 50 MHz to 1 GHz, finding a conventional antenna with a known reasonable gain over the entire band is a challenge. Therefore, a commercial biconical antenna namely BicoLOG 20300 was used [142]. This antenna which is shown in Fig. 6.44 is designed for applications such as EMC. Its gain over a wide range of frequencies (i.e., from 20 MHz-3 GHz) is provided in datasheet [142] and it is plotted in Fig. 6.45. However, since the pattern of the antenna is not provided, it was decided to measure the pattern of this antenna to make sure that it does not have any null at the angle where measurement will be performed. To perform the pattern measurement, a measurement setup is required where one antenna can be kept at a fixed position and other antenna may be rotated around its center. The anechoic chamber in EMC lab has a rotatory disc which is

controlled by a step motor and provides a 360 degrees rotation option (Fig. 6.44). Moreover, the distance between two antennas (center-to-center) is set as 2.28 m.

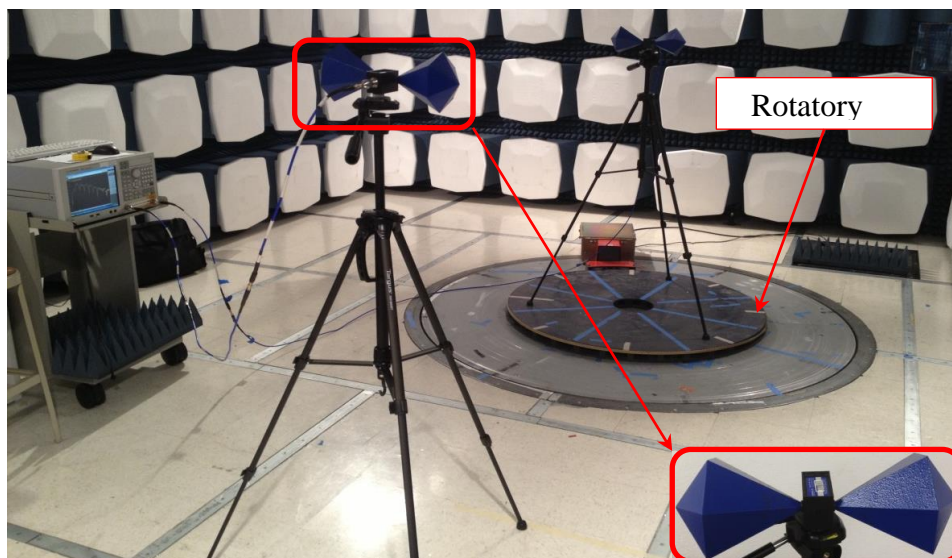


Figure 6.44. Measurement setup to measure pattern of commercially available BicoLOG20300 antenna.

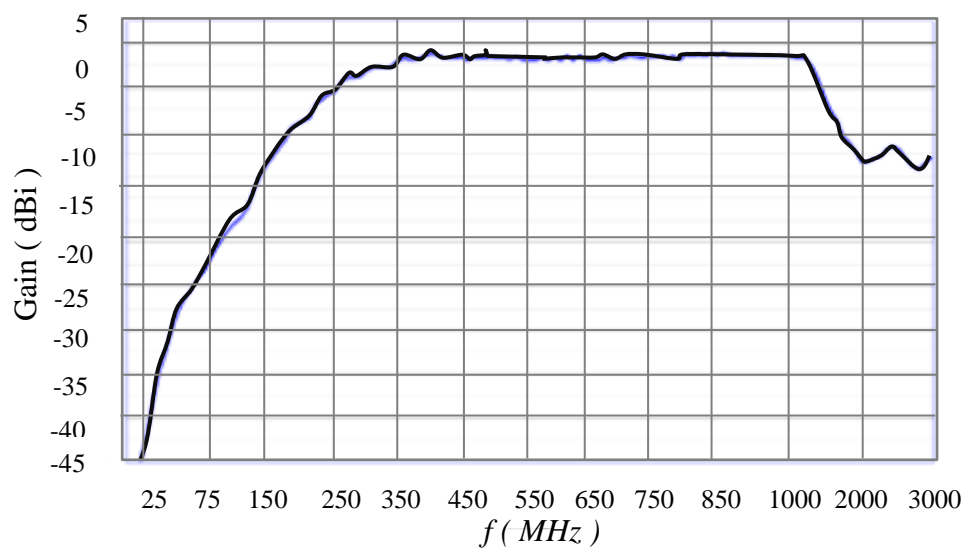


Figure 6.45. BicoLOG20300 antenna's gain versus frequency [142].

The pattern of the Biconical antenna was measured in two configurations, namely: horizontal ( $\theta = 90^\circ$ ) and vertical ( $\theta = 0^\circ$ ). The schematic of the measurement setup is also presented in Fig. 6.46 which shows both of these configurations and presents angle definitions.

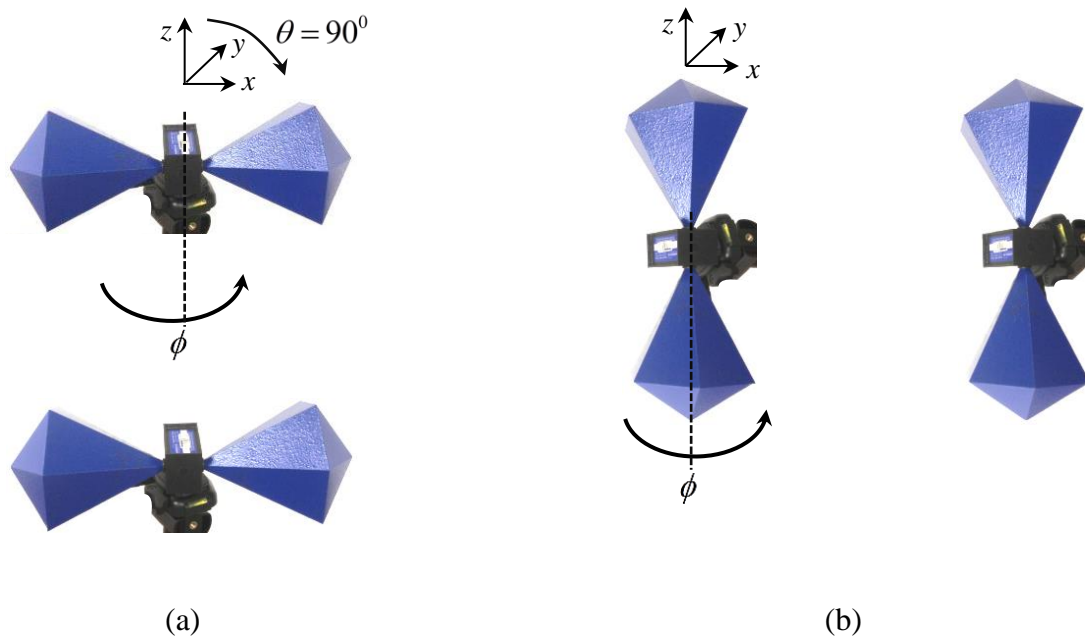


Figure 6.46. BicoLOG pattern measurement setup. (a) horizontal, and (b) vertical.

The measured normalized pattern for horizontal configuration at 60, 350, 460, and 860 MHz are plotted in Fig. 6.47. As it was expected, the maximum value of the pattern occurs at  $\phi = 0^\circ$  and  $\phi = 180^\circ$ . The measured normalized pattern for the vertical configuration is also plotted in Fig. 6.48. It was expected to see an omnidirectional pattern in the vertical configuration. However, the measured pattern is somewhat directive. This may have occurred due to the rotating antenna being off from the center of the rotating disc (table).

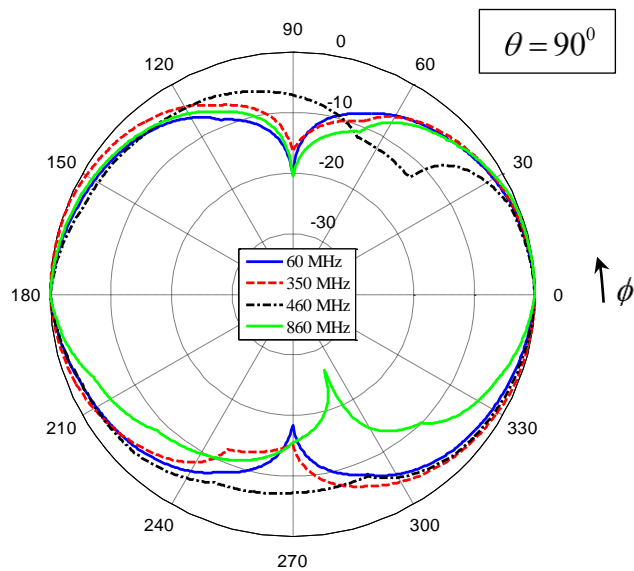


Figure 6.47. BicoLOG's measured normalized horizontal pattern at 60, 350, 460, and 860 MHz.

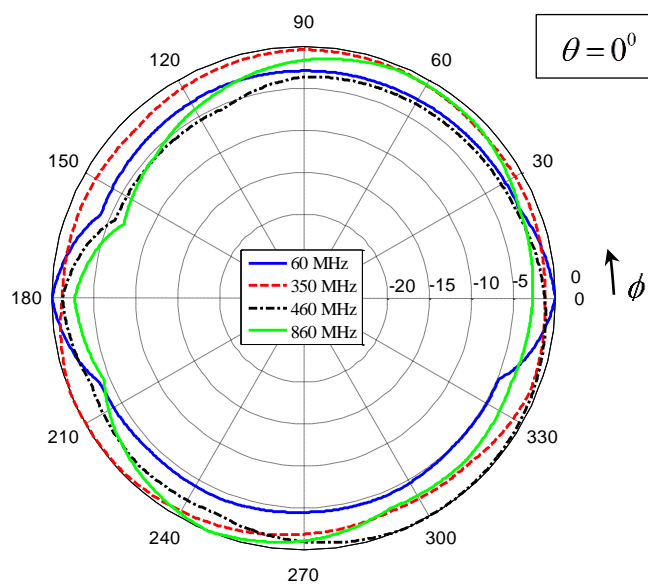


Figure 6.48. BicoLOG's measured normalized vertical pattern at 60, 350, 460, and 860 MHz.

Having the patterns of BicoLOG antenna in horizontal and vertical configurations shows that antenna does not have any nulls. Moreover, having access to the gain information, makes this antenna a good candidate to be used as a reference antenna to measure the designed antenna (Design 3) pattern and gain. At two planes (i.e., XY- and XZ-planes), it is desired to measure the gain pattern (gain versus angle). In here, in order to measure cross-polarization as well as co-polarization, four different cases are considered. First, the designed and the reference antennas are both placed in vertical configuration. Second, the designed antenna is vertical but the reference antenna is in horizontal configuration. These two cases will be used to measure XY-plane pattern. Third, the designed and the reference antennas are both in horizontal configuration. Fourth, the designed antenna is horizontal but the reference antenna is in vertical configuration. These two latest cases can be used for XZ-plane pattern measurement. These different configurations are shown in Fig. 6.49.

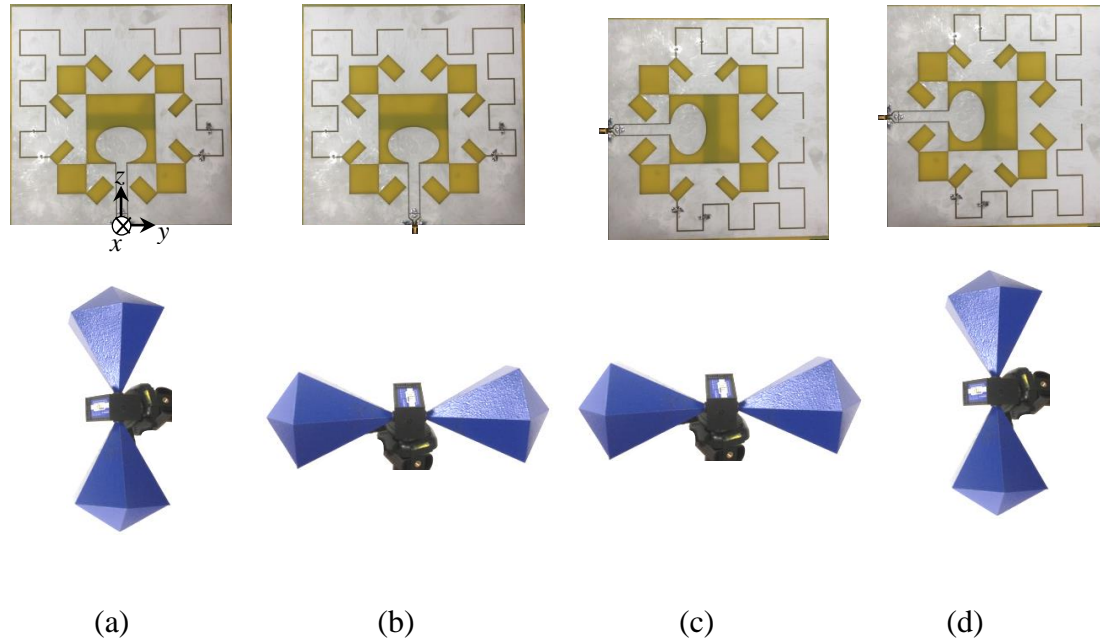


Figure 6.49. Gain pattern measurement setup for antenna Design 3 at four different cases (co- and cross-polarizations in XY- and XZ-planes).

Moreover, two of the actual measurement setups inside of the anechoic chamber are shown in Fig. 6.50 from different angles.



(a)



(b)

Figure 6.50. Two measurement setups to measure designed antenna (Design 3) pattern.

To calculate the gain pattern for the first case, the designed antenna which is called antenna under test (AUT) for future references, is placed at an initial position. The initial position is selected in a way that both antennas (i.e., AUT and reference antennas) face each other ( $\phi = 0^\circ$ ). Then, AUT rotates counter clockwise (CCW). At every step size (i.e., 22.5 degrees), antenna stops and two-port scattering parameters are measured and

saved using a vector network analyzer. This procedure continues until AUT reaches its initial position ( $\phi = 360^\circ$ ). It should be noted that the distance between two antennas was kept as 2.28 m. Then, using the following equation, gain of AUT ( $G_{AUT}(\theta, \phi, f)$ ) is calculated per each angle and frequency:

$$G_{AUT}(\theta, \phi, f) = G_{Reference}(\theta, \phi, f) \frac{S_{21}^{AUT-Bi}(f)}{S_{21}^{Bi-Bi}(f)} \quad (95)$$

where  $G_{Reference}(\theta, \phi, f)$  stands for reference antenna gain. Also,  $S_{21}^{Bi-Bi}(f)$  is measured when two BicoLOG antennas were placed vertically 2.28 m apart (Fig. 6.46 (b)). Moreover,  $S_{21}^{AUT-Bi}(f)$  is measured when rotating BicoLOG was replaced with vertically-positioned AUT (Fig. 6.49 (a)). It should be mentioned that (95) is correct only if the distance between AUT and BicoLOG antenna is kept same as the distance between BicoLOG and BicoLOG antennas.

For each configuration, one frequency is selected and the gain pattern is plotted for that frequency. The selected frequencies are: 60, 350, 460, and 860 MHz for Configurations 1, 2, 3, and 4, respectively. The measured XY-plane co-polarized gain patterns (both AUT and BicoLOG vertical) are shown in Figs. 6.51 for all the selected frequencies. The calculated gain pattern using CST Microwave Studio simulator is also plotted in the same figures for comparison. At 60 MHz, the simulated gain pattern is omnidirectional. The measured gain pattern shows an omnidirectional behavior as well. However, the simulated maximum gain is about -38 dB while the measured maximum gain is -23 dB. As it was mentioned earlier, the resonant frequency of the designed antenna shifted from 48 MHz in the simulation to 60 MHz in the measurement. Then, the calculated gain pattern of the antenna using CST Microwave Studio at 48 MHz is also plotted in Fig. 6.51 (a) which shows a maximum value of -18.7 dB. There are a few reasons to explain the differences between the measured and simulated results. First, the anechoic chamber in EMC lab is not suitable for frequencies below 600 MHz. Second, BiconLOG data sheet only provides a graph for the gain of the antenna (Fig. 6.45) and finding the gain from this graph is not an accurate way to do so. Third, any small alignment mismatch and distance between the center of the AUT and center of the



rotating table may also contribute to this discrepancy. Fourth, the anechoic chamber does not have any absorbers on the ground and the ground path reflections can also affect the results. This ground reflection plays a more significant role when antennas are parallel to the ground plane.

When the antenna is operating in Band 2, the gain pattern was measured at 350 MHz. The difference between the simulation and measurement is insignificant. The maximum gain from simulation is 0.8 dB and from measurement is -1.8 dB (Fig. 6.51 (b)). For Band 3, the gain pattern was measured at 460 MHz, the difference between the simulation and measurement is negligible (Fig. 6.51 (c)). The maximum gain from simulation is 2.7 dB and from measurement is 2.3 dB. For Band 4, the gain pattern was measured at 860 MHz, the simulation and measurement results are in a good agreement (Fig. 6.51 (d)). The maximum gain from simulation is 0.8 dB and from measurement is 2.7 dB.

The same approach was followed for the second case to measure cross-polarization gain pattern in XY-plane for AUT. When the antenna is operating in Band 1, the gain pattern is measured at 60 MHz which is compared with the simulation results at 48 MHz and 60 MHz in Fig. 6.52. There is a significant difference between the shape of the pattern achieved using simulation and measurement. Same reasons provided before can be used to explain this disagreement. The maximum measured gain at 60 MHz is -29 dB while the maximum gain from simulation is -32 dB and -41 dB at 48 and 60 MHz, respectively.

Next, the operating band was switched to Band 2, and its gain was measured at 350 MHz. The measurement and simulation results are compared in Fig. 6.52 (b). The shapes of the patterns are not in a good agreement. The maximum measured cross-polarized gain at 350 MHz is -13 dB while the maximum cross-polarized gain from simulation is -26 dB. The measured cross-polarized gain is even higher than co-polarized gain which does not seem right. Ground effect and possible misalignments could be the major reasons for this difference between measurement and simulation results. In Band 3, the measured cross-polarized gain pattern and simulated cross-polarized gain pattern at 460 MHz are shown in Fig. 6.52 (c). Still the difference between the results is significant. For Band 4 where the measurement and simulation results are compared at 860 MHz

(Fig. 6.52 (d)), the difference is even worse. Therefore, these sets of measurements for cross-polarization may not be trusted.

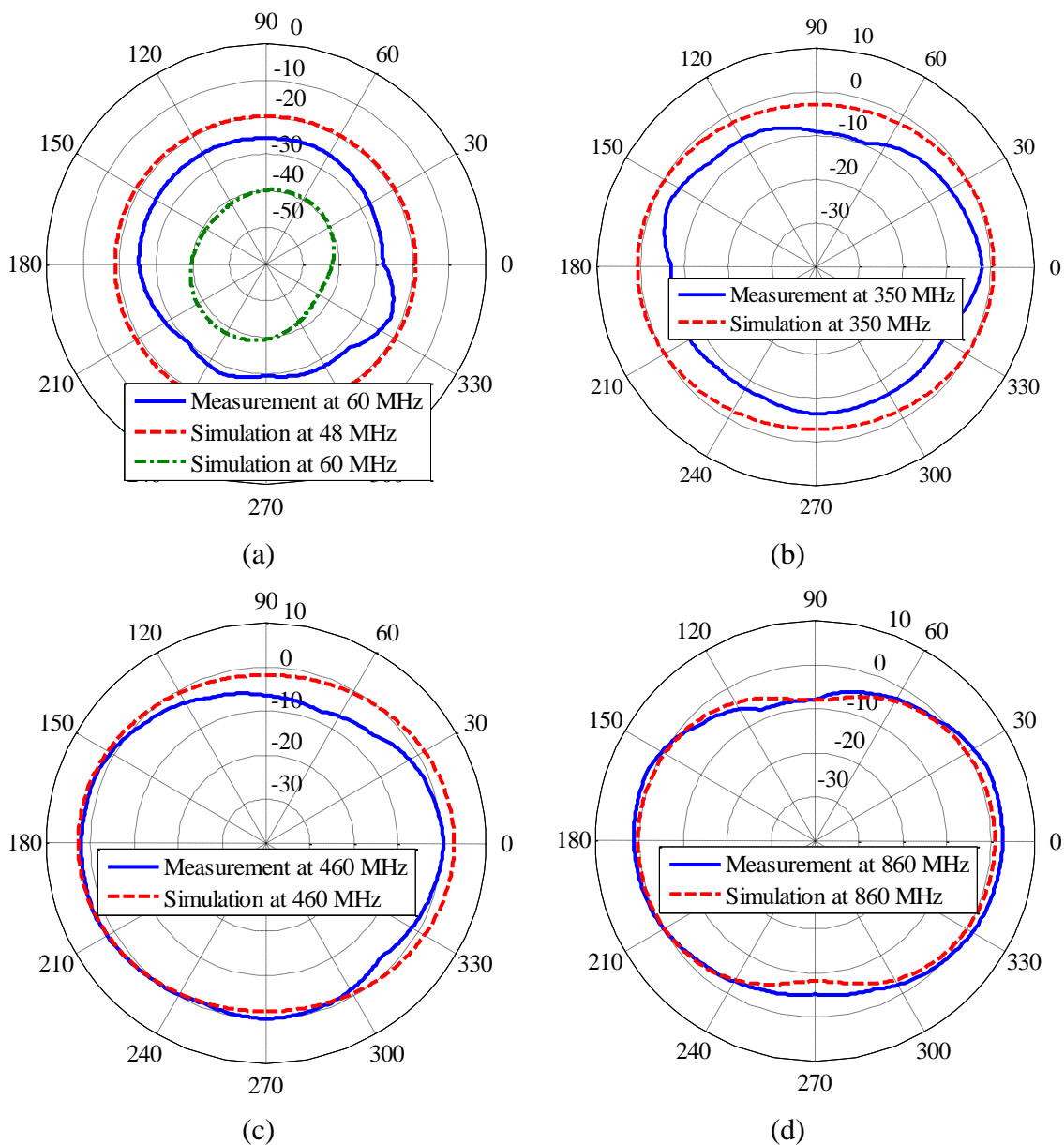


Figure 6.51. Measured and simulated co-polarized XY-plane gain of antenna Design 3. (a) Band 1 for 48 and 60 MHz (b) Band 2 for 350 MHz, (c) Band 3 for 460 MHz, (d) Band 4 for 860 MHz.

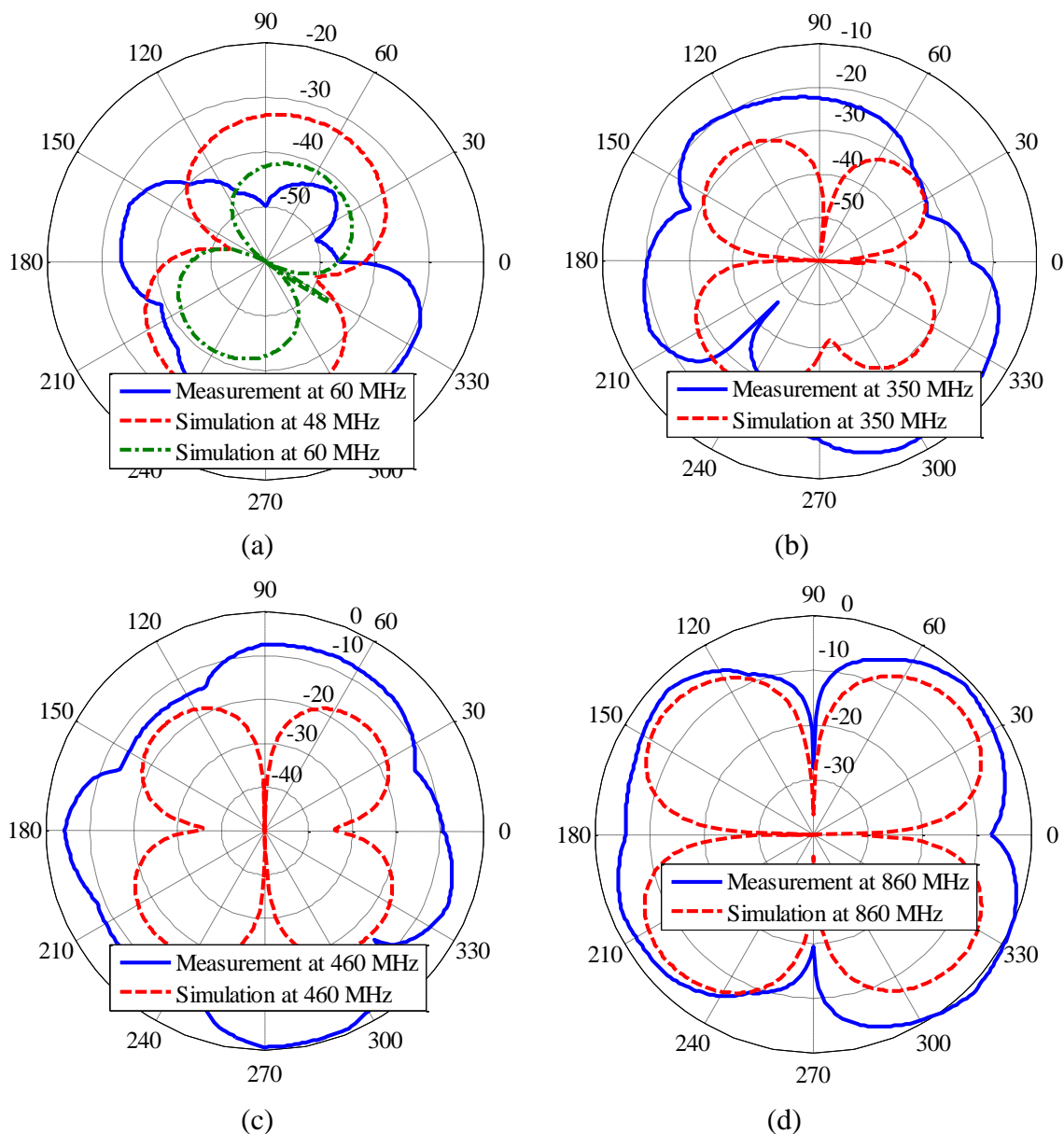


Figure 6.52. Measured and simulated cross-polarized XY-plane gain of antenna Design 3. (a) Band 1 for 48 and 60 MHz (b) Band 2 for 350 MHz, (c) Band 3 for 460 MHz, (d) Band 4 for 860 MHz.

Following the same approach, co-polarization gain pattern in XZ-plane for AUT is measured using the measurement setup shown in Fig. 6.49 (c). When the antenna is operating in Band 1, the gain pattern is measured at 60 MHz which is compared with the simulation results at 48 MHz and 60 MHz in Fig. 6.53. There is a difference between the shape of the pattern obtained by simulation and measurement. Same reasons provided

before can be used to explain this disagreement. The maximum measured gain at 60 MHz is -24 dB while the maximum gain from simulation is -18.5 dB and -38.8 dB at 48 and 60 MHz, respectively. Next, the operating band of the antenna is switched to Band 2, and its gain was measured at 350 MHz. The measurement and simulation results are compared in Fig. 6.53 (b). The shape of the patterns follows each other but the existing nulls in simulation results do not appear in the measurement results. The maximum measured gain at 350 MHz is -8.6 dB while the maximum gain from simulation is 0.8 dB. In Band 3, the measured gain pattern and simulated gain pattern at 460 MHz are shown in Fig. 6.53 (c) which are in a reasonable agreement. The maximum measured gain at 460 MHz is 7.7 dB while the maximum gain from simulation is 2.7 dB. For Band 4, the measurement and simulation results are compared at 860 MHz (Fig. 6.53 (d)). There is a very good agreement between measurement and simulation results. The maximum measured gain at 860 MHz is 0 dB while the maximum gain from simulation is 2.9 dB.

As the last sets of measurements, cross-polarization gain pattern in XZ-plane for AUT was measured using the measurement setup shown in Fig. 6.49 (d). When the antenna is operating in Band 1, the gain pattern is measured at 60 MHz which is compared with the simulation results at 48 MHz and 60 MHz in Fig. 6.54. There is a difference between the simulation and measurement. The maximum measured cross-polarized gain at 60 MHz is -19.7 dB while the maximum cross-polarized gain from simulation is -41.6 dB and -45.9 dB at 48 and 60 MHz, respectively. Next, the operating band of the antenna is switched to Band 2, and its gain is measured at 350 MHz. The measurement and simulation results are compared in Fig. 6.54 (b). The shape of the patterns does not follow each other well. The maximum measured gain at 350 MHz is -13.6 dB while the maximum gain from simulation is -46 dB. In Band 3, the measured gain pattern and simulated gain pattern at 460 MHz are shown in Fig. 6.54 (c) which are not in a reasonable agreement. The maximum measured gain at 460 MHz is -11.2 dB while the maximum gain from simulation is -32.5 dB. For Band 4, the measurement and simulation results are compared at 860 MHz (Fig. 6.54 (d)). There is not a good agreement between measurement and simulation results. The maximum measured gain at 860 MHz is -2 dB while the maximum gain from simulation is -40.7 dB.

Despite a significant disagreement between cross-polarization measurement and simulation results in both XY- and XZ-planes, the co-polarization measurement and simulation results are in a reasonable agreement.

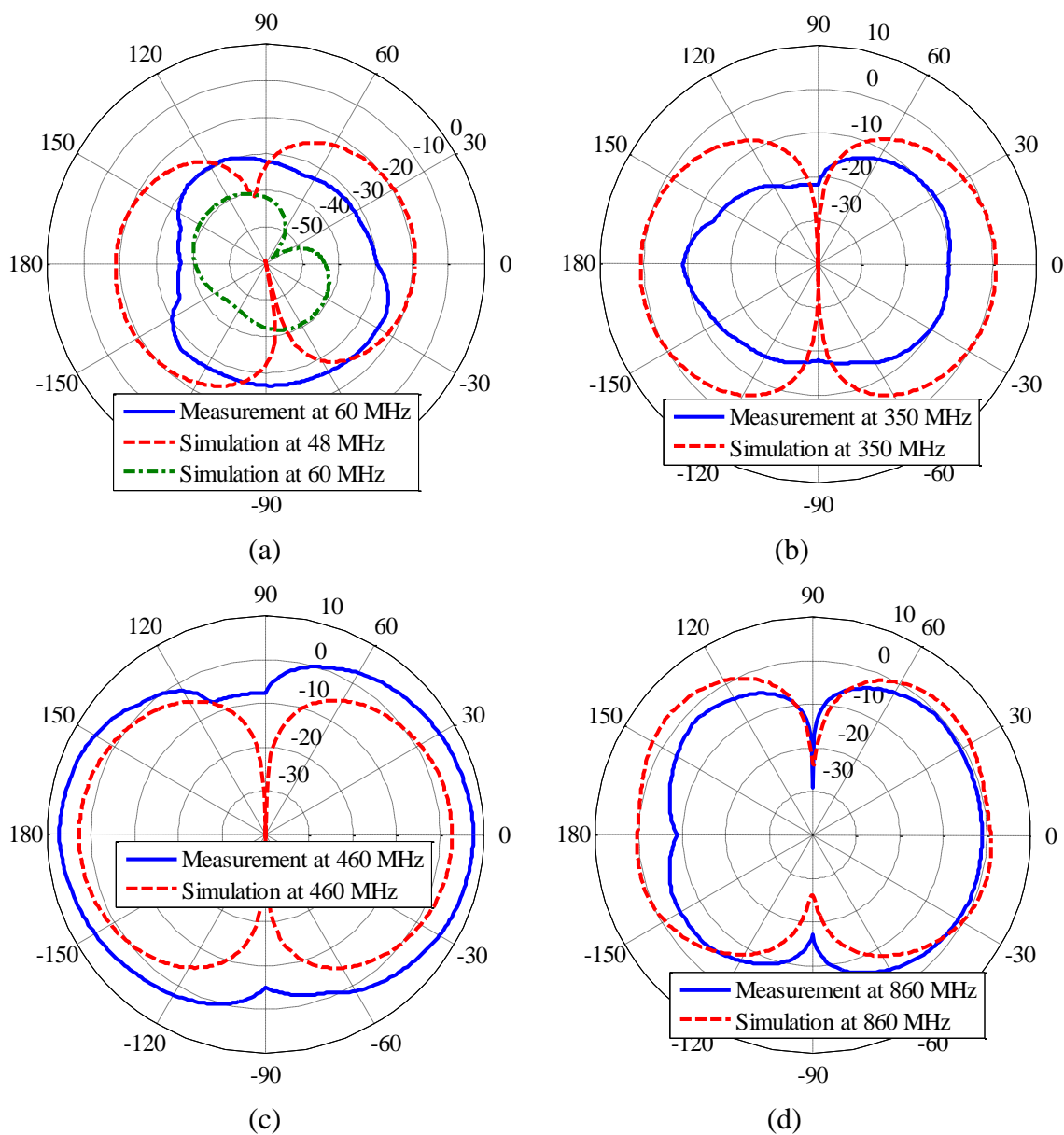


Figure 6.53. Measured and simulated co-polarized XZ-plane gain of antenna Design 3. (a) Band 1 for 48 and 60 MHz (b) Band 2 for 350 MHz, (c) Band 3 for 460 MHz, (d) Band 4 for 860 MHz.

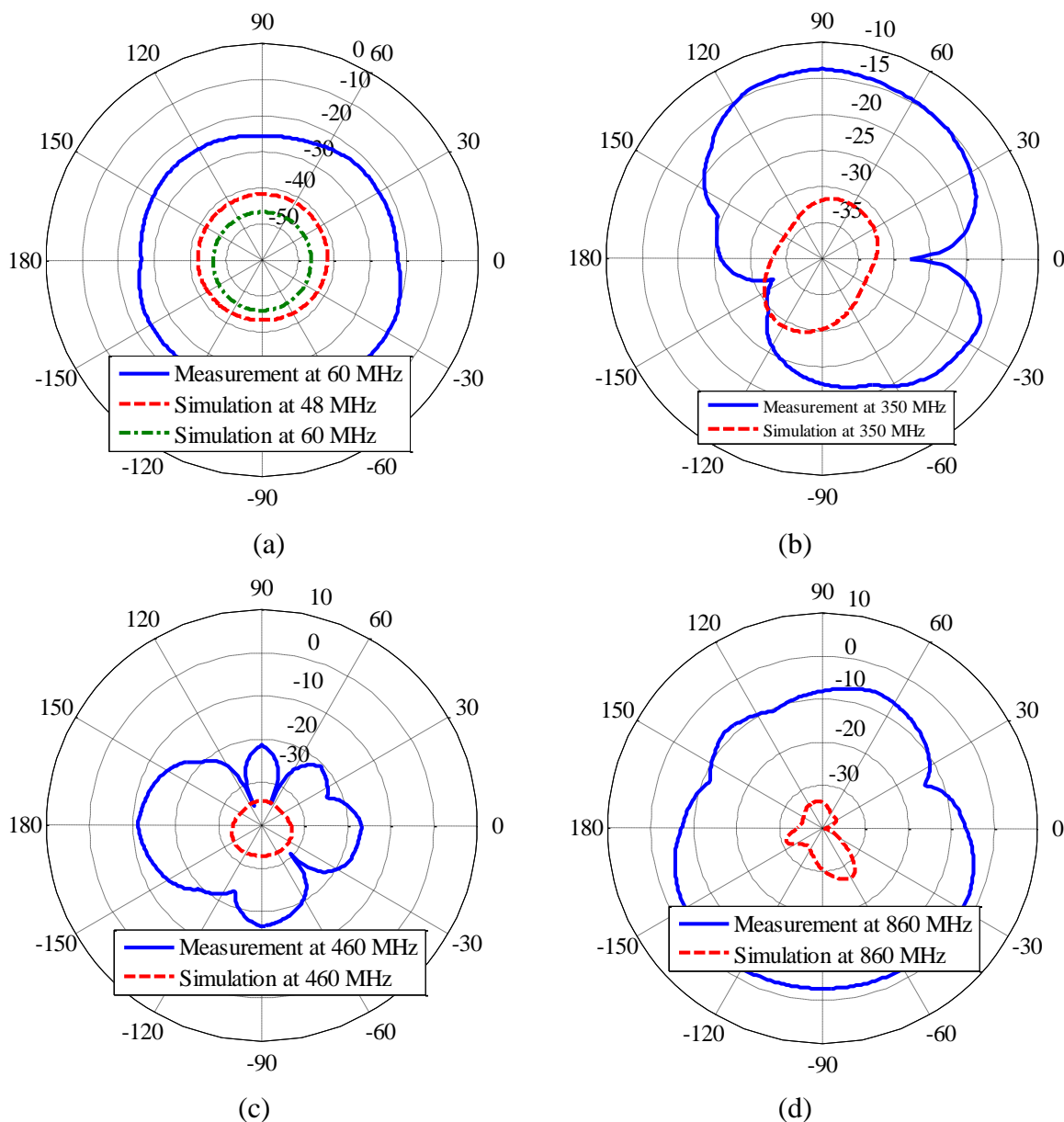


Figure 6.54. Measured and simulated cross-polarized XZ-plane gain of antenna Design 3. (a) Band 1 for 48 and 60 MHz (b) Band 2 for 350 MHz, (c) Band 3 for 460 MHz, (d) Band 4 for 860 MHz.

## 6.4. CONCLUSION

In this section, a methodical procedure for designing reconfigurable antennas was introduced. In term of a design example, the application of the introduced algorithm was explained. As a result, three novel reconfigurable CPW-fed slot antennas were designed, simulated, and tested. The first design (Design 1) was intended to cover three bands in

UHF/L region including public safety bands. The second antenna (Design 2) which adds a modification over Design 1, was supposed to cover one extra band at VHF (i.e., ~100 MHz). However, later, it was found out that in the simulation phase a wrong boundary condition was assumed. This assumption ruined the whole design procedure. Later, by considering Design 1 and 2, and by incorporating some new ideas for miniaturization, a new design (Design 3) was achieved which not only could cover three different bands in UHF/L, but also its lowest operating frequency was extended to below 60 MHz. The measured reflection coefficients and simulated reflection coefficients were in a reasonable agreement. The gain pattern measurement for the final antenna was also performed inside anechoic chamber. The co-polarized gain pattern was in a reasonable agreement with the simulation results, but, the cross-polarization gain pattern was somehow far from the measurement. The ground (floor) effect, misalignment between the antenna under test and reference antenna, and the low quality of the anechoic chamber for frequencies lower than 600 MHz could have contributed dominantly to this error between simulation and measurement results.

## 7. SUMMARY AND FUTURE WORK

In the past decades, development of microwave and millimeter wave imaging systems has attracted attentions of those who involved in the field of nondestructive testing and evaluation, applied geophysics, biomedical, and radar and remote sensing. These applications use microwave imaging techniques for the purpose of detecting and evaluating hidden or embedded objects in a structure. The structure has been commonly assumed to be homogeneous and lossless (or low loss). However, new applications such as nondestructive testing and evaluation of composite structures which are made of different layers of dielectric materials, smart environment with embedded wireless sensor networks, navigation and wireless communication systems, through-wall imaging, intra-wall imaging, structural health monitoring, and medical imaging have introduced new demands for robust imaging techniques applicable to inhomogeneous media. Addressing these new demands requires a significant improvement over the currently-available microwave imaging systems. On the other hand, any microwave imaging system can be divided into two parts namely hardware part and post-processing part. The hardware portion is composed of the measurement setup (i.e., sample and scanning table), antenna, measurement instrument, and recording tools. This portion collects data from the sample under test. In the synthetic aperture-based data collection methods, an appropriate antenna scans over an area above the sample under test and collects data (which is in term of scattering parameters or S-parameters). The primary function of the post-processing portion is then to process the “*collected data*”. Based on this process, electrical (i.e., electrical and magnetic property distribution) and geometrical parameters (i.e., shape, size and location) of an imaged object or an estimated reflectivity function (i.e., qualitative image) may be determined from the collected data. Therefore, any improvement over the currently-available imaging systems should target both post-processing and hardware parts.

In the post-processing portion, many different techniques have been developed to image an embedded object/target inside of a planar layered structure (which is the most applicable case of inhomogeneous media). These techniques can be classified as either quantitative imaging techniques or qualitative imaging techniques. Quantitative imaging



techniques or inverse scattering methods estimate the electrical and geometrical properties (distributions) of an imaged object by solving a nonlinear inverse problem. The nonlinear inverse problem is commonly solved iteratively (i.e., forward iterative procedure). Required computational resources (i.e., time and computer memory) and calculation complexity are the major disadvantages associated with these techniques. On the other hand, qualitative imaging techniques calculate a reflectivity function or qualitative image to represent the object/target profile. Most of the techniques that belong to this category use migration-based algorithms to reconstruct the unknown image profile. The collected data, consisting of reflected or scattered field data from an object or source, can be migrated or back-propagated to the object/target location by adding appropriate time shift (in time domain) or phase shift (in frequency domain), respectively. Synthetic aperture radar (SAR) is one of the most well-known qualitative imaging techniques, which was initially developed for free-space or homogenous media. This method is robust, easy to implement, and fast. However, during the algorithm derivation for the SAR method, it is assumed that the background medium which surrounds the object to be homogeneous, without discontinuity, and lossless. Therefore, using SAR to image an embedded object in a layered structure may result in an image with unfocused and incorrectly positioned indication of the object. Moreover, when considering a lossy layer in the path between the scanning antenna and the object, SAR algorithm is unable to properly determine the location of embedded object.

To address the first limitation of the SAR algorithm, a method, referred to as modified piecewise SAR (MPW-SAR) was developed in here, which takes into account the electrical and physical properties of each layer at a time (hence, piecewise). Moreover, this technique as an improvement over previously studied piecewise SAR, includes the discontinuity between layers using transmission and reflection coefficients. The results show that this technique is suitable for objects with high dielectric contrast compared with their surrounding material (i.e., strong scatterers). However, this technique does not account for multiple reflections within any given layer in the structure and it is not suitable for imaging embedded objects/targets inside lossy materials.

Consequently, to address all of the three limitations of SAR, another method was developed, which is referred to as Wiener filter-based layered SAR (WL-SAR). First, the

relationship between the layered structure, collected data, and the qualitative image was established using the Green's function of layered structures. Mathematical manipulations were then invoked to cast the imaging problem into a deconvolution procedure where Wiener filter deconvolution was used.

Through extensive simulations and experiments the efficacy of both proposed methods to image embedded active/passive targets/objects was verified. It was shown that, MPW-SAR is robust, easy to implement, and fast. However, for a layered structure with loss and high contrast between layers, WL-SAR obtained superior images in comparison with MPW-SAR and SAR.

On the other hand, and from hardware point of view, antenna is necessary for data collection from the sample under test. Rather than conventional requirements for the scanning antenna such as wide beam width and wide bandwidth, having an antenna which its characteristics can be actively changed, may increase the probability of object/target detection in a dynamic and unknown media. This requires that antennas cover a wide range of characteristics (i.e., operating band, polarization, and pattern), or an antenna whose various important characteristics can be tuned. The overall bulkiness, size problem, and noise/interference issues limit the application of wideband or multiband antennas for this purpose. On the contrary, reconfigurable antennas show a great promise and potential to be served for this purpose. Moreover, growing multiradio communication devices spurs additional interest and accelerated the demands for the reconfigurable antennas. Despite many advantages offered by reconfigurable antennas, the topic is fairly recent, and there is not a robust and methodical design procedure for reconfigurable antennas. Most of the reported works in literatures deal with a specific and application-dependent reconfigurable antenna.

Therefore, a methodical reconfigurable antenna design procedure was introduced and explained. Then, based on this proposed methods, three different versions of a novel reconfigurable coplanar waveguide-fed slot antenna were designed that covers three/four distinct bands with reasonable gain. These three antennas were built and tested. The measurement results were compared with the full-wave simulation results. The final version of the reconfigurable antenna could successfully cover all four desired frequency

bands at VHF/UHF/L regions while the lowest operating frequency was as low as 60 MHz.

The work already performed is thorough; however, there is always room for future study and improvement. In the post-processing portion, there are a few things which can be done to improve the microwave imaging system for the layered structures. Finding a more sophisticated procedure to calculate the regularization parameter for WL-SAR method can be useful. An adaptive method can help significantly to improve the introduced WL-SAR method. Also, by considering this fact that many practical applications may require an imaging technique which can be applied on cylindrical and spherical layered structures, the proposed MPW-SAR and WL-SAR can be modified to make them appropriate for these applications. This can be performed by replacing the Green's function of planar layered structure with the Green's function of cylindrical or spherical layered structures. For the hardware part, rather than antenna, the hardware part which includes measurement tools and recording parts may be modified in order to be consistent with a reconfigurable antenna. Making the entire imaging system portable and reconfigurable may increase the performance of the system and its applicability. Moreover, to add extreme flexibility to the collecting antenna, working on recently introduced concept namely reconfigurable pixel antennas may be useful. An initial study was performed on this concept; however, there still exist a bigger room for the future studies.

## BIBLIOGRAPHY

- [1] P.J. Shull, *Nondestructive Evaluation – Theory, Techniques, and Applications*, Marcel Dekker, 2002, New York.
- [2] R. Zoughi, *Microwave Non-Destructive Testing and Evaluation*, The Netherlands: Kluwer Academic Publishers, 2000.
- [3] M. Soumekh, *Synthetic Aperture Radar Signal Processing*, first edition, New York: Wiley, 1999.
- [4] S. Kharkovsky, and R. Zoughi, “Microwave and Millimeter Wave Nondestructive Testing and Evaluation – Overview and Recent Advances,” *IEEE Instrumentation and Measurement Magazine*, vol. 10, no. 2, pp. 26-38, Apr. 2007.
- [5] J. M. Lopez-Sanchez and J. Fortuny-Guash, “3D Radar Imaging Using Range Migration Techniques,” *IEEE Transactions on Antennas and Propagation*, vol. 48, no. 5, pp. 728 - 737, May 2000.
- [6] D. Sheen, D. McMakin, and T. E. Hall, “Three-dimensional Millimeterwave Imaging for Concealed Weapon Detection,” *IEEE Transactions on Microwave Theory and Techniques*, vol. 49, no. 9, pp. 1581-1592, September 2001.
- [7] C. Gilmore, I. Jeffrey, and J. Lovetri, “Derivation and comparison of SAR and frequency–wavenumber migration within a common inverse scalar wave problem formulation,” *IEEE Transactions on Geoscience and Remote Sensing*, vol. 44, no. 6, pp. 1454–1461, Jun. 2006.
- [8] V. Krozer, T. Loffler, J. Dall, A. Kusk, F. Eichhorn, R.K. Olsson, J.D. Buron, P.U. Jepsen, V. Zhurbenko, T. Jensen, “Terahertz Imaging Systems With Aperture Synthesis Techniques,” *IEEE Transactions on Microwave Theory and Techniques*, vol.58, no.7, pp.2027,2039, July 2010.
- [9] Li. Lianlin, W. Zhang, F. Li, “Derivation and Discussion of the SAR Migration Algorithm within Inverse Scattering Problem: Theoretical Analysis,” *IEEE Transactions on Geoscience and Remote Sensing*, vol.48, no.1, pp.415-422, Jan. 2010.
- [10] C. Pichot, L. Jofre, G. Peronnet, J. Bolomey, “Active microwave imaging of inhomogeneous bodies,” *IEEE Transactions on Antennas and Propagation*, vol.33, no.4, pp. 416- 425, Apr. 1985.

- [11] Q. H. Liu, Z. Q. Zhang, T. Wang, G. Ybarra, L. W. Nolte, J. A. Bryan, and W. T. Joines, "Active microwave imaging I: 2-D forward and inverse scattering methods," *IEEE Transactions on Microwave Theory Techniques*, vol. 50, no. 1, pp. 123–133, Jan. 2002.
- [12] C. Yu, M. Yuan, J. Stang, E. Bresslour, R. T. George, G. A. Ybarra, W. T. Joines, and Q. H. Liu, "Active microwave imaging II: 3-D system prototype and image reconstruction from experimental data," *IEEE Transactions on Microwave Theory and Techniques*, vol. 56, no. 4, pp. 991–1000, Apr. 2008.
- [13] W. C. Chew and J. H. Lin, "A frequency-hopping approach for microwave imaging of large inhomogeneous bodies," *IEEE Microwave Guide Wave Letters*, vol. 5, no. 12, pp. 439–441, Dec. 1995.
- [14] F. Li, Q. H. Liu, and L. P. Song, "Three-dimensional reconstruction of objects buried in layered media using born and distorted born iterative methods," *IEEE Geoscience and Remote Sensing Letters*, vol. 1, no. 2, pp. 107–111, Apr. 2004.
- [15] W. C. Chew and Y. M. Wang, "Reconstruction of two-dimensional permittivity distribution using the distorted born iteration method," *IEEE Transactions on Medical Imaging*, vol. 9, pp. 218–225, June 1990.
- [16] L. P. Song, Q. H. Liu, F. Li, and Z. Q. Zhang, "Reconstruction of Three-Dimensional Objects in Layered Media: Numerical Experiments," *IEEE Transactions on Antennas and Propagation*, vol. 53, no. 4, pp. 1556 - 1561, April 2005.
- [17] M. Dehmollaian, K. Sarabandi, "Refocusing Through Building Walls Using Synthetic Aperture Radar," *IEEE Transactions on Geoscience and Remote Sensing*, vol. 46, no. 6, pp.1589-1599, January 2008.
- [18] E. C. Fear, S. C. Hagness, P. M. Meaney, M. Okoniewski, M. A. Stuchly, "Enhancing Breast Tumor Detection with Near-Field Imaging," *IEEE Microwave Magazine*, vol. 3, no. 1, pp.48-56, March 2002.
- [19] M. Vossiek, A. Urban, S. Max, P. Gulden, "Inverse Synthetic Aperture Secondary Radar Concept for Precise Wireless Positioning," *IEEE Transactions on Microwave Theory and Techniques*, vol. 55, no. 11, pp. 2447-2453, November 2007.
- [20] P. C. Chang, R. J. Burkholder, J. L. Volakis, "Adaptive CLEAN With Target Refocusing for Through-Wall Image Improvement," *IEEE Transactions on Antennas and Propagation*, vol.58, no.1, pp.155,162, Jan. 2010.

- [21] I. G. Cumming and F. H. Wong, *Digital Signal Processing of Synthetic Aperture Radar Data: Algorithms and Implementation*, Norwood, MA: Artech House, 2005.
- [22] M. Dehmollaian, M. Thiel, K. Sarabandi, "Through-the-Wall Imaging Using Differential SAR," *IEEE Transactions on Geoscience and Remote Sensing*, vol.47, no.5, pp.1289,1296, May 2009.
- [23] Joseph T. Case (email address; j.t.case@mst.edu), PW-SAR, October 2013.
- [24] J. T. Case, M. T. Ghasr, R. Zoughi, "Optimum Two-Dimensional Uniform Spatial Sampling for Microwave SAR-Based NDE Imaging Systems," *IEEE Transactions on Instrumentation and Measurement*, vol. 60, no. 12, pp.3806-3815, Dec. 2011.
- [25] S. Yang, C. Zhang, H. Pan, A. Fathy, V. Nair, "Frequency-reconfigurable antennas for multiradio wireless platforms," *IEEE Microwave Magazine*, vol.10, no.1, pp.66-83, Feb. 2009.
- [26] A. C. K. Mak, C. R. Rowell, R. D. Murch, and C. L. Mak, "Reconfigurable Multiband Antenna Designs for Wireless Communication Devices," *IEEE Transactions on Antennas and Propagation*, vol. 55, no. 7, pp. 1919–1928, July 2007.
- [27] N. Behdad, and K. Sarabandi, "A Varactor-Tuned Dual-Band Slot Antenna," *IEEE Transactions on Antennas and Propagation*, vol. 54, no. 2, pp. 401-408, Feb. 2006.
- [28] R. Azadegan, K. Sarabandi, "A novel approach for miniaturization of slot antennas," *IEEE Transactions on Antennas and Propagation*, vol.51, no.3, pp. 421- 429, Mar. 2003.
- [29] K. J. Vinoy, J. K. Abraham, V. K. Varadan, "On the relationship between fractal dimension and the performance of multi-resonant dipole antennas using Koch curves," *IEEE Transactions on Antennas and Propagation*, vol.51, no.9, pp.2296,2303, Sep. 2003.
- [30] Y. X. Guo, M. Y-W. Chia, Z. N. Chen, "Miniature built-in multiband antennas for mobile handsets," *IEEE Transactions on Antennas and Propagation*, vol.52, no.8, pp.1936,1944, Aug. 2004.
- [31] C. A. Balanis, *Advanced Engineering Electromagnetics*, John Wiley and Sons, New York, 1989.
- [32] R. E. Collin, *Field Theory of Guided Waves*, Second Edition, New York, IEEE Press, 1991.

- [33] K. A. Michalski, D. Zheng, "Electromagnetic scattering and radiation by surfaces of arbitrary shape in layered media. I. Theory," *IEEE Transactions on Antennas and Propagation*, vol.38, no.3, pp.335-344, Mar. 1990.
- [34] K. A. Michalski, J. R. Mosig, "Multilayered media Green's functions in integral equation formulations," *IEEE Transactions on Antennas and Propagation*, vol.45, no.3, pp.508-519, Mar. 1997.
- [35] Y. P. Chen, L. Jiang, Z. G. Qian, W. C. Chew, "An Augmented Electric Field Integral Equation for Layered Medium Green's Function," *IEEE Transactions on Antennas and Propagation*, vol.59, no.3, pp.960-968, Mar. 2011.
- [36] W. C. Chew, *Waves and Fields in Inhomogeneous Media*, Piscataway, NJ: IEEE Press, 1995.
- [37] W. C. Chew, Si-Y. Chen, "Response of a point source embedded in a layered medium," *IEEE Antennas and Wireless Propagation Letters*, vol.2, no.1, pp.254-258, 2003.
- [38] Y. P. Chen, W. C. Chew, L. Jiang, "A New Green's Function Formulation for Modeling Homogeneous Objects in Layered Medium," *IEEE Transactions on Antennas and Propagation*, vol.60, no.10, pp.4766-4776, Oct. 2012.
- [39] W. H. Hayt and J. E. Kemmerly, *Engineering Circuit Analysis*, Fourth Edition, McGraw-Hill Book Company Inc., USA, 1986.
- [40] [www.mathworks.com](http://www.mathworks.com). Matlab, November 2013.
- [41] A. Hochman, Y. Leviatan, "A Numerical Methodology for Efficient Evaluation of 2D Sommerfeld Integrals in the Dielectric Half-Space Problem," *IEEE Transactions on Antennas and Propagation*, vol.58, no.2, pp.413-431, Feb. 2010.
- [42] Available: <http://www.webee.technion.ac.il/people/leviatan/ndsdp/index.htm>. ND-SDP, November 2013.
- [43] F. Lewis, "Wireless Sensor Networks," *Smart Environments Technologies, Protocols, and Applications*, D. J. Cook and S. K. Das, Eds. New York: Wiley, 2004.
- [44] J. H. Chien, C. Y. Tsai, Y. T. Cheng, C. R. Yang, P. Y. Wang, T. L. Chang, D. S. Lee, C. W. Chang, W. P. Chou, C. C. Chiang, Y. W. Lee, P. H. Chen, "A RFID Tag Based Remote DNA sensing System," *1st IEEE International Conference on Nano/Micro Engineered and Molecular Systems*, 2006. NEMS '06., pp.278,282, 18-21 Jan. 2006.

- [45] C. R. Medeiros, J. R. Costa, C. A. Fernandes, "RFID Reader Antennas for Tag Detection in Self-Confined Volumes at UHF," *IEEE Antennas and Propagation Magazine*, vol.53, no.2, pp.39-50, Apr. 2011.
- [46] M. K. Hu, "On measurements of microwave E and H field distributions by using modulated scattering methods," *IRE Transactions on Microwave Theory and Techniques.*, vol. 8, no. 3, pp. 295–300, May 1960.
- [47] M. A. Abou-Khousa, M. T. Ghasr, S. Kharkovsky, D. Pommerenke, R. Zoughi, "Modulated Elliptical Slot Antenna for Electric Field Mapping and Microwave Imaging," *IEEE Transactions on Antennas and Propagation*, vol.59, no.3, pp.733-741, Mar. 2011.
- [48] M. T. Ghasr, M. A. A-Khousa, S. Kharkovsky, R. Zoughi, D. Pommerenke, "Portable Real-Time Microwave Camera at 24 GHz," *IEEE Transactions on Antennas and Propagation*, vol.60, no.2, pp.1114-1125, Feb. 2012.
- [49] J. T. Case, M. T. Ghasr, and R. Zoughi, "Correcting Mutual Coupling and Poor Isolation for Real-Time 2D Microwave Imaging Systems," *IEEE Transactions on Instrumentation and Measurement*. (In Review)
- [50] J. T. Case, M. T. Ghasr, and R. Zoughi, "Nonuniform Manual Scanning for Rapid Microwave Nondestructive Evaluation Imaging," *IEEE Transactions on Instrumentation and Measurement*, vol. 62, no. 5, pp. 1250-1258, May 2013.
- [51] H. Kajbaf, J. T. Case, Z. Yang, and Y. R. Zheng, "Compressed Sensing for SAR-Based Wideband 3D Microwave Imaging System Using Nonuniform FFT," *To Appear in Institution of Engineering and Technology Radar, Sonar & Navigation*.
- [52] C. A. Balanis, *Antenna Theory: Analysis And Design*, Second Edition, Wiley, 1997.
- [53] N. Wiener, *Extrapolation, Interpretation, and Smoothing of Stationary Time Series with Engineering Application*, *M.I.T. Press and John Wiley and Sons*, 1949.
- [54] F. Honarvar, H. Sheikhzadeh, M. Moles and A. N. Sinclair, "Improving the Time-Resolution and Signal-to-Noise Ratio of Ultrasonic NDE Signals," *Ultrasonics*, Vol. 41, pp. 755–763, 2004.
- [55] H. Karsli, "Further Improvement of Temporal Resolution of Seismic Data by Autoregressive (AR) Spectral Extrapolation," *Journal of Applied Geophysics*, Vol. 59, No. 4, pp. 324–336, 2006.



- [56] D. Meng, V. Sethu, E. Ambikairajah and L. Ge, "A Novel Technique for Noise Reduction in InSAR Images," *IEEE Geoscience and Remote Sensing Letters*, Vol. 4, No. 2, pp. 226–230, Apr. 2007.
- [57] M. Piles, A. Camps, M. Vall-llossera, A. Monerri, M. Talone and J. L. A. Perez, "Deconvolution Algorithms in Image Reconstruction for Aperture Synthesis Radiometers," *IEEE Geoscience and Remote Sensing Symposium*, pp. 1460–1463, July 2007.
- [58] S. Solbo, and T. Eltoft, "A Stationary Wavelet-Domain Wiener Filter for Correlated Speckle," *IEEE Transactions on Geoscience and Remote Sensing*, Vol. 46, No. 4, pp. 1219–1230, Apr. 2008.
- [59] H. Ghennioui, F. Bourzeix, "Architecture solution for real-time deblurring image/video technique," *2011 International Conference on Multimedia Computing and Systems (ICMCS)*, pp.1-5, Apr. 2011.
- [60] G. Pagana, S. Salvador, G. Vecchi, "Signal processing techniques for microwave imaging of the breast," *First International Symposium on Applied Sciences on Biomedical and Communication Technologies*, 2008. ISABEL '08, pp.1-5, Oct. 2008.
- [61] S. Kharkovsky, B. J. Carroll, M. T. Ghasr and R. Zoughi, "Dielectric Property Characterization of Refractory Materials Using Microwave Open-Ended and Completely Filled Waveguide Methods," *Proceedings of the Third International Conference on Electromagnetic Near-Field Characterization and Imaging*, St. Louis, Missouri, Aug. 2007.
- [62] S. Kharkovsky and R. Zoughi, "Millimeter wave nondestructive evaluation of corrosion under paint in steel structures," in *Review of Progress in Quantitative Nondestructive Evaluation 25B*, D.O. Thompson and D.E. Chimenti, Eds. Melville, NY: American Institute of Physics, 2006.
- [63] M. Benedetti, M. Donelli, D. Lesselier, A. Massa, "A two-step inverse scattering procedure for the qualitative imaging of homogeneous cracks in known host media - preliminary results," *IEEE Antennas and Wireless Propagation Letters*, vol.6, pp.592,595, 2007.
- [64] C. Thajudeen, A. Hoorfar, W. Zhang, "Theory and experiment on imaging of walls' interior structures using diffraction tomography," *2012 IEEE Antennas and Propagation Society International Symposium (APSURSI)*, pp.1,2, 8-14 July 2012.

- [65] M.T. Ghasr, D. Simms and R. Zoughi, "Multimodal Solution for a Waveguide Radiating into Multilayered Structures - Dielectric Property and Thickness Evaluation," *IEEE Transactions on Instrumentation and Measurement*, vol. 58, no. 5, pp. 1505-1513, May 2009.
- [66] <http://www.cst.com/Content/Documents/Events/UGM2007/02-Balk.pdf>. CST Microwave Studio, November 2013.
- [67] G. Roqueta, L. Jofre, M. Feng, "Microwave Non-Destructive evaluation of corrosion in reinforced concrete structures," *Proceedings of the 5th European Conference on Antennas and Propagation (EUCAP)*, pp.787,791, 11-15 April 2011.
- [68] N. Qaddoumi, L. Handjojo, T. Bigelow, J. Easter, A. Bray, and R. Zoughi, "Microwave corrosion detection using open-ended rectangular waveguide sensors," *Materials Evaluation*, vol. 58, no. 2, pp. 178–184, Feb. 2000.
- [69] O. Buyukozturk, "Electromagnetic properties of concrete and their significance in nondestructive testing," *Transportation Research Record*, No. 1574, Advances in Concrete and Concrete Pavement Construction, 10-17, 1997.
- [70] A. Muqabel, A. Safaai-Jazi, A. Bayram, A.M. Attiya, S.M. Riad, S.M., "Ultrawideband through-the-wall propagation," *IEE Proceedings Microwaves, Antennas and Propagation*, pp.581,588, 9 Dec. 2005.
- [71] S. Kharkovsky, J. T. Case, M. T. Ghasr, R. Zoughi, S. W. Bae, and A. Belarbi , "Application of microwave 3D SAR imaging technique for evaluation of corrosion in steel rebars embedded in cement-based structures," *Review of Progress in Quantitative Nondestructive Evaluation: Volume 31*, AIP. Conf. Proc. 1430,1516-1523, 2012.
- [72] M. E. Bialkowski, "Ultra wideband microwave system with novel image reconstruction strategies for breast cancer detection," *Microwave Conference (EuMC), 2010 European* , pp.537,540, 28-30 Sept. 2010.
- [73] S. S. Tiang, M. F. Ain, M. Z. Abdullah, "Compact and wideband wide-slot antenna for microwave imaging system," *2011 IEEE International RF and Microwave Conference (RFM)*, pp.63,66, 12-14 Dec. 2011.
- [74] X. Zeng, A. Fhager, M. Persson, P. Linner, H. Zirath, "Accuracy Evaluation of Ultrawideband Time Domain Systems for Microwave Imaging," *IEEE Transactions on Antennas and Propagation*, vol.59, no.11, pp.4279,4285, Nov. 2011.

- [75] D. C. Chang, "UWB Antennas and Their Applications," *International Workshop on Antenna Technology: Small Antennas and Novel Metamaterials*, 2008. iWAT 2008. pp.14,19, 4-6 Mar. 2008.
- [76] M. Klemm, I. Z. Kovcs, G. F. Pedersen, G. Troster, "Novel small-size directional antenna for UWB WBAN/WPAN applications," *IEEE Transactions on Antennas and Propagation*, vol.53, no.12, pp.3884-3896, Dec. 2005.
- [77] Y. Hacene, X. Shuguo, "Study of a novel ultra-wideband monopole antenna for EMC measurement applications," *Environmental Electromagnetics (CEEM)*, 2012 6th Asia-Pacific Conference on , vol., no., pp.393,395, 6-9 Nov. 2012.
- [78] N. Bayatmaku, P. Lotfi, M. Azarmanesh, S. Soltani, "Design of Simple Multiband Patch Antenna for Mobile Communication Applications Using New E-Shape Fractal," *IEEE Antennas and Wireless Propagation Letters*, vol.10, no., pp.873,875, 2011.
- [79] R. L. Haupt, M. Lanagan, "Reconfigurable Antennas," *IEEE Antennas and Propagation Magazine*, vol.55, no.1, pp.49,61, Feb. 2013.
- [80] L. J. Chu, "Physical limitations on omnidirectional antennas," *Journal of Applied Physics*, vol. 19, pp. 1163–1175, Dec. 1948.
- [81] H. A. Wheeler, "Fundamental limitations of small antennas," in *Proceeding IRE.*, vol. 35, Dec. 1947, pp. 1479–1484.
- [82] R. C. Hansen, "Fundamental limitations in antennas," *Proceeding IEEE*, vol. 69, pp. 170–182, Feb. 1981.
- [83] J. S. McLean, "A re-examination of the fundamental limits on the radiation Q of electrically small antennas," *IEEE Transaction on Antennas and Propagation.*, vol. 44, pp. 672–676, May 1996.
- [84] D. H. Werner, S. Ganguly, "An Overview of Fractal Antenna Engineering Research," *IEEE Antennas and Propagation Magazine*, vol.45, no.1, pp. 38- 57, Feb 2003.
- [85] S.R. Best, "On the resonant properties of the Koch fractal and other wire monopole antennas," *IEEE Antennas and Wireless Propagation Letters*, vol.1, pp. 74- 76, 2002.
- [86] R. H. Patnam, "Broadband CPW-Fed Planar Koch Fractal Loop Antenna," *IEEE Antennas and Wireless Propagation Letters*, vol.7, pp.429, 431, 2008.

- [87] D. D. Krishna, M. Gopikrishna, C. K. Anandan, P. Mohanan, K. Vasudevan, "CPW-Fed Koch Fractal Slot Antenna for WLAN/WiMAX Applications," *IEEE Antennas and Wireless Propagation Letters*, vol.7, pp.389,392, 2008.
- [88] C. P. Baliarda, C. B. Borau, M.N. Rodero, J. R. Robert, "An iterative model for fractal antennas: application to the Sierpinski gasket antenna," *IEEE Transactions on Antennas and Propagation*, vol.48, no.5, pp.713,719, May 2000.
- [89] J. P. Gianvittorio, Y. Rahmat-Samii, "Fractal antennas: a novel antenna miniaturization technique, and applications," *IEEE Antennas and Propagation Magazine*, vol.44, no.1, pp.20-36, Feb 2002.
- [90] P. L. Chi, R. Waterhouse, T. Itoh, "Antenna Miniaturization Using Slow Wave Enhancement Factor from Loaded Transmission Line Models," *IEEE Transactions on Antennas and Propagation*, vol.59, no.1, pp.48,57, Jan. 2011.
- [91] C. R. Rowell, R. D. Murch, "A capacitively loaded PIFA for compact mobile telephone handsets," *IEEE Transactions on Antennas and Propagation*, vol.45, no.5, pp.837-842, May 1997.
- [92] K. Sarabandi, R. Azadegan, H. Mosallaei, and J. Harvey, "Antenna miniaturization techniques for applications in compact wireless transceivers," *XXVIIth General Assembly of URSI*, Maastricht, the Netherlands, August 2002.
- [93] R. Azadegan, K. Sarabandi, "A novel approach for miniaturization of slot antennas," *IEEE Transactions on Antennas and Propagation*, vol.51, no.3, pp. 421- 429, March 2003.
- [94] R. Azadegan, and K. Sarabandi, "Bandwidth Enhancement of Miniaturized Slot Antennas Using Folded, Complementary, and Self-Complementary Realizations," *IEEE Transactions on Antennas and Propagation*, vol.55, no.9, pp.2435-2444, Sept. 2007.
- [95] C. Cheype, C. Serier, M. Thevenot, T. Monediere, A. Reineix, B. Jecko, "An electromagnetic bandgap resonator antenna," *IEEE Transactions on Antennas and Propagation*, vol.50, no.9, pp.1285,1290, Sep. 2002.
- [96] D. Guha, M. Biswas, Y.M. Antar, "Microstrip patch antenna with defected ground structure for cross polarization suppression," *IEEE Antennas and Wireless Propagation Letters*, vol.4, no.1, pp.455,458, 2005.
- [97] D. Nashaat, H. A. Elsadek, E. Abdallah, H. Elhenawy, M.F. Iskander, "Multiband and miniaturized inset feed microstrip patch antenna using multiple spiral-shaped defect ground structure (DGS)," *IEEE Antennas and Propagation Society International Symposium*, 2009. APSURSI '09, pp.1-4, 1-5 June 2009.

- [98] A. K. Arya, M.V. Kartikeyan, A. Patnaik, "On the size reduction of microstrip antenna with DGS," *2010 35th International Conference on Infrared Millimeter and Terahertz Waves (IRMMW-THz)*, pp.1-3, 5-10 Sept. 2010.
- [99] J. Rashed and C. T. Tai, "A new class of resonant antennas," *IEEE Transactions on Antennas and Propagation*, vol. 39, no. 9, pp. 1428–1430, Sep. 1991.
- [100] J. Oh, and K. Sarabandi, "A novel approach for miniaturization of circularly polarized patch antennas," *2011 IEEE International Symposium on Antennas and Propagation (APSURSI)*, pp.880, 883, 3-8 July 2011.
- [101] W. S. Chen, C. K. Wu, and K. L. Wong, "Novel Compact Circularly Polarized Square Microstrip Antenna," *IEEE Transactions on Antennas and Propagation*, vol 49, pp. 340-342, Mar. 2001.
- [102] C. T. Rodenbeck, "Planar Miniature RFID Antennas Suitable for Integration With Batteries," *IEEE Transactions on Antennas and Propagation*, vol.54, no.12, pp.3700, 3706, Dec. 2006.
- [103] K. V. S. Rao, P.V. Nikitin, S. F. Lam, "Antenna design for UHF RFID tags: a review and a practical application," *IEEE Transactions on Antennas and Propagation*, vol.53, no.12, pp.3870, 3876, Dec. 2005.
- [104] <http://www.webermarking.com/images/Alien%20RFID%20Inlays.pdf>. Alien RFID Tag, October 2013.
- [105] H. Makimura, Y. Watanabe, K. Watanabe, H. Igarashi, "Evolutional design of small antennas for passive UHF-band RFID," *2010 14th Biennial IEEE Conference on Electromagnetic Field Computation (CEFC)*, pp.1,1, 9-12 May 2010.
- [106] S. Ghadarghadr, A. Ahmadi, H. Mosallaei, "Negative Permeability-Based Electrically Small Antennas," *IEEE Antennas and Wireless Propagation Letters*, vol.7, pp.13-17, 2008.
- [107] Y.-S. Takigawa, S. Kashihara, F. Kuroki, "Integrated Slot Spiral Antenna Etched on Heavily-High Permittivity Piece," *Asia-Pacific APMC Microwave Conference*, pp.1-4, 11-14 Dec. 2007.
- [108] A. Natarajan, A. Komijani, X. Guan, A. Babakhani, A. Hajimiri, "A 77-GHz Phased-Array Transceiver With On-Chip Antennas in Silicon: Transmitter and Local LO-Path Phase Shifting," *IEEE Journal of Solid-State Circuits*, vol.41, no.12, pp.2807-2819, Dec. 2006.
- [109] J.S. Colburn, Y. Rahmat-Samii, "Patch antennas on externally perforated high dielectric constant substrates," *IEEE Transactions on Antennas and Propagation*, vol.47, no.12, pp.1785-1794, Dec 1999.

- [110] H. Mosallaei, K. Sarabandi, "Magneto-dielectrics in electromagnetics: concept and applications," *IEEE Transaction on Antennas and Propagation*, vol.52, no.6, pp. 1558- 1567, June 2004.
- [111] W. L. Stutzman and G. A. Thiele, *Antenna theory and design*, John Wiley & Sons, pp121-128,1998.
- [112] Q. Jinghui, L. Shu, Y. Caitian, Y. Qidi, , "A Novel Printed Fractal Log-Periodic Dipole Antenna," *5th International Conference on Microwave Electronics: Measurements, Identification, Applications, 2005. MEMIA'05*, pp. 50- 53, 13-15 Dec. 2005.
- [113] B. Wang, A. Chen, D. Su, "An improved fractal tree log-periodic dipole antenna," *Asia-Pacific Symposium on Electromagnetic Compatibility and 19th International Zurich Symposium on Electromagnetic Compatibility, APEMC 2008*, pp.831-834, 19-23 May 2008.
- [114] Z. H. Song, S. Tian, J. H. Qiu, "The Simulation and Design of a Meander Archimedean Spiral Antenna," *IEEE Antennas and Propagation Society International Symposium 2006*, pp.3673-3676, 9-14 July 2006.
- [115] I. A. Osaretin, A. Torres, C. C. Chen, "A Novel Compact Dual-Linear Polarized UWB Antenna for VHF/UHF Applications," *IEEE Antennas and Wireless Propagation Letters*, vol.8, no., pp.145-148, 2009.
- [116] M. E. Bialkowski, Y. Wang, "A size-reduced exponentially Tapered Slot Antenna with corrugations for directivity improvement," *Asia Pacific Microwave Conference*, pp.2482-2485, 7-10 Dec. 2009.
- [117] V. Mikhnev, P. Vainikainen, "Wideband tapered-slot antenna with corrugated edges for GPR applications," *33rd European Microwave Conference*, vol.2, pp. 727- 729 vol.2, 7-9 Oct. 2003.
- [118] A. M. Abbosh, "Miniaturization of Planar Ultrawideband Antenna via Corrugation," *IEEE Antennas and Wireless Propagation Letters*, vol.7, no., pp.685-688, 2008.
- [119] R. L. Haupt, M. Lanagan, "Reconfigurable Antennas," *IEEE Antennas and Propagation Magazine*, vol.55, no.1, pp.49-61, Feb. 2013.
- [120] D. R. Lopez, "Real-time Reconfigurable Pixelled Antennas," Master Thesis, Polytechnic University of Catalonia, July 2010.

- [121] G. M. Rebeiz, "RF MEMS switches: status of the technology," *12th International Conference on TRANSDUCERS, Solid-State Sensors, Actuators and Microsystems*, vol.2, pp.1726,1729 vol.2, 8-12 June 2003.
- [122] S. B. Byun, J. A. Lee, J. H. Lim, and T. Y. Yun, "Reconfigurable ground-slotted patch antenna using PIN diode switching," *ETRI J.*, vol. 29, pp. 832–834, Dec. 2007.
- [123] F. Yang and Y. Rahmat-Samii, "A Reconfigurable Patch Antenna Using switchable Slots for Circular Polarization Diversity," *IEEE Microwave and Wireless Components Letters*, 12, 3, pp. 96-98, March 2002.
- [124] E. R. Brown, "RF-MEMS Switches for Reconfigurable Integrated Circuits," *IEEE Transactions on Microwave Theory and Techniques*, 46, 11, pp. 1868-1880, Nov. 1998.
- [125] S. Nikolaou, N. D. Kingsley, G. E. Ponchak, J. Papapolymerou, and M. M. Tentzeris, "UWB Elliptical Monopoles with a Reconfigurable Band Notch Using MEMS Switches Actuated Without Bias Lines," *IEEE Transactions on Antennas and Propagation*, AP-57, 8, pp. 2242-2251, August 2009.
- [126] C. Wu, T. Wang, A. Ren, D.G. Michelson, "Implementation of Reconfigurable Patch Antennas Using Reed Switches," *IEEE Antennas and Wireless Propagation Letters*, vol.10, no., pp.1023,1026, 2011.
- [127] S. Kharkovsky, M. T. Ghasr, M. A. Abou-Khousa, and R. Zoughi, "K-Band Varactor Diode-Tuned Elliptical Slot Antenna for Wideband Imaging," *IEEE Transactions on Antennas and Propagation*, vol.59, no.11, pp.4325,4328, Nov. 2011.
- [128] R.L. Haupt, "Reconfigurable patch with switchable conductive edges," *Microwave and Optical Technology Letters*, vol. 51, no. 7, pp. 1757-1760, Jul 2009.
- [129] J. R. Flemish, H. W. Kwan, R. L. Haupt and M. Lanagan, "A new silicon-based photoconductive microwave switch," vol. 51, no. 1, *Microwave and Optical Technology Letters*, Jan 2009.
- [130] D. M. Pozar and V. Sanchez, "Magnetic Tuning of a Microstrip Antenna on a Ferrite Substrate," *Electronics Letters*, 24, 12, pp. 729-731, June 9, 1988.
- [131] Y.T. Lo and S.W. Lee, *Antenna handbook: theory, applications, and design*, Van Nostrand Reinhold. Company, New York, 1988.
- [132] <http://www.ansys.com>. HFSS, October 2013.

- [133] H. Oraizi and M. Fallahpour, "Nonuniformly spaced linear array design for the specified beamwidth/sidelobe level or specified directivity/sidelobe level with mutual coupling considerations," *Progress in Electromagnetic Research. M*, vol. 4, pp. 185–209, 2008.
- [134] H. Oraizi, M. Fallahpour, "Sum, Difference and Shaped Beam Pattern Synthesis by Non-Uniform Spacing and Phase Control," *IEEE Transactions on Antennas and Propagation*, vol.59, no.12, pp.4505, 4511, Dec. 2011.
- [135] M. Fallahpour, M.A. Baumgartner, A. Kothari, M.T. Ghasr, D. Pommerenke, R. Zoughi, "Compact Ka-Band One-Port Vector Reflectometer Using a Wideband Electronically Controlled Phase Shifter," *IEEE Transactions on Instrumentation and Measurement*, vol.61, no.10, pp.2807,2816, Oct. 2012.
- [136] [http://interoperability.nj.gov/spectrum/pubsaf\\_currfutneeds.pdf](http://interoperability.nj.gov/spectrum/pubsaf_currfutneeds.pdf). Public Safety Bands, September 2013.
- [137] D. M. Pozar, *Microwave Engineering*, 2d Edition, John Wiley & Sons Inc., 1998.
- [138] H.-D. Chen, "Broadband CPW-fed square slot antennas with a widened tuning stub," *IEEE Transactions on Antennas and Propagation*, vol. 51, no. 8, pp. 1982–1986, Aug. 2003.
- [139] <http://sine.ni.com/nips/cds/view/p/lang/en/nid/201987>. NI USB-6009, November 2013.
- [140] <http://www.ni.com/dataacquisition/nidaqmx>. NI Measurement and Automation, November 2013.
- [141] <http://www.mouser.com/ProductDetail/MEDER-electronic-Standex/KSK-1A04-1015/?qs=JzJq8kwFq1kOiE9VTbKirw==>, Reed Switch, October 2013.
- [142] [http://www.aaroniausa.com/test\\_report/BicoLOG-E.pdf](http://www.aaroniausa.com/test_report/BicoLOG-E.pdf), BicoLOG, July 2013.



## VITA

Mojtaba Fallahpour was born in Karaj, Tehran, Iran. He received the B.Sc. degree in Electrical Engineering majoring Electronics from the Iran University of Science and Technology (IUST), in 2005. He received the M.Sc. degree in Electrical Engineering majoring Fields and Waves (Telecommunications) from IUST, in 2008, with honor. He completed his Ph.D. in October 2013 at the Missouri University of Science and Technology (Missouri S&T) which was formerly known as University of Missouri Rolla (UMR) in Electrical Engineering with an emphasis in electromagnetics, antenna, and microwave imaging for nondestructive testing applications. He has worked in signal integrity group in Micron Technology, Inc. and hardware group in Cisco systems, Inc. as an intern from June to December 2012. His research interests include microwave and millimeter-wave inspection and testing of materials (nondestructive testing), microwave measurement instrument design, signal integrity and RF design, synthetic aperture radar (SAR)-based microwave imaging, scattering, computational electromagnetics, array antenna pattern synthesis, optimization techniques for antenna and microwave applications, ultra wideband, miniaturized, and reconfigurable antenna design and implementation.

He has over 15 technical publications consisting of journal articles, conference proceedings, and technical reports. He was honored with the 2009 American Society for Nondestructive Testing (ASNT) Graduate Fellowship Award, first ranked student among Fields and Waves (Telecommunication) students in IUST (2008), first prize in graduate research show case (Missouri S&T, 2011), best representative in council of graduate students (Missouri S&T, 2012), and ASNT student travel reimbursement grant (2013). He is a member of IEEE and Eta Kappa Nu.